UNIVERSITY OF OKLAHOMA

GRADUATE COLLEGE

ADVANCING POLYMER MEMBRANES THROUGH CONFIGURATIONAL FREE VOLUME AND MEASUREMENT INNOVATIONS

A DISSERTATION

SUBMITTED TO THE GRADUATE FACULTY

in partial fulfillment of the requirements for the

Degree of

Doctor of Philosophy

in Chemical Engineering

By

William Joseph Box

Norman, Oklahoma

2024

Downloaded from SHAREOK. Persistent Handle URL: https://hdl.handle.net/11244/340445

ADVANCING POLYMER MEMBRANES THROUGH CONFIGURATIONAL FREE VOLUME AND MEASUREMENT INNOVATIONS

A DISSERTATION APPROVED FOR THE

SCHOOL OF SUSTAINABLE CHEMICAL, BIOLOGICAL, AND MATERIALS ENGINEERING

BY THE COMMITTEE CONSISTING OF

Dr. Michele Galizia, Chair

Dr. Bin Wang

Dr. Ngoc Bui

Dr. Ruilan Guo

Dr. Pejman Kazempoor

© Copyright by William Joseph Box 2024

All Rights Reserved.

Acknowledgements

First, I would like to express my gratitude to my advisor, Dr. Michele Galizia. His continuous support and guidance for the last four and a half years have been instrumental in making this work possible. His actions consistently exemplified the ideals he taught, especially regarding the importance of human capital.

I am also thankful to my colleagues, namely Lucas and Matthew, both of which also played crucial roles in making this work possible. I don't know anyone else willing to entertain so many unhinged side-project ideas, but clearly it was for the best, as some of them have received awards and even wound-up becoming core to this dissertation.

To my friends, who kept me company on Discord late into the night, at coffee shops, and on our yearly float trips and other events: I would not have maintained my sanity if it weren't for the degree of camaraderie that we share, and of course the occasional distractions.

Finally, to Sarah, my parents, and the rest of my family: because of your support, life continued to move forward as I made my way through grad school.

Financial support by the US National Science Foundation (NSF) under the grant CBET-1926868 (*Interfacial Engineering*), which funded this work, is also gratefully acknowledged.

Contents

Acknowledgements ---- iv
Contents ---- v
List of Tables ---- x
List of Figures ---- xii
Abstract ---- xxi
Chapter 1. Motivation, Introduction, and Theory ---- 1
1.1. Motivation ---- 1
1.2. The Solution-Diffusion Model ---- 3
1.2.1. Permeability ---- 3
1.2.2. Selectivity ---- 5
1.3. Glassy polymers and their influence on membrane behavior ---- 6
1.3.1. Glassy and rubbery polymers ---- 6
1.3.2. Energetics of gas sorption, diffusion, and permeation ---- 8
1.4. Membrane performance limitations ---- 11
1.4.1. Physical aging ---- 11
1.4.2. Plasticization ---- 12
1.4.3. The Robeson upper bound ---- 13
1.5. Configurational Free Volume ---- 15
1.5.1. Current understanding ---- 15
1.5.2. Open questions ---- 16
1.6. Phase Equilibria Models ---- 17
1.6.1. The Dual Mode Model ---- 17
1.6.2. The Guggenheim-Anderson-DeBoer Model ---- 21
1.7. Transient (Diffusion) Models ---- 22
1.7.1. Transient Fickian Sorption ---- 23
1.7.2. The Berens-Hopfenberg Model ---- 24
1.8. Model Analyses ---- 25
1.8.1. Deconvolution of Diffusivity Contributions ---- 26
1.8.2. Zimm-Lundberg Cluster Criteria ---- 27

1.8.3. Isosteric Heat of Sorption----28
1.8.4. Partial Molar Volume----29
1.9. Experimental Analysis and Uncertainty ----29
1.9.1. Linear Error Propagation (LEP)----30
1.9.2. Monte Carlo Error Propagation (MCEP) ----32
1.9.3. Uncertainty Contributions ----34
1.9.4. Uncertainty of Fitting Parameters ----36
1.10. Experimental methods----38
1.10.1. Vapor sorption experiments ----38
1.10.2. Gas Sorption Experiments----41
1.10.3. Optical Dilation Experiments----44
Chapter 2. Entropically Driven Sorption in Polymers Exhibiting Configurational Free Volume----47
2.1. Abstract----47
2.2. Introduction and motivation----48
2.3. Experimental methods----49
2.3.1. Membrane fabrication and thermal rearrangement ----49
2.3.2. Vapor solubility and diffusivity measurements ----50
2.4. Results and Discussion ----51
2.4.1. Equilibrium vapor sorption isotherms----51
2.4.2. Vapor diffusion coefficients----59
2.4.3. General correlations and comparison with other materials ----64
2.4.4. Implications----68
2.5. Conclusions----69
Chapter 3. The Mechanism of Light Gas Sorption in Configurational Free Volume -----71
3.1. Abstract----71
3.2. Introduction ----72
3.3. Experimental ----74
3.3.1. Sorption and transport measurements----74
3.4. Results and Discussion ----74
3.4.1. Pure-gas sorption as a function of temperature and triptycene content ----74

3.4.2. Isosteric heats of sorption ---------- 79
3.4.3. Pure- and mixed-gas solubility-selectivity ---------- 83
3.4.4. Mechanism of light gas transport through configurational free volume ---- 87
3.5. Conclusions ---------- 96
Chapter 4. Computer Vision Based Measurement of Pure- and Mixed-Gas Swelling in Polymers Exhibiting Configurational Free Volume ---------- 98
4.1. Abstract ---------- 98
4.2. Introduction and Background ---------- 99
4.3. Experimental Methods ---------- 103
4.3.1. Materials ---------- 103
4.3.2. Swelling measurements ---------- 104
4.4. Computer vision based data analysis ---------- 105
4.5. Results and Discussion ---------- 109
4.5.1. Reproducing literature polycarbonate swelling data ---------- 109
4.5.2. CO_2-induced swelling in TPBOs and TPHIs precursors exhibiting systematically varied amount of triptycene units ---------- 111
4.5.3. CO_2 partial molar volumes in TPBOs ---------- 117
4.5.4. Pure- and mixed-gas ethane-induced swelling ---------- 122
4.5.5. Analysis of the experimental uncertainty ---------- 125
4.5.6. Assessment of image stabilization efficacy ---------- 129
4.6. Conclusions ---------- 131
Chapter 5. Evaluating the Experimental Uncertainty in Gas and Vapor Sorption Experiments ---------- 134
5.1. Abstract ---------- 134
5.2. Introduction ---------- 135
5.3. Validity and limitations of the proposed approach ---------- 137
5.3.1. Vapor sorption measurements ---------- 137
5.3.2. Gas sorption measurements ---------- 139
5.4. Results and Discussion ---------- 142
5.4.1. Case Study 1: methanol vapor sorption in Celazole® polybenzimidazole 142
5.4.2. Case Study 2: gas sorption in a triptycene-based polybenzoxazole -------- 145

5.4.3. Comparison between the MCEP and LEP methods ---------- 147
5.4.4. Contribution of individual variables to gas/vapor sorption uncertainty from linear error propagation ---------- 149
5.4.5. Contribution of individual variables to gas/vapor sorption uncertainty from Monte Carlo error propagation ---------- 156
5.4.6. Recommendations and best practices for accurate and reliable sorption measurements ---------- 158
5.5. Conclusions ---------- 161
Chapter 6. Summary and Recommendations for Future Research ---------- 162
6.1. Summary ---------- 162
6.2. Future work ---------- 164
Appendices ---------- 167
A1. Polymer Synthesis Protocols ---------- 167
A2. Comparison between water vapor isotherms in PIM-1 and TPBO-0.25 -------- 171
A3. Zimm-Lundberg analysis for TPBO-0.25 ---------- 172
A4. Berens-Hopfenberg parameters ---------- 173
A5. Comparison among Berens-Hopfenberg (BH), modified Berens-Hopfenberg (MBH) and Fick's model fitting to methanol sorption kinetics in TPBO-0.25 --------- 174
A6. Numerical considerations on the Berens-Hopfenberg model fitting ---------- 175
A7. Peng-Robinson Parameters Used in this Work ---------- 177
A8. Pure CO_2, CH_4, and N_2 sorption isotherms at multiple temperatures and triptycene molar content ---------- 178
A9. Pure CH_4 and N_2 Sorption Isotherms in TPBOs ---------- 181
A10. Analysis of fitted dual mode parameters ---------- 183
A11. Isosteric heats as function of triptycene content for both CO_2 and CH_4 -------- 184
A12. Dual mode prediction of CO_2/CH_4 mixed-gas solubility and solubility-selectivity, comparison with pure-gas data and uncertainty analysis ---------- 185
A13. Ideal and real CO_2/CH_4 solubility selectivity as a function of temperature ---- 186
A14. Logarithm of permeability versus 1/FFV ---------- 187
A15. Evaluation of $\boldsymbol{DD}$ and $\boldsymbol{DH}$ ---------- 188
A16. Dual-mode parameters for TPBOs as function of penetrant fugacity ---------- 189

A17. Analytical assessment of the effect of polymer swelling (i.e., change in polymer density) on sorption uncertainty ---------- 192

A18. Comparison between linear error propagation and Monte Carlo methods: an example ---------- 196

A19. Analytical LEP uncertainty of vapor sorption measurements ---------- 198

A20. Coefficient of variation and sorption uncertainty ---------- 199

A21. Monte Carlo Scatterplots of selected CO_2 sorption steps ---------- 200

A22. Monte Carlo Scatterplots of selected methanol sorption steps ---------- 202

A23. Reproducibility of sorption data and variability among samples ---------- 204

A24. Evaluation of the final equilibrium pressure during barometric (pressure decay) sorption measurements ---------- 205

A25. Image Stabilization Algorithm Applied to Dilatometry Images ---------- 206

A26. Selected Polycarbonate and TPBO-0.25 Dilation Analyses (Animated) --------- 209

A27. Camera calibration factor ---------- 215

A28. Verification of both Isotropic Dilation Behavior via Polycarbonate and Apparatus Consistency via TPBO-0.25 using CO_2 Dilation ---------- 217

A29. Dual Mode and Dual Mode Dilation Parameters Used in This Work ---------- 220

A30. Propagating Uncertainty through the Fractional Dilation Formula ---------- 222

A31. Evidence of Thermally Induced Camera Position Error ---------- 226

A32. n-Butane swelling kinetics in TPBOs ---------- 228

References ---------- 229

List of Tables

Table 1: *Constraints used for the dual mode fitting of sorption data at multiple temperatures in TPBOs.* ----------19

Table 2. *Structure and properties of TPBO-0.25* [20] *and PIM-1* [109].----------50

Table 3: *Critical parameters and kinetic diameter of the vapors considered in this study and in the Vopicka's study*[109].----------55

Table 4: *Fitted GAB model parameters for vapor sorption isotherms in TPBO-0.25 at 25°C.* --55

Table 5: *Comparison between 1-butanol/methanol sorption- and diffusion-selectivity at 25°C in TPBO-0.25 and PIM-1. Data for PIM-1 are from ref.* [109]. *Uncertainties for TPBO-0.25 were estimated using linear error propagation* [96,98,103]. ----------69

Table 6: *Pure-gas permeability and diffusion coefficients, selectivity and diffusivity-selectivity in TPBOs and conventional polymer membrane materials at 35°C and 1 MPa (i.e., 10 atm).*------89

Table 7: *Dual-mode mobility parameters for CO_2, CH_4, and N_2 in TPBOs, PIM-1, polysulfone (PSF), polycarbonate (PC) and 6FDA-6FpDA polyimide (PI). Data are at 35°C for all polymers except PIM-1, for which they are available at 25°C. Uncertainty of D_D and D_H values for TPBOs are shown in Figure 18A-B.* ----------91

Table 8: *Experimental parameters used in various TPBO and TPHI dilation experiments.* -- 112

Table 9: *Best fit value of the Dual Mode Dilation Model for TPBOs and conventional glassy polymers.* ---------- 122

Table 10: *Typical calibrations and setting used in this study to run swelling measurements.* 128

Table 11: *Technical details of the vapor sorption apparatus considered in this study.*---------- 139

Table 12: *Technical details of the gas sorption system considered in this study.* ---------- 141

Table A1. *Structure and physical properties of TPBOs.*..... 168

Table A2: *Berens-Hopfenberg fittings of 1-propanol diffusion in TPBO-0.25 at 25°C*..... 173

Table A3: *Berens-Hopfenberg fittings of methanol diffusion in TPBO-0.25 at 25°C*..... 173

Table A4: *Berens-Hopfenberg fittings of 1-butanol diffusion in TPBO-0.25 at 25°C*..... 173

Table A5: *Peng-Robinson parameters used to calculate gas sorption from pressure data.* 177

Table A6: *Fitted parameters of the temperature-constrained dual mode model for CO_2.* 189

Table A7: *Fitted parameters of the temperature-constrained dual mode model for CH_4.* 189

Table A8: *Fitted parameters of the temperature-constrained dual mode model for N_2.* 189

Table A9: *Dual-mode parameters for CO_2, CH_4, and N_2 at multiple temperatures in TPBOs.* 190

Table A10: *Fitted dual mode dilation and dual mode values for CO_2 sorption in various polymers used in this work at 35°C. Uncertainties were determined using the jackknife uncertainty method[199].* 220

List of Figures

Figure 1: *Structure and size of triptycene units.* 3

Figure 2: *Qualitative diagram of the glassy and rubbery regions of polymers, measured by specific volume, as well as the contributions to the total polymer phase volume including the regular free volume (green area), conformational (excess) free volume (red area), configurational free volume (pink area), and occupied volume of the polymer itself i.e., the Van-der-Waals volume (blue area). Additionally, the dashed blue line denotes the theoretical equilibrium volume of the polymer in a glassy state, and the red arrow denotes the affect of physical aging over time.* 7

Figure 3: *CO_2/CH_4 Robeson upper bounds in 1991 (dotted line), 2008 (dashed line), and 2019 (solid line). Data taken from various sources* [1,20,21,60]. *Highlighted polymer types are thermally rearranged polymers (blue), PIMs (red), benzotriptycene containing PIMs (orange), TPBOs (green), TPBO-Acs (purple, and TPI-PBOs (yellow).* 14

Figure 4: *Schematic of the Monte Carlo Error Propagation (MCEP) method.* 33

Figure 5: *A) Schematic of the constant volume pressure decay apparatus used to measure vapor sorption/adsorption in polymers and porous materials. B) Schematic of a typical vapor sorption measurement using the differential method.* 39

Figure 6: *A) Schematic of the constant volume pressure decay apparatus used to measure gas sorption/ adsorption in polymers and porous materials. B) Schematic of a typical gas sorption measurement using the differential method. Numbers denote step order for calculating concentration from pressure measurements. $Vfiller$ accounts for any other material (e.g., stainless steel beads) possibly used to reduce the total sampling chamber volume, $VS0$.* 42

Figure 7: *Swelling apparatus: scheme (A) and annotated image (B).* 45

Figure 8: *Experimental solubility isotherms: A) methanol and water at 25°C in TPBO-0.25; B) 1-propanol and 1-butanol at 25°C in TPBO-0.25; C) methanol, ethanol, 1-propanol, and 1-butanol in PIM-1 at 25°C* [109]; *D) methanol, ethanol, and 1-propanol in poly(trimethyl silyl norbornene) (PTMSN) at 35°C* [89]; *E) methanol, ethanol, and 1-propanol in Teflon AF2400 at 25°C as a function of vapor activity* [110]. *Solid lines are the GAB model fittings. Error bars for TPBO-0.25 sorption isotherms and activity values, which were calculated using linear error propagation, are too small to show.* 51

Figure 9: *Sorption kinetics in TPBO-0.25 at 25°C: A) methanol (activity jump 0.0-0.038) and B) 1-propanol (activity jump 0.16-0.20). Black dots are experimental data, and solid red lines are the modified Berens-Hopfenberg Model (A) and Berens-Hopfenberg Model (B) fittings* [78,84]. *Dimensionless sorption is defined as $MsorbedtMsorbedt\infty$.* 60

Figure 10: *A) Vapor concentration-averaged diffusion coefficients, $\bar{D}i$, in TPBO-0.25 at 25°C as a function of equilibrium concentration. B) Mobility coefficients (i.e., thermodynamically-corrected diffusion coefficients, Li) at 25°C as a function of equilibrium concentration.* 62

Figure 11: *A) Vapor solubility coefficients, S, in (cm^3(STP)/g(polymer))/bar, for various polymers as a function of vapor critical temperature* [89,109,110]. *TPBO-0.25 (black circles, 25°C and activity 0.1). PIM-1 (red squares, 25°C and activity 0.1). PTMSN (blue diamonds, 35°C and activity 0.1). Teflon AF2400 (green triangles, 25°C and activity 0.67). Dashed lines are drawn to guide the eye. B) Alcohol diffusion coefficient, $\bar{D}i$, at 25°C in PIM-1 (activity 0.2)* [109] *and TPBO-0.25 (activity 0.1) as a function of critical volume. Diffusivity data for poly(sulfone) (PSF) and PDMS at 25°C are shown for the sake of comparison* [125]. 65

Figure 12: *CO_2 (A), CH_4 (B) and N_2 (C) sorption isotherms at 35°C in TPBO samples exhibiting different molar amount of triptycene units. Continuous lines represent the dual mode fitting. Experimental uncertainty was calculated using linear error propagation [98].* 76

Figure 13: *CO_2 sorption isotherms at multiple temperatures in A) TPBO-0.25, B) TPBO-0.50, C) TPBO-0.75 and D) TPBO-1.00. Solid symbols: experimental data. Continuous lines: dual mode fitting. Experimental uncertainty was calculated using linear error propagation [96,98].* 78

Figure 14: *Isosteric heat of N_2, CH_4 and CO_2 sorption in TPBO-0.25 (A), TPBO-0.50 (B), TPBO-0.75 (C) and TPBO-1.00 (D) as a function of penetrant concentration in the polymer. Error bars were estimated using the standard error of weighted linear regression [98]. Continuous lines are drawn to guide the eye.* 80

Figure 15: *Dual mode prediction of CO_2 (A) and CH_4 (B) mixed-gas isotherms from a 30% mol CO_2 / 70% mol CH_4 gas mixture in TPBOs as a function of mixed-gas fugacity at 35°C (solid lines), and comparison with pure gas sorption isotherms at the same temperature (dashed lines). Estimated uncertainty is shown in (Figure A12, Appendices).* 84

Figure 16: *Dual mode prediction of mixed-gas CO_2/CH_4 solubility-selectivity for a 30%mol CO_2 / 70% mol CH_4 mixture in TPBOs as a function of mixed-gas CO_2 fugacity at 35°C (solid line), and comparison with pure-gas CO_2/CH_4 solubility-selectivity (dashed line). Estimated uncertainty is shown in the Appendices (Figure A13).*..... 86

Figure 17: *Pure-gas CO_2 permeability (A) [20] and diffusivity (B) in TPBOs as a function of triptycene molar content and pressure at 35°C; pure-gas CO_2/CH_4 selectivity at 35°C and 1 MPa as a function of triptycene molar content (C). Similar results were obtained at other pressure values. Solid symbols are experimental data, and lines are drawn to guide the eye.*..... 88

Figure 18: *Henry's and Langmuir's mode CO_2 (A) and CH_4 (B) diffusion coefficients, as well as CO_2/CH_4 Henry's (i.e., $DDCO2DDCH4$) and Langmuir's (i.e., $DHCO2DHCH4$) diffusivity-*

selectivity (C) in TPBOs at 35 °C as a function of triptycene molar content. $DHCO2$ drops to zero in TPBO-1.00. $DHCH4$ drops to zero when the triptycene molar content in the polymer is equal to 75% mol or larger. The Langmuir's diffusivity-selectivity, $DHCO2DHCH4$, approaches infinite when the triptycene molar content is equal to 75% mol or larger. Uncertainty was calculated using linear error propagation [97,98]. 95

Figure 19: *Illustrated (A) and real (B) image analysis process. From left to right: The initial sample image after stabilization, the resulting convolved image, and the summed pixel values (green bars) in addition to the fit continuous function (blue line), and finally the chosen boundary position (red line).* 106

Figure 20: *Schematics of image stabilization. The top row (A, B, C) displays a simplified pixel-scale version of the algorithm with a camera moving downwards during an experiment. The bottom row (D, E, F) denotes the same situation in a real experiment. The original reference in D is shown in red in Figures E and F, with the current image shown in green. Overlapping pixels between the reference and current image shown as yellow. The distance needed to shift for the current image to minimize overlap error with F is denoted by "Drift" in Figure F.* 109

Figure 21: *Percent volumetric swelling of polycarbonate upon CO_2 exposure at 35°C, as a function of CO_2 concentration in the polymer. Filled colored symbols are data from this work, where runs 2 and 3 were done in parallel. Continuous lines represent previous literature data. Error bars were estimated via linear error propagation [96–98] without covariance.* 110

Figure 22: *Fractional swelling of TPBOs at 35°C as a function of CO_2 concentration (A), and pressure (B). Relevant polymers are included for comparison. Error bars were estimated via linear error propagation* [96–98] *for both concentration and swelling. All TPBO samples were run in parallel.* 113

Figure 23: *Fractional TPBO-1.00 and TPHI-1.00 swelling at 35°C, as a function of CO_2 concentration. Error bars were estimated via linear error propagation [96–98] for both concentration and dilation. Samples were run in parallel.* 116

Figure 24: *CO_2 partial molar volumes in TPBOs and other reference polymers (grey) as a function of CO_2 concentration in the polymer. Circles denote error arcs representing one standard deviation from the sampled point, calculated via linear error propagation and neglecting covariance for each data point calculated [96,199]. Solid horizontal lines denote fit VD values for each TPBO sample, with the grey line displaying the VD for PIM-1. Each curve includes 100 sampled points.* 118

Figure 25: *Fractional swelling of A) TPBO/TPHI-0.00, B) TPBO/TPHI-0.25, C) TPBO/TPHI-0.50, D) TPBO/TPHI-0.75, and E) TPBO/TPHI-1.00 at 35°C as a function of pure-gas (solid*

lines) and mixed-gas (dashed lines) ethane fugacity. Error bars were estimated via linear error propagation [96–98]. All samples were run in parallel. F) Comparisons among TPBOs. 124

Figure 26: *Sensitivity analysis predicting overall uncertainty (A) and fractional uncertainty contributions from the input variables (B) of a simulated swelling experiment with similar experimental conditions as the TPBO/TPHI runs, i.e., with characteristics described in Table 10 and a constant fractional volume swelling of 7% as a function of the total polymer sample length used in the real experiment.* 127

Figure 27: *TPBO-0.25 swelling kinetics upon exposure to n-butane at 35°C as a function of time. The solid red line denotes the percent swelling found while correcting for camera movement during the experiment, the solid blue line denotes the same image data and analysis, but without any image stabilization. Dashed lines denote experimental uncertainty, found via linear error propagation [96–98], via one standard deviation from the measured value.*..... 130

Figure 28: *Experimental methanol vapor sorption isotherms in Celazole® PBI at A) 25°C, B) 35°C, and C) 45°C as a function of pressure. Error bars are calculated via linear error propagation and are superimposed over a corresponding Monte Carlo error propagation (1,000,000 iterations). Lines are drawn to guide the eye. Experimental data are from ref. [26,58].*..... 143

Figure 29: *Experimental CO_2 sorption isotherms in TPBO-0.25 at A) 5°C, B) 20°C, C) 35°C, and D) 50°C as a function of pressure. Error bars are calculated via linear error propagation, and are superimposed over the corresponding Monte Carlo error propagation (100,000 iterations). Lines are drawn to guide the eye. Experimental data are from ref. [58].* 146

Figure 30: *Percent difference between Monte Carlo and linear error propagation for every step in the isotherm. A) Methanol in PBI at 35°C and B) CO_2 in TPBO-0.25 at 35°C. Each line represents a different pressure step.* 148

Figure 31: *Individual linear error propagation uncertainty contributions to experimental methanol sorption isotherms in PBI at A) 25°C, B) 35°C, and C) 45°C. Contributions of temperature and sample chamber volume are negligible and, for this reason, they are not shown.* 150

Figure 32: *Individual linear error propagation uncertainty contributions to experimental CO_2 sorption isotherms in TPBO-0.25 at A) 5°C, B) 20°C, C) 35°C, and D) 50°C. Dark blue plots denote contributions that provide a negligible contribution to the overall uncertainty, including final charge pressure, Pitzer acentric factor, penetrant critical temperature, penetrant critical pressure, polymer density, polymer mass, and final sample chamber pressure.*..... 153

Figure 33: *Fractional uncertainty contributions of CO_2 sorption in TPBO-0.25 at 35°C using the true chamber volumes uncertainty (continuous lines, $\sigma VCharge$= 0.04 cm^3, $\sigma VSampling$= 0.06*

cm³) and the halved chamber volumes uncertainties, (dashed lines, $\sigma VCharge$= 0.02 cm³, $\sigma VSampling$= 0.03 cm³), while all other uncertainties remained constant. Lines are drawn to guide the eye. The chamber volumes are $VC = 18.442\ cm3$ and $VS = 15.707\ cm3$. 156

Figure 34: *Percentage deviation of MCEP method from LEP method in evaluating the contribution of a single experimental variable to the sorption experimental uncertainty as a function of the number of Monte Carlo iterations. A) Contribution of polymer mass to uncertainty of methanol vapor sorption in PBI at 35°C. B) Contribution of the charge chamber volume to uncertainty of CO_2 sorption in TPBO-0.25 at 35°C. The insert is shown to confirm that the two methods converge to the same result.*..... 157

Figure A1: *Synthetic route for producing triptycene containing polyhydroxyimide (TPHI) and triptycene containing polybenzoxazole (TPBO).*..... 170

Figure A2: *Experimental water vapor sorption isotherms at 25°C in TPBO-0.25 (red circles) and PIM-1 (blue circles) as a function of water vapor activity. Continuous lines are the GAB model fittings. Data for PIM-1 are from ref. [109]* 171

Figure A3: *Zimm-Lundberg predicted clusters size: methanol (solid blue squares), 1-propanol (solid red diamonds), 1-butanol (solid green diamonds), and water (solid sky circles) in TPBO-0.25 at 25°C. Lines are drawn to guide the eye.* 172

Figure A4: *A) Methanol sorption kinetics (in units of dimensionless sorption $MtM\infty$) plotted as a function of time on a logarithmic scale (colored lines). Experimental sorption kinetics were fitted to the modified Berens-Hopfenberg model (black lines). B) Alternative model results for step 1 (red points), namely Fickian model (green line), Berens-Hopfenberg model (yellow line) and the modified Berens-Hopfenberg model (black line).*..... 174

Figure A5: *CO_2 sorption in TPBOs at varying temperatures ranging from 20°C to 50°C taken at pressures up to 3 MPa. Solid points represent experimental data, continuous lines represent the dual mode fitting. Error bars were calculated using linear error propagation [96,98].* 178

Figure A6: *CH_4 sorption in TPBOs at varying temperatures ranging from 20°C to 50°C taken at pressures up to 3 MPa. Solid points represent experimental data, continuous lines represent the dual mode fitting. Error bars were calculated using linear error propagation [96,98].* 179

Figure A7: *N_2 sorption in TPBOs at varying temperatures ranging from 20°C to 50°C taken at pressures up to 3 MPa. Solid points represent experimental data, continuous lines represent the dual mode fitting. Error bars were calculated using linear error propagation [96,98].* 180

Figure A8: *CH_4 sorption in TPBOs as a function of triptycene content at temperatures ranging from 5°C to 50°C taken at pressures up to 3 MPa. Solid points represent experimental data, continuous lines represent the dual mode fitting. Error bars were calculated using linear error propagation [96,98].* 181

Figure A9: *N_2 sorption in TPBOs as a function of triptycene content at temperatures ranging from 5°C to 50°C taken at pressures up to 3 MPa. Solid points represent experimental data, continuous lines represent the dual mode fitting. Error bars were calculated using linear error propagation [96,98].* 182

Figure A10: *Logarithm of KD (i.e., Henry's solubility coefficient) vs. penetrant critical temperature at 35°C. A): TPBO-0.50, B): TPBO-0.75, and C): TPBO-1.00. The three data points in each figure refer to N_2 (critical T = 126K), CH_4 (critical T = 190.1K) and CO_2 (critical T = 304.9K). As expected, the slope of this correlation is 0.015 K^{-1}.* 183

Figure A11: *Isosteric heats of CO_2 (A) and CH_4 (B) sorption in TPBOs as a function of penetrant concentration. Error bars are obtained using the standard deviation of weighted linear regression [98,101].* 184

Figure A12: *CO_2 and CH_4 mixed-gas sorption isotherms (solid lines, predicted using the dual mode model) from a 30%mol CO_2/70%mol CH_4 gas mixture in TPBOs as a function of mixed gas fugacity at 35°C: A) CO_2 and B) CH_4. Uncertainty was calculated via linear error propagation [96,98]. Dual mode fittings of pure-gas data are shown for the sake of comparison (dashed lines).* 185

Figure A13: *Dual mode predictions of CO_2/CH_4 real (continuous lines) and ideal (dashes lines) solubility-selectivity for a 30%mol CO_2 / 70%mol CH_4 mixture in TPBOs as a function of mixed CO_2 fugacity at 35°C. Uncertainty associated to ideal solubility-selectivity was linearly propagated from the original isotherms. Uncertainty associated to real (i.e., mixed-gas) selectivity was estimated via the percent error resulting from linear error propagation of the original isotherms. TPBO-0.25 data is taken from [75] and shown for comparison. Legend: sky lines represent TPBO-0.25. Red lines represent TPBO-0.50. Green lines represent TPBO-0.75. Blue lines represent TPBO-1.00.* 185

Figure A14: *Real (solid lines) and ideal (dashed lines) CO_2/CH_4 solubility selectivity in TPBOs as a function of temperature, predicted via the dual mode model. CO_2 fugacity = 0.3 MPa, CH_4 fugacity = 0.7 MPa.* 186

Figure A15: *Logarithm of CO_2 and CH_4 permeability as a function of polymer's FFV^{-1} at 35°C and 1 MPa (i.e., 10 atm).* 187

Figure A16: *Pure gas CO_2 (A), CH_4 (B) and N_2 (C) permeability at 35°C as a function of $CH'b1 + bf$ in TPBO-0.25 (blue dots), TPBO-0.50 (red dots), TPBO-0.75 (orange dots), and TPBO-1.00 (yellow dots). Dashed lines are drawn to guide the eye.* 188

Figure A17: *Graphical representation of the constraint represented by Equation A1, that is, overlapping condition for the error bars when using the dry and swollen polymer density (A). Swelling thresholds in the case of CO_2 sorption in TPBO-0.25 at 35°C (B). Swelling thresholds in the case of methanol sorption in Celazole PBI at 35°C (C). Swelling thresholds in the case of methanol sorption in Celazole PBI at 35°C using two different dry polymer density uncertainties (D).* 195

Figure A18: *Application of the Monte Carlo method to evaluate the uncertainty of the function $fx, y, z = xy + z$. 2700 iterations were used.* 196

Figure A19: *Coefficient of variation, CV, (A) and error (i.e., uncertainty) (B) of methanol vapor sorption in PBI as a function of pressure. Isotherms are shown at 25°C (green), 35°C (blue), and 45°C (red). Lines are drawn to guide the eye.* 199

Figure A20: *Coefficient of variation, CV, (A) and error (i.e., uncertainty) (B) of CO_2 sorption in TPBO-0.25 as a function of pressure. Isotherms are shown at 5°C (light blue), 20°C (red), 35°C (green), and 50°C (dark blue). Lines are drawn to guide the eye.* 199

Figure A21: *100,000 Monte-Carlo simulations of selected CO_2 sorption steps in TPBO-0.25 plotted as a function of pressure (MPa). Color is assigned via a bivariate probability density function using the data's covariance matrix. Marginal histograms (red lines) denote the pressure or concentration distribution. Error ellipses (solid, dashed, and dotted black lines) show the 68.2%, 95%, and 99.7% confidence intervals, respectively. Figures are labeled for A) 5°C step 1, B) 5°C step 9, and C) 20°C step 1, D) 20°C step 13, E) 35°C step 1, F) 35°C step 22, G) 50°C step 1, H) 50°C step 14.* 201

Figure A22: *1,000,000 Monte-Carlo simulations of selected methanol vapor sorption steps in PBI plotted as a function of pressure (MPa). Color is assigned via a bivariate probability density function using the data's covariance matrix. Marginal histograms (red lines) denote the pressure or concentration distribution. Error ellipses (solid, dashed, and dotted black lines) show the 68.2%, 95%, and 99.7% confidence intervals, respectively. Figures are labeled for A) 25°C step 1, B) 25°C step 7, and C) 35°C step 1, D) 35°C step 5, E) 45°C step 1, F) 45°C step 4.* 203

Figure A23: *Results of two independent N_2 sorption measurements in TPBO at 35°C, using two different polymer samples. The casual error, i.e., the departure between the two measurements, falls within the uncertainty window predicted by the linear error propagation method.* 204

Figure A24: *A) methanol vapor sorption kinetics in Celazole at 25°C, step 1 (activity jump 0.06-0.14). B) Equilibrium pressure, at the end of the same sorption step: open circles are experimental pressure data; continuous red line is the average equilibrium pressure used to calculate the equilibrium solubility; dashed red line is the standard deviation of pressure reading.* 205

Figure A25: *Example image shifting search process going through three steps. The overall result is shown in the upper left quadrant of the figure. Red arrows denote shift attempts, values in the images' "pixels" represent the overlap error calculated by that corresponding shift. The optimal position found both in steps one and two is shown in gray, while the optimal position found in step 3 is shown in green.*..... 208

Figure A26: *Polycarbonate run 2 dilation analysis animation at 27.7 atm. The top row, from left to right, displays the original image, the cropped region (shifted), the convolved image, the edge position likelihood estimate and corresponding continuous function fit, and the final position indicator (yellow line). The middle row denotes shifting corrections, which were not significant in this step. The bottom row tracks distance over time, as well as the X/Y shift optimized, which did not exceed 0.25 pixels.*..... 209

Figure A27: *Dilation analysis animation of a thermally rearranged polymer (TPBO-0.25) being dilated with butane at 0.68 atm. The top row, from left to right, displays the original image, the cropped region (shifted), the convolved image, the edge position likelihood estimate and corresponding continuous function fit, and the final position indicator (yellow line). The middle row denotes shifting corrections where red is the reference image, green is the current image, and yellow denotes pixel overlap. The bottom row tracks distance over time, as well as the X/Y shift optimized.*..... 211

Figure A28: *Dilation analysis animation of a thermally rearranged polymer (TPBO-0.25) being dilated with butane at 1.14 atm. The top row, from left to right, displays the original image, the cropped region (shifted), the convolved image, the edge position likelihood estimate and corresponding continuous function fit, and the final position indicator (yellow line). The middle row denotes shifting corrections where red is the reference image, green is the current image, and yellow denotes pixel overlap. The bottom row tracks distance over time, as well as the X/Y shift optimized.*..... 212

Figure A29: *Dilation analysis animation of a thermally rearranged polymer (TPBO-0.25) being dilated with butane at 0.33 atm. The top row, from left to right, displays the original image, the cropped region (shifted), the convolved image, the edge position likelihood estimate and corresponding continuous function fit, and the final position indicator (yellow line). The middle row denotes shifting corrections where red is the reference image, green is the current image, and yellow denotes pixel overlap. The bottom row tracks distance over time, as well as the X/Y shift optimized.*..... 214

Figure A30: *Camera calibration for sample distance estimation based on dimensionless camera track position markers, which are arbitrary (but evenly spaced) points along the camera track. The calibration curve relates the number of pixels observed by the camera to the length that many pixels represent, expressed in pixels per centimeter.* 215

Figure A31: *Example image for determining the apparatus pixel to length calibration factor for a single camera position.* 216

Figure A32: *Fractional dilation of orthogonally cut polycarbonate samples (4, blue and 5, purple) at 35°C, as a function of CO_2 concentration in the polymer sample and compared to previous data shown in this work (runs 1-3). Error bars were estimated via linear error propagation*[96–98] *without covariance. Run 1 was completed alone, runs 2 and 3 were completed in parallel and runs 4 and 5 were completed in parallel.* 217

Figure A33: *Fractional dilation of TPBO-0.25 samples at 35°C, as a function of CO_2 pressure. Samples were taken from multiple batches spanning 2023, beginning with April, 2023 (green), June, 2023 (yellow), and November 2023 (blue). Error bars were estimated via linear error propagation*[96–98] *without covariance.* 219

Figure A34: *Image stabilization shifts in pixels (left Y axis) required to stabilize a dilation experiment's sample images over several hundred hours. Shift distances are shown in pixels for the X axis (blue curve) and Y axis (red curve) of the sample image at a given experiment time (hours). The right Y axis denotes the outdoor air temperature in °C on the University of Oklahoma Norman Campus (green curve) at the same time the data was being taken.* 226

Figure A35: *Butane in TPBO-0.25 (red line), TPBO-0.75 (green line), and TPBO-0.00 (purple line) dilation kinetics in percent volume dilation at 35°C as a function of time since the first dilation step. Dashed lines denote experimental uncertainty found via linear error propagation*[96–98]*, one standard deviation from the measured value.* 228

Figure A36: *Butane dilation kinetics expressed as for various TPBO polymers, including 00 (purple), 25 (red), 50 (orange), 75 (green), and 100 (blue) at 35°C as a function of time and at 0.88 atm. Dashed lines denote experimental uncertainty found via linear error propagation*[96–98]*, one standard deviation from the measured value.* 228

Abstract

This dissertation explores the impacts of configurational free volume, introduced through triptycene units, on the transport properties of condensable vapors and gases in thermally rearranged polybenzoxazole-based polymers as well as their polyhydroxyimide precursors which are not thermally treated. Through a series of in-depth studies, we elucidate the fundamental mechanisms governing solubility, diffusivity, and selectivity in these materials, offering insights into their potential applications in molecular separations. Chapter 1 presents pioneering findings on how triptycene-containing polybenzoxazoles (TPBOs) mediate condensable vapor transport, demonstrating size-controlled (entropically driven) sorption and diffusion, quite unlike conventional glassy polymers. This configurational free volume facilitates the tuning of sorption and diffusion selectivity, potentially unlocking routes to de-bottleneck limitations in current state-of-the-art membrane performance. Chapter 2 extends this investigation to light gases (N_2, CH_4, and CO_2), proposing a mechanism for molecule transport in configurational free volume. By varying triptycene content, we analyze the effects (and lack thereof) on the components of CO_2/CH_4 selectivity, uncovering that configurational free volume exclusively regulates light gas diffusion selectivity in the Langmuir mode without affecting the other components of selectivity. Chapter 3 addresses the critical issue of data reliability in solubility measurements, proposing a standardized methodology for estimating uncertainty in sorption and adsorption measurements. This

study lays out a framework for understanding factors that contribute to measurement error, and comprehensively addresses accurate comparison between solubility measurements within a single lab, as well as across laboratories worldwide, which is critical in the previous two chapters. Chapter 5 investigates the swelling behavior of TPBOs, revealing that configurational free volume and thermal rearrangement collectively and synergistically enhance swelling resistance, a crucial factor for membrane stability and performance in real-world applications. It also brings in techniques from Chapter 3 and data science to demonstrate a novel dilatometry analysis method. This comprehensive study not only lays out an advancement in our understanding of configurational free volume, but also provides measurement and error analysis standardizations in the membrane field. The work may be of practical use to researchers seeking to improve the rational design of membranes and the design of extremely accurate apparatuses geared towards membrane and polymer sciences, such as the sorption and dilation apparatuses discussed herein.

Chapter 1. Motivation, Introduction, and Theory

1.1. Motivation

Membranes have become competitive among separation technologies. If we limit the discussion to gas separations, membranes cover roughly 20% of this market [1]. Measured by yearly revenue, the gas separations market is primarily comprised of hydrogen recovery, nitrogen gas generation, natural gas sweetening, and vapor separations. Of these "big four" (and smaller markets), nitrogen generation takes up almost the same market share as all the other gas separation markets combined. While improvements in membrane performance for these four industries are still useful for commercial optimization [2], the expansion of the membrane industry as a whole is contingent on the development of materials that target very specific separations and outperform alternatives, such as distillation and adsorptive methods of separation. In this case, outperformance implies (in addition to total selective ability and productivity of the process) the longevity of the material and its ability to withstand harsh environments, which is a major bottleneck in the adoption of membranes for the separation of many types of mixtures [1,3]. For this reason, the development of competitive and novel membrane materials has an important prerequisite: the fundamental understanding of structure-property correlations between the materials themselves and the various components of their performance. As a high-level example, the understanding that increasing the total fractional free volume (FFV) of a polymer is correlated with the

increase of component diffusivity, as reported by Thran et. al [4], or that decreasing membrane thickness is correlated with an increase in the rates of progression of the two main detrimental phenomena that adversely affect membrane materials, that is, physical aging and plasticization [5–7], which will be discussed extensively later in this work. Understanding the fundamental mechanisms by which the design of membrane materials affects their properties allows for the rational design of membranes that target specific separations, and by extension, begin to open the industry up to new sectors. This is far from the entire development process that would bring a membrane to market, however, it is the first necessary step in the production of these next generation materials [1].

Some notable strategies that are already in development include crosslinking [8–10], or the binding of adjacent polymer chains together, restricting the polymers ability to deform and generally increasing its selection ability; mixed matrix membranes [11–13], or the inclusion of filler materials with exceptional separating capability into a polymer, improving the resulting membrane's performance and occasionally its stability [14]; and thermal rearrangement [15–17], or applying heat to chemically rearrange the polymer (typically a polyimide) backbone into a far more stable and rigid polymer. There is, of course, even the possibility of combining strategies and the opportunity to understand how these modifications to the material structure synergize with one another [18,19], which is also what this work seeks to accomplish.

In this work, we investigate the utilization and fundamental transport properties of iptycene groups in the polymer backbone. These iptycene units are large paddlewheel-like structures that generate very regular and stable microcavities into the polymer, known as "configurational free volume" (CFV) [20–24] (see Figure 1), which will be discussed further in Section 1.5.

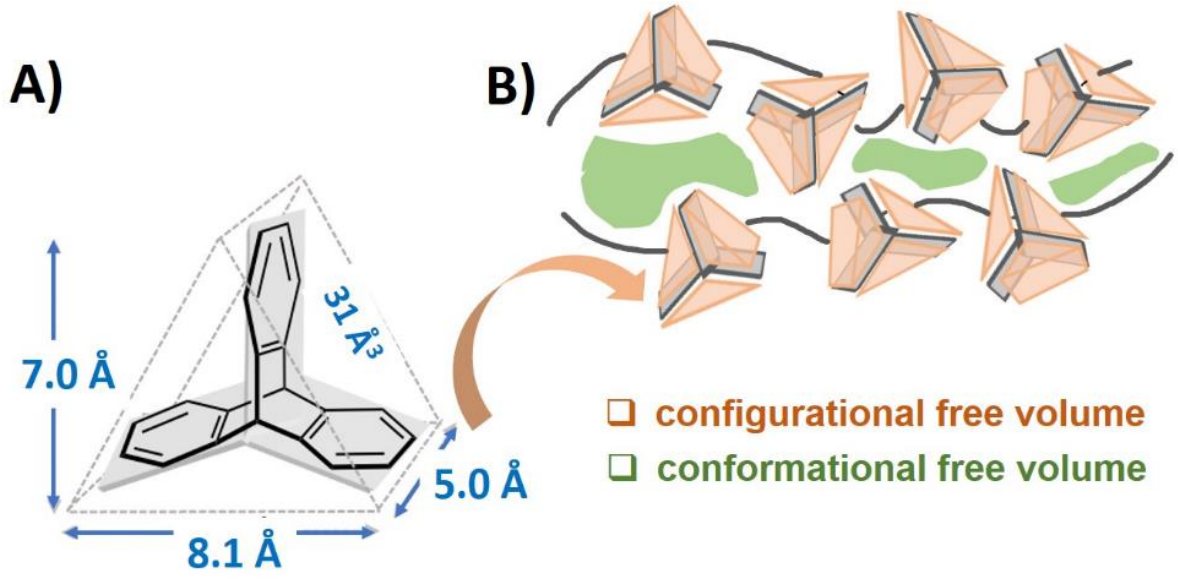


Figure 1: *Structure and size of triptycene units. (A) and conformational versus configurational free volume in glassy polymers (B).*

1.2. The Solution-Diffusion Model

1.2.1. Permeability

Permeability is defined as the extent to which a material is able to transport another material through it, irrespective of thickness or pressure [1]. It is often more concisely called pressure and thickness normalized flux, and thus it is an intrinsic property of polymers, unlike *permeance*, which is only pressure normalized flux. It is also a measure

of membrane productivity, as higher permeabilities require lower pressures when used in real applications, which reduces operational costs.

Polymers that tend to perform well in gas and vapor separations, as well as some liquid phase separations, have no permanent channels or pores within their structure. These so called "dense" polymers, abide by a transport model known as the Solution-Diffusion Model [25]. This model describes the permeability of a component i transporting through the membrane as the product of its solubility coefficient (S_i, which is equal to concentration over pressure), and its concentration averaged diffusivity coefficient ($\overline{D}_i$) (see Equation 1).

$$P_i = \overline{D}_i S_i \qquad \text{Equation 1}$$

In this mechanism [26], the term *concentration averaged* diffusivity coefficient refers to the average diffusivity that is observed as the membrane transitions from one concentration to another.

$$\overline{D}_i = \frac{1}{C_{i,2} - C_{i,1}} \int_{C_{i,1}}^{C_{i,2}} D_i^{eff}(C) dC \qquad \text{Equation 2}$$

Where D_i^{eff} is the effective *local* diffusivity which would be observed at an infinitesimal change in concentration, and $C_{i,1}$ and $C_{i,2}$ are the component (i.e., penetrant) concentrations in the polymer at the beginning and the end of an experimental step, respectively.

1.2.2. Selectivity

The ratio of the more highly permeating species i in a membrane to the lower permeability species j is referred to as the *selectivity* (α_{ij}) of the membrane [25] (see Equation 3).

$$\alpha_{ij} = \frac{P_i}{P_j} = \frac{\bar{D}_i}{\bar{D}_j} \times \frac{S_i}{S_j} = \alpha_{ij}^S \times \alpha_{ij}^D \qquad \text{Equation 3}$$

Selectivity is defined in two ways, the *ideal* selectivity and the *real* or sometimes called *mixed-gas* selectivity. Ideal selectivity is defined as the ratio of permeabilities measured in single-component experiments at a given temperature and pressure, or in other words, data taken when the membrane was only exposed to a single, pure component. Real selectivity is found by measuring an actual mixture of the two components in question. As mixtures of components (especially when at least one component is a condensable gas) can compete and interact with each other, which will be discussed later on in this work, real selectivities may change as a function of the composition of the mixture in question. For example, measuring a 50/50% by mole mixture of CO_2/CH_4 as compared to an 20/80% mixture, which would have less competitive effects from CO_2. The development of instruments which can measure and quantify the permeability and selectivity of real mixtures is also considerably harder and more expensive than an apparatus which would do the same for the pure cases. For these two reasons, and to prevent ambiguities in this work, it should be stated that membrane literature primarily

presents selectivities with the assumption that they are ideal unless otherwise specified as real.

Selectivity can also be expressed as the ratio of the solubility and diffusivity components of the two species (see Equation 3), referred to as the solubility selectivity (α_{ij}^{S}) and the diffusivity selectivity (α_{ij}^{D}). Solubility selectivity is (typically) driven by enthalpic factors, whereas diffusivity selectivity is driven by entropic ones [27]. Enthalpic components that affect this behavior include the relative condensabilities (proxied by critical temperature or critical volume) of the penetrants i and j, and polymer-penetrant interactions. Entropic components that affect diffusivity selectivity include the size of the penetrants (proxied by kinetic diameter), and the penetrants ability to assume additional conformational states while confined in the polymer matrix e.g., the ability for n-butane to rotate and bend within the polymer and isobutane's lack thereof. These correlations have been studied extensively in the 1990's [25,27–32].

1.3. Glassy polymers and their influence on membrane behavior

1.3.1. Glassy and rubbery polymers

This understanding is important due to the nature of the kinds of polymers which tend to be competitive in gas and vapor separations, that is, glassy polymers [27]. Glassy polymers are polymers which do not reside at equilibrium density, instead, exhibiting slightly lower densities than their theoretical maximum at a given pressure and

temperature due to steric hinderances in the motion of the polymer chain (see Figure 2) [31,33]. These hinderances are overcome when the polymer is heated above its *glass transition* temperature (T_g), or the temperature at which the polymer transitions from a glassy state to a rubbery state. Once above the T_g, the polymer will behave as an equilibrium material.

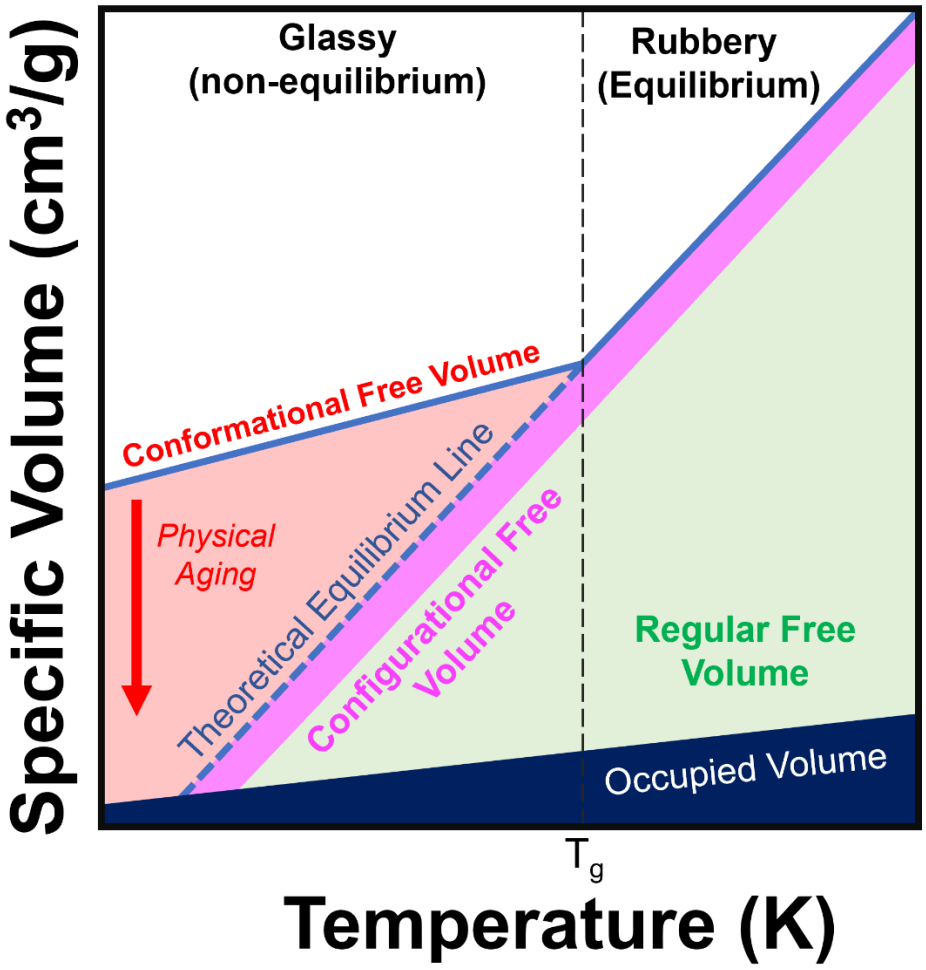


Figure 2: *Qualitative diagram of the glassy and rubbery regions of polymers, measured by specific volume, as well as the contributions to the total polymer phase volume including the regular free volume (green area), conformational (excess) free volume (red area), configurational free volume (pink area), and occupied volume of the polymer itself i.e., the Van-der-Waals volume (blue area). Additionally, the dashed blue line denotes the theoretical equilibrium volume of the polymer in a glassy state, and the red arrow denotes the affect of physical aging over time.*

Because glassy polymers reside below their maximum density, they contain extremely small, unconnected, and semi-permanent voids within their phase referred to as *nonequilibrium* or *conformational* free volume [34,35]. These terms originate from the fact that the free volume within the polymer occurs due to the conformational nature of the polymer chains and isn't simply interstitial space between adjacent chains. When discussing dual mode theory later in this chapter, these nonequilibrium and interstitial spaces are what the Langmuir and Henry modes are comprised of, respectively [36]. This conformational free volume is the key to what gives glassy polymers their advantage in separating small components.

1.3.2. Energetics of gas sorption, diffusion, and permeation

In solution diffusion theory, an energy penalty must be paid for a component to partition into the polymer phase [37]. This is modeled as the energy necessary to "open" a site for the component to occupy in the interstitial space between polymer chains *and occupy it*. This is the activation energy of permeation (E_P, See Equation 4), which is composed of the energies necessary to deform (and subsequently occupy) the polymer space, known as the enthalpy of sorption (ΔH_S) and the energy necessary to diffuse through that opened space, or the energy of diffusion (E_D).

$$P = P_0 \cdot e^{-\frac{E_P}{RT}} = D_0 \cdot e^{-\frac{E_D}{RT}} \times S_0 \cdot e^{-\frac{\Delta H_S}{RT}} \qquad \text{Equation 4}$$

Where P_0, D_0, S_0 are pre-exponential constants relating to entropic contributions, and E_P, E_D, and ΔH_S are the activation energies of permeation, diffusion, and the enthalpy of sorption, respectively [27]. The enthalpy of sorption can be separated by $\Delta H_S = \Delta H_{condense} - \Delta H_{deform}$, or the combination of a deformation energy and a condensation energy [38]. Glassy polymers, which contain conformational free volume elements, can be thought of as containing permanently opened sites through which sorption can occur without paying the deformation component of the energy penalty. For this reason, glassy polymers tend to have far superior solubility coefficients for penetrants than their rubbery counterparts [39]. It was found that this increase in solubility is essentially the only reason that glassy polymers can outperform rubbery ones to the degree observed in literature [39], as when solubility is indiscriminately increased, the overall permeation due to the solution diffusion mechanism increases as well. The byproduct of this trend, however, is that selectivity in glassy polymers is primarily determined between the differences in component diffusion, or the diffusivity selectivity [4], rather than solubility selectivity. This has critical implications on the direction of the membrane field with respect to small components. Polymer chain rigidity and fractional free volume (FFV) were discovered to be fundamentally tied to the increase in both overall diffusivity and diffusivity selectivity [40], that is, creating a rigid, glassy polymer with inefficient chain packing and thus high internal free volume will result in a membrane material for separating based on size alone. However, solubility and solubility-based selection has

proven far more difficult to tame, and remains as the primary route to improving membrane performance [40–42]. The reason for this difficulty resides primarily in the fact that solubility selectivity and diffusivity-selectivity tend to work against each other [43]. Components which are large in size tend to also be more condensable, and as a consequence, a larger component will be selected against with respect to diffusion, but favorably in solution. For example, pairs of alkane / alkenes such as ethylene / ethane [44] and some "regular" separations, e.g., methanol / n-butanol and CH_4/N_2. Other difficulties include isomers separations such as n-propanol / isopropanol [45]. There are notable exceptions to this, such as CO_2/CH_4 as well as CO_2/N_2 separations, which occur in the case that the more condensable component (in this case CO_2) is actually smaller than the less condensable component, but these are mostly solved separations [1] as they are easier to optimize. Most early routes focused on mitigating the opposing solubility selectivity in glassy polymers by tuning the functional groups present on the polymer itself [1,28,42,46,47], such as using fluorinated polymer chains rather than traditional hydrocarbon based polymers [42,48–50]. In fact, many of the strategies proposed earlier in this chapter were also originally conceptualized to help align solubility and diffusivity selectivities to synergize rather than compete with each other, with configurational free volume and the inclusion of iptycene groups being no exception. As we will see in Chapter 2, configurational free volume succeeds in this endeavor [51].

1.4. Membrane performance limitations

1.4.1. Physical aging

The benefits of glassy polymers as membrane materials are not without cost. Glassy polymers, and membrane materials as a whole, suffer from multiple complications hinted at previously in this chapter. The first, and only one exclusive to glassy polymers, is physical aging [52,53]. Physical aging is the gradual collapse of the nonequilibrium (conformational) free volume with the polymer, which can be thought of as the polymer's slow approach to its theoretical equilibrium density, that is, the density values which minimizes Gibbs free energy at a given T and p. As a nonequilibrium material, the density of glassy polymers, and the nature of the free volume within it, are also subject to change and are dependent on age, thermal history, and previous exposure to other materials. Aging results in a decrease in the membranes permeability and an increase in its selectivity, but overall, this effect is an unwelcome detriment to the overall performance of the membrane [52]. To make matters more complex, the rate at which this aging occurs in very thin membranes, which are typically used in real applications) occurs at exceptionally higher rates than bulky membranes [5,6]. The effect of accelerated aging becomes significant near $1\mu m$ in membrane thickness, in which they are considered thin films. This effect can be mitigated by filler agents or crosslinking, and even thermal rearrangement [54], but these methods have complexities of their own [14,52,55]. Incorporating configurational free volume, by way of iptycene groups, has shown

promise in completely halting physical aging [24], even in the case of extremely thin membranes.

1.4.2. Plasticization

For both glassy and rubbery polymers, highly condensable penetrants (such as CO_2, ammonia, alcohols, water, and hydrocarbons) can cause the polymer matrix to plasticize, or in other words, deform and lose cohesion between polymer chains, which become more mobile, losing part of their size-sieving ability [56,57]. Plasticization causes essentially the opposite effect as that of physical aging, that is, a sharp increase in permeability with a loss of selectivity. Intuitively, this can be thought of as the membrane no longer being able to act as a filter, simply allowing components indiscriminately pass through it. Many of the techniques that encourage resistance to physical aging in polymers also apply to plasticization. For example, crosslinking and filler agents that hinder polymer chains from moving apart from one another [8,9,58]. Though discoveries have been made regarding configurational free volume's effect on physical aging [24], plasticization has remained elusive. Thus, a major question this work seeks to answer is the efficacy of configurational free volume in the inhibition of plasticization as well as polymer swelling, which is the physical effect (and measured proxy) of plasticization [42,59].

1.4.3. The Robeson upper bound

The last, and arguably most famous of the main complications to membrane performance, is the Robeson upper bound [30,39,60,61], which is a tradeoff observed between the permeability of a component, and the selectivity between that component and another. That is, modifying a polymer to increase its permeability tends to decrease its selectivity, and vice versa. This results in a bounding line when plotting the two measures of membrane performance that researchers strive to surpass. Tradeoffs are studied extensively for many gas pairs and are named by the pair itself. For example, the CO_2/CH_4 upper bound (see Figure 3) [61], the He/CH_4 upper bound [62], and the ethylene/ethane upper bound [44].

It should be noted that upper bound behavior is not entirely representative of membrane potential for acceptance into real applications, especially when pointing out state-of-the art polymers, for two key reasons. First, the upper bound represents a snapshot of the membrane performance often at the best possible time, which is usually before any aging, significant plasticization, or degradation of the polymer occurs. Thus, polymers which perform well, but disproportionately suffer from complications such as aging, can be misrepresented as industrially competitive. Second, as referenced earlier in Section 1.2.2, these bounds *almost* always use ideal selectivities. Consequentially, mixing effects are not accounted for, which may hide significant synergies and detrimental interactions that would occur in a real setting [1,36,63].

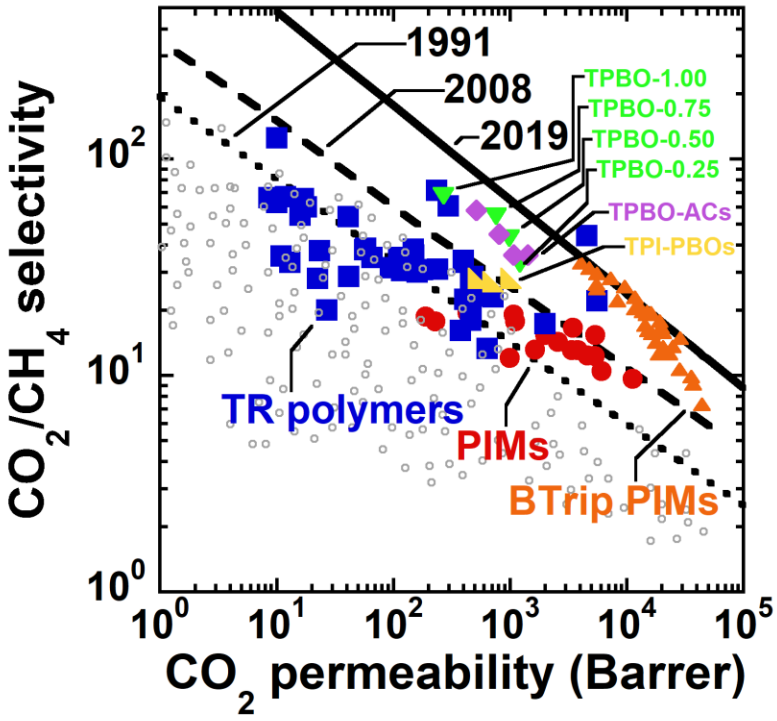


Figure 3: *CO_2/CH_4 Robeson upper bounds in 1991 (dotted line), 2008 (dashed line), and 2019 (solid line). Data taken from various sources* [1,20,21,60]. *Highlighted polymer types are thermally rearranged polymers (blue), PIMs (red), benzotriptycene containing PIMs (orange), TPBOs (green), TPBO-Acs (purple, and TPI-PBOs (yellow).*

The concept of performance upper bounds, as well as permeability-selectivity tradeoffs, were first introduced, empirically, in 1991 [30]. They were then later refined with additional fundamental considerations in 2008 [61] and updated with the current state of the membranes available at that time. This also gives us historical insight into which methods successfully pushed the envelope of membrane performance. For example, the 2008 upper bound for CO_2/CH_4 is largely attributable to the development of thermally rearranged polymers and polymers of intrinsic microporosity (PIMs) (See Figure 3) [61]. He/CH_4 separations were greatly advanced through perfluorinated polymers, which mitigate the counteracting solubility selectivity that tends to favor CH_4 [64]. In fact,

virtually all polymers at the time that defined the 2008 He/CH_4 upper bound were perfluorinated. In 2019, configurational free volume found itself as the deciding factor in the next upper bound, with the 2019 CO_2/CH_4 upper bound being comprised of iptycene containing polymers [60].

1.5. Configurational Free Volume

1.5.1. Current understanding

In polymers, configurational free volume is typically, but not necessarily required to be, generated by iptycene groups placed within the polymer in some fashion. This volume is (by definition) due to the molecular configuration of a structure within the polymer, rather than the conformation of the polymer chains themselves (see Figure 2). This definition is quite general. Configurational free volume may be generated by any group that creates permanent free volume elements from any internal structure. This includes filler phases (i.e., mixed matrix membranes or MMMs) such as inter-penetrating polymer networks (PPNs) [65,66]; including them as pendant groups [67]; and even including the iptycene group in the backbone of the polymer itself [21]. As a product of this, the free volume elements given by configurational free volume are inherently stable, and while they themselves do not physically age or plasticize, other (conformational) elements in the same polymer as well as the bulk polymer matrix itself still may. Any conformational free volume elements available for transport in glassy polymers, which come from frustrated chain packing, makes these materials susceptible to physical aging

[1,23,52,54,68–70]. It has been previously demonstrated that configurational free volume definitively increases resistance to physical aging [24], and that the inclusion of these elements is directly tied with an increase in total (overall) performance, that is, being correlated with surpassing the 2008 CO_2/CH_4 and CO_2/N_2 upper bounds [60] and defining the 2019 upper bounds for these separations. Essentially, the inclusion of iptycenes into membrane materials in general appears to unlock many of the bottlenecks constraining the field, as demonstrated clearly in Figure 3 [20,23,60], but the mechanisms by which it does so are not fully understood. This work seeks to identify the key aspects of configurational free volume that require better fundamental understanding and shed light on them, targeting specifically configurational elements generated by way of iptycene groups.

1.5.2. Open questions

At the inception of this project, the current understanding of configurational free volume was quite limited. Previous work shed light primarily on the overall characteristics and performance of materials that included it, but studies in the domain of fundamental mechanisms of transport were, for the most part, lacking. Prior to this work, unanswered questions included:

1. How does sorption, diffusion, and permeation behavior change when the penetrant is larger than the configurational free volume element size?

2. Through what mechanism does configurational free volume regulate selectivity?
3. How does configurational free volume directly affect plasticization and swelling? That is, can configurational free volume mitigate plasticizing and swelling effects as is known to do with aging?

These questions are answered over the course of three individual studies which seek to elucidate the behavior of configurational free volume using separate experimental domains. That is, 1. vapor sorption, 2. gas sorption, and 3. gas dilation, respectively.

1.6. Phase Equilibria Models

Though glassy polymers are non-equilibrium materials (see Section 1.3.1), there are still models which describe them. These models can derived *a priori* (fundamental models) or *a posteriori* (empirical models), though both types of models have utility in understanding and predicting membrane behavior.

1.6.1. The Dual Mode Model

The Dual Mode Sorption Model provides a phenomenological, although physically sound quantitative description of small molecule sorption in glassy polymers as a function of pressure or fugacity [36], enabling a direct correlation of the transport properties with the membrane structure [36,71–73]. According to the dual mode approach, penetrant concentration in the polymer, C, is given by the sum of two

concentrations. The first is the equilibrium contribution, in the rubber-like component of the polymer phase referred to as the Henry's population or Henry mode. The second is sorption in pre-existing free volume pockets, known as the Langmuir's population or Langmuir mode [71,74]. Specifically, Langmuir mode elements can be created by both conformational and configurational free volume pockets alike. This model strikes a balance between predictive capacity, physical meaning of the fitted parameters, and ease of use. Consequently, it is one of the most widely used models for gas solubility in membrane literature. The base model is as follows (see Equation 5)

$$C = k_D f + \frac{C_H' b f}{1+bf} \qquad \text{Equation 5}$$

where k_D is the Henry's constant, C_H' is the Langmuir sorption capacity, b is the Langmuir affinity parameter and f is the penetrant fugacity in the external gas phase. Pressure is an acceptable alternative to fugacity in most cases, however, some extensions to this model require that the more appropriate quantification of driving force (fugacity) be used.

The dual mode model can be extended to fit solubility data that spans temperature as well as pressure by constraining [15,75] the original three parameters to functions of temperature (see Table 1).

Table 1: *Constraints used for the dual mode fitting of sorption data at multiple temperatures in TPBOs.*

dual mode parameter	*constraint*		*introduced parameters*
K_D	$K_D = K_{D_0} \exp\left(-\frac{\Delta H_{K_D}}{RT}\right)$	*Van't Hoff relationship*	K_{D_0}, ΔH_{K_D}
C'_H	$C'_H = C'_{H_0} - mT$	*temperature dependence of* C'_H	C'_{H_0}, m
b	$b = b_0 \exp\left(-\frac{\Delta H_b}{RT}\right)$	*Van't Hoff relationship*	b_0, ΔH_b

These constraints introduce a Van't Hoff dependence on temperature for the Henry mode constant (K_{D_0}, ΔH_{K_D}) and Langmuir mode affinity (b_0, ΔH_b). These parameters give useful information regarding the energy released upon sorbing into these two modes, thus the constraints on the model provide not only a way to increase the physically realistic picture of the model, but also extract useful information from it.

The Dual Mode Model can also be used to both fit and, more typically, predict mixing effects that occur due to competition in the Langmuir mode that occurs in glassy polymers [26,36,76]. Doing so uses the Langmuir affinity parameter, b_i, which predicts the component i that is the most competitive and thus able to occupy this space in the polymer most frequently, seen in Equation 6.

$$C_i = k_{D,i} f_i + \frac{C'_{H,i} b_i f_i}{1 + \sum_{j=1}^{n} b_j f_j} \qquad \text{Equation 6}$$

Where the subscript i referrers to the component of interest in a mixture with n components.

Using the solution-diffusion model, the Dual Mode Model can be extended to describe not only equilibrium sorption, but also small molecule transport in glassy polymers [74]. This can be done by assigning a mobility to both the Henry and the Langmuir populations, giving rise to the dual sorption-mobility model [71,74]:

$$\wp = k_D D_D \left(1 + \frac{KF}{1+bf}\right) \qquad \text{Equation 7}$$

where D_D and D_H are the diffusion coefficients of the Henry's and Langmuir's population, respectively. These coefficients are assumed constant throughout the range being fit. F and K are constants defined as $F = D_H/D_D$ and $K = C_H' b/k_D$, respectively [74]. All the remaining parameters have the usual physical meaning and are taken from the analysis of single component experiments. To fit these parameters two sets of data are required: a sorption isotherm with its dual mode parameters already fit, and a permeation isotherm of the component over a similar pressure range. After this, Equation 7 is re-expressed as $\wp = k_D D_D + \frac{C_H' b}{1+bf} D_H$ [74] and the D_H and D_D parameters of the partial immobilization model are fit via linear regression, where $k_D D_D$ is the intercept and D_H is the slope, respectively, of the plot $\wp$ vs $\frac{C_H' b}{1+bf}$. This model is valid when the aforementioned plot is linear, as nonlinearities would invalidate assumptions imposed in the derivation of the model and by extension invalidate the meaning extracted from D_H and D_D.

Finally, The Dual Mode Dilation Model developed by Kamiya [77–79] may be used to describe and gain understanding of dilation with respect to glassy polymers. The mode itself describes fractional dilation $\frac{\Delta V}{V_0}$ (see Section 4.2) as a function of pressure:

$$\frac{\Delta V}{V_0} = V_D \left(k_D p + \frac{f C_H' b p}{1 + b p} \right) \qquad \text{Equation 8}$$

where V_D represents the effective condensed molar volume of the penetrant in the polymer phase in $\frac{cm^3}{mol}$, and f is a fitting parameter that typically varies from 0 to 1 and represents how much the Langmuir mode contributes to polymer phase dilation [77]. As an example, an f value of 1 would suggest that the Langmuir and Henry mode contribute equally to dilation, proportionally to the amount of sorbed polymer in the respective phases. An f value of 0 would suggest that no matter how much material sorbs into the Langmuir phase, it does not contribute to volume changes of the polymer phase as a whole and the Henry mode is the only contributor to dilation. The rest of the parameters are fit directly from sorption data using the standard dual mode model [36,80].

1.6.2. The Guggenheim-Anderson-DeBoer Model

The Guggenheim-Anderson-de Boer (GAB) model describes small molecule sorption in polymers as a function of penetrant activity [81–83]. The fundamental hypothesis underlying this model is that vapor molecules are adsorbed in multiple layers on the surface of a solid material. Unlike the Dual Mode Model, the GAB model is typically used as a more precise interpolation tool and for extracting physical meaning from the fit

parameters, and it is also able to capture upward concavity in concentration isotherms typically expressed by highly swelling penetrants such as vapors. As a result of this, the GAB model is typically used in lieu of dual mode mechanisms when swelling affects sorption behavior. The model is parametrized as follows:

$$C = \frac{C_p k A a}{(1-ka)(1-ka+Aka)} \quad \text{Equation 9}$$

where C is the amount of penetrant sorbed in the polymer, expressed in units of $\frac{g}{g_{pol}}$ or cm^3(STP)/cm^3(polymer), a is the penetrant activity (i.e., relative pressure, usually approximated as $\frac{p}{p_0}$, where p is the pressure and p_0 the penetrant vapor pressure at the experimental temperature being considered [13,75]). C_p, A, and k are the three model parameters. Specifically, C_p is the sorption capacity of the first monolayer of penetrant adsorbed on the polymer surface, A is the dimensionless heat of sorption of this first monolayer, and k describes the dimensionless heat of sorption of higher layers.

1.7. Transient (Diffusion) Models

Transient diffusion is the movement of material into a polymer that occurs during the shift from one static pressure (i.e., equilibrium) to another. In sorption experiments, if the polymer geometry is known ahead of time, the rate at which equilibrium is achieved provides the information necessary to calculate the concentration averaged diffusivity coefficient $\overline{D}_i$ [78]. This is typically (as it is in this work) done using "slab geometry", or in other words, a rectangular polymer *slab* with even thickness along the length of the

sample. Several models have been previously derived in membrane literature which allow for the fitting of $\overline{D}_i$ from sorption kinetics. Fitting the parameters of these models requires the use of nonlinear optimization techniques with care taken to avoid some of the spurious local minima that show up in some of the more advanced calculations. For information regarding how to set up and perform these fittings, as well as convergence criteria and cutoffs for infinite sums, see Section 2.4.2 and Section A6, Appendices.

1.7.1. Transient Fickian Sorption

In transient diffusion with which swelling and surface concentration effects do not occur, Fickian diffusion in slab geometry will adequately describe the kinetics of sorption. These kinetics are given by:

$$M_t = M_f\left[1 - \frac{8}{\pi^2}\sum_{n=0}^{\infty}\frac{1}{(2n+1)^2}exp\left(-(2n+1)^2 k_f t\right)\right] \qquad \text{Equation 10}$$

Where M_t is the dimensionless mass uptake of the penetrant in the polymer at time t. M_f and k_f are the equilibrium mass uptakes and Fickian rate constant in g and s^{-1}, respectively [78]. Once fit to a set of transient sorption data, the concentration averaged diffusivity coefficient may be determined by:

$$\overline{D}_i = \frac{k_f \ell^2}{\pi^2} \qquad \text{Equation 11}$$

Where ℓ is the total membrane thickness in cm, resulting in a diffusivity with units of $\frac{cm^2}{s}$. As $\lim_{t\to\infty}\frac{M_t}{M_f} = 1$, M_f may be normalized to one, simplifying the optimization to a single fitting parameter.

1.7.2. The Berens-Hopfenberg Model

In cases where polymer swelling occurs, additional mass uptake may occur over much longer periods of time in addition to normal Fickian sorption. Modeling this requires an extra term with two additional fitted parameters in what is referred to as the Berens-Hopfenberg model [78,84]:

$$M_t = M_F\left[1 - \frac{8}{\pi^2}\sum_{n=0}^{\infty}\frac{1}{(2n+1)^2}exp(-(2n+1)^2 k_F t)\right] + M_r[1 - exp\,(-k_r t)] \qquad \text{Equation 12}$$

Where the introduced terms M_r and k_r are the equilibrium mass uptake and rate of mass uptake in g and s^{-1}, respectively. Once again, constraining $\lim_{t\to\infty}\frac{M_t}{M_f+M_r} = 1$ removes one fitted parameter from the optimization process, significantly simplifying the acquisition of the parameters.

In most cases (as in polymers which sorb little mass) changes in vapor concentration at the polymer surface are negligible, therefore the Berens-Hopfenberg model can be used "as is" with very little residual error. However, when considering highly sorbing vapors (such as methanol, in this work) the concentration at the polymer surface may change exponentially over time [78,85]. In this circumstance, a modified version of the Berens-Hopfenberg model must be used to estimate vapor diffusion coefficients from the analysis of experimental sorption kinetics while modeling the concentration of the penetrant at the polymer surface as $C = C_0\left(1 - e^{-\beta t}\right)$ [78,86], resulting in the modified model:

$$M_t = M_f \left[1 - exp\,(-\beta t) \sqrt{\frac{4k_f}{\pi^2 \beta}}\, tan \sqrt{\frac{\pi^2 \beta}{4k_f}} - \frac{8}{\pi^2} \sum_{n=0}^{\infty} \frac{exp\left(-(2n+1)^2 k_f t\right)}{(2n+1)^2 \left[1 - (2n+\frac{1)^2 k_f}{\beta} \right]} \right] + \qquad \text{Equation 13}$$

$$M_r[1 - exp\,(-k_r t)]$$

where β is a time constant, which is treated as an adjustable parameter along with the other four fitted terms and characterizes how fast the bulk vapor phase reaches the surface of the polymer, where it then can proceed with diffusion into the polymer phase itself. This modification assists as well in situations where high concentration differences between two equilibrium pressures are observed, i.e., when a sorption step traverses a large pressure jump.

1.8. Model Analyses

Once experimental data has been fit to some of the models discussed in Sections 1.6 and 1.7, a number of downstream analyses are available to further gain insight into the data and phenomena being investigated. These include the ability to separate diffusivities into kinetic and thermodynamic contributions, determine clustering effects with condensable vapors, calculate sorption enthalpies, and others. These analyses are of utmost importance when investigating the *fundamental* or *molecular level* behavior of polymer phenomena and are used extensively in subsequent chapters to elucidate the effects of configurational free volume.

1.8.1. Deconvolution of Diffusivity Contributions

Diffusion coefficients in polymers can be decomposed into a purely kinetic term and a thermodynamic factor [87]. This correction becomes particularly valuable when considering components with strong interactions with the polymer, and is critically important when investigating vapor diffusion in polymers due to the strong non-idealities occurring in these systems [26,88]. In contrast, light gases mix with polymers more ideally, therefore correcting the diffusion coefficient for thermodynamic non-idealities is not strictly necessary. The analysis is as follows:

$$\overline{D}_i = \frac{L_i}{RT} \cdot \frac{\partial \mu_i}{\partial \ln(\omega_i)} = L_i \cdot \alpha_i \qquad \text{Equation 14}$$

where L_i is the mobility coefficient or thermodynamically corrected diffusion coefficient, that is, the kinetic contribution to $\overline{D}_i$, α_i is the thermodynamic contribution, and μ_i and ω_i are the penetrant chemical potential and mass fraction in the polymer mixture, respectively. By applying the definition of activity in terms of chemical potential, the thermodynamic contribution can be expressed in terms of penetrant activity a_i as $\alpha_i = \frac{\partial \ln(a_i)}{\partial \ln(\omega_i)}$, allowing α_i to be directly calculated from equilibrium sorption isotherms. Finally, from $\overline{D}_i$ and α_i, L_i can be obtained. As discussed in detail in previous studies, L_i represents a *purely* kinetic parameter which accounts for the frictional resistance offered by the polymer chains to penetrant diffusion [89]; it is related to penetrant molecular size, as well as to the polymer structure. In contrast, α_i measures the polymer-penetrant

interactions [89]. If α_i is larger than 1, polymer-penetrant interactions are favorable (i.e., attractive). In contrast, if α_i is lower than 1, polymer-penetrant interactions are unfavorable (i.e., repulsive). Finally, if α_i = 1, polymer-penetrant mixing is ideal and $\overline{D}_i = L_i$ (i.e., the diffusion coefficient does not need to be corrected for thermodynamic non-ideality).

1.8.2. Zimm-Lundberg Cluster Criteria

The Zimm-Lundberg clustering criteria estimates whether molecule clusters are forming within the polymer phase. Clustering, represented in a way practical to membrane science, is the phenomena of molecules organizing into larger groups that translate as a whole unit, and essentially behave as a larger molecule that is both more condensable and diffuses more slowly within the polymer. Fundamentally, this function quantifies the degree of non-random penetrant distribution within the polymer matrix. The function itself is given as [90–92]:

$$\frac{G_{11}}{\tilde{V}_1} = -(\phi_1 - 1)\left[\frac{\partial\left(a/\phi_1\right)}{\partial a}\right]_{T,p} - 1 \qquad \text{Equation 15}$$

where G_{11} is the cluster integral, $\tilde{V}_1$ is the partial molar volume of the penetrant, ϕ_1 is the penetrant volume fraction in the polymer phase (i.e., $\phi_1 = \frac{C\frac{\tilde{V}_1}{22414}}{\left(1+C\frac{\tilde{V}_1}{22414}\right)}$, where C is the concentration expressed in cm^3(STP)/cm^3(polymer) and $\tilde{V}_1$ is the penetrant molar volume in cm^3/mol [30]) and a is the penetrant activity, which can be approximated as $a \approx \frac{p}{p_{vap}}$ for

low pressure vapors. The size of the average cluster is given [91] as $\frac{\phi_1 G_{11}}{\tilde{V}_1} + 1$, and clustering is considered to take place when the amount of molecules in a cluster is greater than one [90,92]. The extent of clustering is given by the degree to which the cluster function (i.e., Equation 15) is greater than -1 [90].

1.8.3. Isosteric Heat of Sorption

A Van't Hoff-type relationship describes the temperature dependence of gas sorption in polymers [38,87], that is, the solubility at a specific pressure can be described as a function of temperature by $S = S_0 \cdot exp\left(-\frac{\Delta H_s}{RT}\right)$ where ΔH_s is the enthalpy of sorption and S_0 is a pre-exponential constant. As discussed in Section 1.3.2, the enthalpy of sorption is given by the sum of the penetrant condensation enthalpy and the penetrant/polymer mixing enthalpy, which takes into account *i)* the polymer-penetrant interactions and *ii)* the deformation work needed to open gaps between polymer chains to accommodate penetrant molecules in the Henry's mode [58,87]. The analysis of sorption isotherms at multiple temperatures provides the isosteric heat of sorption, that is, the concentration dependence of ΔH_s [38]:

$$\left[\frac{d(\ln(p))}{d\left(\frac{1}{T}\right)}\right]_C = \frac{\Delta H_s}{ZR} \qquad \text{Equation 16}$$

where p is the pressure corresponding at each concentration (C) at a given temperature T, and Z is the compressibility factor of the penetrant in the fluid phase [38].

1.8.4. Partial Molar Volume

With a combination of polymer dilation data and solubility measurements, it is possible to calculate the partial molar volume of the penetrant within the polymer phase itself [77,78,93]. Dilation data is necessary in this case, as it quantifies the change in the polymer phase with respect to the amount of material entering it. Penetrant partial molar volume, or $\bar{V}_{pen}$, can be estimated as follows:

$$\bar{V}_{pen} = \frac{\partial V_{pol.\ phase}}{\partial n_{pen}}|_{T,p,n_{j\neq i}} = \left[\frac{d}{dp}\left(\frac{\Delta V}{V_0}\right) + \beta\right]\frac{dp}{dC} \qquad \text{Equation 17}$$

where $\frac{\Delta V}{V_0}$ is the experimentally measured polymer fractional dilation (discussed extensively in Chapter 4), $\frac{dp}{dC}$ is the pressure derivative with respect to concentration, which is usually taken analytically by fitting the sorption data with the dual mode model (see Section 1.6.1). Finally, β is the polymer compressibility factor, which is often neglected as compressibility is insignificant compared to the dilation observed at the pressure ranges tested [76,78]. This hypothesis is even further justified based on the polymers used in this work, i.e., TPBOs, considering their very high chain rigidity [94,95].

1.9. Experimental Analysis and Uncertainty

A major component of this work is understanding the confidence with which the data obtained. In this work, it is of utmost importance to determine whether certain sets of data are measurably different from one another, or if they are similar within the experimental error. Further, membrane literature previously lacked established criteria

on whether certain corrections needed to be made to improve the accuracy of solubility data, as well as how uncertainty should be appropriately quantified in the first place [96]. To answer these questions and push the standard of how uncertainty is reported in membrane literature, a number of techniques are needed, including standard linear error propagation (LEP), Monte Carlo error propagation (MCEP), jackknifing, bootstrapping, and scaled hessian matrix techniques for carrying uncertainty forward from measurements and fitted parameters. Here, we discuss the methods that are extensively used in this work.

1.9.1. Linear Error Propagation (LEP)

Uncertainty in calculated quantities using independently measured variables may be quantified using linear error propagation (LEP). LEP approximates changes in the calculated variable by assuming that the response in changes to the measured quantities behave linearly[97,98]. This is usually expressed by the following relationship:

$$\sigma_f^2 = \sum_{i=1}^{n} \left(\frac{\partial f}{\partial x_i}\sigma_{x_i}\right)^2 + \sum_{i=1}^{n} \sum_{j\neq i}^{n} \left(\frac{\partial f}{\partial x_i}\right)\left(\frac{\partial f}{\partial x_j}\right)\sigma_{ij}^2 \qquad \text{Equation 18}$$

Where σ_f is the standard deviation of the calculated variable f, σ_{x_i} is the standard deviation of the measured variable i, $\frac{\partial f}{\partial x_i}$ is the first order partial derivative of f with respect to variable i, and σ_{ij}^2 is the covariance between measured variables i and j. Covariance is a measure of the dependence of one measured variable on the measurement of another and is quantified by the right-hand term in Equation 18. Covariance is

generally omitted when it can be reasonably assumed that all measured quantities do not interact with one another [96–98]. This technique is valid when the uncertainty of all measured variables ($[x_i, x_j, \ldots, x_n]$) are small enough that their effect on the calculated quantity f can be assumed linear. In this case, this means that either the quantities are small enough that highly nonlinear responses in f are hidden by the tangent line approximation, or the response of f to changes in x_i are already approximately linear originally [98]. Essentially, within the linear error propagation method, the uncertainty associated to a given function f is proportional to the input (i.e., independent variables) uncertainty. Consequently, for non-linear functions, linear error propagation remains accurate only for small measurement errors.

Complications in linear error propagation calculations can result from the use of iterative functions. When two functions that share an independent measurement, i.e., $f(x, y)$ and $g(x, z)$, are used as intermediate steps, they become functionally correlated such that a change in the independent variable x will now affect both f and g. If the uncertainties of f and g are then accidentally treated as independent quantities in subsequent calculations, the propagated error will not be accounted for accurately. Therefore, the uncertainty of penetrant concentration of a single sorption step cannot be taken as independent of previous steps. Unfortunately, many independently measured variables are shared among subsequent differential sorption steps, such as temperature, polymer density, and chamber volumes. Therefore, a pitfall of linear error propagation when

applied specifically to a constant volume-variable pressure sorption apparatus is to do the work for the first step and reuse this calculated uncertainty in the next ones, without handling the resulting functional correlation. In this work, we account for and quantify this effect, as well as verify the uncertainty results through Monte Carlo methods [99].

1.9.2. Monte Carlo Error Propagation (MCEP)

In addition to analytical techniques, random sampling techniques such as the Monte Carlo Error Propagation method (MCEP) allow for the quantification of uncertainty with far fewer assumptions than are made in LEP, but at a computational cost multiple that is orders of magnitude higher as well [98–100], as millions of simulations need to be run in most cases. In essence, this technique simulates repeat experiments by re-doing the experimental calculations while randomly altering the measured quantities (see Figure 4). In other words, for a function $f = f(x, y, z, \dots)$, one may randomly select $\hat{x}, \hat{y}, \hat{z}, \dots$ within their measured distributions and calculate $\hat{f}(\hat{x}, \hat{y}, \hat{z}, \dots)$, simulating one "repeat experiment". Typically, these distributions are assumed to be gaussian, which is valid in most cases for most types of measurements, however any input distribution is acceptable. $\hat{f}$ is then calculated using these randomly selected values, and the process is repeated until a corresponding distribution is determined for f. If f is also gaussian, then the error may then be reported as a variance or standard deviation similar to LEP. Unlike LEP, MCEP does not inherently assume the nature of the output f's distribution, a linear response, or continuous behavior [97,98], and as such is much more general. It is also

easier to implement programmatically, as it requires resampling rather than the calculation of partial derivatives, which can be tedious in complex calculations. Practically speaking, this method is very demanding, as the time required to compute enough iterations to reach a stable, near constant value (see, Figure A21, Section A21, Appendices and Figure 30) can also be quite high.

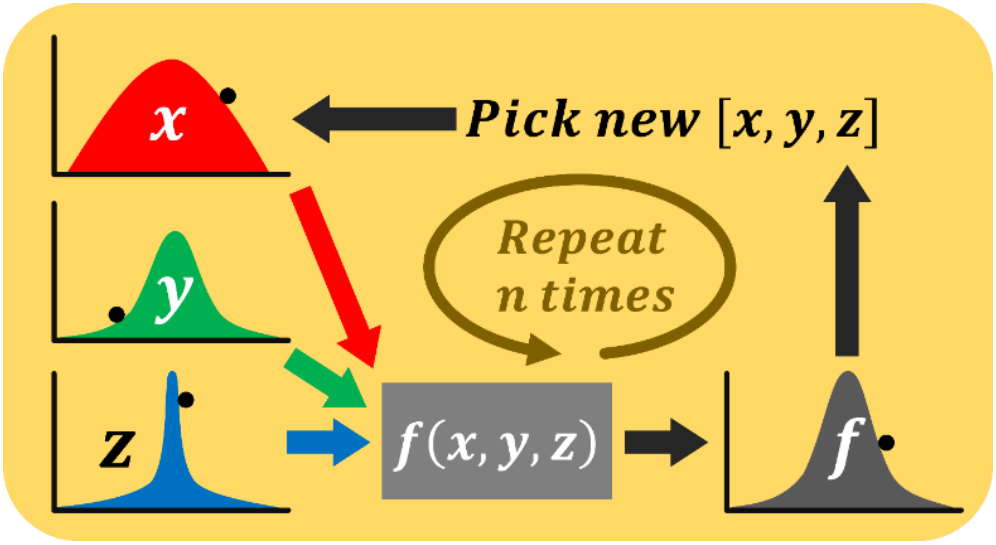


Figure 4: *Schematic of the Monte Carlo Error Propagation (MCEP) method.*

Finally, the example discussed in Section A18, Appendices, demonstrates how to compare MCEP results with LEP results. This is useful due to the fact that MCEP uses far fewer assumptions than LEP, providing a very useful strategy to verify LEP validity. Namely, it can decisively determine if typical measured uncertainties are "small enough" such that the calculated uncertainty σ_f can be said to be linearly proportional to the input values.

1.9.3. Uncertainty Contributions

When evaluating the uncertainty of a function that depends on multiple variables, it may be important, for practical reasons, to quantify the contribution of each variable to the overall output uncertainty. This information can be useful, for example, to identify the major source of uncertainty and optimize the design of an experimental apparatus and collect experimental data exhibiting the highest possible accuracy. Likewise, given a set of experimental sorption data, it may be relevant to know how much of the associated uncertainty is due to a specific input variable. In this study, we provide two similar definitions for the contribution each experimental variable makes to the overall uncertainty of the final sorption data, one for linear error propagation, and one for Monte Carlo error propagation. This definition for the LEP method starts from Equation 18, which, after some algebra, provides the following expression to evaluate the fractional contribution of each independent variable to the overall variance:

$$1 = \sum_{i=1}^{n} \left[\frac{\left(\frac{\partial f}{\partial x_i} \sigma_{x_i} \right)^2}{\sigma_f^2} \right] \qquad \text{Equation 19}$$

Where each variable has the previously defined meaning and each term in the summation represents the fractional uncertainty contribution of the measurement involved in the calculation of f [96,97].

A similar, considerably simpler process can be applied to evaluate the individual variable contribution to the overall uncertainty using the Monte Carlo method. To do this, we used

a sensitivity analysis in which we run Monte Carlo simulations while restricting all uncertain variables to their nominal values, except for a single measurement or groups of measurements. The result of these simulations is a modified uncertainty, σ'_{F_i}, which quantifies the contribution of each variable i. This process is repeated for all variables of interest and the corresponding uncertainties are the given contributions for that measurement or measurement group. If the uncertainty due to all variables being used in the MCEP simulation is σ_F, we can define the uncertainty contribution as the fractional variance in a similar way to LEP, that is, $\left(\frac{\sigma'_F}{\sigma_F}\right)^2$. For example, for both LEP and MCEP methods, the contribution of a measured pressure to the moles of penetrant sorbed by the polymer during a given sorption step depends on the pressure measurements in previous steps, therefore, to assess the contribution of the pressure transducer's uncertainty, we consider them as a single contribution.

If non-linear error responses in MCEP are insignificant, and functional covariance is accounted for, then the contributions resulting from this analysis should align completely with the contributions defined by LEP, i.e., the total uncertainty of the calculated result is sufficiently approximated by the sum of the individual, independently simulated contributions to uncertainty.

This relationship proves incredibly useful to investigate which variables affect a particular type of experiment the most, and as will be seen in Chapter 5, can be used to highlight where improvements in an experiment will be the most effective [96].

1.9.4. Uncertainty of Fitting Parameters

In addition to the uncertainty of calculated values, it is often required to quantify the uncertainty of fitted parameters. This work employes three techniques to accomplish this task, which will be discussed briefly here. The first is the jackknifing technique [98], which repeats each fitting with a single datum omitted, then analyzing the resulting distribution of fitting values. For example, to obtain the uncertainty of the three dual mode parameters fitted to 8 sorption data points, one would perform 8 additional fittings, each omitting a single sorption data point followed by taking the normalized standard deviation of the resulting fitting distribution. This technique is quite fast, requiring only n additional fittings per data point present in the original optimization, but does not quantify covariance between fitted parameters and fails for large datasets [98], as dropping a single datum is unlikely to significantly alter the fit and thereby explore the range of possible valid (i.e., that result in comparable residual error) fitting parameters.

Bootstrapping [98] is a similarly purposed technique analogous to MCEP that involves resampling the original dataset with replacement. That is, for a data set of n measurements, randomly pick n values from the dataset with the possibility of picking the same measurement from the set multiple times and perform a fitting on the resulting dataset to acquire new fitting parameters. This process is repeated (typically many thousands of times) before analyzing the resulting distribution of fitted parameters, allowing for the quantification of each parameter's error. Like jackknifing, this method

does not quantify covariance between fitted parameters, but works in the presence of large sets of data and fails for small ones due to the high likelihood that the smaller data set will not include enough unique data points to acquire a valid fit.

Finally, a direct method to quantify fitting uncertainty exists that works by applying linear error propagation techniques to the sum of squared residual errors of the fitting itself. The intuition behind this technique is obtained by interpreting the concavity of the loss (i.e., the sum of squared residual errors or SSE) function at its local minimum as the confidence with which the fitted parameters are known. That is, a shallow, wide minimum with respect to a fitted parameter would suggest low confidence, as moving that parameter around this space would not change the SSE significantly. In contrast, a narrow, deep SSE function with respect to a fitted parameter suggests high confidence, as a small change in that parameter would greatly impact the SSE [101]. As this method is analytical, it also provides the ability to determine covariance between values as it quantifies the variance matrix of the parameters themselves. Informally referred to as the "Inverse Hessian Method", it is defined as follows [101–103]:

$$COV = \frac{H^{-1}}{DOF} = \frac{\left[\left.\frac{\partial^2(SSE(x))}{\partial x_i \partial x_j}\right|_{\min(SSE(x))}\right]^{-1}}{n-p} \qquad \text{Equation 20}$$

Where DOF is the number of degrees of freedom in the optimization, defined as the difference between the number of data points used in the optimization (n) and the number of parameters being fit (p). H is the hessian matrix of the residual error (SSE)

function with respect to the fitted parameters (x). Once this covariance matrix has been determined, the standard deviations of the fitted parameters are then the root of the diagonal of the covariance matrix, or $\sigma_{x_i} = \sqrt{COV_{ii}}$ [101,102].

This method is preferred in most cases but isn't always possible to calculate for a multitude of reasons. For example, if fitting a model in which not all parameters are used (or, more practically, the model has very low dependency on that parameter) then the derivative of the SSE function with respect to that parameter will be zero or close to zero, resulting in a hessian matrix with an undefined inverse. Calculating this hessian matrix can also prove computationally difficult, and in cases where this method fails or is impractical, jackknifing or bootstrapping provide practical alternatives. This work utilizes the inverse hessian method preferentially and defaults to jackknife and bootstrap methods when needed.

1.10. Experimental methods

1.10.1. Vapor sorption experiments

Condensable vapors, such as water, alcohols (i.e., methanol, 1-propanol 1-butanol), and large hydrocarbons have their solubility measured in a *vapor sorption apparatus* (see Figure 5). Vapor sorption isotherms were collected at 25°C using a constant-volume dual-chamber pressure decay system. The experimental setup generally consists of a sampling chamber, which contains a known mass of polymer, and a charge chamber, which houses

a pressure transducer [26,58,75]. The two chambers are connected through a valve. The charge chamber is also connected to both a vacuum line and vapor generator (See Figure 5A)

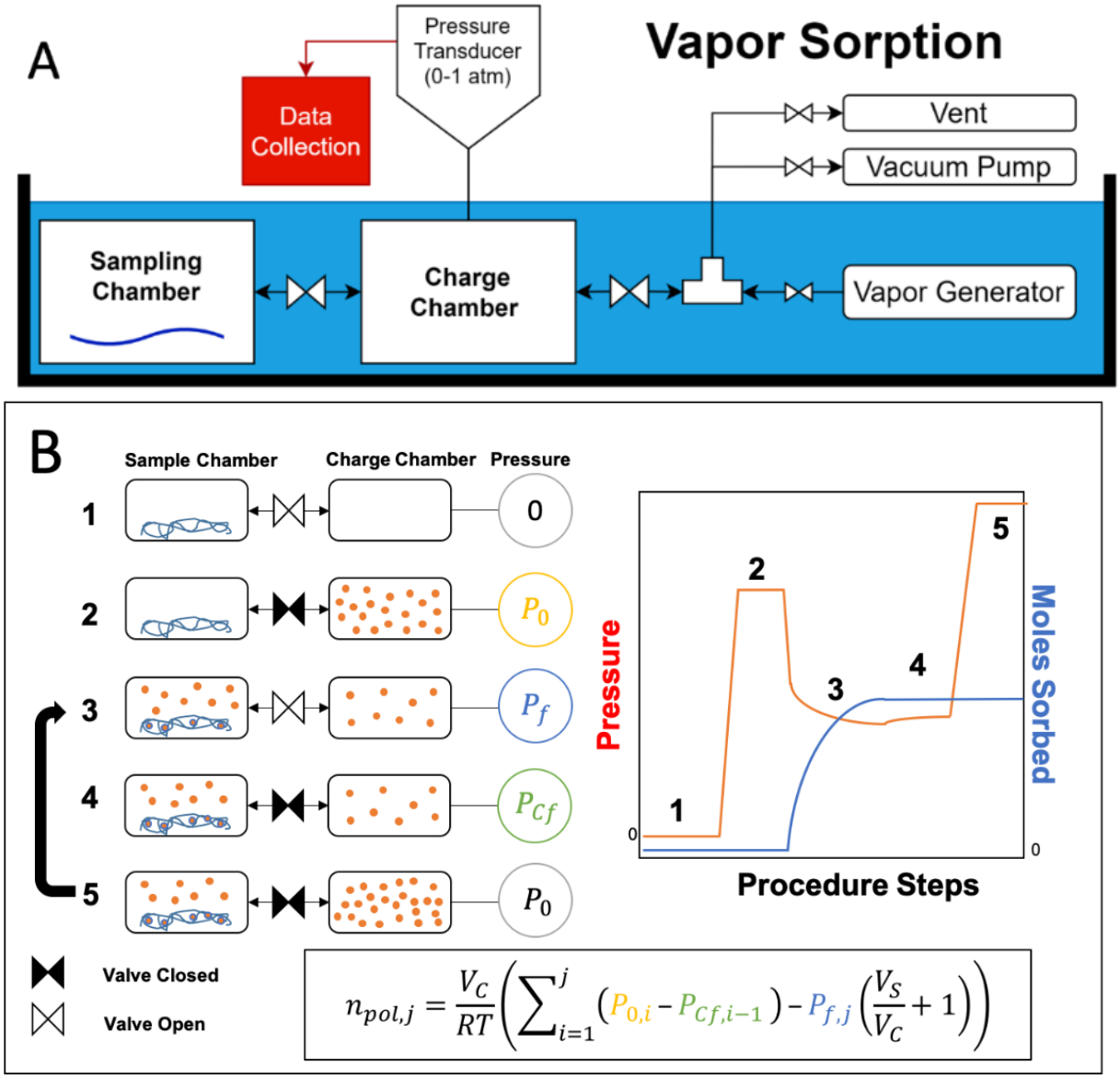


Figure 5: *A) Schematic of the constant volume pressure decay apparatus used to measure vapor sorption/adsorption in polymers and porous materials. B) Schematic of a typical vapor sorption measurement using the differential method.*

The entire apparatus is submerged in a water bath to maintain the temperature to the desired value. First, a full vacuum is pulled throughout the system to remove air and any trace of solvent or humidity trapped in the polymer (Figure 5B, step 1). Then, the valve between the two chambers is closed and the charge chamber is filled with vapor and a few minutes are allowed for the pressure reading to stabilize (Figure 5, step 2). The sorption experiment starts by opening the valve separating the two compartments. The single transducer now reads the pressure of the combined sampling and charge chamber volume. A step pressure decrease is observed, due to vapor expansion, followed by a slower exponential decay resulting from vapor being sorbed in the polymer sample (Figure 5B, step 3). Equilibrium is reached when pressure attains a constant value for several hours. Further measurements are taken in a stepwise fashion, by closing the valve to the sampling chamber (Figure 5B, step 4), adding more vapor to the charge chamber (Figure 5B, step 5) and repeating the procedure described above. Vacuum is not pulled in between steps, making the analysis in this report specific to the *differential* sorption method.

Temperature was controlled using a Techne© TU-20HT immersion circulator with an accuracy of $\pm 0.5°C$, and pressure was measured using an MKS© PDR2000 dual-capacitance manometer with a full scale of 500 Torr and an error of $\pm 0.25\%$ of the reading. The charge and sorption chamber volumes were determined using the Burnett method [104] and were found to be $29.477 \pm 0.098\, cm^3$ and $7.614 \pm 0.023\, cm^3$,

respectively. Vapor was generated using liquid-phase penetrant stored in a vessel submerged in the water bath, connected to a valve upstream of the sampling and charge chamber. A more in-depth explanation of this apparatus can be found in Chapter 5, Section 5.3.1.

Experimental sorption kinetics were fit to the Berens-Hopfenberg model to estimate the vapor diffusion coefficient, $\overline{D}_i$, as a function of concentration, as specified in the previous section. Before sorption begins, the polymer sample's thickness was measured using a *Mitutoyo* caliper with a resolution of 0.001mm at multiple points and averaged. Experimental uncertainty of solubility and diffusivity data were calculated using linear error propagation[96,98].

1.10.2. Gas Sorption Experiments

Pure-gas sorption isotherms were measured within the temperature range of 5−50°C and up to 35 atm. Sorption measurements were run using a dual-chamber pressure decay sorption apparatus (see Figure 6), equipped with two Honeywell Super TJE pressure transducers (0-500 $psia$, accuracy $\pm$ 0.05%). Pressure data were automatically collected using a custom-made Labview® acquisition program and run using in-house packages written in the Julia programming language.

The setup used to measure gas sorption is similar to that used for vapor sorption measurements, but with two key differences. First, during the sorption process the valve

between the charge and sampling chambers is closed, which means that an additional pressure transducer must be added to the sampling chamber (see Figure 6A) [75].

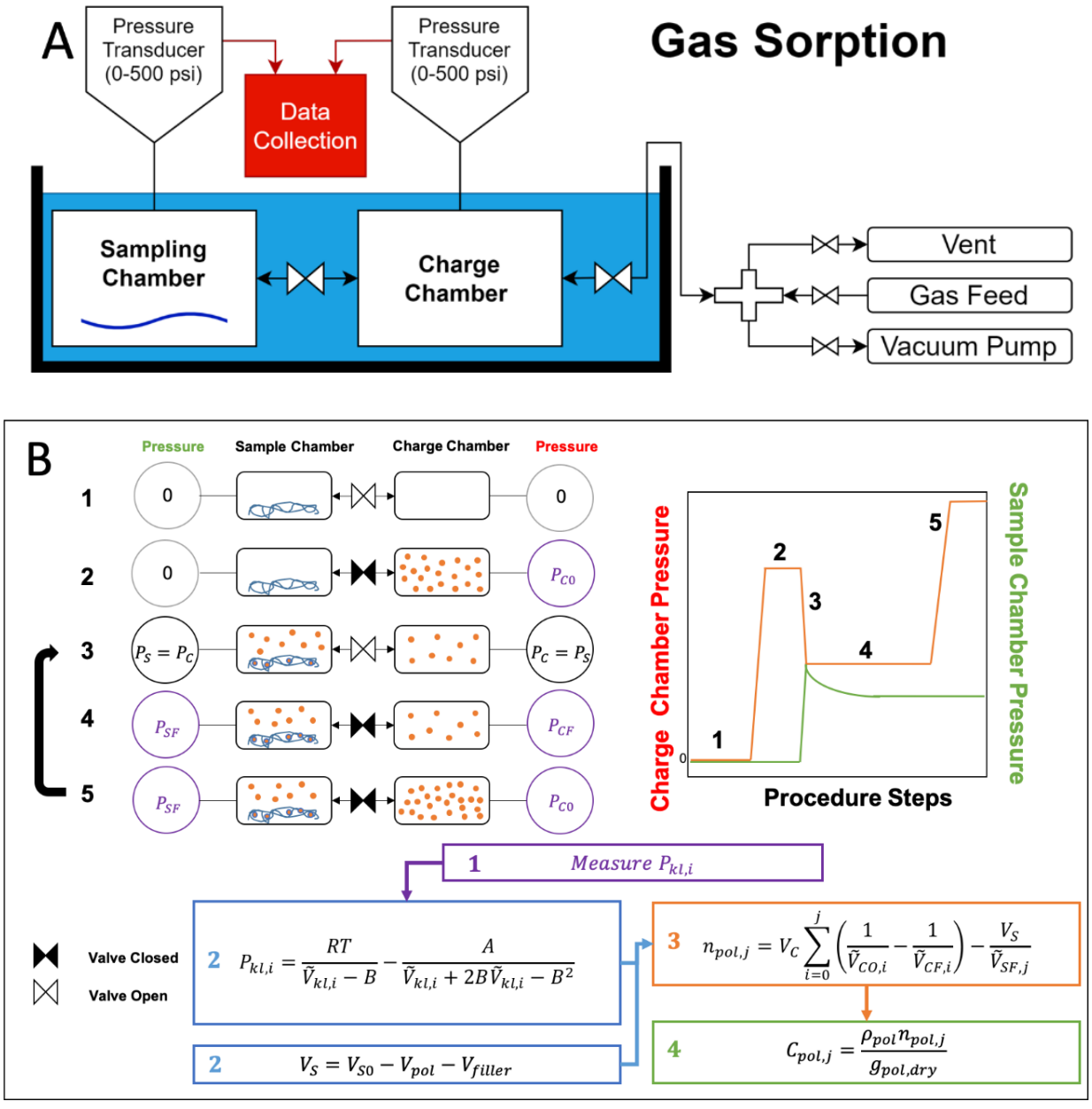


Figure 6: *A) Schematic of the constant volume pressure decay apparatus used to measure gas sorption/ adsorption in polymers and porous materials. B) Schematic of a typical gas sorption measurement using the differential method. Numbers denote step order for calculating concentration from pressure measurements.* V_{filler} *accounts for any other material (e.g., stainless steel beads) possibly used to reduce the total sampling chamber volume,* V_{S0}.

This choice helps minimize the effective volume of the chamber, enhance the signal-to-noise ratio and make sorption measurements more accurate.

The gas sorption apparatus consists of a charge chamber (18.442 ± 0.04 cm^3) which holds an initial quantity of gas, and a sampling chamber (15.707 ± 0.06 cm^3) which houses the polymer sample (see Figure 6A and B, step 1). Temperature was maintained constant using a water bath Techne TU-20HT heater (Cole Parmer). To run experiments at $5°C$ and $20°C$, a C1283-60 immersion cooler (Cole Parmer) was used. Prior to the measurement, polymer samples were weighed using a Mettler Toledo analytic balance.

Gas solubility data is collected stepwise. First, vacuum is pulled overnight in both the sampling and charge chambers, as well as in the service lines. The charge chamber then is filled with an initial quantity of gas, while the sampling chamber (housing around 0.1g to 0.5g of polymer sample) is still under full vacuum. Once the charge chamber pressure stabilizes (~10 to 15 minutes), the valve between the charge and sampling chambers is opened for 5 seconds before being closed again, which is the primary difference between gas and vapor sorption experiments. Pressure decay occurs in the sampling chamber over the course of anywhere from several hours to multiple days. Once the pressure in the sampling chamber stabilizes, the next step is run. These further steps occur by supplying additional gas to the charge chamber and repeating the process described above. Finally, a molar balance is used to calculate the number of moles of gas sorbed in the polymer.

The equilibrium gas fugacity at the end of any step is calculated using the Peng-Robinson equation of state (PREoS), whose input parameters are listed in Table A5.

Additional information regarding gas sorption experiments can be found in Chapter 5, Section 5.3.2.

1.10.3. Optical Dilation Experiments

The swelling apparatus considered in this study uses a Jerguson gage (Jerguson Gage & Valve Co.) and is placed within a built in-house thermostatic hood to regulate the temperature. The Jerguson gage is connected to a charging vessel lined with a built in-house gas pre-heating unit and an Omega pressure transducer. A DMK 33UX174 camera manufactured by The Imaging Source™ is fixed to a track-mounted stand capable of being moved via a threaded rod to center it with the sample. The camera collects images based on a timer, which is adjusted by the experimenter depending on the purpose of the experiment (see Figure 7).

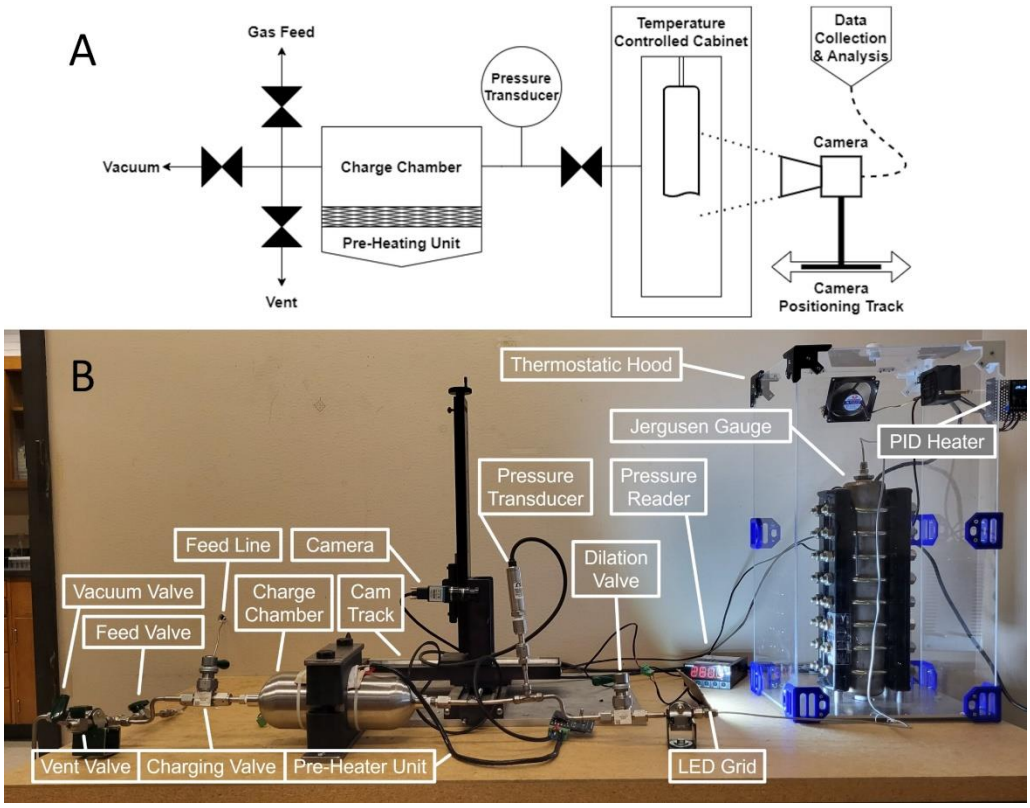


Figure 7: *Swelling apparatus: scheme (A) and annotated image (B).*

To run the experiment, a rectangular polymer sample is hung on a wire stand built to be placed securely within the Jerguson gage. The stand itself is made solely of metal parts, such that no material within the gage other than the polymer itself will absorb the penetrant gas and potentially dilate along with the sample. If the sample is known to curl or otherwise not remain perfectly straight during dilation, brass coupons may be used to constrain the sample while still allowing dilation to occur. Vacuum is pulled throughout the system over a period of 24 hours prior to the swelling experiment. Just before the first step, a reference image is taken at vacuum to serve as the point-of-comparison when determining how many pixels (see Section 4.4) the sample has dilated at any given future

point in time. To start the experiment, the charge chamber is filled with the gas through the charging valve, while the valve connecting it to the Jerguson gage is closed. At this point, the camera begins taking images at a pre-defined rate. The valve connecting the charging chamber to the Jerguson gage is then slowly opened, allowing the gas to reach the polymer; at this point, sample swelling begins. Within the first few seconds of dilation, image collection is slowed to around once per minute, and finally once per hour if the step is to be run overnight. Once equilibrium has been reached, new measurements are taken by repeating the stepwise procedure described above. The analysis, limitations, and optimizations of this experimental technique will be discussed in detail in Chapter 4, as this is one of the objectives of this work.

Chapter 2. Entropically Driven Sorption in Polymers Exhibiting Configurational Free Volume[†]

2.1. Abstract

This chapter reports findings that, for the first time, show the effect of configurational free volume (i.e., triptycene units) on condensable vapors transport in polymers. Alcohol and water vapor solubility and diffusivity isotherms at 25°C in a triptycene-containing polybenzoxazole (TPBO) exhibiting configurational free volume are presented as a function of vapor activity, discussed, and used to develop fundamental structure-property correlations. This chapter provides evidence that, despite conventional glassy polymer alcohol diffusion being size-controlled and sorption enthalpy-controlled (which, as discussed in Section 1.3.2, may create a trade-off between sorption- and diffusion-selectivity), alcohol sorption and diffusion in TPBO-0.25 are both size-controlled, which makes it potentially easier to simultaneously tune sorption- and diffusion-selectivity to achieve highly selective separations. To put these results in a broader perspective, alcohol sorption and diffusion properties of TPBO are compared with those of conventional glassy polymers exhibiting conformational free volume, such as PIM-1, Teflon AF2400, polynorbornene, polysulfone, as well as (rubbery) PDMS. Finally, new exciting

[†] Reproduced, with permission from Box, et al. [51]

opportunities to exploit these unique TPBO's features for large scale molecular separations are discussed.

2.2. Introduction and motivation

Despite the *leit-motif* of configurational free volume appearing to be a promising strategy for the design of next generation polymer membranes, the fundamental mechanism of small molecule transport in iptycene-based polymers is not yet fully understood. In particular, the few published fundamental sorption and transport data in these materials refer to light gases, such as CH_4, CO_2, N_2 and He, with little or no information available about the sorption and transport behavior of bulky condensable vapors [20,75]. As the first component of this project, the scope of this study is to shed fundamental light on the influence of triptycene groups on vapor transport. Alcohols were chosen as model penetrants due to their importance as energy sources. Biofuels are, indeed, dilute alcohol/water mixtures, and energy-efficient separation technologies are crucially important to produce fuel-grade alcohols[105,106].

While in conventional glassy polymers vapor diffusion is size- (i.e., entropy-) controlled and sorption is enthalpy-controlled as discussed in Section 1.2.2 [1,87,89,107], which may create a trade-off between sorption- and diffusion-selectivity, this study provides evidence that vapor diffusion and sorption coefficients in TPBO are both size- (i.e., entropy-) controlled, which makes it easier to simultaneously tune sorption-and diffusion-selectivity to achieve highly selective molecular separations. This result comes

from synergy between the exceptional size-sieving ability of iptycene units and the beneficial effect of size-controlled sorption. To the best of our knowledge, size-controlled sorption in polymers has never been reported before and will be the main object of investigation and discussion in this paper.

The unique transport mechanism of condensable vapors in TPBO, as well as the lack of solubility in organic solvents make this material attractive for the separation of organic species via organic solvent nanofiltration (OSN) and reverse osmosis (OSRO), pervaporation as well as vapor permeation [108]. In this study, the vapor sorption and transport properties in TPBO are presented, thoroughly discussed, and used to develop fundamental structure-property correlations to serve as a guide to design iptycene-based materials for the separation of organic species in vapor and liquid phase.

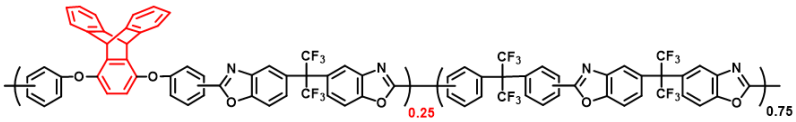
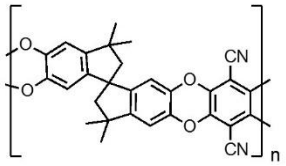
2.3. Experimental methods

2.3.1. Membrane fabrication and thermal rearrangement

The material considered in this study is a thermally rearranged polybenzoxazole containing 25% mol of triptycene units, i.e., TPBO-0.25, fabricated from a co-polyimide precursor with controlled triptycene molar content, or triptycene-dianhydride(0.25)-6FDA(0.75)-6FAP(1.0). Details about the synthesis protocol of the triptycene-based poly(hydroxyimide) precursor are provided in previous studies [20] and are summarized in Section A1, Appendices. Thermal rearrangement of the precursor to polybenzoxazole was achieved by pre-heating the triptycene-based poly(hydroxyimide) precursor to

300°C under nitrogen purge for 2 h [20]. Following this step, the temperature was raised to 450 °C at 10°C/min and maintained for 30 min, after which the film was cooled down to room temperature (cooling rate = 10°C/min), to become fully converted to thermally rearranged samples (i.e., TPBO) [20]. The structure and physical properties of TPBO-0.25 are shown in Table 2, along with those of PIM-1, which is a standard microporous polymer that is considered for the sake of comparison throughout this paper.

Table 2. *Structure and properties of TPBO-0.25* [20] *and PIM-1* [109].

material	*density* (g/cm^3)	T_g (°C)	*d-spacing* (Å)
TPBO-0.25 	*1.393 ±0.002*	*> 400*	*6.8*
PIM-1 	*1.143*	*442*	*6.6*

2.3.2. Vapor solubility and diffusivity measurements

Water and alcohol (i.e., methanol, 1-propanol 1-butanol) vapor sorption isotherms were collected at 25°C using a constant-volume dual-chamber pressure decay system and experimental procedure described in Section 1.10.1.

Experimental sorption kinetics were fit to the Berens-Hopfenberg model (See Section 1.7.2) to estimate the vapor diffusion coefficient, $\overline{D}_i$, as a function of concentration. Before sorption begins, the polymer sample's thickness was measured using a *Mitutoyo* caliper

with a resolution of 0.001mm at multiple points and averaged. Experimental uncertainty of solubility and diffusivity data were calculated using linear error propagation [97,98].

2.4. Results and Discussion

2.4.1. Equilibrium vapor sorption isotherms

Pure vapor sorption isotherms in TPBO-0.25 are shown in Figure 8A-B in units of g(penetrant)/g(pol) as a function of vapor activity. Equilibrium penetrant activity was calculated as $a = p/p_0$, where p_0 was taken from NIST.

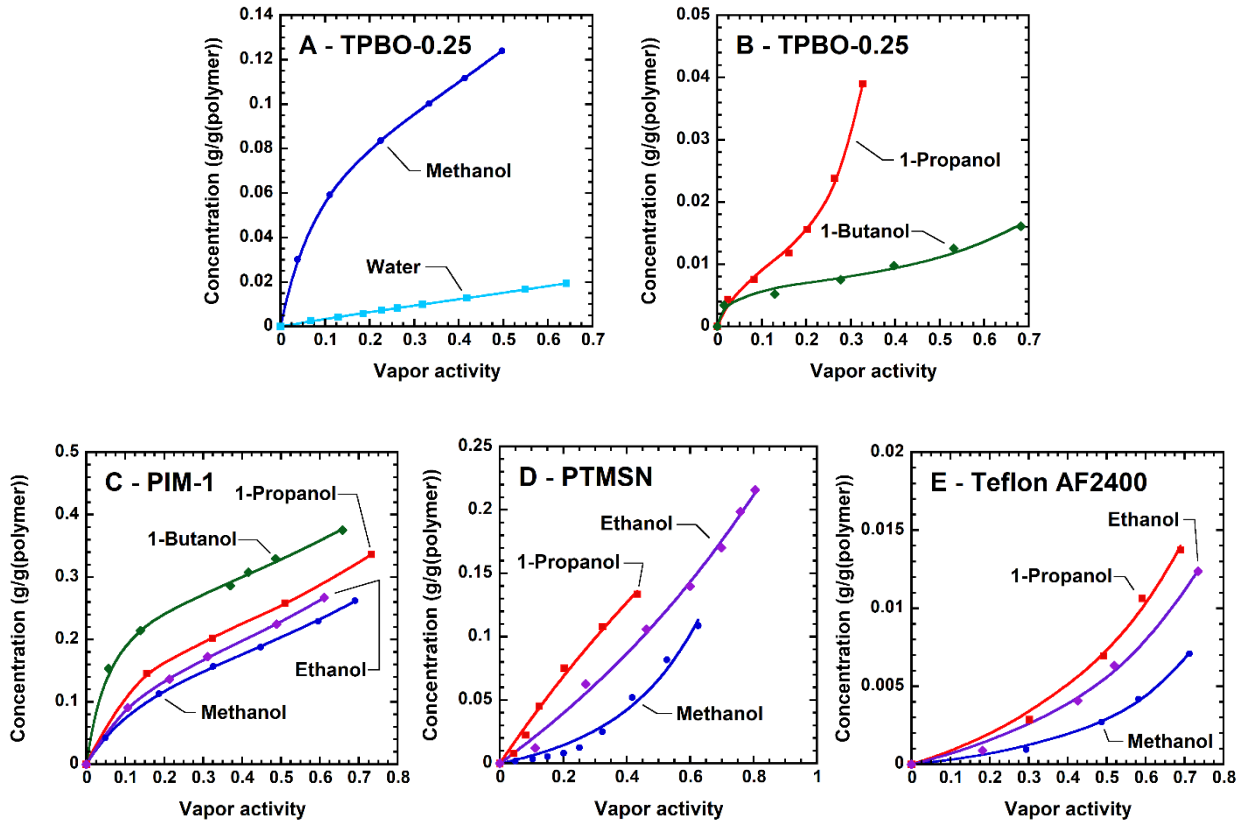


Figure 8: *Experimental solubility isotherms: A) methanol and water at 25°C in TPBO-0.25; B) 1-propanol and 1-butanol at 25°C in TPBO-0.25; C) methanol, ethanol, 1-propanol, and 1-butanol in PIM-1 at 25°C* [109]*; D) methanol, ethanol, and 1-propanol in poly(trimethyl silyl norbornene) (PTMSN) at 35°C* [89]*; E) methanol, ethanol, and 1-propanol in Teflon AF2400 at 25°C as a function of vapor activity* [110]*. Solid lines are the GAB model fittings. Error bars for TPBO-0.25*

sorption isotherms and activity values, which were calculated using linear error propagation, are too small to show.

Water and methanol sorption isotherms (cf., Figure 8A) follow the typical behavior observed in glassy polymers. Specifically, water vapor sorption isotherm is linear with activity, while methanol sorption isotherm exhibits the standard dual mode behavior [111]. In sharp contrast, larger alcohols (i.e., 1-propanol and 1-butanol, see Figure 8B) isotherms exhibit the dual mode shape at activity below 0.1, with a prominent upturn at higher activities. The maximum uncertainty of sorption data, which was calculated using linear error propagation, was ±1.2% [96].

Figure 8A shows that methanol sorption in TPBO-0.25 is remarkably high, with a concentration exceeding 0.1 g/g(pol) starting from an activity of 0.35. This value is 40% lower than methanol solubility in PIM-1 at the same temperature [109], but much larger than the corresponding solubility in poly(trimethylsilyl norbornene) (PTMSN) [107] and Teflon AF2400 [110]. PIM-1, PTMSN and Teflon AF2400 were chosen as terms of comparison as they also are high free volume glassy polymers exhibiting ultra-high T_g and for which vapor sorption data are available.

Interestingly, alcohols sorption in TPBO-0.25 markedly decreases with increasing condensability and molecular size (i.e., methanol >> 1-propanol > 1-butanol, see Figure 8A-B). In sharp contrast, alcohol sorption in conventional glassy polymers, such as PIM-1, PTMSN and Teflon AF systematically increases with increasing condensability and molecular size (i.e., methanol < ethanol < 1-propanol < 1-butanol, see Figure 8C, D, and

E) [107,109,110]. It is well known that small molecule sorption in polymers results from the interplay between enthalpic and entropic factors [89,94,107,112]. Enthalpic factors relate to polymer-penetrant interactions and penetrant condensability, according to the picture that penetrants exhibiting larger critical temperature (i.e., larger condensability) are more prone to sorb in the polymer phase in a condensed-like state. Entropic factors relate to penetrant molecular size, according to the physical picture that it becomes more difficult to accommodate penetrant molecules in the polymer matrix as their size increases (that is, sorption decreases with decreasing configurational entropy). For most of the polymers studied in the literature, enthalpic effects overwhelm entropic effects, therefore gas and vapor sorption systematically increase with increasing penetrant critical temperature (which means, in most cases, with increasing penetrant molecular size, see Table 3) [87,89,110,112–114]. As shown in a previous study, this rule applies to TPBO-0.25 when considering the sorption of light gases, so that gas solubility increases in the order: CO_2 > CH_4 > N_2 > He [75]. Interestingly, when considering bulky vapors sorption in TPBO-0.25, this rule is no longer valid. Even though a limited number of vapors have been investigated in this study, due to their slow sorption kinetics, TPBO-0.25 represents an interesting exception to the behavior described above, as alcohol sorption decreases with increasing condensability and molecular size. Alcohol's polarity decreases with increasing the length of its organic tail, therefore their interactions with hydrophobic polymers (such as PTMSN, PIM-1 and Teflon AF) become more

thermodynamically favorable in the order: methanol < ethanol < 1-propanol < 1-butanol. Therefore, enthalpic factors related to polymer-penetrant interactions and penetrant condensability make the sorption of bulkier alcohols in polymers larger than that of lower alcohols [107,109,110]. Analogous to PIM-1, PTMSN and Teflon AF, TPBO-0.25 is a hydrophobic material, owing to its structure made of fused aromatic rings. Although the ether group on the TPBO-0.25 backbone exhibits some polarity, which would promote the sorption of lower polar alcohols, it is sterically shielded by the bulky triptycene unit in close proximity (see Table 2). This conclusion is supported by the fact that water vapor sorption in TPBO-0.25 and PIM-1 at 25°C are fairly similar at low activity. At activities larger than 0.5, water sorption in TPBO-0.25 is even lower than PIM-1 (See Figure A2, Appendices). Therefore, it does not seem reasonable to attribute the high sorption of lower alcohols in TPBO-0.25 to a favorable interaction between alcohol –OH groups and ether groups on the polymer backbone. We attribute this size-controlled sorption behavior in TPBO-0.25 to entropic factors. Indeed, while methanol (kinetic diameter = 3.6Å, see Table 3) can fit in the internal cleft of triptycene units, bulkier alcohols are less likely to fit in the triptycene units, which could cause the observed size-exclusion effect. Different analyses, including PALS measurements and molecular simulations, provided an estimate of the size of the internal free volume of triptycene units. Specifically, PALS analysis conducted on TPBO-0.25 indicated that the average cavity size is about 7Å [20]. This number, however, does not provide the size of the internal free volume of triptycene

units, but the average size of free volume elements, including conformational and configurational free volume. A separate study indicated that the internal size of triptycene units is < 4Å [115]. Finally, based on purely geometric considerations, one may consider the void space between two arene blades of triptycene units as a triangular prism whose volume is 31Å [61]. If this volume is approximated as that of a sphere, the diameter would be around 3.9Å [115]. Therefore, we can infer that, among the alcohols considered in this study, only methanol can fit into the configurational free volume sites, while 1-propanol and 1-butanol are excluded as their molecular size exceeds that of configurational free volume sites (see Table 3).

Table 3: *Critical parameters and kinetic diameter of the vapors considered in this study and in the Vopicka's study*[109].

vapor	*critical temperature (K)*	*critical volume (L/mol)*	*kinetic diameter* [116] *(Å)*
water	*647.0*	*0.0559*	*2.65*
methanol	*513.0*	*0.116*	*3.60*
ethanol	*516.2*	*0.168*	*4.50*
1-propanol	*536.9*	*0.217*	*4.70*
1-butanol	*563.1*	*0.274*	*5.00*

Sorption isotherms were fit to the GAB model (see Section 1.6.2 and Table 4). Uncertainty of the GAB parameters were calculated using the jackknife resampling method [96,101,103] (see Section 1.9.4).

Table 4: *Fitted GAB model parameters for vapor sorption isotherms in TPBO-0.25 at 25°C.*

vapor	C_p *(g/g(pol))*	*A*	*k*
water	0.0233 ± 0.00329	3.25 ± 0.13	0.47 ± 0.05
methanol	0.0962 ± 0.0098	18.31 ± 0.18	0.62 ± 0.01

1-propanol	0.00914 ± 0.00102	9.73 ± 4.28	2.36 ± 0.13
1-butanol	0.00601 ± 0.00098	73.36 ± 30.72	0.89 ± 0.10

As expected, the sorption capacity of the first alcohol monolayer, C_p, decreases with increasing the number of alcohol carbon atoms. This behavior, which is justified based on steric considerations, has been observed in other polymers, such as PIM-1 [109]. The methanol C_p value, about 0.096 g/g(pol), is comparable to methanol total sorption, indicating that most of methanol is sorbed within the first monolayer, with negligible clustering. The same conclusion (i.e., lack of clustering) can be drawn for water, for which C_p is close to the total water concentration in the polymer. The parameter k measures the penetrant propensity to form clusters. While clustering looks negligible for water, methanol and 1-butanol (for which k assumes relatively low values), 1-propanol is, among the vapors considered in this study, the one that clusters the most, based on its much larger k value. Finally, the heats of sorption of the first alcohol monolayer (A) do not follow a specific trend as a function of alcohols size, analogously to what was observed by Vopicka et al. in PIM-1 [109].

It should be noted that the relatively high uncertainty in the GAB model parameter A is the result of the fact that the first monolayer usually becomes saturated within the first or second sorption step (see Section 1.6.2). This means that one or two data points contain the information needed to determine this parameter, and since parameter uncertainties

in this work are determined using drop-one-off (that is, jackknife) resampling, the loss of this data point produces a larger uncertainty on *A*.

The Zimm-Lundberg model was used to explain the prominent upturn in the sorption isotherms of higher alcohols and de-couple the effects of swelling and clustering. The Zimm-Lundberg analysis shows clustering for 1-propanol, while methanol, water and 1-butanol do not cluster according to this analysis (See Section A3, Appendices). This picture is fully consistent with the results of the GAB fitting discussed above. However, we should note that the Zimm-Lundberg model provides a very empirical analysis of clustering, therefore a FTIR-based investigation in underway to get a more realistic picture. Regardless, our analysis is still meaningful by way of the fact that two independent models (GAB and Zimm-Lundberg) point towards the same conclusions, as far as clustering is concerned. A still open question, however, is why methanol and water cluster less than 1-propanol. Due to its smaller alkyl tail, methanol is more polar than 1-propanol, and therefore it is expected to exhibit a larger clustering propensity. This result could be rationalized based on two effects: *i)* a fraction of sorbed methanol and water molecules (the only penetrants that can fit into the configurational free volume sites) are confined inside the triptycene units, which hampers methanol and water molecules to self-hydrogen bond; *ii)* the polymer swelling produced by methanol, due to its extremely high sorption, creates additional room to accommodate the penetrant, which similarly hampers methanol molecules to get close enough to create higher order aggregates. The

low methanol clustering propensity is consistent with the analysis of diffusion coefficients presented in Section 2.4.2 Molecular simulations and experimental FTIR studies are underway to shed more light on this aspect. Finally, the higher 1-propanol clustering propensity relative to 1-butanol is consistent with the higher polarity of the former alcohol. The conclusion is that the upturn exhibited by the 1-butanol sorption isotherm is due to polymer swelling, while that exhibited by the 1-propanol sorption isotherm could be either due to polymer swelling or clustering. The analysis of diffusion coefficients in Section 2.4.2 will clarify this aspect.

Koros et al. measured alcohol adsorption isotherms at 35°C in zeolite imidazolate frameworks, namely ZIF-8, ZIF-71 and ZIF-90 [117]. Although these isotherms exhibit a sigmoidal behavior at activity below 0.05, at activities above 0.1 sorption increases in the order: methanol > ethanol ≅ 1-propanol. Krishna and co-workers combined experiments and Monte Carlo simulations to show that alkane sorption in zeolites is size-driven (that is, entropy-driven), as it decreases with increasing the number of carbon atoms. They highlighted three types of entropic effects: a *size-effect*, which favors the sorption of the component exhibiting the smallest number of carbon atoms; a *configurational effect*, which, at given number of carbon atoms, favors the sorption of linear versus branched isomers. Finally, for zeolites exhibiting cylindrical channels, such as AFI and MOR, they highlighted a *length effect*, based on which the sorption of double branched isomers is

favored over linear alkanes. Therefore, an interesting similarity exists between vapor sorption in polymers exhibiting configurational free volume and sorbents [118].

Although it would be useful to include in this study other vapors besides alcohols, the time needed to reach sorption equilibrium in the presence of hydrocarbon vapors is unreasonably long. For this reason, in this preliminary study we limit our analysis to alcohol vapors.

2.4.2. Vapor diffusion coefficients

Vapor diffusion coefficients were determined as a function of vapor concentration in TPBO-0.25 from the analysis of the experimental sorption kinetics. As mentioned in the theoretical section, the Berens-Hopfenberg model was used to fit the experimental sorption kinetics of all vapors considered in this study, except for methanol. Due to its high solubility in TPBO-0.25, changes in methanol concentration at the polymer surface are expected, therefore the modified Berens-Hopfenberg method was used in the latter case to provide a more accurate estimate of the diffusion coefficient. A comparison among different fitting approaches for methanol sorption kinetics are shown in Section A5, Appendices. The models were implemented in *Julia* with an n cutoff of 15 (See Equation 12 and 13) and using LM-BFGS-B, an optimization algorithm. As shown by Moon et al. [78], considering more than 5 terms in equations 12 and 13 do not provide significant differences in the fitting quality. Examples of methanol and 1-propanol sorption kinetics

in TPBO-0.25 at 25°C, with the corresponding Berens-Hopfenberg fittings, are shown in Figure 9 A-B. The best-fit parameters, k_F, k_r and β, are shown in Section A4, Appendices.

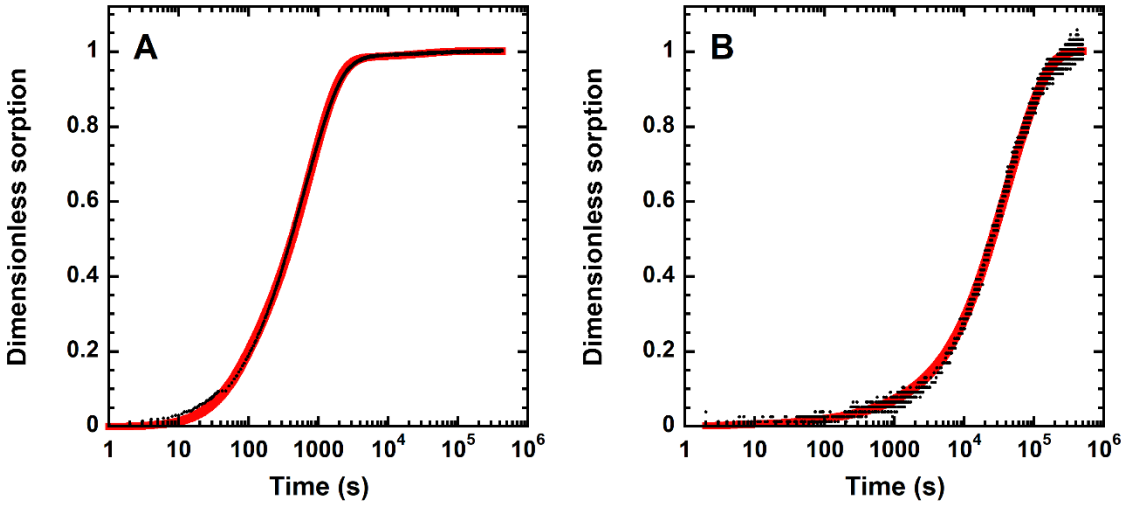


Figure 9: *Sorption kinetics in TPBO-0.25 at 25°C: A) methanol (activity jump 0.0-0.038) and B) 1-propanol (activity jump 0.16-0.20). Black dots are experimental data, and solid red lines are the modified Berens-Hopfenberg Model (A) and Berens-Hopfenberg Model (B) fittings* [78,84]. *Dimensionless sorption is defined as* $\frac{M_{sorbed}(t)}{M_{sorbed}(t_\infty)}$.

Vapor diffusion coefficients in TPBO-0.25 at 25°C, $\overline{D}_i$, are shown in Figure 10A as a function of vapor equilibrium concentration in the polymer. Experimental uncertainty of diffusion coefficients was calculated via bootstrap resampling.

As expected, diffusion coefficients decrease with increasing penetrant size in the order: water > methanol > 1-propanol ≅ 1-butanol. The trends of diffusion coefficients as a function of concentration, however, depend on the single vapor. For example, water and 1-propanol diffusion coefficients are fairly constant with concentration. In striking contrast, methanol diffusion coefficients increase markedly with increasing

concentration. Finally, 1-butanol diffusion coefficients slightly decrease with increasing concentration in the polymer.

To properly analyze vapor diffusion in TPBO, it is recommendable to correct the diffusion coefficient for thermodynamic non-idealities. This correction is normally unnecessary for the analysis of light gas diffusion coefficients in polymers, due to the fact that the gas-polymer binary interactions do not depart substantially from ideal behavior, except in a limited number of cases [114,119–122]. However, this simplification does not necessarily apply to condensable vapors, whose mixing with the polymer to form a condensed-like phase may deviate considerably from ideality [26,88]. Vapor diffusion coefficients in polymers are influenced by at least three factors [26,88,89]: *i)* polymer relaxation and swelling, *ii)* vapor clustering, and *iii)* polymer-vapor molecular interactions. If we limit our analysis to the concentration averaged diffusion coefficient, $\overline{D}_i$ (See Figure 10A), these three effects are difficult to isolate, therefore it is important to correct $\overline{D}_i$ for thermodynamic non-idealities to get its purely kinetic component, L_i (i.e., the mobility factor, see Figure 10B).

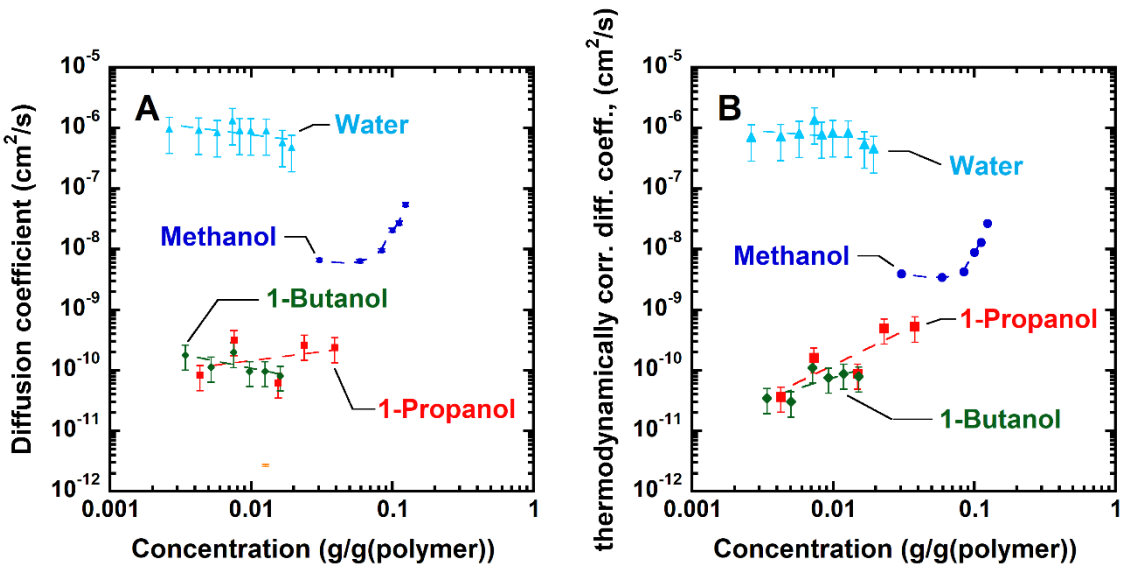


Figure 10: *A) Vapor concentration-averaged diffusion coefficients, $\overline{D}_i$, in TPBO-0.25 at 25°C as a function of equilibrium concentration. B) Mobility coefficients (i.e., thermodynamically-corrected diffusion coefficients, L_i) at 25°C as a function of equilibrium concentration.*

Water mobility and diffusion coefficients are pretty constant with concentration, which is likely due to the low water concentration in the polymer. This fact, as well as the lack of water clustering shown by the GAB and Zimm-Lundberg models, indicates that water vapor does not plasticize TPBO-0.25. Therefore, we expect that humidity should not influence remarkably the TPBO performance in membrane applications.

As expected, mobility coefficients (see Figure 10B) systematically decrease with increasing penetrant size, which mirrors the behavior of the concentration averaged diffusion coefficient. Interestingly, while 1-propanol and 1-butanol diffusion coefficients are very close to each other, the mobility coefficient of 1-propanol exceeds, as expected, that of 1-butanol. The methanol mobility coefficient is initially constant with increasing methanol concentration in the polymer, and then it increases. This result indicates that

methanol molecules are initially accommodated in pre-existing sorption sites, which correspond to Langmuir sites in the traditional dual mode nomenclature [111]. These sorption sites likely include triptycene units which, based on their size and geometry, may accommodate methanol molecules. At higher activities, polymer swelling pulls polymer chains apart and reduces the frictional resistance to penetrant transport, which may explain the increase in the methanol mobility coefficient. This picture is consistent with the results of the GAB and Zimm-Lundberg analyses (see Sections 1.6.2 and 1.8.2, respectively) which rule out the occurrence of methanol clustering. The latter phenomenon, if present, would cause a decrease of methanol diffusivity with concentration, as clusters diffuse much more slowly compared to single molecules [123]. This conclusion, however, must be interpreted cautiously: as mentioned above, an FTIR investigation is underway to shed more light on the issue of clustering. We conclude that TPBO swelling caused by methanol sorption overwhelms methanol clustering. Ongoing molecular simulations will shed light on the possibility that a portion of methanol molecules are confined in the triptycene units, which would help rationalize the apparent lack of methanol clustering.

The 1-propanol and 1-butanol mobility coefficients increase with increasing penetrant concentration in the polymer, indicating that, also in this case, swelling overwhelms clustering.

2.4.3. General correlations and comparison with other materials

The equilibrium and transient sorption data discussed in Sections 2.4.1 and 2.4.2 indicate that, while TPBO's vapor diffusion behavior does not depart from that of conventional polymers, its vapor sorption behavior is atypical. The penetrant sorption coefficient in polymers, S_i, is defined as $S_i = C_i/p$ [107,114,124] where C_i is the equilibrium concentration and p the corresponding equilibrium pressure. It has been shown that the logarithm of the sorption coefficient increases linearly with increasing penetrant critical temperature [114] or in other words:

$$ln(S_i) = \alpha + \beta T_C \qquad \text{Equation 21}$$

In Figure 11A, the experimental alcohol sorption coefficients in PIM-1 at 25°C and activity 0.1, reported by Vopicka et al. [109], systematically increase with increasing alcohol condensability and size. The same behavior has been observed in PTMSN at 35°C [89] and Teflon AF2400 at 25°C [110] (Figure 11A). Even though sorption data in TPBO-0.25 were collected for a limited number of vapors, due to the long times needed to reach equilibrium, the behavior of TPBO-0.25 deviates from that of conventional glassy polymers, as, at least for alcohols, sorption does not increase with increasing alcohol condensability and molecular size, but it exhibits a slightly decreasing trend (Figure 11A). As discussed above, we hypothesize that, in contrast with conventional polymers, where alcohol sorption is enthalpy-driven, alcohol sorption in TPBO-0.25 is entropy-driven (i.e., size-driven). The unique size-driven sorption behavior exhibited by TPBO might

originate from the extremely regular and rigid configuration-based free volume pockets provided by triptycene units, which are expected to control vapor sorption based on entropic factors instead of enthalpic factors.

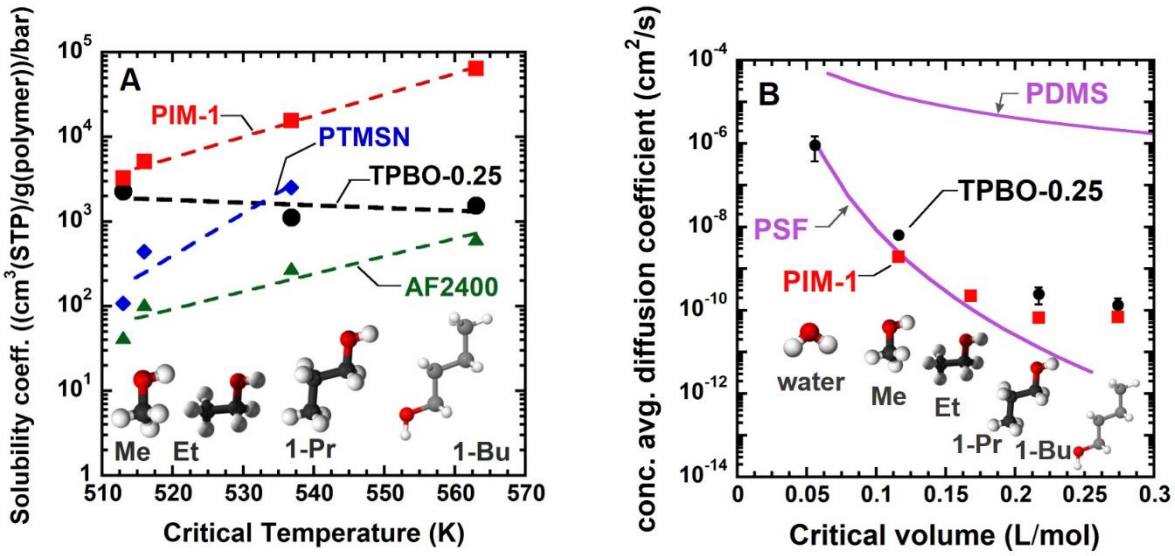


Figure 11: *A) Vapor solubility coefficients, S, in (cm³(STP)/g(polymer))/bar, for various polymers as a function of vapor critical temperature* [89,109,110]. *TPBO-0.25 (black circles, 25°C and activity 0.1). PIM-1 (red squares, 25°C and activity 0.1). PTMSN (blue diamonds, 35°C and activity 0.1). Teflon AF2400 (green triangles, 25°C and activity 0.67). Dashed lines are drawn to guide the eye. B) Alcohol diffusion coefficient, $\overline{D}_i$, at 25°C in PIM-1 (activity 0.2)* [109] *and TPBO-0.25 (activity 0.1) as a function of critical volume. Diffusivity data for poly(sulfone) (PSF) and PDMS at 25°C are shown for the sake of comparison* [125].

The slope of the infinite dilution light gas solubility coefficient versus T_C (that is, β in Equation 21) is about 0.016-0.020K^{-1} for hydrocarbon-based polymers and 0.009-0.012K^{-1} for perfluoropolymers [114]. The validity of this correlation for TPBO-0.25, PIM-1 and Teflon AF2400 has been verified in previous studies [75,87,109,114]. Specifically, when considering He, N_2, CH_4 and CO_2 sorption data at 35°C and in the limit of infinite dilution in TPBO-0.25, β = 0.015K^{-1} [75]. The kinetic diameter of He, N_2, CH_4 and CO_2 is smaller

than the internal size of triptycene units, i.e., light gases can be accommodated into the configurational free volume delimited by the arene blades in the triptycene groups. As expected, the slope of the alcohols sorption coefficient versus T_C does not match the values shown above, due to profound differences between gas and vapor sorption. Indeed, in contrast with light gases, alcohol vapors *i)* give rise to mutual- and self-interactions, *ii)* are much bulkier, and *iii)* produce a more severe polymer swelling, if not plasticization. Moreover, due to activity (i.e., $a = p/p_0$) limitations, vapor sorption isotherms contain less data points than light gas sorption isotherms, therefore it is hard to provide a precise estimate of vapor sorption coefficients at infinite dilution. For this reason, the vapor sorption coefficients shown in Figure 11A are not taken at vanishing activity, which obviously complicates the comparison of β values among gases and vapors. A more detailed analysis of the β value for condensable vapor sorption in polymers would require solubility data for a variety of vapors exhibiting different properties (polarity, condensability and size), while here we can rely only on 3 or 4 alcohols. For the sake of completeness, we report that, at 25°C, β = 0.057K^{-1} for PIM-1 (considering methanol, ethanol, 1-propanol and 1-butanol sorption data, see Figure 11A) and -0.0072K^{-1} for TPBO-0.25 (considering methanol, 1-propanol and 1-butanol sorption data, see Figure 11A).

Vapor diffusion coefficients at 25°C and activity 0.1 in TPBO-0.25 are shown in Figure 11B as a function of penetrant critical volume. Diffusivity data at 25°C in PIM-1 (activity 0.2,

ref. [109]) are shown as well for the sake of comparison. Alcohol diffusion coefficients in TPBO-0.25 slightly exceed those in PIM-1, which is consistent with the larger average *d*-spacing exhibited by TPBO-0.25 relative to PIM-1 (See Table 2). As expected, diffusion coefficients systematically decrease with increasing penetrant size, therefore, TPBO's behavior does not depart from that typically observed in other polymers [87].

To put the results of this study in a broader perspective, diffusion coefficients in TPBO are compared to previously reported data for glassy polysulfone (PSF, a model size-selective polymer) and rubbery poly(dimethyl siloxane) (PDMS, a model soluble-selective polymer) at 25°C [125]. As shown in Figure 11B, alcohol diffusion coefficients in TPBO lie close to those of glassy PSF, which demonstrates the TPBO size-sieving behavior.

The results discussed above indicate that both vapor sorption and diffusion coefficients in TPBO-0.25 are entropy-driven, that is, both vapor sorption and diffusion coefficients decrease with increasing vapor size. In conventional polymers, the vapor sorption coefficient increases with increasing penetrant size and the diffusion coefficient decreases with increasing penetrant size, which may create a trade-off between sorption- and diffusion-selectivity. In contrast, vapor solubility-selectivity and diffusivity-selectivity in TPBO are both size-controlled (i.e., entropy-controlled) which, based on the solution-diffusion model, may help optimize selectivity in separations involving bulky organic species.

2.4.4. Implications

The unique entropy-based vapor sorption and transport mechanism exhibited by TPBO highlights an interesting synergy between solubility- and diffusivity- coefficients, both of which decrease with increasing penetrant size, allowing for solubility- and diffusivity-selectivities to work together, rather than against each other. This feature may help maximize selectivity in a variety of separations involving bulky organic species, such as organic solvent nanofiltration, organic solvent reverse osmosis and vapor permeation. For example, these separations may beneficially impact the production of ethanol and biofuels. Ethanol is a common solvent in the pharmaceutical industry and can be contaminated with variable amounts of methanol and water at the end of the production process. Azeotropic and extractive distillation, which are used to efficiently separate ethanol from other alcohols and water, are energy intensive and require large investment costs, therefore it could be convenient to replace them with a membrane process [126].

To highlight the practical implications of entropy-driven alcohols transport in TPBO-0.25, we report, in Table 5, the pure component 1-butanol/methanol sorption- and diffusion-selectivity estimated using the data shown in Figure 11 A-B. While PIM-1 sorption-selectivity offsets the benefit of diffusion-selectivity, TPBO-0.25 sorption- and diffusion-selectivity are both favorable to methanol. We want to stress that the numbers reported in Table 5 do not necessarily reflect the actual TPBO performance, as they are pure vapor selectivities.

Table 5: *Comparison between 1-butanol/methanol sorption- and diffusion-selectivity at 25°C in TPBO-0.25 and PIM-1. Data for PIM-1 are from ref.* [109]. *Uncertainties for TPBO-0.25 were estimated using linear error propagation* [96,98,103].

	1-butanol/methanol sorption-selectivity[a]	*1-butanol/methanol diffusion-selectivity*[b]
TPBO-0.25	*1.40 ± 0.01*	*48 ± 20*
PIM-1	*0.050*	*28*

[a] *estimated at an activity of 0.1*

[b] *estimated at an activity of 0.2.*

2.5. Conclusions

Alcohol and water vapor equilibrium and transient sorption in a glassy polybenzoxazole exhibiting configurational free volume (TPBO-0.25) was studied experimentally at 25°C as a function of vapor activity and compared to vapor transport in conventional glassy polymers exhibiting conformational free volume. Methanol sorption in TPBO-0.25, which is concave to the activity axis, is 40% lower than in PIM-1 and 50 times larger than in Teflon AF2400 at 25°C. Sorption isotherms of higher alcohols, such as 1-propanol and 1-butanol, exhibit a marked upturn at activity above 0.2, which, based on the GAB and Zimm-Lundberg analysis, was attributed to polymer swelling.

In striking contrast with conventional glassy polymers, alcohol sorption in TPBO is entropy controlled, as it does not increase with increasing alcohol molecular size and critical temperature, with methanol (critical temperature = 239.9°C, kinetic diameter = 3.6Å) being the most soluble and 1-butanol (critical temperature = 289.9°C, kinetic diameter = 5Å) being the least soluble alcohol among those considered in this study. The

opposite behavior is observed in conventional glassy polymers exhibiting conformational free volume, where vapor sorption is enthalpy driven and increases with increasing molecular size and condensability. This unique feature of TPBO was attributed to the triptycene units, which may effectively exclude molecules larger than their internal configurational free volume via a purely entropy-driven mechanism.

Vapor diffusion in TPBO-0.25 is accompanied by non-Fickian relaxation. Experimental vapor sorption kinetics were fitted to the Berens-Hopfenberg diffusion-relaxation model, to get the concentration-averaged diffusion coefficient as a function of vapor concentration in the polymer. Concentration-averaged diffusion coefficients were then corrected for thermodynamic non-ideality. Vapor diffusion coefficients in TPBO-0.25 at 25°C lie close to the polysulfone values when reported as a function of vapor critical volume, which highlights the strong size-sieving ability exhibited by TPBO. Similar to conventional glassy polymers, vapor diffusion coefficients decrease with increasing vapor's molecular size. Therefore, vapor sorption and diffusion coefficients in TPBO-0.25 are both size-controlled, which makes it easier to simultaneously tune sorption-and diffusion-selectivity to achieve highly selective separations. These unique features make TPBO an interesting candidate for vapor separations and, possibly, organic liquids separation.

Chapter 3. The Mechanism of Light Gas Sorption in Configurational Free Volume‡

3.1. Abstract

A possible mechanism of small molecule transport in glassy polymer membranes containing configurational free volume (i.e., triptycene moieties) is proposed. To this aim, a family of triptycene-containing polybenzoxazoles (TPBOs) exhibiting systematically varied molar amount of triptycene units, ranging from 25% to 100%, was selected to perform a light gas (N_2, CH_4 and CO_2) fundamental sorption-transport study. The dual mode sorption-mobility model was used to isolate the effect of configurational free volume on penetrant transport. CO_2 and CH_4 Henry's and Langmuir's mode diffusion coefficients were estimated and used to quantify the Henry's and Langmuir's contributions to CO_2/CH_4 diffusivity-selectivity as a function of the triptycene molar content in TPBOs. Interestingly, while the Henry's CO_2/CH_4 diffusivity-selectivity changes little with increasing amount of configurational free volume, the Langmuir's CO_2/CH_4 diffusivity-selectivity increases up to infinity when the molar triptycene concentration in the polymer is 75% or higher, showing that the diffusion of larger molecules (i.e., CH_4) is increasingly hindered relative to smaller molecules (i.e. CO_2) diffusion when more configurational free volume is incorporated in the polymer. In sharp

‡ Reproduced, with permission from Box, et al. [43]

contrast, pure- and mixed-gas sorption, as well as solubility-selectivity, is essentially unaffected by the triptycene molar content. According with this physical picture, the analysis of isosteric heats of CO_2 sorption indicates that TPBOs plasticization resistance is independent of triptycene content.

3.2. Introduction

Since 1991, the introduction of advanced polymer synthesis strategies allowed membrane separations to become competitive with traditional thermal-based separation technologies. A plethora of novel functional polymers, purposely designed to achieve specific molecular separations, were synthesized with the scope of addressing three major issues: the selectivity/permeability trade-off, physical aging, and plasticization [1,23,30,40,55,61,68,119,127–133].

Although it was originally reported solely for gas separation membranes, the existence of a selectivity/permeability trade-off has also been observed in liquid separation membranes, including water purification and organic solvents separation [134–137]. As a consequence, most of the gas separation upper bounds first reported by Robeson in 1991 [30], were updated in 2008 [61] taking in consideration new materials appeared in the market in the previous seventeen years: perfluoropolymers, which were the subject of intense research in the late ‘90s, were mostly responsible for this improvement [60,61]. For this reason, most of research in the field has focused on the discovery and development of advanced membrane materials that can surpass the upper bound while

achieving an economically attractive performance. In 2019, the discovery of a new class of polymers of intrinsic microporosity (PIMs) bearing benzotriptycene moieties allowed to further push up and re-define the upper bound in several gas separation applications [60].

Since the pioneering study reported by Park in 2011 [138], glassy polymers containing triptycene units and their derivatives emerged as an interesting platform of materials [20,23,115,127,139,140]. As discussed in Section 1.5, triptycene groups, made of three benzene rings arranged in a 3D paddlewheel-like configuration, provide their unique configurational free volume, which promotes high permeability while maintaining it stable over long-term operation [127,139,141,142]. Iptycene-based materials are garnering increasing attention in membrane science. However, despite the current progress, fundamental understanding of small molecule transport in glassy polymers exhibiting configurational free volume is still poor and incomplete. Only recently, Box et al. (Chapter 2) reported that the transport of bulky vapor molecules in thermally rearranged triptycene-based polybenzoxazoles (TPBOs) is limited by entropic factors, with both sorption and diffusion being controlled by penetrant size [51]. To fill this fundamental knowledge gap, in this study we provide a detailed description of the molecular mechanism of light gas transport in polymers exhibiting configurational free volume, which builds off of that work. Here, a series of thermally rearranged polybenzoxazoles (TPBOs) exhibiting systematically varied molar amounts of triptycene units was selected

as a platform to develop structure-property correlations, with the final goal of understanding the mechanism by which configurational free volume regulates selectivity in membrane separations.

3.3. Experimental

3.3.1. Sorption and transport measurements

Pure gas N_2, CH_4 and CO_2 sorption isotherms at multiple temperatures (20, 27, 35 and 50°C for TPBO-0.50, TPBO-0.75, TPBO-1.00; 5, 20, 35 and 50°C for TPBO-0.25) and up to 35 atm were measured using a dual volume barometric apparatus, whose main features and procedures are summarized in Section 1.10.2. The Peng-Robinson equation of state was used to solve the molar balances needed to generate the sorption isotherms [143]. Pure gas N_2, CH_4 and CO_2 permeability data at 35°C were taken from ref. [20]. Diffusion coefficients at 35°C were calculated via the solution-diffusion model (See Section 1.2) [25], using experimental solubility and permeability data.

3.4. Results and Discussion

3.4.1. Pure-gas sorption as a function of temperature and triptycene content

Pure-gas CO_2 sorption isotherms at 35°C in TPBOs exhibiting systematically varied molar amount of triptycene units (i.e., 25, 50, 75, 100%) are shown in Table A1 (Appendices), in the units of cm^3(STP)/cm^3(polymer), as a function of CO_2 fugacity. Experimental uncertainty was estimated using linear error propagation [96,98], taking into account the uncertainty of *i)* the volumes of the sorption and charge chambers, *ii)* the pressure

transducers reading, *iii)* the temperature controller reading and *iv)* the polymer density. Pure gas fugacity was calculated at any temperature and pressure using the Peng-Robinson equation of state (See Table A5, Appendices) [98].

All the isotherms, at all temperatures and for all TPBO samples, exhibit the typical dual mode shape. CO_2 sorption isotherms in TPBOs at 35°C are, within the experimental uncertainty, superimposed over each other (See Figure 12A), which indicates that gas solubility in TPBOs is essentially independent of the triptycene content, despite the free volume decreases from 22.6% to 17.4% with increasing the triptycene molar content from 25% to 100% (See Table A1). Similar results were obtained at the other temperatures inspected, 20, 27 and 50°C (See Figure A5 in the Appendices).

Similar to CO_2, CH_4 and N_2 solubility in TPBOs at any temperature is essentially independent of the triptycene molar content. For the sake of brevity, CH_4 and N_2 sorption isotherms in TPBOs at 35°C are shown in Figure 12B-C, respectively, while isotherms at other temperatures are shown in Figure A6 and Figure A7 (Appendices) respectively.

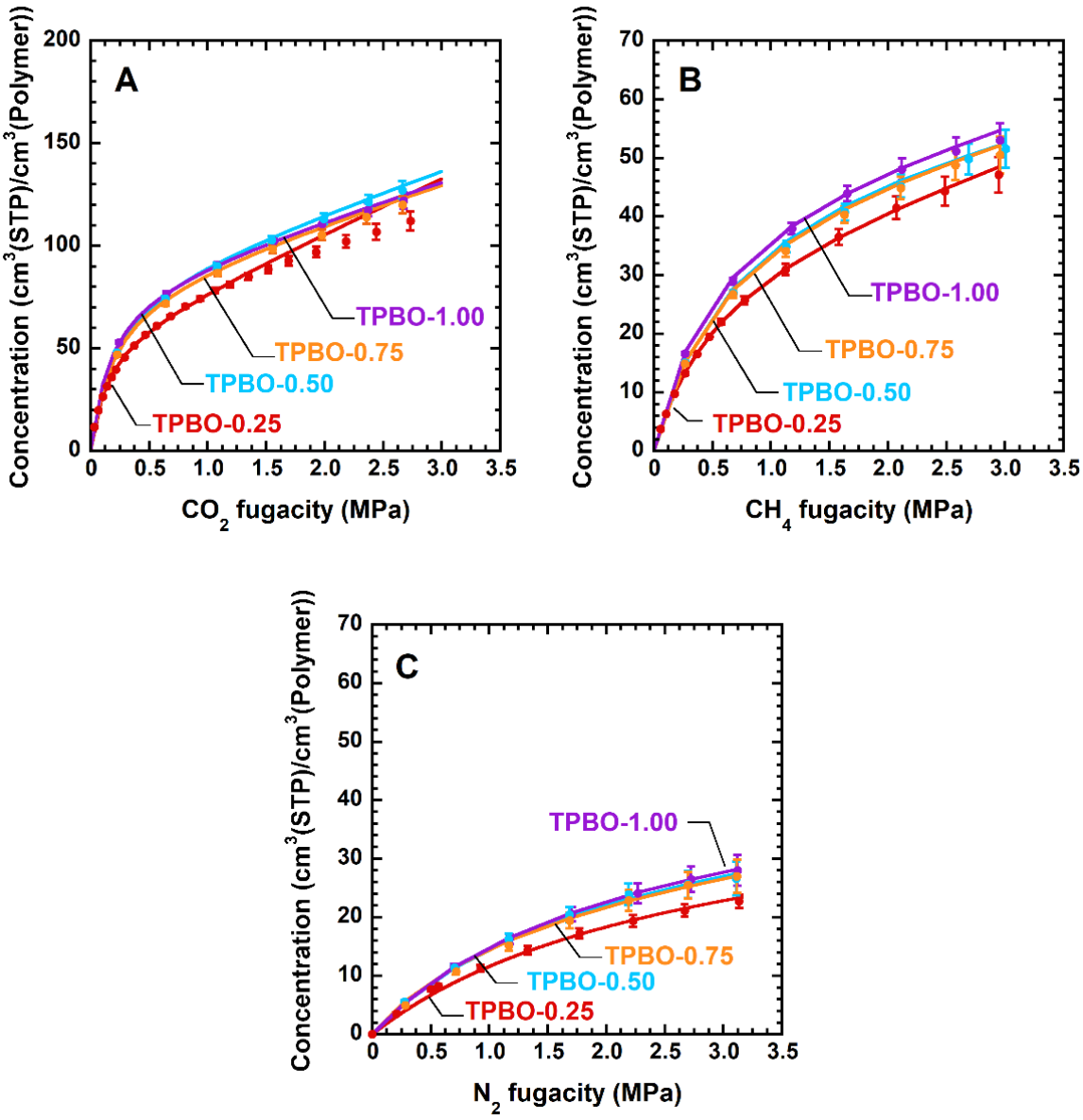


Figure 12: *CO_2 (A), CH_4 (B) and N_2 (C) sorption isotherms at 35°C in TPBO samples exhibiting different molar amount of triptycene units. Continuous lines represent the dual mode fitting. Experimental uncertainty was calculated using linear error propagation [98].*

Sorption isotherms in TPBO-0.25 apparently deviate from those collected for other TPBO samples (i.e., TPBO-0.50, TPBO-0.75, TPBO-1.00). It is worth mentioning that sorption data in TPBO-0.25 were measured in a previous study from this laboratory [75], using samples from a previous synthesis batch, which explains the origin of this slight

deviation. However, if we take the experimental uncertainty into account (See Figure 12), these differences turn out to not be significant.

CO_2 sorption isotherms at multiple temperatures (20-50°C for TPBO-0.50, TPBO-0.75 and TPBO-1.00, 5-50°C for TPBO-0.25) and given triptycene molar content are shown in Figure 13. For the sake of brevity, CH_4 and N_2 sorption data in the same temperature range are shown in Figure A8 and Figure A9 of the Appendices. Consistently with the typical behavior of glassy polymers, at any given external fugacity, gas sorption in TPBOs decreases with increasing temperature [38].

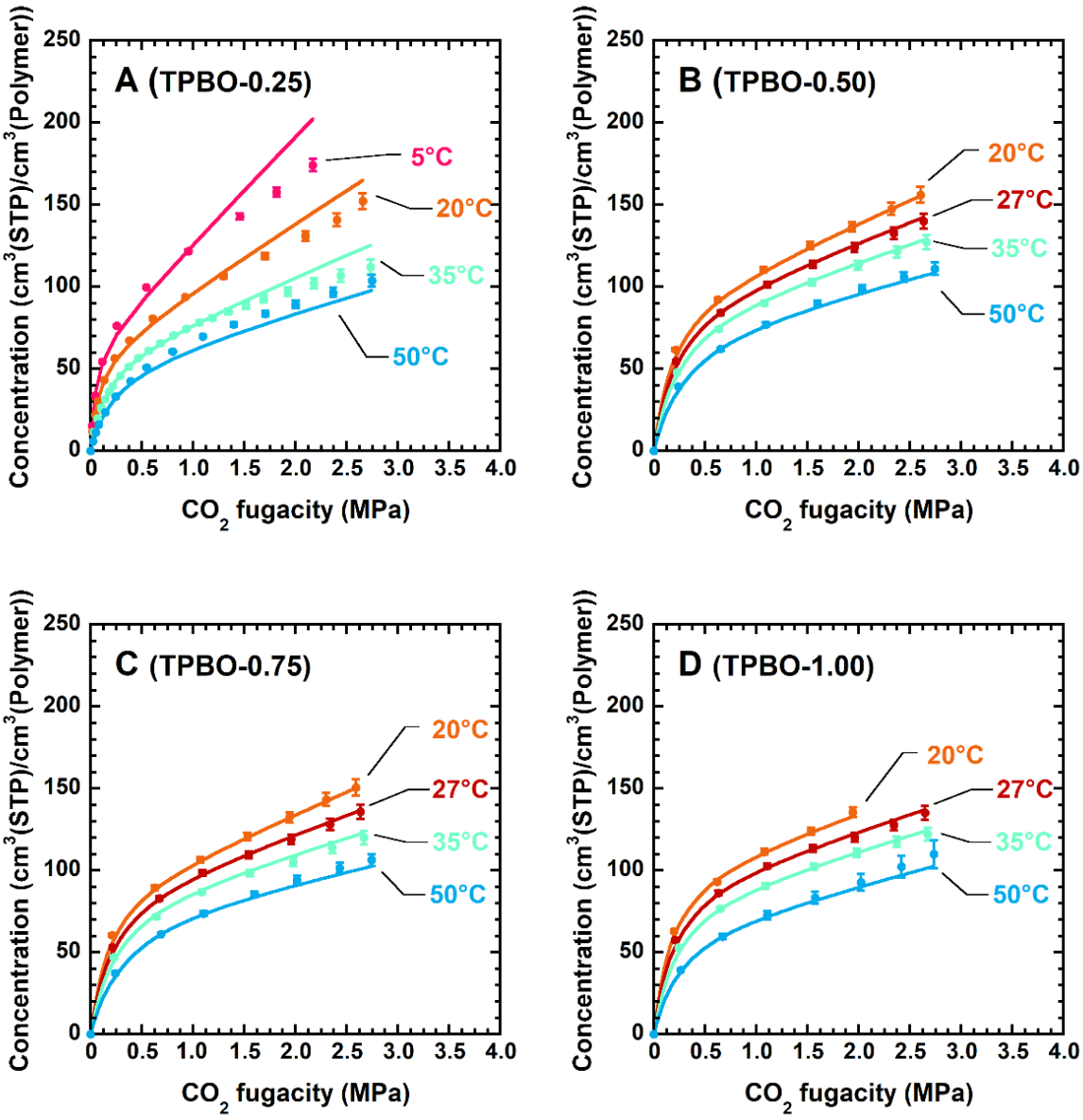


Figure 13: *CO_2 sorption isotherms at multiple temperatures in A) TPBO-0.25, B) TPBO-0.50, C) TPBO-0.75 and D) TPBO-1.00. Solid symbols: experimental data. Continuous lines: dual mode fitting. Experimental uncertainty was calculated using linear error propagation [96,98].*

As shown in Figure 12 and Figure 13, the dual mode model was used to correlate the experimental sorption isotherms. Since different sets of dual mode parameters can describe a given set of experimental data [15,75], the fitting was performed with constraints on K_D, C_H' and b as a function of temperature (See Section 1.6.1, Table 1).

The six introduced fitting parameters (i.e., $K_{D\,0}$, ΔH_{K_D}, $C'_{H\,0}$, m, b_0 and ΔH_b) provide a good parametrization of the sorption isotherms collected for each TPBO sample at multiple temperatures. No significant difference in fitting accuracy was observed in the constrained fitting compared to that of the individual dual mode fittings. The complete set of dual mode parameters for N_2, CH_4 and CO_2 sorption in TPBOs are shown in Section A16, Appendices, along with the uncertainty analysis, which was carried out through linear error propagation [97,98] and the Hessian Method discussed in 1.9.4. For the sake of brevity, a general discussion of the results of dual mode modeling is reported in the Section A10, Appendices. For example, consistently with the dual mode analysis of gas sorption in triptycene-free thermally rearranged polymers proposed by Stevens et al. [15], ΔH_{K_D} and ΔH_b are negative, indicating that K_D and b decrease with increasing temperature. Moreover, at any given temperature and in all TPBO samples, the logarithm of K_D increases linearly with penetrant critical temperature (i.e., $ln(K_D) = MT_C + N$) with a slope of 0.015K^{-1}, which is consistent with previous literature reports (See Figure A10, Appendices) [15,75,144]. Remarkably, the latter feature is captured by the model without imposing any additional constraints, which confirms that the model fitting is self-consistent and physically meaningful.

3.4.2. Isosteric heats of sorption

The isosteric heat of sorption, that is, the enthalpy of N_2, CH_4 and CO_2 sorption as a function of penetrant concentration in TPBOs, is shown in Figure 14.

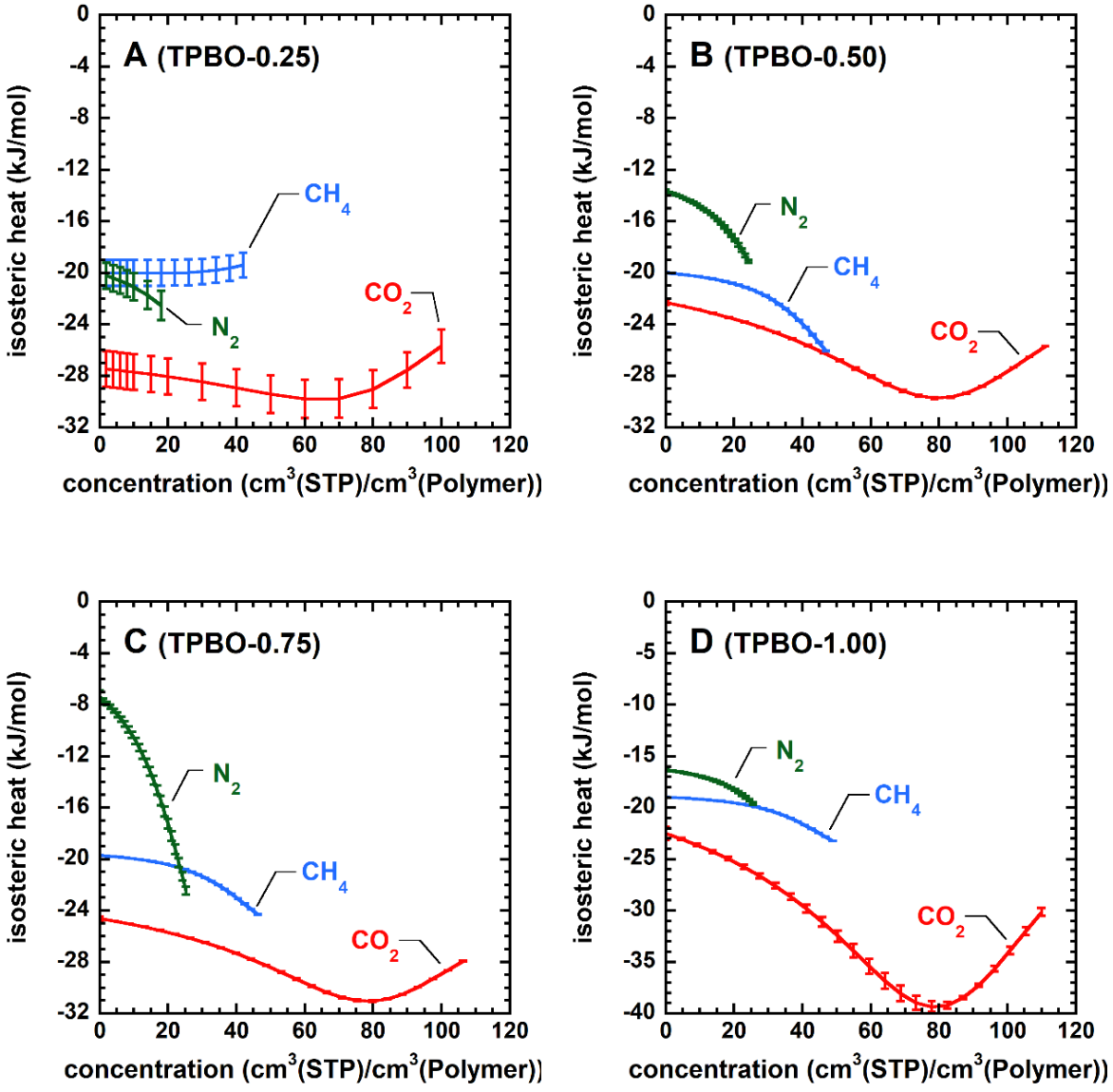


Figure 14: *Isosteric heat of N_2, CH_4 and CO_2 sorption in TPBO-0.25 (A), TPBO-0.50 (B), TPBO-0.75 (C) and TPBO-1.00 (D) as a function of penetrant concentration in the polymer. Error bars were estimated using the standard error of weighted linear regression [98]. Continuous lines are drawn to guide the eye.*

As noted in previous studies, taking into account the compressibility factor in Equation 16 (i.e., Z, estimated using the Peng-Robinson equation of state) does not produce any relevant effect on the calculated isosteric heats, therefore Z was assumed equal to one

[75,87]. As expected, in all the TPBO samples and at any given concentration, sorption becomes more exothermic with increasing penetrant condensability [124], that is, $\left|\Delta H_s^{CO_2}\right|$ (critical temperature = $304.19K$) > $\left|\Delta H_s^{CH_4}\right|$ (critical temperature = $190.8K$) > $\left|\Delta H_s^{N_2}\right|$ (critical temperature = $126.2K$) [145].

In all of the TPBO samples and within the experimental uncertainty, the isosteric heat of CH_4 and N_2 sorption slightly decreases or remains essentially constant with increasing penetrant concentration in the polymer. This behavior, which has been observed several times in glassy polymers, is consistent with the relatively low methane and nitrogen solubility in polymers, and their poor swelling ability [87]. In this condition, most of penetrant molecules are sorbed in the Langmuir's mode and, as long as more penetrant is sorbed in the matrix, the overall environment becomes more affine to penetrant molecules, which makes the sorption process more thermodynamically favorable (i.e., more exothermic) [75,87]. In striking contrast, the isosteric heat of CO_2 sorption exhibits a well detectable minimum at the concentration of about 80 cm^3(STP)/cm^3(polymer) in all of the TPBO samples. At concentrations below 80 cm^3(STP)/cm^3(polymer), swelling is negligible as the vast majority of CO_2 molecules are sorbed in the Langmuir's mode. Above this concentration, sorption in the Henry's mode becomes significant and polymer swelling begins taking place [58]. This behavior is indicated by the sorption process becoming less exothermic at high CO_2 concentration, as the positive contribution of the deformation work needed to open transient gaps between polymer chains (i.e, ΔH_{mix})

partially overwhelms the largely negative contribution of the condensation enthalpy (i.e, ΔH_{cond}), according to the relationship previously discussed in Section 1.3.2, that is, $\Delta H_s = \Delta H_{cond} + \Delta H_{mix}$. The fact that the position of the minimum is the same in all TPBO samples (i.e., ≅ 80 cm^3(STP)/cm^3(polymer)), is consistent with sorption being independent of triptycene content. Moreover, this result indicates that triptycene units, while suppressing the membrane aging propensity, do not help reduce swelling. In fact, if triptycene units were able to reduce swelling and plasticization, the position of the minimum of isosteric heat of CO_2 sorption should progressively shift to higher CO_2 concentration in TPBO samples containing higher molar amount of triptycene units. Some recent permeability data in iptycene-containing polymers confirm this picture, although a systematic study of plasticization and swelling in these materials was still lacking at the time of this work [23], however, Chapter 4 will provide understanding in this regard.

Although the isosteric heat of sorption for any given penetrant is fairly independent of the triptycene molar content (See Figure A11, Appendices), the minimum in the isosteric heat of CO_2 sorption becomes slightly more exothermic with increasing triptycene content. This result might reflect an increased affinity between CO_2 molecules and the triptycene units. Moreover, quadrupole interactions between polar CO_2 molecules and electron-rich triptycene clefts, as well as the larger concentration of ether groups at higher molar triptycene content, may contribute to this effect. Interestingly, these results are

corroborated from the fact that while the isosteric heats of N_2 and CH_4 sorption in TPBOs are similar, in absolute value, to the corresponding values reported by Stevens et al. [15] in the case of polybenzoxazoles without triptycene groups, the isosteric heat of CO_2 sorption in TPBOs is up to 40% larger than in triptycene-free polybenzoxazoles. As mentioned above, however, this behavior could alternatively be ascribed to the larger concentration of ether groups in TPBO samples exhibiting larger triptycene molar content. Molecular simulations are underway to explain the fundamental origin of this behavior.

3.4.3. Pure- and mixed-gas solubility-selectivity

As shown in previous studies, the dual mode model provides a reliable prediction of mixed-gas sorption, as well as mixed-gas solubility-selectivity, using the three parameters, K_D, C'_H and b, retrieved from the analysis of experimental pure-gas sorption isotherms at the same temperature [146,147]. Therefore, using Equation 3 and Equation 6, mixed gas CO_2- CH_4 sorption isotherms in TPBOs from a 30%mol CO_2/70%mol CH_4 gas mixture were predicted at 35°C as a function of mixed-gas penetrant fugacity and compared to pure-gas sorption isotherms (See Figure 15). Mixed-gas CO_2 and CH_4 fugacity at 35°C and at the composition of interest was calculated, at multiple total pressures, with the Peng-Robinson equation of state, using a CO_2-CH_4 interaction parameter, k_{ij}, equal to 0.09 [148].

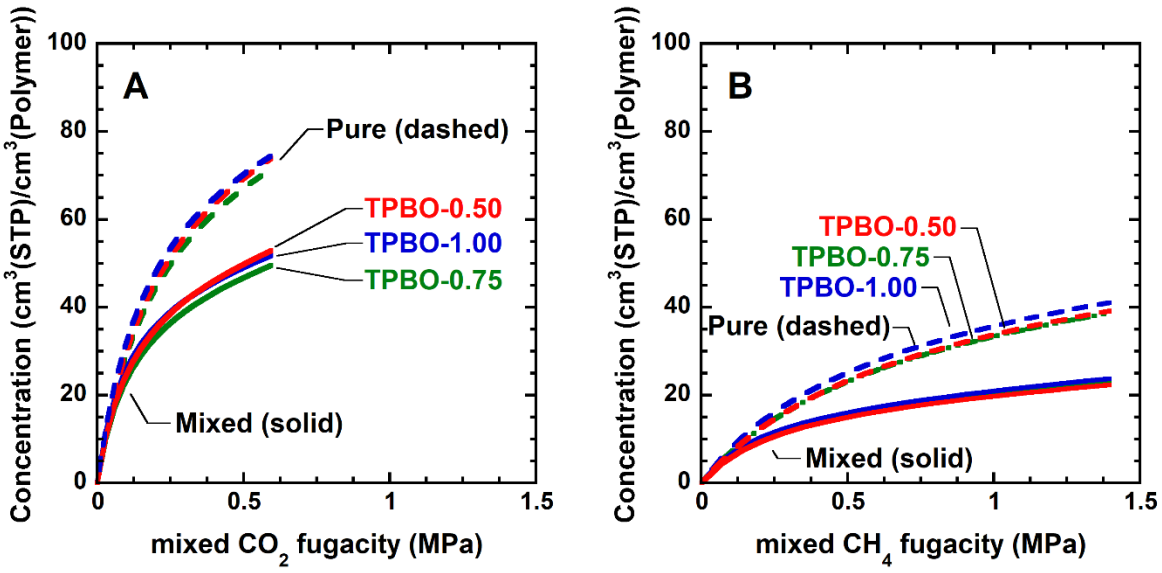


Figure 15: *Dual mode prediction of CO_2 (A) and CH_4 (B) mixed-gas isotherms from a 30% mol CO_2 / 70% mol CH_4 gas mixture in TPBOs as a function of mixed-gas fugacity at 35°C (solid lines), and comparison with pure gas sorption isotherms at the same temperature (dashed lines). Estimated uncertainty is shown in (Figure A12, Appendices).*

As expected, in all TPBOs, sorption of the less condensable component (i.e., CH_4) in mixed-gas conditions is suppressed much more than that of the more condensable component (i.e., CO_2) relative to the pure gas conditions at the same temperature and fugacity. Specifically, at mixed gas fugacity of 0.6 MPa and 1.4 MPa for CO_2 and CH_4, respectively, sorption was reduced by 24-31% for CO_2 and 40-43% for CH_4 relative to pure gas at the same fugacity, with no substantial difference among TPBO samples, that is, irrespective of the triptycene molar content (See Figure 15). Therefore, competitive sorption is essentially independent of triptycene content, indicating that configurational free volume has little or no effect on pure- and mixed-gas solubility and solubility-selectivity. To avoid any confusion and make the reading easier, error bars are not shown

in Figure 15. The uncertainty of predicted mixed-gas sorption data is provided in the Appendices (Figure A12 and Figure A13).

The results discussed above indicate that competitive sorption enhances mixed-gas CO_2/CH_4 solubility-selectivity relative to ideal solubility-selectivity. As shown in Figure 16, for any TPBO sample, the predicted mixed-gas sorption-selectivity exceeds the experimental pure-gas sorption-selectivity by 18.3% $\pm$ 4% at a CO_2 fugacity of 0.5 MPa. As discussed above, however, the increase in mixed-gas solubility-selectivity relative to ideal solubility-selectivity is fairly independent of polymer's triptycene molar content. To compare pure-gas and mixed-gas sorption selectivity on a more realistic basis, ideal (i.e, pure-gas) solubility-selectivity shown in Figure 16 was calculated using pure-gas solubility data at the same fugacity as the mixed-gas case at any given pressure.

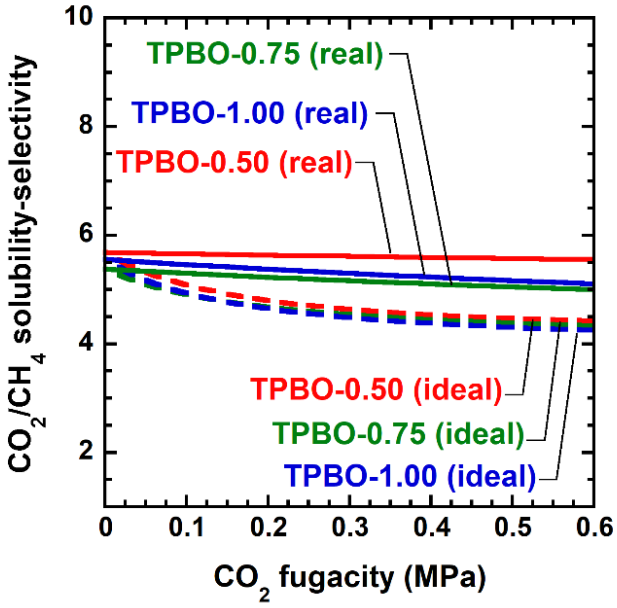


Figure 16: *Dual mode prediction of mixed-gas CO_2/CH_4 solubility-selectivity for a 30%mol CO_2 / 70% mol CH_4 mixture in TPBOs as a function of mixed-gas CO_2 fugacity at 35°C (solid line), and comparison with pure-gas CO_2/CH_4 solubility-selectivity (dashed line). Estimated uncertainty is shown in the Appendices (Figure A13).*

Using the dual mode parameters estimated from the analysis of experimental pure-gas sorption isotherms, CO_2/CH_4 solubility-selectivity at CO_2 and CH_4 fugacity of 0.3 MPa and 0.7 MPa, respectively, is predicted to increase with decreasing temperatures (See Figure A14, Appendices).

The most relevant result of this pure- and mixed-gas sorption study is that the incorporation of configurational free volume does not influence sorption and sorption-selectivity, therefore, according to the solution-diffusion model, diffusivity-selectivity is the only property affected by changes in triptycene content. This aspect will be discussed in the following Section (3.4.4).

3.4.4. Mechanism of light gas transport through configurational free volume

Pure-gas CO_2 and CH_4 permeability data at 35°C collected by Luo et al. [20] and solubility data at 35°C from this study were used to estimate pure-gas diffusivity in TPBOs at 35°C up to 1 MPa. At given pressure, pure-gas permeability and diffusivity decrease with increasing triptycene molar content (See Figure 17 A-B). In contrast, pure-gas CO_2/CH_4 selectivity at 35°C and given pressure (i.e., 1MPa) increases with increasing triptycene content in TPBOs (See Figure 17C). Since, as discussed in Section 3.4.1, light gas solubility in TPBOs is essentially independent of triptycene molar content, we can conclude that, based on the solution-diffusion model, the permeability decrease and selectivity increase with increasing triptycene molar content are ascribed to a change in the diffusion behavior only, which means that incorporation of triptycene unity on the polymer backbone only influences the membrane size-sieving ability, with negligible or no effect on sorption and sorption-selectivity. This physical picture, however, is limited to light gasses. As shown in a previous study from this laboratory [51], when the penetrant kinetic diameter exceeds the size of the configurational free volume elements, i.e., for bulky vapor molecules, sorption becomes size-controlled, meaning that triptycene groups reduce the sorption of vapor molecules whose size exceeds their internal size.

In Figure 17A-B, experimental CO_2 pure-gas permeability [20] and diffusivity isotherms (calculated as $\frac{P}{S}$) at 35°C in TPBOs exhibiting increasing molar amount of triptycene units are shown as a function of pressure. At any given pressure, the decrease in gas

permeability with increasing triptycene molar content mirrors the parallel decrease in diffusivity.

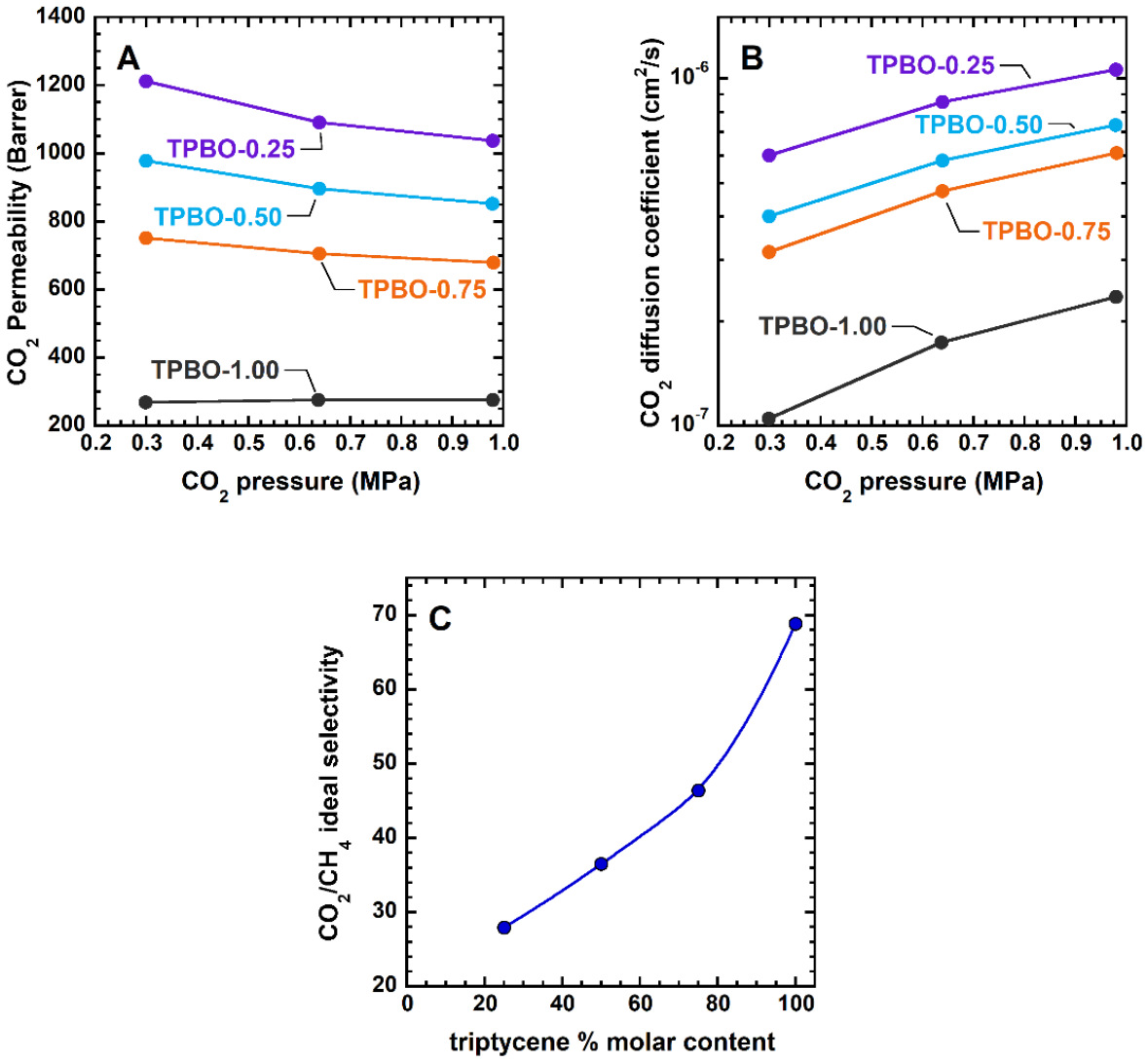


Figure 17: *Pure-gas CO_2 permeability (A) [20] and diffusivity (B) in TPBOs as a function of triptycene molar content and pressure at 35°C; pure-gas CO_2/CH_4 selectivity at 35°C and 1 MPa as a function of triptycene molar content (C). Similar results were obtained at other pressure values. Solid symbols are experimental data, and lines are drawn to guide the eye.*

As demonstrated below, this behavior is due to the strong size-sieving ability of triptycene units. To put these results in perspective, in Table 6 CO_2, CH_4 and N_2

permeability, diffusion coefficients and CO_2/CH_4 diffusivity-selectivity in TPBOs at 35°C and 1 MPa (i.e., 10 atm) are compared to benchmark polymers. Interestingly, TPBOs exhibit much larger diffusivity-selectivity compared to other polymers, which confirms that the size-sieving ability benefits much more than solubility-selectivity from configurational free volume.

Table 6: *Pure-gas permeability and diffusion coefficients, selectivity and diffusivity-selectivity in TPBOs and conventional polymer membrane materials at 35°C and 1 MPa (i.e., 10 atm).*

polymer	*permeability (Barrer)*			*diffusion coefficient (10^8 cm^2/s)*			$\alpha_{\frac{CO_2}{CH_4}}$ *(ideal)*	$\alpha_{D,\frac{CO_2}{CH_4}}$ *(ideal)*
	CO_2	CH_4	N_2	CO_2	CH_4	N_2		
TPBO-0.25	*1042*	*37*	*57*	*125*	*9.3*	*37*	*28.2*	*13.4*
TPBO-0.50	*853*	*23*	*38*	*86*	*5.3*	*20*	*37.1*	*16.2*
TPBO-0.75	*680*	*15*	*27*	*69*	*3.3*	*14*	*45.3*	*20.9*
TPBO-1.00	*276*	*4.0*	*8.5*	*23*	*0.86*	*4.3*	*69.0*	*26.7*
PTMSP [50]	*21432*	*12192*	*5882*	*3300*	*3600*	*4300*	*1.75*	*0.9*
PDMS [149]	*3978*	*1200*	*380*	*2200*	*2200*	*3200*	3.3	1.0
PIM-1 [150]	*4419*	*388.5*	*288*	*360*	*73*	*130*	*11.4*	*4.9*
cellulose acetate [151]	*4.8*	*0.15*	/	*1.8*	*0.45*	/	*32.0*	*4*
Teflon® AF2400 [87]	*2332*	*383.4*	*475.7*	*678*	*290*	*600*	*6.1*	*2.3*
PEO [152]	*15.9*	*0.70*	*0.22*	*31*	*6.6*	*5.1*	*22.7*	*4.7*

Moreover, if the logarithm of permeability is plotted versus 1/FFV (Figure A15, Appendices), significant deviations from the expected linear trend are observed, which provides further evidence of the unique role played by configurational free volume in regulating small molecule transport in TPBOs.

To provide a more fundamental analysis of small molecule transport through configurational free volume-based polymers, the Henry's (i.e., D_D) and Langmuir's (i.e.,

D_H) mode contributions to CO_2 and CH_4 diffusion coefficients in TPBOs at 35°C were calculated using the dual-mode mobility model described in Section 1.6.1, Equation 7 [74,150]. To do so, for each penetrant and TPBO sample, permeability was plotted as a function of $\frac{C'_H b}{1+bf}$, to obtain a nice linear correlation, whose slope and intercept provide D_H and D_D, respectively. Details are provided in Section A15, Appendices. N_2 was excluded from this analysis, due to the larger uncertainty of permeability and solubility data relative to CH_4 and CO_2. Table 7, D_H and D_D values are compared among several glassy polymers of interest in gas separation. Uncertainties, calculated using the error propagation method, are shown in Figure 18A-B. Interestingly, while for any given penetrant in conventional glassy polymers D_D exceeds D_H by, at maximum, one order of magnitude, in TPBOs D_D exceeds D_H by at least two orders of magnitude [150], which highlights the superior size-sieving ability offered by triptycene units (i.e., configurational free volume).

Table 7: *Dual-mode mobility parameters for CO_2, CH_4, and N_2 in TPBOs, PIM-1, polysulfone (PSF), polycarbonate (PC) and 6FDA-6FpDA polyimide (PI). Data are at 35°C for all polymers except PIM-1, for which they are available at 25°C. Uncertainty of D_D and D_H values for TPBOs are shown in Figure 18A-B.*

polymer	*gas*	*D_D (10^8 cm^2/s)*	*D_H (10^8 cm^2/s)*	*F*
TPBO-0.25	*CO_2*	*265.0*	*17.15*	*0.065*
	CH_4	*43.43*	*0.359*	*0.008*
TPBO-0.50	*CO_2*	*293.2*	*9.64*	*0.033*
	CH_4	*43.73*	*0.110*	*0.003*
TPBO-0.75	*CO_2*	*265.4*	*5.60*	*0.021*
	CH_4	*23.30*	*0.000*	*0.000*
TPBO-1.00	*CO_2*	*119.2*	*0.000*	*0.000*
	CH_4	*6.31*	*0.000*	*0.000*
PIM-1 [150]	*CO_2*	*1296.6*	*34.12*	*0.026*
	CH_4	*364*	*3.344*	*0.009*
PSF [153]	*CO_2*	*4.53*	*0.535*	*0.118*
	CH_4	*0.69*	*0.120*	*0.174*
PC [153]	*CO_2*	*6.22*	*0.485*	*0.078*
	CH_4	*1.09*	*0.125*	*0.115*
6FDA-6FpDA [154]	*CO_2*	*25.5*	*1.530*	*0.060*
	CH_4	*2.78*	*0.236*	*0.085*

Reporting D_H and D_D as a function of the molar triptycene content in TPBOs provides an opportunity to isolate and evaluate quantitatively the role of configurational free volume on light gas transport. Interestingly, for both CO_2 and CH_4, the ratio D_H/D_D (referred to as F, see Equation 7) in TPBOs systematically decreases with increasing the triptycene molar content, that is, with increasing the amount of configurational free volume (See Table 7). This result indicates that penetrant molecules trapped in the configurational free volume exhibit a very low mobility or no mobility at all as long as more triptycene units

are incorporated in the polymer, which is consistent with the internal size of triptycene units being comparable to the penetrants size. This physical picture is further confirmed by the fact that the CO_2 and CH_4 Henry's (i.e., D_D) diffusion coefficients in TPBOs at 35°C are fairly constant, within the uncertainty, with increasing triptycene molar content, although a decrease is observed in the case of CH_4 in the TPBO-1.00 sample (See Figure 18A-B) compared to the average of the other TPBO samples exhibiting lower triptycene molar content. This decrease, however, is not significant if we consider the uncertainty associated to D_D (See Figure 18A-B). In contrast, the Langmuir's diffusion coefficient (i.e., D_H) decreases steadily with increasing triptycene molar amount. Interestingly, the decrease of CH_4 Langmuir's diffusivity with increasing triptycene content is steeper than the corresponding decrease of CO_2 Langmuir's diffusivity, which is consistent with CH_4 being a bulkier penetrant (kinetic diameter = 3.8Å) than CO_2 (kinetic diameter = 3.3Å) [155]. Therefore, the CH_4 size-exclusion becomes more effective with increasing amount of configurational free volume in the polymer. According to this physical picture, while $D_H^{CO_2}$ drops to zero (i.e. F = 0) in TPBO-1.00, $D_H^{CH_4}$ drops to zero already in TPBO-0.75, which, again, is consistent with CH_4 being a larger molecule than CO_2.

Different approaches have been used to estimate the size of the internal free volume of triptycene units. For example, PALS (Positron Annihilation Lifetime Spectroscopy) measurements suggest that the average free volume size is about 7Å [20]. However, due to the nature of PALS measurements, this number provides the average size of all the free

volume elements, including conformational and configurational free volume elements. Molecular simulations provide, for a single triptycene unit, an internal size less than 4 Å [115]. Finally, if we consider the space between two arene blades of triptycene units as a prism whose internal volume has been estimated to be 31 $Å^3$, the diameter of the corresponding sphere would be about 3.9 Å [115]. All these considerations indicate that the internal size of triptycene units is comparable to that of CH_4 molecules (kinetic diameter = 3.8Å), therefore triptycene units exclude CH_4 much more efficiently than CO_2 (kinetic diameter = 3.3Å), which supports the fact that $D_H^{CH_4}$ decreases faster than $D_H^{CO_2}$ with increasing molar amount of triptycene units in the polymer backbone.

The most relevant conclusion of this transport study is that penetrant ability to move within Langmuir sites of TPBOs is severely inhibited as the amount of triptycene increases. This result unequivocally demonstrates that the high size-sieving ability of TPBOs is essentially ascribed to configurational free volume, whose size is well-defined, stable and comparable to the size of one single molecule. In sharp contrast, the size of conformational free volume pockets generated by inefficient chain packing is randomly distributed and unstable over long-term operation [20,69].

To provide a more quantitative evaluation of the enhanced size-sieving ability provided by configurational free volume, the Henry's (i.e., $D_D^{CO_2}/D_D^{CH_4}$) and Langmuir's (i.e., $D_H^{CO_2}/D_H^{CH_4}$) contributions to pure-gas CO_2/CH_4 diffusivity-selectivity have been estimated (See Figure 18C). Although Henry's mode CO_2/CH_4 ideal diffusivity-selectivity

at 35°C is essentially constant, within the experimental uncertainty, with increasing triptycene molar contents from 25 to 100%, the Langmuir's mode diffusivity-selectivity ranges from 48 in TPBO-0.25 to 88 in TPBO-0.50, and it becomes practically infinite in TPBO-0.75 and TPBO-1.00. This result further supports the idea that triptycene units can finely regulate small molecule transport based on their size, indicating that the superior TPBOs' size-sieving ability is due primarily to configurational free volume, with other possible effects being negligible or at least less relevant.

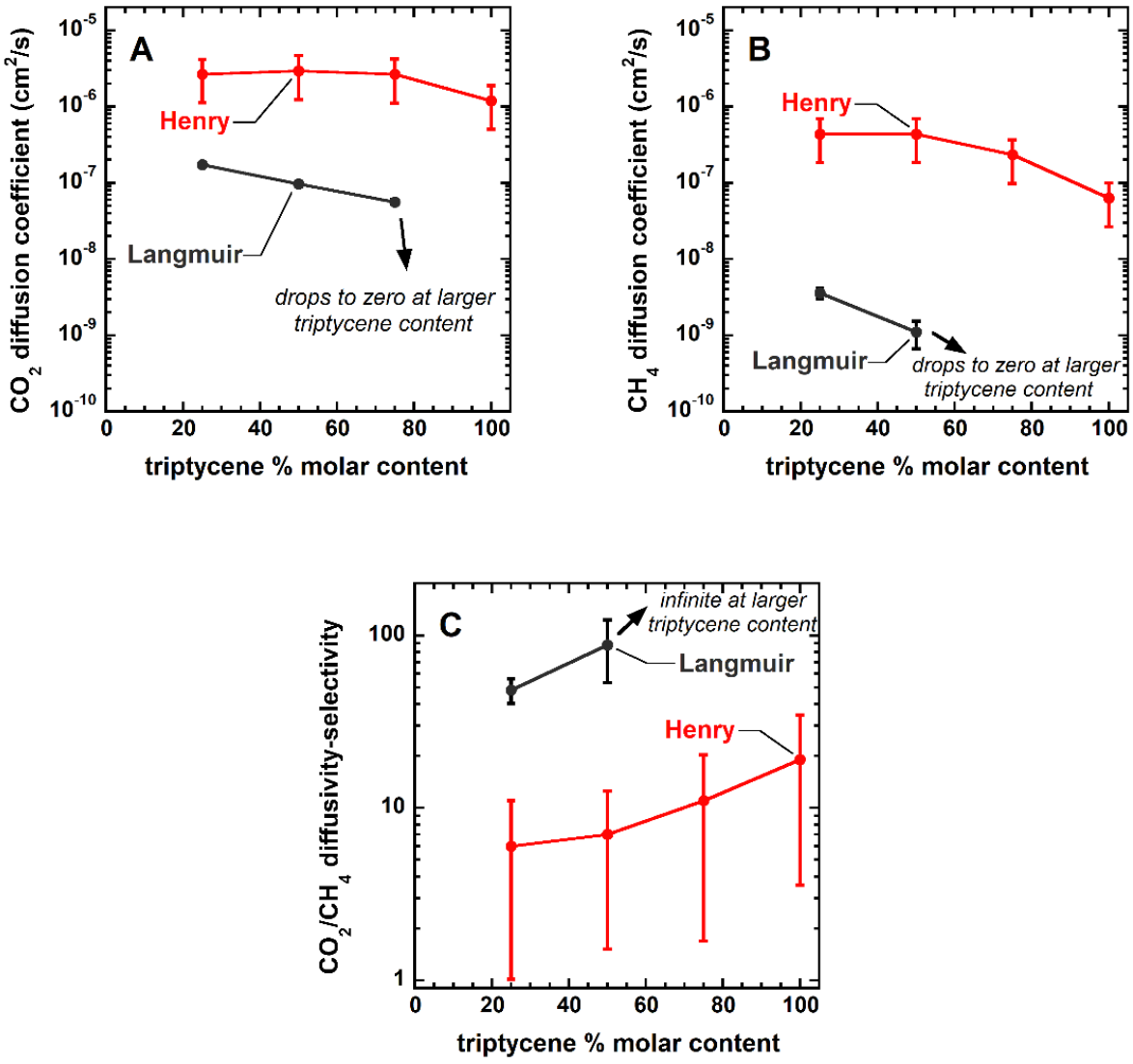


Figure 18: *Henry's and Langmuir's mode CO_2 (A) and CH_4 (B) diffusion coefficients, as well as CO_2/CH_4 Henry's (i.e., $D_D^{CO_2}/D_D^{CH_4}$) and Langmuir's (i.e., $D_H^{CO_2}/D_H^{CH_4}$) diffusivity-selectivity (C) in TPBOs at 35 °C as a function of triptycene molar content. $D_H^{CO_2}$ drops to zero in TPBO-1.00. $D_H^{CH_4}$ drops to zero when the triptycene molar content in the polymer is equal to 75% mol or larger. The Langmuir's diffusivity-selectivity, $D_H^{CO_2}/D_H^{CH_4}$, approaches infinite when the triptycene molar content is equal to 75% mol or larger. Uncertainty was calculated using linear error propagation [97,98].*

3.5. Conclusions

A class of polybenzoxazoles (TPBOs) with systematically varied molar amount of triptycene units (i.e., configurational free volume) was selected to propose a possible mechanism of small molecule transport in glassy polymers exhibiting configurational free volume. At given temperature and pressure, pure-gas permeability decreases and ideal selectivity increases with increasing triptycene molar content in TPBOs. The analysis of pure-gas N_2, CH_4 and CO_2 sorption isotherms indicates that gas solubility and solubility-selectivity are essentially independent of triptycene molar content. Similarly, mixed-gas CO_2/CH_4 sorption isotherms predicted using the dual mode model show that competitive sorption (i.e., mixed-gas solubility-selectivity) is independent of triptycene molar content. Therefore, the decrease in gas permeability with increasing triptycene content in TPBOs mirrors the parallel decrease in diffusion coefficient, and the increase in selectivity with increasing molar amount of triptycene units mirrors the parallel increase in diffusivity-selectivity (i.e., size-sieving ability).

The dual mode sorption-mobility analysis indicates that small molecule diffusion in TPBOs is progressively hindered with increasing triptycene molar content (that is, with increasing configurational free volume), with a stronger hinderance offered to the transport of larger molecules. Interestingly, while the Henry's CO_2/CH_4 diffusivity-selectivity (i.e., $D_D^{CO_2}/D_D^{CH_4}$) changes little with increasing triptycene molar content, the Langmuir's CO_2/CH_4 diffusivity-selectivity (i.e., $D_H^{CO_2}/D_H^{CH_4}$) rapidly increases with

increasing amount of configurational free volume, to become infinite when the molar amount of triptycene units in the polymer is equal to 75% or larger. Therefore, configurational free volume provides a unique opportunity to precisely control diffusivity-selectivity in a predictable fashion. Equally important, in contrast with conformational free volume, configurational free volume exhibits excellent resistance to physical aging, which makes configurational diffusivity-selectivity highly stable over long-term operation. This physical picture, however, is limited to light gasses. As shown in a previous study [51], when the penetrant kinetic diameter exceeds the size of the configurational free volume elements, sorption becomes size-controlled, meaning that triptycene units influence both sorption and diffusion coefficients.

Finally, the analysis of isosteric heats of sorption reveals that the TPBOs plasticization resistance does not increase with increasing triptycene molar content. Ongoing and future work will investigate the effect of configurational free volume content on the simultaneous transport of gas (i.e., small) and vapor (i.e., bulky) molecules.

Chapter 4. Computer Vision Based Measurement of Pure- and Mixed-Gas Swelling in Polymers Exhibiting Configurational Free Volume [§]

4.1. Abstract

Although polymer swelling (i.e., dilation) data are crucial to assess the long-term stability of polymer membranes and correct sorption isotherms for highly sorbing penetrants, the swelling propensity of new generation membranes exhibiting configurational free volume has never been investigated. To fill this gap, in this paper we study pure and mixed-gas swelling of a series of thermally rearranged polybenzoxazoles (TPBOs) and their poly(o-hydroxyimide) precursors exhibiting systematically varied amount of configurational free volume (i.e, triptycene units). The individual and synergistic effects of configurational free volume and thermal rearrangement on the polymer swelling propensity are presented and discussed. To do so, we use a newly developed experimental approach based on computer vision, which is capable of correcting most of the limitations of traditional methods used to measure swelling and achieve superior accuracy. We show that thermally rearranged glassy polymers exhibiting configurational free volume exhibit better swelling resistance relative to conventional polymers. The fundamental origin of this behavior resides, as explained by the dual mode theory, on the fact that the Langmuir's mode swelling propensity in thermally rearranged triptycene-

[§] Currently in review to submit for publication.

based polymers is much lower than in glassy polymers exhibiting only conformational free volume. Differences between pure-gas and mixed-gas induced swelling are also highlighted and discussed. Finally, a thorough investigation of the swelling measurement uncertainty and precision is provided and discussed, including an analysis of the major factors affecting experimental uncertainty.

4.2. Introduction and Background

Polymer swelling (i.e., dilation) data are needed to assess the stability of polymer membranes in the presence of highly condensable, highly soluble gases, vapors and liquids [56,172]. Swelling generally enhances permeability and reduces selectivity in membrane separations, which is considered, although with a few exceptions [59,173], an undesirable effect [109,174]. Extreme swelling propensity may lead to plasticization (see Section 1.4.2), which dramatically amplifies the effects mentioned above [175]. If available, dilatometry data serve, *per se*, as a useful measure of polymer swelling. Of equal importance, the quantification of polymer volume change as a function of pressure allows for improved accuracy in other experiments, such as gas/vapor sorption measurements (as covered in 1.10.1 and 1.10.2) via the barometric (i.e., pressure decay) technique, where sample volume changes are often neglected due to lack of available swelling data [176]. These changes in volume can be significant at high pressures and in the presence of condensable penetrants [89], leading to major experimental errors associated with sorption measurements.

Fractional volumetric swelling (i.e., $\frac{\Delta V}{V_0}$) is defined as the polymer volume change during sorption normalized to the initial volume [176]. As polymer swelling is considered isotropic, fractional elongation (i.e., $\frac{L_f - L_i}{L_i}$), which is more convenient to directly measure than volume changes, may be used to calculate fractional volumetric swelling:

$$\nu = \frac{\Delta V}{V_0} = \frac{V_f - V_i}{V_i} \times 100\% = \left[\left(\frac{L_f}{L_i}\right)^3 - 1\right] \times 100\% \qquad \text{Equation 22}$$

where ν is the fractional swelling, ΔV is the volume change of the sample, V is the samples volume, L is the sample length, and i and f refer to the sample in the initial (i.e., at vacuum) and final (i.e., swollen) states.

Though polymers exhibiting configurational free volume have attracted interest due to a favorable combination of relatively high permeability, superb selectivity in several separations, and superior long-term stability against physical aging [21,24,43,60,94,95,115,177–179]. As discussed in previous contributions [21,24,43,51,95] and sections in this work (1.5, 3.4.4, 2.4), iptycene groups made of three (i.e., triptycene) or five (i.e., pentiptycene) benzene rings arranged in a paddlewheel-like configuration, provide their unique internal, configurational free volume, which, being non-collapsible, greatly enhances the membrane long-term stability. Additionally, while the size of excess conformational free volume pockets in conventional glassy polymers is randomly distributed, the size of configurational free volume elements is uniform and it is

comparable to the size of a small molecule (e.g., ~3.8 $\dot{A}$)[20], which promotes high selectivity.

Thermally rearranged polybenzoxazoles containing triptycene moieties (TPBOs), first reported by Guo et al., abundantly outperform the 2008 upper bound in several gas separation applications, and exhibit a unique physical aging resistance [21,180]. Little or no information, however, has been provided so far on their swelling behavior. This study aims at filling this gap by proposing, for the very first time, a systematic study of the swelling propensity of this important class of polymers. To do so, however, a reliable, accurate, and fast experimental procedure to measure swelling is needed. This need comes from the fact that in this study we consider a family of TPBOs exhibiting systematically varied amount of configurational free volume. As shown in a recent contribution [43] (Chapter 3), gas sorption isotherms in these materials overlap irrespective of their triptycene (i.e., configurational free volume) content, therefore, for reliable comparisons among samples, there is a need for a very accurate approach to measure swelling. Unfortunately, this level of accuracy cannot be guaranteed by conventional optical experimental methods [176,181–183], which offer an uncertainty as high as 25%, if the sample length is observed directly from the camera with no downstream analysis or error correction. The proposed approach provides an ideal environment for automated data collection using computer vision analysis, rather than

manual data collection [184], in addition to corrections for various sources of systematic error, as discussed later.

In conventional optical swelling measurements, a sample is traditionally hung in a Jerguson gage under temperature control, after which the apparatus is evacuated and then charged with a dilating gas. Finally, a camera is used to measure length changes in the polymer sample as it dilates, repeating the process stepwise at multiple pressures [176]. Alternatively, some researchers have used dilatometry apparatuses that utilize a linear variable differential transformer (LVDT) to measure changes in sample length via a metal rod connected to the sample [93]. These sensors possess superior resolutions, capable of resolving a $\pm 1 \mu m$ change in length, but they suffer from a high cost and complexity of construction. Ellipsometry has also been used to measure the swelling of thin polymer films [76]. Critical issues for using these techniques are that *i)* only one sample may be tested at a time, which makes swelling measurements across multiple samples extremely time-consuming, and *ii)* random errors, which make it difficult to compare multiple samples.

While the hardware used in this work to measure polymer dilation (see Section 1.10.3) closely follows the optical experimental design reported previously [176,185], the element of novelty discussed in this paper refers primarily to the software and analysis of the collected data, including postprocessing steps to clean the data of common sources of systematic and random error, such as camera motion, and estimate random experimental

uncertainty. Moreover, the possibility to run multiple measurements in parallel significantly reduces the experimental uncertainty, leading to more accurate results. The availability of more accurate and reliable swelling data will help us better understand the long-term stability exhibited by polymers with configurational free volume.

4.3. Experimental Methods

4.3.1. Materials

A series of thermally rearranged polybenzoxazoles exhibiting systematically varied molar amount of triptycenes (i.e., 0, 25, 50, 75, 100%) was used for the pure- and mixed-gas swelling study. Details about TPBO synthesis and fabrication are provided in Section A1, Appendices. The corresponding non-thermally rearranged triptycene-containing poly(hydroxyimide) (TPHI) precursors were also included in the experimental campaign. All samples used in this study are free-standing (i.e., dense, backing-free films), with a thickness in the range of 30-100 μm.

The new swelling apparatus was first tested by reproducing the CO_2-induced dilation data in polycarbonate films originally reported by Koros et al. [186] and Handa and Zhang [183]. Polycarbonate films, $130 \pm 2\ \mu m$ thick, were provided by Sigma Aldrich. Gas cylinders were supplied by Air Gas, with a purity $> 99.99\%$ A nitrogen-ethane mixture, whose certified composition was 80-20%mol, was also supplied by Air Gas.

4.3.2. Swelling measurements

The apparatus structure is detailed in Section 1.10.3.

TPBOs swelling was measured at 35°C using pure gas carbon dioxide, ethane and n-butane. TPHI swelling upon pure CO_2 exposure was measured at 35°C. TPBOs swelling upon exposure to a nitrogen (80%mol)-ethane (20%mol) mixture was also measured at 35°C. This mixture was selected in view of its relevance in gas processing and polymer manufacturing [187].

The novelty of this swelling measurement technique resides in the downstream analysis of the data, and less so the apparatus itself. Camera-based dilation apparatuses have been designed and proposed in literature prior [176,188,189], as well as alternative methods using ATR-FTIR[184], transmission-FTIR [58], LVDT measurement systems [93], line scan cameras [190] and thickness measurement techniques using reflectometry [191]. The newly proposed design requires cheap components due to the data analysis method being capable of mitigating the effects of the noise that previous techniques do not account for, such as camera drift over time. Moreover, this experimental procedure is completely automated, requiring only an experimenter to start and end data collection, and then run the data analysis. Notably, since multiple samples may be placed in the apparatus to dilate at the same time and the initial length reference point is specific to each sample, this new approach saves considerable time and opens the possibility of running duplicate swelling measurements at given temperature and pressure in a single

experiment. Finally, while only certain dilatometry methods could provide dilation kinetics, such as the FTIR-ATR and LVDT, achieving this with optical dilatometry is tedious due to the number of images which need to be carefully processed. An automated optical analysis method with high resolution and accuracy makes it possible to track dilation kinetics with an excellent degree of accuracy, even though this study focuses on equilibrium swelling [93,182,184,190,192].

4.4. Computer vision based data analysis

To process the images, a region of interest is first specified by the experimenter. This region encloses the area where the polymer sample boundary could travel during the experiment. If needed, the region of interest is then shifted to account for any minor movements of the camera throughout the experiment, which could result from a variety of sources, such as *i)* a fluctuating room temperature affecting the camera stand through thermal expansion, *ii)* inadvertent bumping of the apparatus by an experimenter, or *iii)* vibrations from the ground. The details of this stabilization method are provided in Section A25, Appendices. Once the image is stabilized (see Figure 19, left column), the region of interest undergoes horizontal boundary detection using *image convolution* [193–195]. Specifically, the corrected image of the polymer boundary is "convolved" over by an adjustable matrix known as a Sobel filter, whose parameters are chosen to detect horizontal boundaries [193–195]. The result of this operation is a "convolved" image (see Figure 19, middle column) where areas that contained horizontal boundaries are

highlighted, and all other features in the image are suppressed. After this operation, each row of the resulting convolved image is summed into a single value (see Figure 19, right column). This results in a set of values which give a confidence that the polymer boundary exists as a function of position along the vertical axis in the original image. Next, a continuous function is fitted to this likelihood data and this functions' maximum is chosen as the boundary position. The function itself could be a polynomial or Gaussian distribution, so long as it adequately represents the discrete boundary likelihood data. In this work, a second order polynomial fits reasonably well and is computationally efficient compared using to a normal distribution.

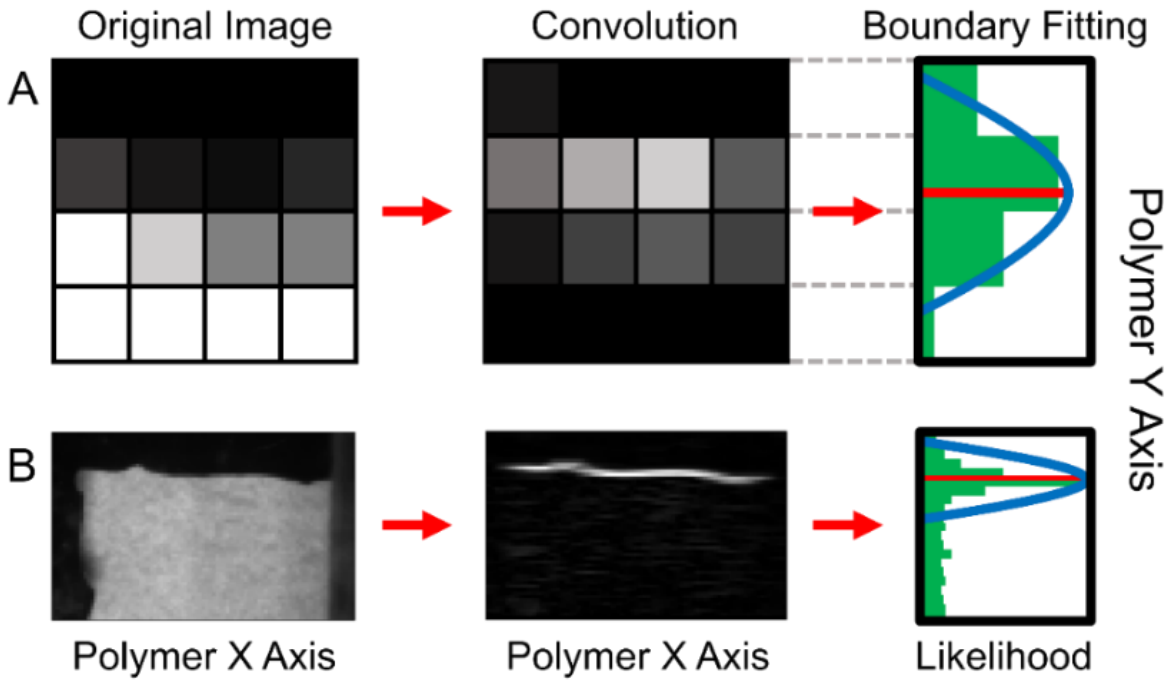


Figure 19: *Illustrated (A) and real (B) image analysis process. From left to right: The initial sample image after stabilization, the resulting convolved image, and the summed pixel values (green bars) in addition to the fit continuous function (blue line), and finally the chosen boundary position (red line).*

This entire image analysis process is then repeated, in an automated fashion, for every image taken during data collection, ensuring consistent and accurate boundary location. The choice to use a fitting function is the key to achieving sub-pixel resolution of the polymer's length change. If the convolved image row with the highest summed value were to be chosen as the boundary location instead of fitting a function to the highest and adjacent rows, the boundary location's resolution would be limited to the resolution of the camera. Rather, incorporating the adjacent boundary likelihoods into the analysis provides a more realistic picture of where the boundary resides. Animations demonstrating the consistency, resolution, and overall picture of the analysis steps are shown in Section A26, Appendices.

After determining the boundary position independently for each image, these values are compared to the reference position taken at vacuum before the experiment begins. The pixel distance change of the sample boundary from the initial reference image to the current image being analyzed, Δpx, is found by $\Delta px = px_i - px_{ref}$, where px is the found image boundary position in pixels from the top of the image, and subscripts i and ref refer to the current and reference images, respectively. A pixel-to-length calibration (ϑ) between the camera and the swelling cell is then used to convert this pixel change into a length change (See Section A27, Appendices), the result of which is then plugged into Equation 23. Equation 22 can be expressed in terms of the three directly measured variables acquired in this apparatus as follows:

$$\frac{\Delta V}{V_0} = \left(\frac{L_i + \frac{\Delta px}{\vartheta}}{L_i}\right)^3 - 1 \qquad \text{Equation 23}$$

where L_i is the initial length of the polymer sample, ϑ is the camera pixel to polymer distance conversion factor, and Δpx is the change in polymer length, in pixels, during one step. The same reference image used earlier for determining length changes is also used to stabilize the image itself. To stabilize an image, the operator first picks a square location on the image which contains some visual detail which remains still (at least with respect to the top of the polymer sample) throughout the entire experiment. This could be an intentionally placed target next to the Jerguson gage. This region is then compared with the same unmoving region in the first image taken during the experiment (see Figure 20), and an (x, y) shift is programmatically chosen that maximizes the overlap between the two images (see Section A25, Appendices for this algorithm). Each image is stabilized independently of adjacent images in time, and from the same starting point $(x, y) = (0, 0)$ in the optimization.

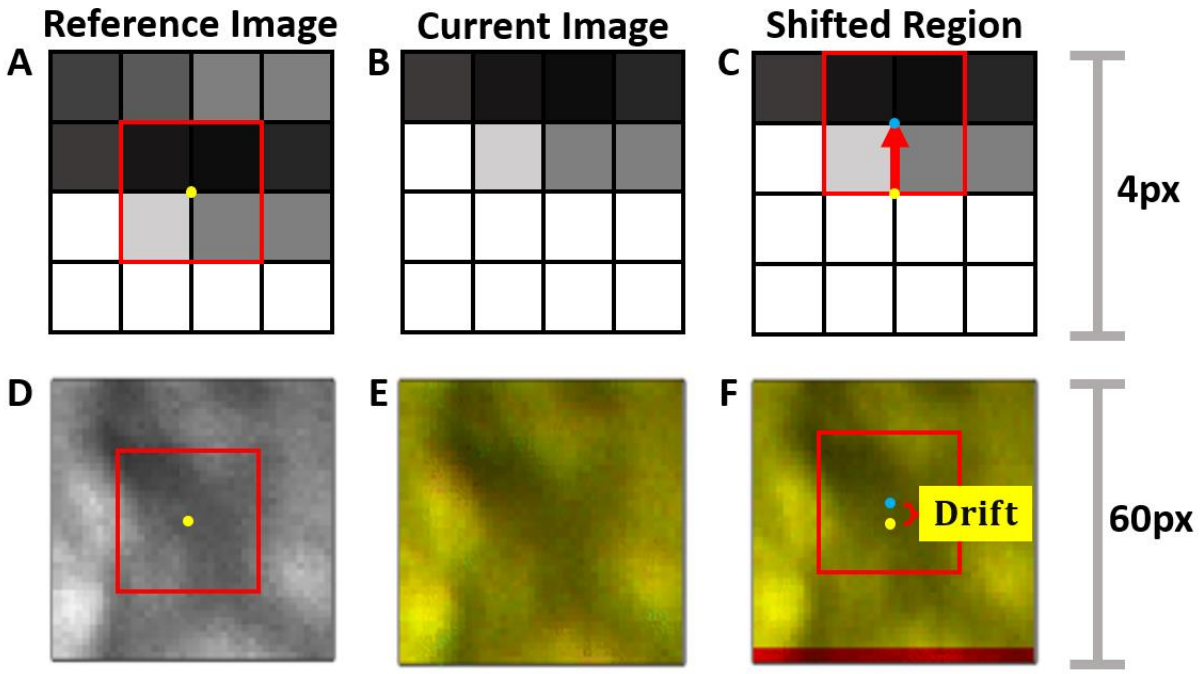


Figure 20: *Schematics of image stabilization. The top row (A, B, C) displays a simplified pixel-scale version of the algorithm with a camera moving downwards during an experiment. The bottom row (D, E, F) denotes the same situation in a real experiment. The original reference in D is shown in red in Figures E and F, with the current image shown in green. Overlapping pixels between the reference and current image shown as yellow. The distance needed to shift for the current image to minimize overlap error with F is denoted by "Drift" in Figure F.*

4.5. Results and Discussion

4.5.1. Reproducing literature polycarbonate swelling data

Before measuring TPBO and TPHI swelling, it is important to test the reliability of the apparatus and analysis procedure by reproducing CO_2-induced dilation data in polycarbonate at 35°C originally reported by Koros et al. [186] and Handa et al. [183]. This test will also provide the proof of concept that multiple samples can be run simultaneously, without compromising the quality of the measurements. Results shown in Figure 21 (labeled as runs 1, 2 and 3) used a pixel to centimeter ratio of $126.5 \pm 0.7 \frac{px}{cm}$.

Run 1 used a single polycarbonate strip whose length was $8.60 \pm 0.16\ cm$, while runs 2 and 3 were done simultaneously, using two samples with initial lengths of $5.91 \pm 0.15\ cm$ and $5.85 \pm 0.18\ cm$, respectively. Additional polycarbonate results (labeled as runs 4 and 5), which also verify the assumption of isotropic swelling, can be found in Section A28, Appendices.

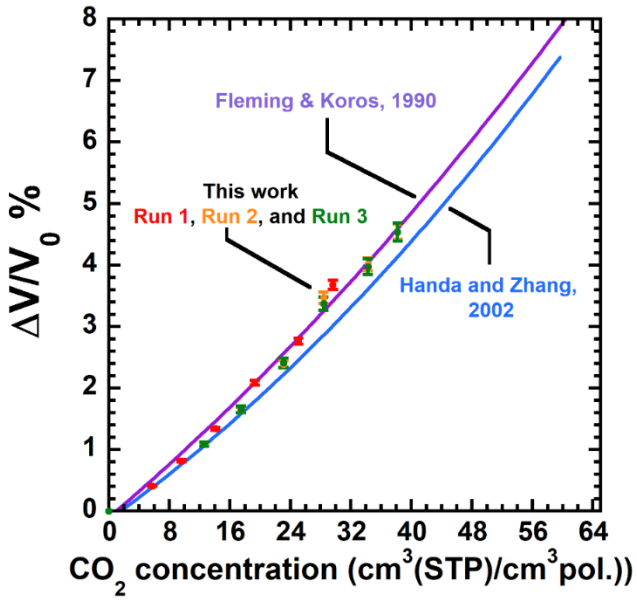


Figure 21: *Percent volumetric swelling of polycarbonate upon CO_2 exposure at 35°C, as a function of CO_2 concentration in the polymer. Filled colored symbols are data from this work, where runs 2 and 3 were done in parallel. Continuous lines represent previous literature data. Error bars were estimated via linear error propagation [96–98] without covariance.*

As shown in Figure 21, runs 1, 2 and 3 follow each other nearly identically, exhibiting minor mutual departure, which is within the experimental uncertainty. They are also consistent with previous data reported by Koros and Handa. This behavior indicates that systematic error, as opposed to random error, is the major contributor to the overall noise in this apparatus. Put in another way, if random error from the camera, the downstream

image analysis results, the initial polymer sample length, or any other quantity not shared between the two samples were significant sources of error, then runs 2 and 3 would be expected to deviate from each other far more than they currently do. Overall, the uncertainty of swelling measurements due to random error in typical experimental conditions (see Section 4.5.3, Table 10) ranges from 2% to 5%, which is significantly lower than the 25% uncertainty observed in previously reported swelling measurements [185]. Considering this, as well as that the initial sample length is the primary contributor to the random error of the measurement (at least 80% of the total uncertainty, see Figure 26), it is likely that the overall accuracy of measurements in this apparatus will be nearly entirely determined by the appropriate control of possible systematic errors, such as sample curling during dilation, sample slipping from its initial position in the Jerguson gage, the existence of shadows and other lighting artifacts that modify the apparent sample boundary, or as discussed in Section 4.5.6, *Stabilization Efficacy*. This finding highlights the advantages of this apparatus' ability to run experiments in parallel, as some systematic problems, such as temperature control issues, gas purity, pressure transducer uncertainty, or issues in any other shared factor, will affect samples equally.

4.5.2. CO_2-induced swelling in TPBOs and TPHIs precursors exhibiting systematically varied amount of triptycene units

CO_2-induced swelling in TPBOs at 35°C is shown in Figure 22A as a function of CO_2 concentration in the polymer. The experimental conditions are shown in Table 8.

Table 8: *Experimental parameters used in various TPBO and TPHI dilation experiments.*

sample	*initial length (cm)*	*pixel-to-length conversion (px/cm)*	*sample thickness (μm)*
TPBO-0.00	3.55 ± 0.06	135.10 ± 0.68	53 ± 8
TPBO-0.25	2.41 ± 0.09		35 ± 4
TPBO-0.50	2.82 ± 0.06		70 ± 20
TPBO-0.75	4.48 ± 0.08		80 ± 30
TPBO-1.00	3.39 ± 0.11		60 ± 20
TPHI-1.00	6.20 ± 0.10		91 ± 5

Concentration data are taken from a previous study [43,75]. In Figure 22B, swelling data are plotted as a function of pressure. Using concentration, rather than pressure, generally provides a stronger basis to make comparisons among samples, as it allows for swelling to be compared at given number of molecules accommodated in the polymer matrix. TPBO-0.00, which is a thermally rearranged polybenzoxazole without triptycene units, was tested as baseline material [21]. The TPBO series were previously shown to exhibit virtually identical light gasses solubilities (i.e., CO_2, CH_4, N_2), irrespective of the triptycene (i.e., configurational free volume) content [43]. Therefore, an unanswered, follow up question is: *does swelling propensity depend on triptycene content?* And, more generally, *do configuration-based polymers also exhibit good swelling resistance, in addition to excellent physical aging resistance?* [24,127] Being thermally rearranged polybenzoxazoles, these materials exhibit, *per se*, high rigidity. As discussed later, thermal rearrangement affects the TPBOs' swelling propensity. Moreover, it is possible that residual stresses from the thermal rearrangement process may cause these polymers to exhibit differences in their swelling propensity [3,196,197], even though this was not observed in sorption data

(see Figure 22). Some evidence supports the existence of residual stresses formed presumably during the thermal rearrangement stage, which are relaxed during the first step of swelling with highly sorbing penetrants (see Section A26, Appendices). As a result, brass coupons were used in future experiments, which forced samples to remain straight during the experiment. In addition to this precaution, all samples were cut and prepared from random orientations.

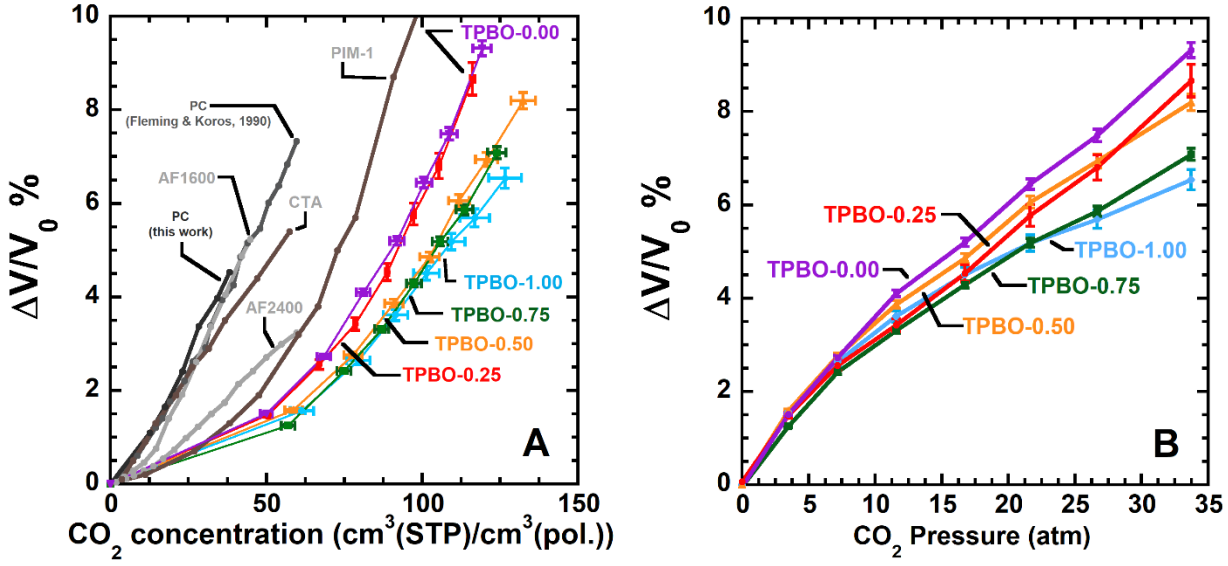


Figure 22: *Fractional swelling of TPBOs at 35°C as a function of CO_2 concentration (A), and pressure (B). Relevant polymers are included for comparison. Error bars were estimated via linear error propagation* [96–98] *for both concentration and swelling. All TPBO samples were run in parallel.*

As shown in Figure 22A, TPBO samples exhibiting low triptycene content (25%) or no triptycene at all, exhibit a quantitatively similar swelling behavior. At a given CO_2 concentration, TPBO samples exhibiting higher triptycene content (i.e., ≥50%) exhibit a comparable swelling propensity to each other, which is slightly lower than that exhibited

by TPBO-0.00 and TPBO-0.25. Therefore, incorporating configurational free volume has a beneficial effect on the swelling stability. Specifically, if the CO_2 content is 120 cm^3(STP)/cm^3pol, TPBO-1.00 exhibits a volumetric swelling of about 5%, while a swelling of 7.5% was measured in TPBO-0.00. This result is interesting, as sorption isotherms appear fairly superimposed among all TPBO samples for light gasses [43]. A similar trend is observed if swelling is represented as a function of pressure (see Figure 22B). Especially at high pressure, where higher accuracy is achieved, swelling decreases systematically with increasing triptycene molar content, which, again, points out the beneficial effect of configurational free volume on polymer swelling resistance.

At this point, it is possible to use the dilation data to correct the CO_2 sorption isotherms reported previously and collected via the pressure-decay method for systematic error introduced by assuming constant density (i.e., no swelling). Previous work in Chapter 5 resulted in a criteria being derived which determines whether or not these corrections are necessary (see Equation A3), or more specifically, whether or not swelling corrections will change the calculated sorption by more than what can be measurably resolved [96]. Equation A1 and Equation A3 can be solved simultaneously for the percent swelling and swollen polymer density, to obtain the swelling threshold at which the choice of using the dry or swollen polymer density results in no overlap of the uncertainty range (i.e., the maximum percent swelling that may occur before corrections are needed given a ϕ value). For $\phi = 1$, i.e., within one standard deviation, and at the highest pressures tested,

corrections for polymer swelling do not alter the results of our previous TPBOs sorption study. That is, even after correcting for polymer swelling, CO_2 sorption isotherms in TPBOs as a function of triptycene content are still superimposed. As an example, corrections on CO_2 sorption in TPBO-1.00 change the concentration measured at the highest pressure tested by less than 4%, however, the random uncertainty on this measurement is 8%.

In Figure 22A, TPBO dilation upon CO_2 exposure at 35°C is compared to that of other materials of interest in membrane science, such as CTA (cellulose triacetate), Teflons AF, and PIM-1 [76,174,186,198]. At a given CO_2 concentration, TPBOs exhibit a much more pronounced swelling stability compared to other materials. This behavior may be ascribed to either configurational free volume or thermal rearrangement. Barring systematic error, which is minimal due to the data being collected all in one single experiment, the larger swelling propensity exhibited by TPBO-0.00 relative to its triptycene-based analogs may be due to the lack of configurational free volume. Specifically, TPBO-0.00 swelling exceeded the average swelling of the rest of the TPBO samples by 11.5%. When considering only the TPBO polymers across varying triptycene content, the swelling data in Figure 22 provide a glimpse of evidence that configurational free volume may assist in the reduction of polymer swelling, at least in the case of CO_2. Measurements are underway to investigate other condensable penetrants.

To separate the effects of configurational free-volume and thermal rearrangement, we ran separate sorption and swelling measurements using the non-thermally rearranged analogs of each TPBO sample, that is, the precursor series of polyhydroxyimides (TPHIs)[20] exhibiting systematically varied triptycene content. The only difference between each TPBO and its TPHI analog, is that the latter was not thermally rearranged. As shown in Figure 23, at any given CO_2 concentration and for a 100% triptycene content, TPHI swells more than TPBO, indicating that thermal rearrangement from the polyimide to the polybenzoxazole form also contributes to the swelling resistance exhibited by TPBO, synergistically with the triptycene content itself.

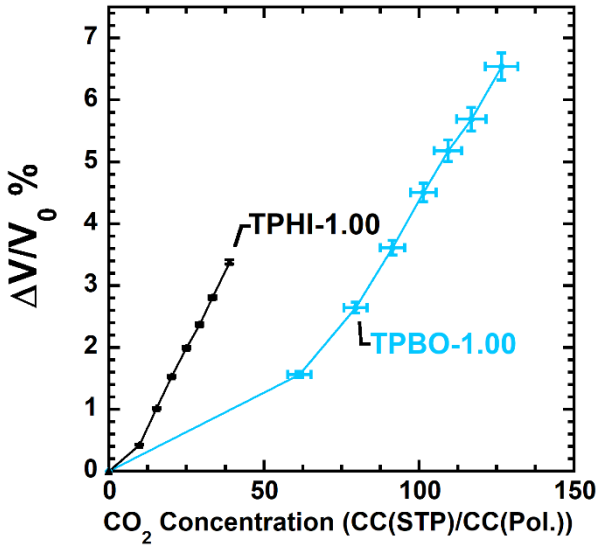


Figure 23: *Fractional TPBO-1.00 and TPHI-1.00 swelling at 35°C, as a function of CO_2 concentration. Error bars were estimated via linear error propagation [96–98] for both concentration and dilation. Samples were run in parallel.*

4.5.3. CO_2 partial molar volumes in TPBOs

To further investigate the effects of dilation across triptycene contents, polymer dilation and solubility measurements were combined to calculate the CO_2 partial molar volume within the polymer phase [77,78,93]. This analysis, however, was limited to the TPBO series, for which sorption data are available with higher accuracy relative to the TPHI analogs. Penetrant partial molar volume, $\bar{V}_{pen}$, is estimated using the technique discussed in Section 1.8.4. The rest of the parameters are fit directly from sorption data using the standard dual mode sorption model [36,80] (Section 1.6.1). All dual mode parameters are tabulated in Section A29, Appendices.

As shown in Figure 24, at given CO_2 concentration in the polymer, the CO_2 partial molar volumes in the TPBO series decreases with increasing triptycene molar content: TPBO-0.00 > TPBO-0.25 > TPBO-0.50 ≈ TPBO-0.75 > TPBO-1.00. The relative V_D values are denoted by the flat horizontal lines.

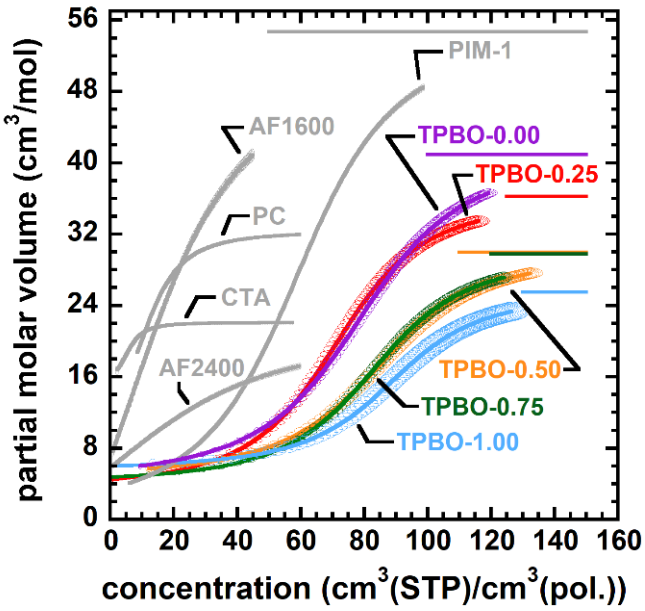


Figure 24: *CO_2 partial molar volumes in TPBOs and other reference polymers (grey) as a function of CO_2 concentration in the polymer. Circles denote error arcs representing one standard deviation from the sampled point, calculated via linear error propagation and neglecting covariance for each data point calculated [96,199]. Solid horizontal lines denote fit V_D values for each TPBO sample, with the grey line displaying the V_D for PIM-1. Each curve includes 100 sampled points.*

As explained by dual mode theory, lower partial molar volume values indicate that the Langmuir region is being filled preferentially. This behavior is a product of the low volume the penetrant occupies when in a partially condensed state in the polymer's microcavities, i.e., Langmuir's mode. As Langmuir's mode gets saturated, penetrant molecules start to sorb in the Henry's mode. At that point, polymer swelling starts to occur more dramatically, and a corresponding increase in partial molar volume is observed as the penetrant occupies a larger fraction of the space available within the polymer.

In hydrocarbon-based polymers exhibiting low fractional free volume, partial molar volume is immediately concave-down with an increase in concentration, and a saturation point is eventually reached. This is apparent in polycarbonate (PC in Figure 24, $FFV \approx 16.3\%$) [4,186] and cellulose triacetate (CTA in Figure 24, $FFV \approx 17\%$) [57], where the partial molar volume sharply increases, followed by a leveling-off as the non-equilibrium free volume is saturated and the polymer phase volume eventually begins to increase linearly with CO_2 concentration. This latter state is then reflected by a constant partial molar volume as CO_2 concentration increases, as there is now a constant change in polymer volume as more penetrant molecules are sorbed. Perfluorinated polymers, such as Teflon® AF2400 [35,200] and Teflon® AF1600 [35], despite exhibiting high FFV (32 and 28%, respectively), behave similarly to low FFV polymers in terms of their partial molar volumes. Due to their anomalously low cohesive energy density, perfluoropolymers host penetrant molecules preferentially in the Henry's mode rather than in the Langmuir's mode, which is consistent with their relatively high swelling propensity [132,198,201,202].

PIM-1 shows an intermediate behavior between that of conventional polymers exhibiting conformational free volume (perfluoropolymers, CTA, PC) and TPBOs. Specifically, PIM-1's swelling becomes important at larger CO_2 concentrations (i.e., ≈20 cm^3(STP)/cm^3pol) than in conventional polymers [76,203], but still lower than in TPBOs (i.e., ≈60 cm^3(STP)/cm^3pol). Moreover, CO_2 partial molar volume in PIM-1 is much larger than in TPBOs, which confirms that the latter exhibits better dimensional stability. TPBOs exhibit

both regular nonequilibrium free volume sites, as well as configurational free volume pockets (that is, free volume generated by the internal clefts of triptycene units[24,43]), which can theoretically host penetrant molecules without causing swelling or, at least, causing less swelling than the Henry's counterpart.

To shed fundamental light on the swelling propensity of the configurational free volume and its effect on TPBO overall swelling behavior, the f and V_D values obtained by fitting TPBO swelling data to the dual mode dilation model (see Equation 8), were analyzed as a function of triptycene molar content. As discussed in a previous study [43] and summarized in Section A29, Appendices, all TPBOs exhibit similar light gas solubility and, as such, similar dual mode sorption parameters (k_D, $C_H^{'}$, and b). Interestingly, V_D decreases with increasing triptycene content in the TPBOs series from 0 to 100%, meaning that sorbed penetrant molecules become more confined as more configurational free volume is incorporated in the polymer. In contrast, f increases with increasing triptycene content in the TPBOs series from 0 to 100%, suggesting that the Langmuir mode contributes more and more to swelling, as more configurational free volume is incorporated in the polymer (See Section A29, Appendices). However, although f increases with increasing TPBO's triptycene content, its values for TPBOs (i.e., 0.10-0.20) are much lower than those exhibited by conventional rigid glassy polymers containing only conformational free volume, such as polybenzimidazoles (for which f = 0.33) [204], Matrimid® polyimide (f = 0.42-0.78) [77] and cellulose triacetate (f = 0.75) [76]. These

results indicate that TPBO Langmuir's mode swelling propensity, which includes the configurational free volume swelling propensity, is lower than that exhibited by the Langmuir mode in conventional rigid polymers exhibiting only conformational free volume, which explains the overall better swelling resistance exhibited by configuration-based polymers relative to conventional conformation-based polymers. This picture is consistent with the rigidity exhibited by triptycene units, as well as with their ability to interlock polymer chains and form $\pi - \pi$ stacking interactions.

However, a still open question is whether thermal rearrangement, other than configurational free volume, is also responsible for the observed swelling behavior. To separate the individual and synergistic effects of configurational free volume vs thermal rearrangement on the TPBO swelling behavior, we compared vis-à-vis the results of the dual mode analysis of dilation data in TPBO-1.00 and its non-thermally rearranged precursor, TPHI-1.00, at given amount of configurational free volume. Interestingly, the V_D values of CO_2 in the two materials, TPBO-1.00 and TPHI-1.00, are, within the uncertainty, essentially the same (i.e., 25.50 ± 1.12 and 25.81 ± 0.98, respectively, see Table 9). In contrast, the f value in TPHI-1.00 (i.e., 0.35 ± 0.04) is larger than in TPBO-1.00 (i.e., 0.22 ± 0.02), but still lower than in conventional glassy polymers, that is: $f^{TPBO} < f^{TPHI} < f^{conv.glassy\ polym.}$. These results indicate that thermal rearrangement and configurational free volume synergistically contribute to the peculiar swelling behavior exhibited by TPBOs.

Table 9: *Best fit value of the Dual Mode Dilation Model for TPBOs and conventional glassy polymers.*

polymer	V_D (cm^3/mol)	f	Ref.
TPBO-0.00	40.95 ± 0.42	0.10 ± 0.01	this study
TPBO-0.25	36.21 ± 0.71	0.09 ± 0.01	this study, [75]
TPBO-0.50	29.97 ± 0.61	0.15 ± 0.01	this study
TPBO-0.75	29.77 ± 0.66	0.13 ± 0.01	this study
TPBO-1.00	25.50 ± 1.12	0.22 ± 0.02	this study
TPHI-1.00	25.81 ± 0.98	0.35 ± 0.04	this study
Matrimid®	21	0.42-0.78	[77]
cellulose triacetate	22.09 ± 0.17	0.65 ± 0.04	[76]
Lexan® (BPA Polycarbonate)	27	0.3	[77]

4.5.4. Pure- and mixed-gas ethane-induced swelling

Exposure to light hydrocarbons, which are common contaminants in natural gas and other process streams, causes swelling effects in polymer membranes [205]. Therefore, we decided to measure TPBO and TPHI swelling upon exposure to pure ethane, a model hydrocarbon, as well as 20:80% mol ethane-nitrogen gas mixture. Five TPHI and five TPBO samples ranging from triptycene contents of 0% to 100% were tested in parallel. Nitrogen-induced swelling of TPBO and TPHI is negligible and, as such, it is not discussed. Pure and mixed-gas swelling data at 35°C are shown in Figure 25A-E as a function of ethane fugacity in the contiguous external gas phase, which was calculated via the Peng-Robinson equation of state, using a penetrant-penetrant interaction parameter, k_{ij}, equal to 0.0515 [206] Due to material limitations, mixed and pure ethane dilation data were collected using the same samples, with vacuum being held for 3 days

between the mixed-gas measurement and the subsequent pure-gas measurement to ensure full desorption of the residual penetrant.

At a pure ethane fugacity of 10 atm, TPBOs and their non-thermally rearranged TPHI analogs exhibit a volumetric swelling of approximately 4% and 1.5%, respectively. To put these numbers in perspective, poly(ethylene oxide) (PEO)-based polymers swell by about 2% [207] upon exposure to ethane at similar conditions, and PDMS [208] swells by about 8%. Unfortunately, ethane sorption and swelling data are rare, therefore more comparisons are not possible.

Figure 25F shows a resolvable relationship between triptycene content and swelling, where an increase in triptycene content results in a decrease in polymer swelling at given ethane fugacity. This trend is quantitatively similar to that discussed in Section 4.5.2 for CO_2-induced swelling. Pure and mixed gas ethane-induced swelling in all TPHI samples is much lower than in the corresponding TPBO analogs, even though the comparison was made on a fugacity basis. Although a concentration-based comparison would be more appropriate, ethane sorption in TPHI takes an unreasonably long time to attain equilibrium, therefore it could not be practically measured.

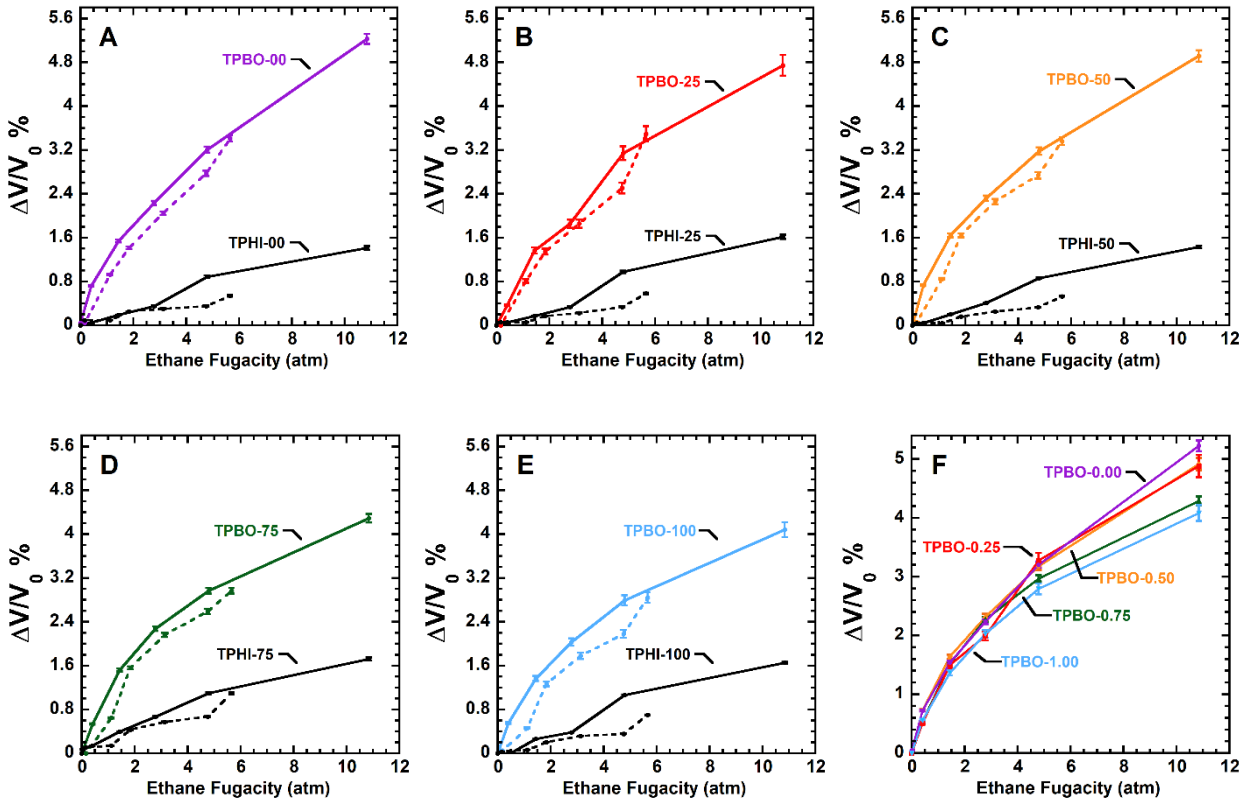


Figure 25: *Fractional swelling of A) TPBO/TPHI-0.00, B) TPBO/TPHI-0.25, C) TPBO/TPHI-0.50, D) TPBO/TPHI-0.75, and E) TPBO/TPHI-1.00 at 35°C as a function of pure-gas (solid lines) and mixed-gas (dashed lines) ethane fugacity. Error bars were estimated via linear error propagation [96–98]. All samples were run in parallel. F) Comparisons among TPBOs.*

Interestingly, TPBO and TPHI swelling in mixed gas ethane is, at a given fugacity, about $8 \pm 5\%$ lower on average than the corresponding pure ethane-induced swelling. This result is consistent with previous swelling data reported for thick and thin films of PIM-1 and PTMSP by Ogieglo et al. [76]. However, at relatively high fugacity (i.e., high pressure), the mixed gas TPBOs' swelling isotherm approaches the pure-gas one, indicating that differences between pure- and mixed-gas might be due to the experimental uncertainty. In the case of TPHI this behavior is somehow less evident, likely due to the higher experimental uncertainty associated with the very low swelling.

As a matter of fact, although previous studies claimed that mixed-gas induced swelling was lower than pure-gas induced swelling, no error bars were reported to substantiate this claim. The lower swelling measured in mixed gas condition relative to the pure gas swelling at the same fugacity could be explained by invoking the competitive sorption mechanism, as well as the fact that ethane is the less abundant component in the mixture [209–211]. However, alternative explanations could be provided for the observed behavior. Since the first swelling measurement with these samples was run in mixed-gas conditions, one may hypothesize that sample conditioning occurred. Two features of Figure 25 support this claim. Firstly, the final data point for each of the triptycene contents in the mixed TPBO runs (the more resolved of the two types of polymers due to the higher overall swelling) nearly intersect the subsequent pure run [186,192,212]. Secondly, the swelling isotherms in the pure case tend to be smoother than in the mixed-gas case. Residual stresses locked in the thermally rearranged polymers (i.e., TPBOs) may play a role in this behavior. The topic of residual stresses is discussed in Section A26, Figure A28, Appendices.

4.5.5. Analysis of the experimental uncertainty

As data is being processed through many steps, understanding the results' uncertainty is critical to its comparison to existing literature data. Uncertainty is initially linearly propagated considering all the parameters involved in the swelling measurements, such as the initial sample length, L_i, the camera pixel change to distance ratio at a given camera

position, ϑ, and the number of pixels the sample changed in one step, Δpx. The uncertainty of the fractional swelling, ν, measured in a given step can be expressed as follows:

$$\sigma_\nu = 3 \cdot \frac{(L_i\vartheta+\Delta px)^2}{(L_i\vartheta)^3} \sqrt{\Delta px^2 \left(\frac{\sigma_{L_i}^2}{L_i^2} + \frac{\sigma_\vartheta^2}{\vartheta^2}\right) + \sigma_{\Delta px}^2} \qquad \text{Equation 24}$$

The derivation of this expression is provided in Section A30 of the Appendices. In addition to the overall uncertainty, the fractional uncertainty contribution of each of these measurements to the total uncertainty of ν can also be found using the same technique used for the gas and vapor sorption apparatuses (Chapter 5). The overall error can be minimized with an experiment that maximizes the initial polymer sample length (larger L_i) and minimizes the distance from the sample to the camera (larger ϑ). Figure 26A demonstrates this concept, where simulating sample (i.e., any polymer in similar experimental conditions with a fractional dilation of 7%) dilation results in an inverse relationship between the measurement uncertainty and the sample's initial length.

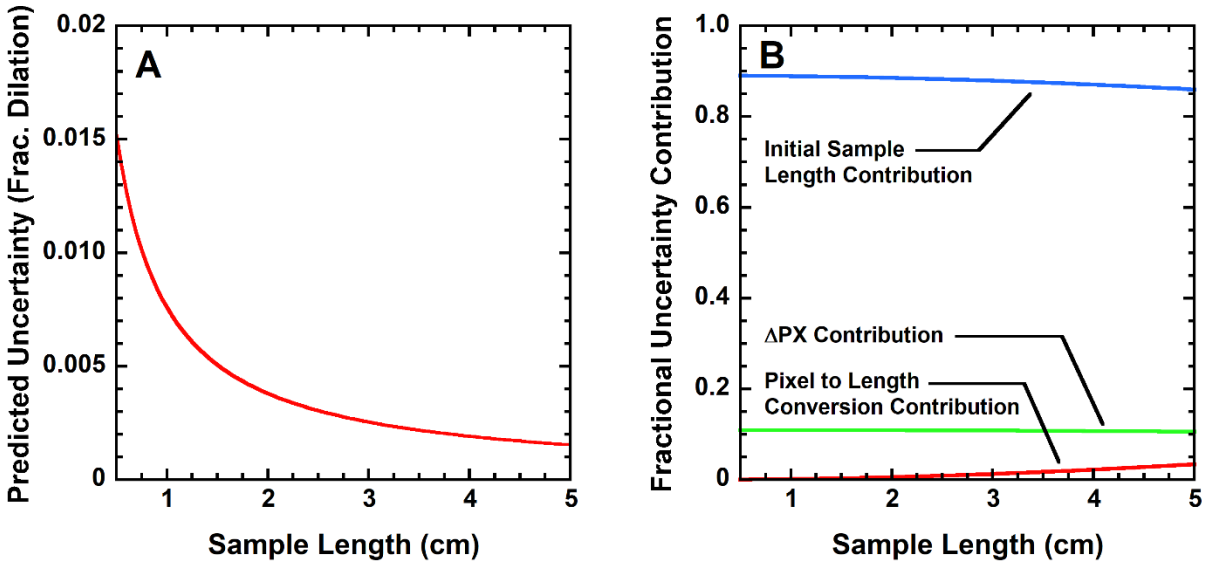


Figure 26: *Sensitivity analysis predicting overall uncertainty (A) and fractional uncertainty contributions from the input variables (B) of a simulated swelling experiment with similar experimental conditions as the TPBO/TPHI runs, i.e., with characteristics described in Table 10 and a constant fractional volume swelling of 7% as a function of the total polymer sample length used in the real experiment.*

Furthermore, the sensitivity analysis of this error shown in Figure 26B (i.e., the contributions that make up the error in Figure 26A) demonstrates that the sample length is also the dominating factor controlling the precision of the experiment. As the initial sample length surpasses 2.5 *cm*, the overall uncertainty of the experiment is predicted to be at 0.75% or less, with sample length still accounting for more than 85% of this uncertainty. Though maximizing sample length doesn't guarantee a lack of other systematic errors that may introduce imprecision in the experimental results, it does ensure the minimization of these three random errors.

Table 10: *Typical calibrations and setting used in this study to run swelling measurements.*

Variable	Value	Typical Uncertainty	Sensitivity Analysis in Figure 26
L_i	2 – 5 cm	0.05 - 0.3 cm	variable $\pm$ 0.1 cm
Δpx	Varies based on L_i and penetrant. Usually spans 2-20 px	0.05 – 0.25 px	$\Delta px_j \pm 0.125$ px $\Delta px_j = \vartheta(\nu+1)^{\frac{1}{3}} \cdot L_{ij} - L_{ij}$ for each simulated L_i in the analysis where ν is the given fractional dilation by the penetrant
ϑ	105 – 136 px/cm	0.5 – 0.5 px/cm	125 $\pm$ 0.5 px/cm

The calibration factor ϑ can be found experimentally by suspending a ruler in the Jerguson gage and determining the pixels corresponding to incremental distance changes (see Table 10). In this work, 40 measurements were taken per camera position along the track, and a calibration curve is provided where uncertainties on ϑ are acquired directly through the standard error of weighted linear regression (see Section A27, Figure A30, Appendices).

Finally, noting the derivation in Section A30, Appendices and the fact that for typical experimental values, $\frac{\sigma_\vartheta^2}{\vartheta^2} \approx 0$ and $\Delta px^2 \left(\frac{\sigma_{L_i}^2}{L_i^2}\right) \gg \sigma_{\Delta px}^2$**.** The fractional dilation uncertainty in Eq. 6 may be simplified to the following rough approximation:

$$\sigma_\nu \approx 3 \cdot \frac{(L_i\vartheta+\Delta px)^2}{L_i^4\vartheta^3} \Delta px \cdot \sigma_{L_i} \qquad \text{Equation 25}$$

σ_{L_i}, being linear, has little impact on the overall uncertainty when changed compared to the capacity of the other variables, which are larger in their absolute order. This also implies that, while maximizing the initial sample length greatly benefits the experiments

precision, the actual precision by which the initial sample length is measured is less impactful to the random experimental error. For this reason, it is acceptable to use the most accurate method of length measurement, rather than seeking out new equipment or methods to acquire extremely precise initial lengths. In this work, the sample's initial length is found by scanning the sample with a Canon LiDE 220 scanner with a resolution of 600 DPI. Scans of the sample were then measured in the image processing software ImageJ as a pixel distance, then converted to centimeters. For example, with a 600 DPI scanner: $cm_{sample} = px_{sample} \cdot \frac{1\ inch}{600\ px} \cdot \frac{2.54\ cm}{1\ inch}$. Uncertainty on this sample length is assumed to be the width of the marker that indicates where the sample is clamped, which is a conservative overestimate of the precision by which the sample is measured.

4.5.6. Assessment of image stabilization efficacy

To demonstrate both the necessity and value of image stabilization, TPBO-0.25 [20,21] swelling upon exposure to n-butane was measured at 35°C and up to 2 atm with and without image stabilization, all other analysis parameters remaining the same. This polymer-penetrant pair represents an interesting test case, as, differently from what observed in the presence of CO_2, the polymer dilated significantly (around 11%) at the maximum pressure reached (i.e., 2 atm) and rather slowly, taking up to four days per step to complete. This experiment used a comparatively long initial sample length of $5.5 \pm 0.3\ cm$ and a camera pixel to centimeter ratio of $126.5 \pm 0.7 \frac{px}{cm}$, which in theory should

minimize the effects of both systematic and random error as a longer initial sample length will result in a higher pixel change detected by the camera (see Section 4.5.5). Despite this, the uncorrected data fluctuated dramatically (see Figure 27) only 24 hours into the experiment.

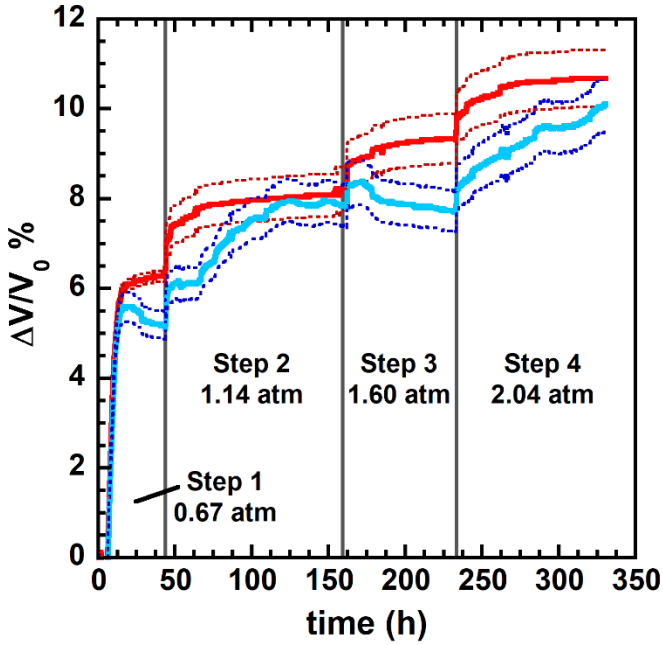


Figure 27: *TPBO-0.25 swelling kinetics upon exposure to n-butane at 35°C as a function of time. The solid red line denotes the percent swelling found while correcting for camera movement during the experiment, the solid blue line denotes the same image data and analysis, but without any image stabilization. Dashed lines denote experimental uncertainty, found via linear error propagation [96–98], via one standard deviation from the measured value.*

This experiment identifies camera position exclusively as the most significant source of systematic error in a typical experiment (e.g., an experiment where no samples break or slip from their fixture, or temperature controllers do not experience malfunctions). Therefore, image stabilization is essential to extract meaningful experimental information, from both the transient and equilibrium stages. It was later determined in

this apparatus, where the camera was mounted to a stable metal track and all components of the apparatus were bolted to the same lab bench, that temperature fluctuations were the primary source of long-term camera position error (see Section A31 and A32, Appendices). This contrasts with short-term camera position changes, such as from the table being jostled by an experimenter or building vibrations affecting the sample or camera, which tend to cause random (and temporary) errors that may be mitigated by simply taking more images. Unless one can incorporate the camera into the temperature-controlled portion of the apparatus (which may yield issues of its own, due to the electronics within the camera and differences between the camera mount and sample mounts' coefficients of thermal expansion), this source of systematic error may only be corrected via a mount made of a material with an extremely low coefficient of thermal expansion, or image stabilization.

4.6. Conclusions

The swelling (i.e., dilation) propensity of polymer membranes exhibiting configurational free volume has been investigated in pure- and mixed-gas conditions. A series of thermally rearranged polybenzoxazoles exhibiting systematically varied molar amount of triptycene units, as well as their non-thermally rearranged analogs were considered. The individual and synergistic effects of configurational free volume and thermal rearrangement on polymer swelling propensity was studied. To do so, a new experimental approach based on computer vision was developed, which can achieve

superior accuracy by correcting the limitations of conventional swelling measurements. The analysis process involves stabilizing the images against camera motion, detecting the polymer boundary using image convolution, and combining subsequent images to quantify equilibrium and transient swelling. A thorough investigation of the uncertainty and precision associated with swelling measurements is provided, including an analysis of the major factors affecting experimental uncertainty.

We show that configurational free volume and thermal rearrangement synergistically contribute to enhance swelling resistance. The dual mode theory helps elucidate the fundamental origin of this phenomenon. Finally, polymer swelling in nitrogen (80%mol)-ethane (20%mol) mixed-gas conditions is slightly lower than in pure-ethane conditions at the same ethane fugacity, which agrees with the competitive sorption mechanism, and with ethane being the less abundant component in the mixture. Alternative possible explanations for this phenomenon are discussed.

Chapter 5. Evaluating the Experimental Uncertainty in Gas and Vapor Sorption Experiments[**]

5.1. Abstract

High quality, accurate and reliable sorption and adsorption data provide the basis for designing large scale, energy efficient membrane/adsorption processes for gas and liquid separations and evaluate their techno-economic feasibility. As highlighted by Prof. David Sholl during his plenary lecture at the 2020 NAMS (*North American Membrane Society*) conference, the lack of uncertainty associated to published sorption/adsorption data represents one of the major roadblocks to progress in separation technologies. In this study, a standard methodology to estimate the uncertainty associated to sorption/adsorption measurements is proposed. A systematic analysis of the experimental uncertainty of gas and vapor sorption/adsorption measurement in polymers using the barometric method is performed in a variety of operative conditions, to individuate which factors contribute the most to the overall uncertainty under different experimental operation modes. This effort should push researchers in the field to adopt a standardized method to estimate the experimental uncertainty, which is expected to make experimental data coming from different laboratories in the world easier to compare.

[**] Reproduced, with permission from Box, et al. [96]

Finally, the validity of the linear error propagation method, generally used to evaluate the uncertainty of sorption/adsorption data, is demonstrated by a *vis-à-vis* comparison with the Monte Carlo statistical method. Fundamental aspects and practical implications are highlighted and discussed.

5.2. Introduction

As worldwide energy demand increases, a more rational use of natural resources has become necessary. As 15% of the world's energy consumption is due to chemical separations [156], membrane technologies, used as both stand-alone and integrated processes, provide a viable pathway towards energy-efficient separations [1,68,156]. Although energy-efficient and eco-friendly separations are possible, the perceived risk in implementing them must be minimal. The availability of high quality, accurate, and reliable transport data (e.g., sorption and adsorption isotherms, permeability and selectivity data) is one of the major roadblocks to the design of new processes and to the evaluation of their technical and economic feasibility [156–160].

More generally, the need for accurate and reproducible data is a major issue in several other areas of science [159–164]: for example, in drug discovery, attempts to reproduce 53 landmark papers' data were successful in only 11% of the cases [165]. A major issue is the availability of uncertainty associated with published experimental data [159,163,166]. Often, membrane- and sorbent-related papers do not report details about how the experimental uncertainty was estimated, which prejudices the quality and usability of the

reported data [166,167]. A critical issue is the lack of a standard, universally adopted method to estimate the experimental uncertainty, which often makes experimental data coming from different laboratories around the world difficult to compare [159,163,166,167].

The scope of this study is to provide a unifying approach to calculate the experimental uncertainty associated with gas and vapor sorption/adsorption measurements in polymers using the barometric (i.e., pressure decay) method. This is of major interest in membrane science, as well as related fields, such as batteries, gas storage, adsorption and controlled drug release. This need has been highlighted by Prof. David Sholl at Georgia Institute of Technology during his plenary lecture at the 2020 NAMS (*North American Membrane Society*) conference.

Ideally, experimental uncertainty should be calculated by comparing a series of repeated measurements, which encompasses the effects of both systematic and random errors. In practice, there exist multiple impracticalities that prohibit this approach. For example, running enough sorption tests to satisfy statistical requirements would be extremely time consuming. Moreover, the cost of materials, whose availability is often limited to a few milligrams, can be prohibitive if repeated experiments are needed. To overcome these issues, the experimental uncertainty can be estimated in a predictive fashion using the so called error propagation methods, that is, using the experimental uncertainty associated to relevant parameters that affect the experiment [98,103]. In this paper, we propose a

general, unifying methodology to evaluate the uncertainty associated to gas and vapor sorption/adsorption measurements in polymers using the barometric technique, which is expected to make experimental data from different laboratories easier to compare.

5.3. Validity and limitations of the proposed approach

The generalized analysis presented in this study refers to sorption/adsorption measurements via the pressure decay method, which is used in several laboratories around the world to measure gas and vapor sorption/adsorption isotherms in polymers and porous materials [103,168,169].

5.3.1. Vapor sorption measurements

Measured from the setup described in Section 1.10.1., the number of moles of vapor sorbed in the polymer at any equilibrium pressure was determined from the penetrant mass balance (see Figure 5B). Specifically, the number of moles of vapor sorbed in the polymer at the end of any sorption step is equal to the initial number of moles of vapor fed to the system minus the number of moles in the external, contiguous vapor phase when sorption equilibrium is reached. Since vapor sorption experiments are run using the differential mode, the penetrant mass balance must take into account that some vapor will be left in the sampling chamber when closing the valve in between differential steps. Finally, the number of moles of vapor sorbed in the polymer during the previous step must be added.

To get the number of moles from pressure data, an equation of state must be used. The ideal gas equation of state is normally applied to run these calculations, based on the low-pressure operating conditions that usually accompany vapor sorption experiments (≪ 500 Torr) [26,58,75,89]. The reliability of this method has been proved by elaborating the pressure data using the ideal gas equation of state and a generalized (i.e., Peng-Robinson [143]) equation of state, which provided the same results. Replacing the ideal gas equation of state into the penetrant mass balance, provides the following expression for the number of moles of vapor sorbed in the polymer at any given step *j*:

$$n_{pol,j} = \frac{V_C}{RT}\left(\sum_{i=1}^{j}\left(P_{0,i} - P_{Cf,i-1}\right) - P_{f,j}\left(\frac{V_S}{V_C} + 1\right)\right) \qquad \text{Equation 26}$$

where V_S is the sampling chamber volume, V_C is the charge chamber volume, T is the absolute temperature and R is the universal gas constant. The volumes V_S and V_C are accurately measured using the Burnett method [104]. The subscripts "*c*" and "*s*" refer to the charge and sorption chamber, respectively, while "*0*" and "*f*" stand for initial and final, respectively. P_0, P_{Cf}, and P_f refer to the initial charge, final charge, and final overall pressures, respectively. Finally, the vapor concentration in the polymer at step *j*, $C_{pol,j}$, that is, the ratio between the number of moles of vapor sorbed by the polymer to the polymer volume, is calculated as follows:

$$C_{pol,j} = \frac{(n_{pol,j})\rho_{pol}}{m_{pol,dry}} \qquad \text{Equation 27}$$

where ρ_{pol} is the polymer density and $m_{pol,dry}$ is the mass of the dry polymer sample.

The technical features of the vapor sorption apparatus considered in this study are shown in Table 11. As a case study, in this paper we consider methanol vapor sorption data at multiple temperatures in a Celazole® polybenzimidazole (PBI), reported previously by Bye et al. [26] and Loianno et al. [58].

Table 11: *Technical details of the vapor sorption apparatus considered in this study.*

	Experimental range/value	*Uncertainty*	*Source*
Pressure sensor (MKS PDR2000 dual-capacitance manometer)	*0-500 Torr*	*0.25% of the reading*	*manufacturer*
Temperature controller (Techne TU-20HT immersion circulator)	*-20 to 120°C*	*± 0.5°C*	*manufacturer*
Charge chamber volume	*29.4778 cm³*	*± 0.098 cm³*	*Burnett method*
Sampling chamber volume	*7.63068 cm³*	*± 0.023 cm³*	*Burnett method*
Polymer mass (measured using a Mettler-Toledo ME54T3 analytical balance, weighing capacity = 52 g)	*0.005 to 0.01 g*	*± 0.0005 g*	*manufacturer*
Celazole® polybenzimidazole (PBI) density (measured with an Archimede's balance)	*1.27 g/cm³*	*± 0.014 g/cm³*	*[26]*

5.3.2. Gas sorption measurements

The penetrant mass balance discussed for the vapor sorption apparatus was adjusted to reflect the procedure for gas sorption (Section 1.10.2). The moles of gas sorbed by the polymer at any given step j (Figure 6) is:

$$n_{pol,j} = V_C \sum_{i=0}^{j} \left(\frac{1}{\tilde{V}_{Co,i}} - \frac{1}{\tilde{V}_{Cf,i}} \right) - \frac{V_S}{\tilde{V}_{Sf,j}} \qquad \text{Equation 28}$$

where V_S is the sampling chamber volume and V_C is the charge chamber volume. The balance is completed by applying an equation of state to solve for the gas molar volume ($\tilde{V}_{kl}$), where *k* refers to either the charge chamber (*c*) or the sample chamber (*s*) and *l* refers to either the initial (*0*) or final (*f*) states, as indicated in the mole balance. Since gas sorption measurements are run at high pressures, the ideal gas equation of state is no longer viable, therefore the Peng-Robinson or any other generalized equation of state must be used to convert the experimentally measured pressure data into number of moles [143]:

$$P_{kl} = \frac{RT}{\tilde{V}_{kl}-B} - \frac{A}{\tilde{V}_{kl}+2B\tilde{V}_{kl}-B^2} \quad \text{Equation 29}$$

where P_{kl} is the pressure (in the volume *k* at state *l)* used to solve for the corresponding molar volumes $\left(\tilde{V}_{kl}\right)$. *A* and *B* are the Peng-Robinson parameters, which are related to penetrant critical properties as follows [148]:

$$A = \frac{0.457535(RT_C)^2}{P_C}\left[1 + (0.37464 + 1.54226\omega - 0.26992\omega^2)\left(1 - \sqrt{\frac{T}{T_C}}\right)\right] \quad \text{Equation 30}$$

$$\boldsymbol{B = \frac{0.077796(RT_C)}{P_C}} \quad \text{Equation 31}$$

where T_C, P_C and ω are the penetrant critical temperature, critical pressure and Pitzer acentric factor, respectively [148]. Finally, Equation 27 is used to calculate the gas concentration in the polymer. The calculation pathway is shown in Figure 6B.

To further improve the accuracy, the volume occupied by the polymer sample was subtracted from the volume of the sorption chamber.

The technical features of the gas sorption apparatus considered in this study are shown in Table 12. As a case study, in this paper we consider CO_2 sorption data at multiple temperatures in a thermally rearranged polybenzoxazole bearing triptycene groups (TPBO-0.25), reported previously by Loianno et al. [75] and Box et al. [43] We stress the fact that although the methodology devised in this work to estimate the experimental uncertainty is of general validity in the case of pressure-decay based sorption/adsorption experiments, the results shown specifically reflect the features of the experimental setup used in our laboratory.

Table 12: *Technical details of the gas sorption system considered in this study.*

Gas Sorption Apparatus	*Experimental range/value*	*Uncertainty*	*Source*
Pressure sensors (Honeywell Super TJE)	*0 to 500 psi*	*0.5% of the reading*	*manufacturer*
Temperature (Techne TU-20HT immersion circulator)	*-20 to 120°C*	*± 0.5°C*	*manufacturer*
Charge chamber volume	*18.442 cm^3*	*± 0.04*	*Burnett method*
Sampling chamber volume	*15.707 cm^3*	*± 0.06*	*Burnett method*
TPBO mass (measured using a Mettler-Toledo ME54T3 analytical balance, weighing capacity = 52 g)	*0.1 to 0.5 g*	*± 0.0005 g*	*manufacturer*
TPBO density (measured using an Archimede's balance)	*1.393 g/ml*	*± 0.002 g/ml*	[75]
CO_2 Pitzer acentric factor (ω)	*0.228*	*± 0.006*	[170,171]
CO_2 critical pressure	*72.86 atm*	*± 0.127 atm*	[170]
CO_2 critical temperature	*304.13 K*	*± 0.092 K*	[170]

Finally, the effect of polymer swelling is neglected in the subsequent analysis. In Section A17 (Appendices), a detailed, quantitative discussion of the effect of polymer swelling on sorption uncertainty is provided.

5.4. Results and Discussion

The uncertainty associated to a variety of experimental gas and vapor sorption data collected in this laboratory was calculated using the LEP and MCEP methods. We will consider first vapor sorption data collected using the procedure shown in Figure 5B (see Section 5.3.1), and then gas sorption data collected using the procedure shown in Figure 6B (see Section 5.3.2). Obviously, the procedure described hereafter applies also for adsorption measurements in porous materials.

5.4.1. Case Study 1: methanol vapor sorption in Celazole® polybenzimidazole

Methanol vapor sorption isotherms in Celazole® polybenzimidazole (PBI) at 25, 35, and 45°C, in units of cm^3(STP)/cm^3(polymer), are shown in Figure 28A-B-C, respectively, as a function of vapor partial pressure[26,58]. The uncertainty calculated via the linear error propagation method (i.e., error bars) is compared directly with the uncertainty calculated via the Monte Carlo method. A generalized analytical expression for the concentration uncertainty, using LEP, can be found in Section A19, Appendices.

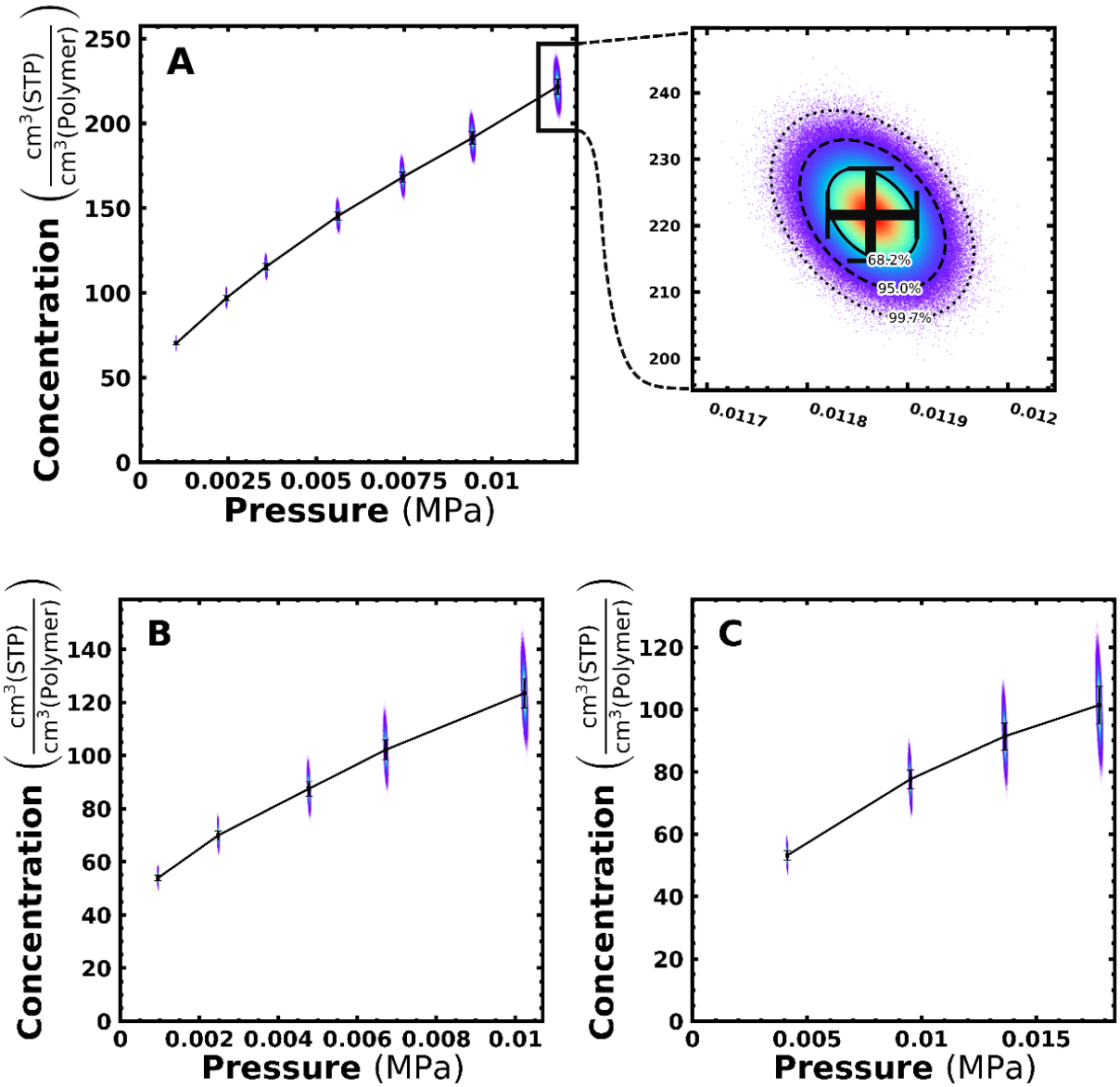


Figure 28: *Experimental methanol vapor sorption isotherms in Celazole® PBI at A) 25°C, B) 35°C, and C) 45°C as a function of pressure. Error bars are calculated via linear error propagation and are superimposed over a corresponding Monte Carlo error propagation (1,000,000 iterations). Lines are drawn to guide the eye. Experimental data are from ref. [26,58].*

At first glance, uncertainty values from the Monte Carlo method may appear larger relative to that calculated via the linear error propagation. This stems from the MCEP method providing a full Gaussian distribution of possible values in both the X and Y directions, rather than the single standard deviation that is shown by a single error bar,

which is what LEP directly provides. Error bars residing within one standard deviation align between the two methods, which can be verified by the comparison shown later (see Figure 28).

The differential method used to run sorption measurements experiences a growing coefficient of variation with increasing penetrant partial pressure. The coefficient of variation, which is defined as $CV = \frac{\sigma}{\mu} \times 100\%$, where μ is the mean value of the measurement and σ is its standard deviation (see Section A20 of the Appendices), is a measure of how "spread out" the possible values of the measurement are from the average value. This growth in CV is essentially due to the impact of the uncertainty of the moles of penetrant sorbed by the polymer during previous steps. For example, for the methanol vapor isotherm in *Celazole*® PBI at 25°C, the CV of the concentration at the first sorption step, at 0.00102 MPa, is 1.44% (see Figure 28A and Figure A19A). At step 7 (i.e., the last step in that isotherm at 0.012 MPa), the CV is 2.07%, which indicates that CV increases with the total number of sorption steps (see Figure 28A and Figure A19A). Growth notwithstanding, it is unclear whether other factors may impact the CV significantly, such as the polymer mass and density. However, some variables can be ruled out as significant contributors to error, such as temperature. For example, the uncertainty of vapor sorption isotherms increase with increasing pressure without following a specific trend with temperature for both CV (25°C < 45°C < 35°C) and overall error (45°C < 25°C < 35°C) (see Figure A19A-B). The sensitivity of the concentration to

polymer mass (and other variables) will be further explored during the analysis of variable error contributions (see Section 5.4.4). Overall, the uncertainty of vapor sorption data spans from 2.07% (at 25°C, 0.012 MPa) to 5.85% (at 45°C, 0.018 MPa).

5.4.2. Case Study 2: gas sorption in a triptycene-based polybenzoxazole

The uncertainty of CO_2 sorption isotherms in a triptycene-containing polybenzoxazole (TPBO-0.25) at 5, 20, 35, and 50°C with pressures ranging from 0 up to around 3.5MPa is shown in Figure 29 [58]. The total uncertainty spans from 5.7% (at 5°C, 2.62 MPa) to 9.6% (at 35°C, 3.23 MPa) of the total concentration value. The uncertainty analysis accounts for all variables listed in Table 11.

In the case of gas sorption, at a given temperature, CV increases with increasing pressure and, at any given pressure, it increases with increasing temperature (see Figure A20A). However, the absolute error appears independent of temperature (see Figure A20B). Specifically, at pressures up to 1 MPa, the CV associated to CO_2 sorption in TPBO-0.25 varies from 2.3% to 4.0% (73% increase) between the 5 and 50°C isotherms respectively, while the uncertainty changes from $\pm$ 2.81 to $\pm$ 2.65 cm^3(STP)/cm^3(pol) (i.e., 6% decrease). The change in CV with temperature becomes smaller at higher pressures. At 2.5 MPa and in the same temperature range as before, CV changes from 5.5% to 7.6% (40% increase) while the uncertainty changes from $\pm$ 9.31 cm^3(STP)/cm^3(pol) to $\pm$ 7.17 cm^3(STP)/cm^3(pol) (i.e., 23% decrease). The increase in CV with temperature is not due to a change in absolute uncertainty, but rather to the fact that sorption decreases by about 50% with

increasing temperature, due to negative sorption enthalpy [58]. This result suggests that changing temperature, at least at moderate pressures, does not have a large impact on the uncertainty.

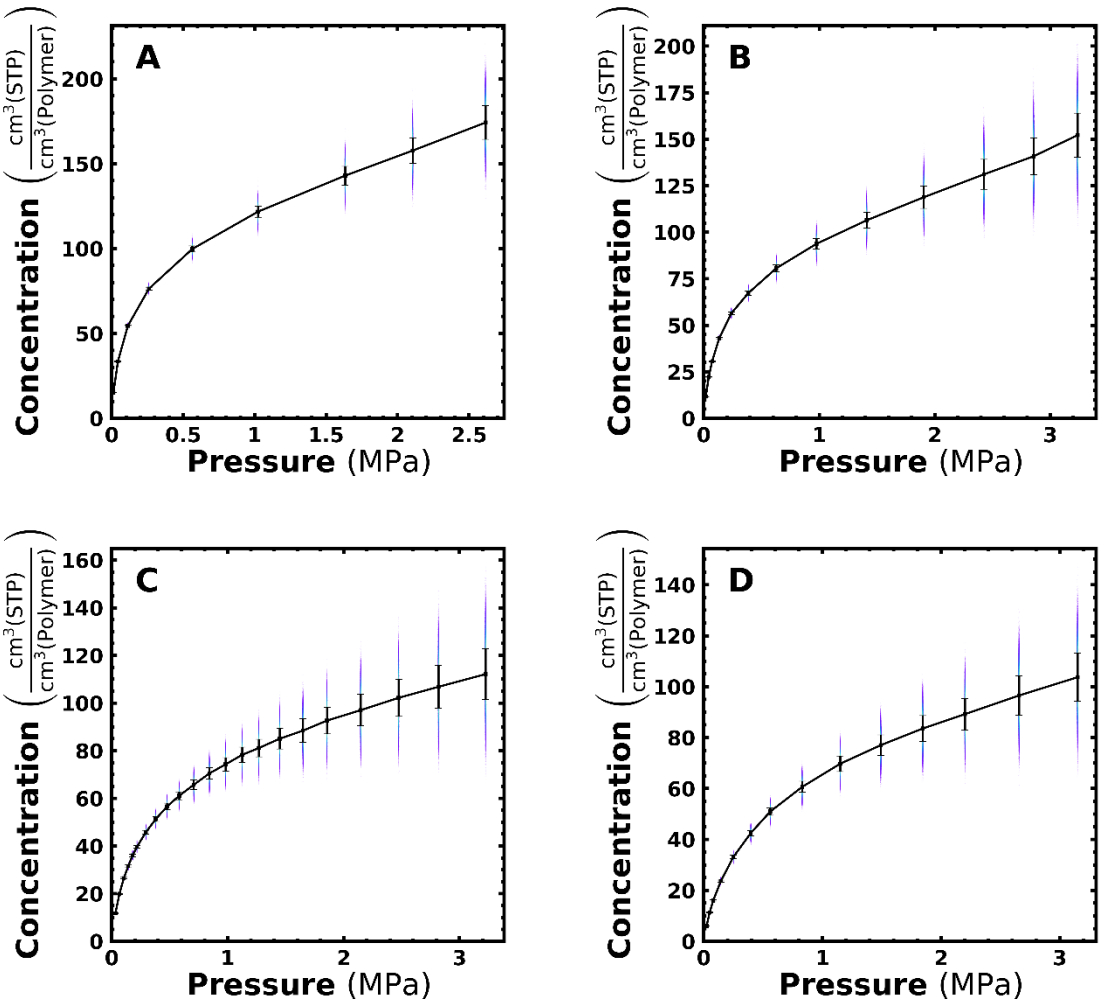


Figure 29: *Experimental CO_2 sorption isotherms in TPBO-0.25 at A) 5°C, B) 20°C, C) 35°C, and D) 50°C as a function of pressure. Error bars are calculated via linear error propagation, and are superimposed over the corresponding Monte Carlo error propagation (100,000 iterations). Lines are drawn to guide the eye. Experimental data are from ref. [58].*

5.4.3. Comparison between the MCEP and LEP methods

Monte Carlo error propagation, when performed with a sufficient number of iterations, is both more robust to large measurement errors and more precise compared to linear error propagation, at the cost of being relatively computationally expensive. This is even more true in cases where cubic equations of state must be solved multiple times per iteration, as in the case of gas sorption measurements. Specifically, in this work, performing the Monte Carlo analyses on a single six core processor required about eight seconds per step per million iterations for vapor sorption calculations, and 400 seconds per step per million iterations for gas sorption calculations. The reason for this discrepancy between the computational cost of the two setups is primarily due to the equations of state used (i.e., Peng-Robinson for gas sorption and ideal gas for vapor sorption). Propagating error linearly, in contrast, is near-instantaneous for both vapor and gas sorption measurements (i.e., a few microseconds using the same processor) once derivatives have been calculated. Therefore, it is necessary to evaluate if linear error propagation can accurately approximate the MCEP methods in an effort to avoid time-intensive calculations. To do this, uncertainty associated to vapor and gas sorption data were propagated using the Monte Carlo method in several independent runs, that is, by increasing the number of iterations by an order of magnitude in each run. The Monte Carlo results were then compared to the outcomes of linear error propagation.

Figure 30A-B show the percent difference between Monte Carlo and linear error propagation for every step in the vapor and gas sorption isotherm, respectively. Interestingly, the percent difference between MCEP and LEP methods in the vapor sorption apparatus approaches 0.05% at around 1M iterations and does not appear to decrease further (see Figure 30A). In contrast, the gas sorption apparatus was limited by the amount of time the computation could be run and did not approach a constant value, but instead had a percent difference of around 0.1% at 1M iterations (see Figure 30B). If a sufficient number of Monte Carlo iterations have been run, the average percent difference should become constant with additional iterations.

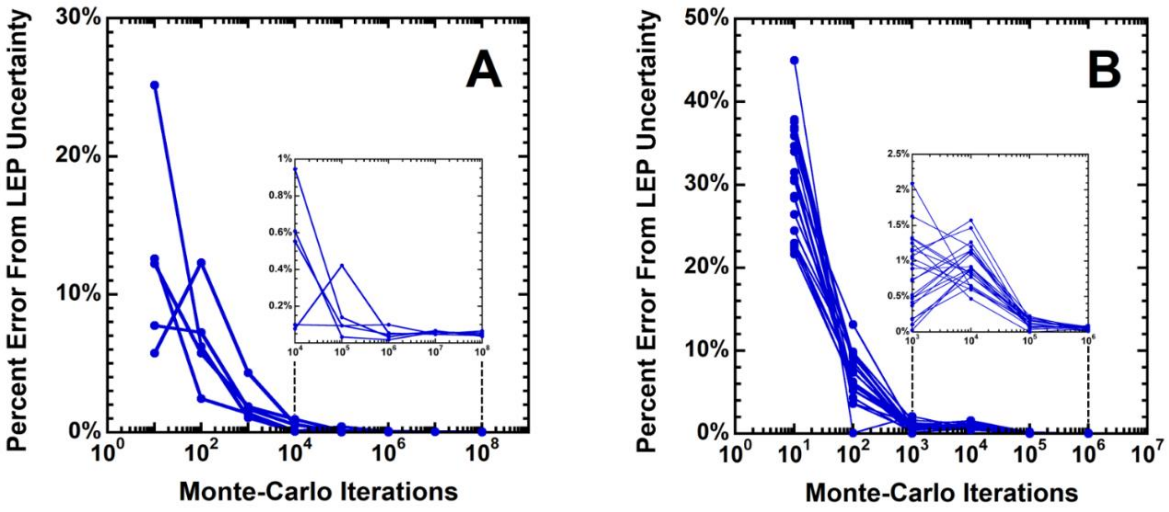


Figure 30: *Percent difference between Monte Carlo and linear error propagation for every step in the isotherm. A) Methanol in PBI at 35°C and B) CO_2 in TPBO-0.25 at 35°C. Each line represents a different pressure step.*

Since the linear error propagation library used in this work accounts for functional correlation, the 0.05% difference between the Monte Carlo and linear methods seen in the vapor sorption apparatus can be attributed to the nonlinear uncertainty response which

LEP does not account for, but MCEP does. Therefore, when measuring gas and vapor sorption/adsorption in polymers with the barometric (i.e., pressure decay) method, linear error propagation can be safely used, at least for typical experimental conditions.

If Monte Carlo error propagation is the only method available due to cumbersome derivative calculations, or if error propagation software is not available, Figure 30 provides useful guidelines for determining how many iterations are necessary to achieve equivalent results to that of LEP, or at least an acceptable approximate thereof.

5.4.4. Contribution of individual variables to gas/vapor sorption uncertainty from linear error propagation

In this Section, the contribution of the individual experimental variable to the overall uncertainty associated to gas and vapor sorption data, defined by Equation 19, will be assessed. This information (see Figure 31 and Figure 32) may be helpful to optimize the design of an experimental apparatus, as well as to devise the best standard operating procedure to generate the highest quality data possible.

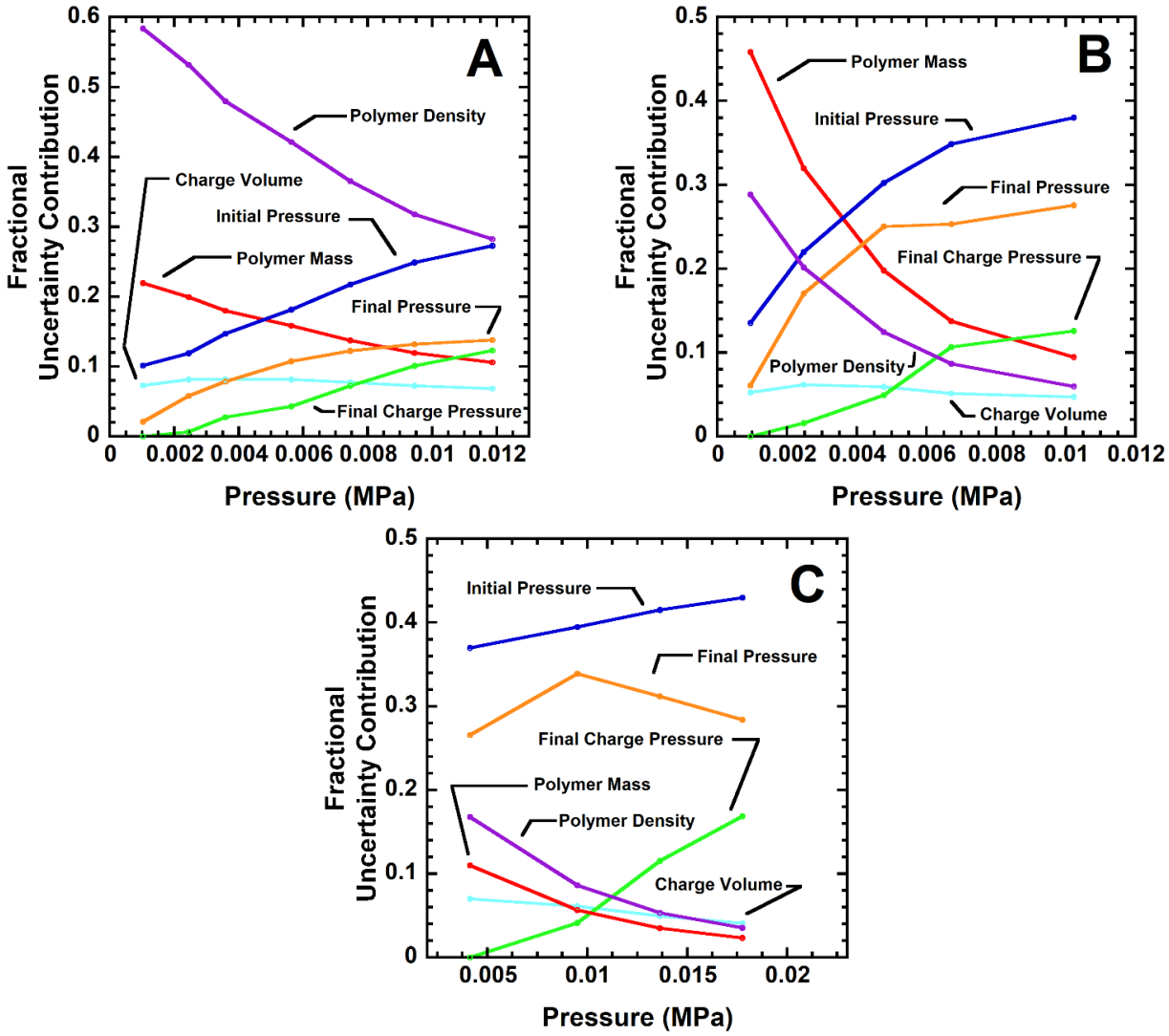


Figure 31: *Individual linear error propagation uncertainty contributions to experimental methanol sorption isotherms in PBI at A) 25°C, B) 35°C, and C) 45°C. Contributions of temperature and sample chamber volume are negligible and, for this reason, they are not shown.*

Using the LEP uncertainty contribution analysis, it can be shown that, at least when the apparatus available in our laboratory is used (see Figure 5A), vapor sorption experiments acquire most of their error from polymer density, polymer mass, and initial pressure measurement (see Figure 5A, step 2), that is, the pressure in the charge chamber before each step begins. Initially, the polymer density is the dominating contributor to error (see Figure 31A-B-C).

However, as the isotherm progresses and the number of pressure measurements used in the isotherm increases, polymer density and mass quickly stop contributing to the total error as much as other variables, such as the initial pressure (see Figure 5B, step 2). This is a direct result of the way pressure measurements affect subsequent steps in the isotherm. Indeed, while polymer density and mass are used once at the end of each sorption step's calculation and are not re-used or re-measured between steps, the initial pressure of previous steps affect subsequent steps and its contribution propagates throughout them, allowing even small initial contributions to error to become much more significant after multiple sorption steps have been completed. This is consistent with the behavior of the other pressure measurements (such as final charge pressure), whose contribution to the total uncertainty increases as additional sorption steps are run.

Other variables, such as the volume of the charge chamber, contribute a near-constant amount to the overall uncertainty, but decrease in their fractional contribution as other variables increase in their own contributions. Interestingly, the contribution of the dry polymer density and mass initially appear less relevant at 45°C compared to the 25°C and 35°C isotherms. This cannot be due to the density and mass values used in the experiments, as the sample masses increase in the order 35°C (0.0036g) < 45°C (0.0056g) < 25°C (0.0074g) and density is assumed constant throughout all isotherms, although this does justify the small increase in polymer mass contribution from the 25°C to 35°C isotherms. One main difference in the 45°C isotherm is the pressure for the first sorption

step (i.e., 0.00413 MPa), which is roughly 4 times larger than the step 1 pressures observed in the 25°C (i.e., 0.00102 MPa) and 35°C (i.e., 0.000951 MPa) isotherms, as well as the higher average pressure step size, which is around twice as large for the 45°C isotherm ($\Delta P = 0.00454$ MPa per step) as compared to the 35°C and 25°C isotherms ($\Delta P = 0.00232$ MPa and 0.00207 MPa per step, respectively). This is also reflected in the high initial pressure contributions in the 45°C isotherm, step 1, as compared to the step 1 contributions in the 35°C and 25°C isotherms. Obviously, this is consequence of the methanol vapor pressure being an increasing function of temperature (methanol activity is evaluated as P/P^*, where P is the equilibrium final pressure and P^* is the methanol vapor pressure at the experimental temperature). Finally, as expected, the final charge pressure, that is, the final pressure in the charge chamber at the end of the sorption measurement, does not contribute to the first step, as it is only used to calculate moles of gas sorbed during the next steps.

In striking contrast, uncertainty in gas sorption experiments is dominated by the chamber volumes (see Figure 32). The sampling and charging chamber volumes collectively account for at least 80% of the total isotherm uncertainty at any step for all gas sorption isotherms.

The pressure transducer's contributions do not increase enough with increasing pressure, despite appearing to follow a similar trend as in the vapor sorption apparatus. These results are essentially due to the comparatively small pressure differences observed

between the beginning and end of sorption steps in the gas apparatus compared to the vapor apparatus. Therefore, small uncertainty in the sampling chamber volume will vastly alter the number of moles calculated by the Peng-Robinson equation of state, that is, the molar balance used to generate sorption data.

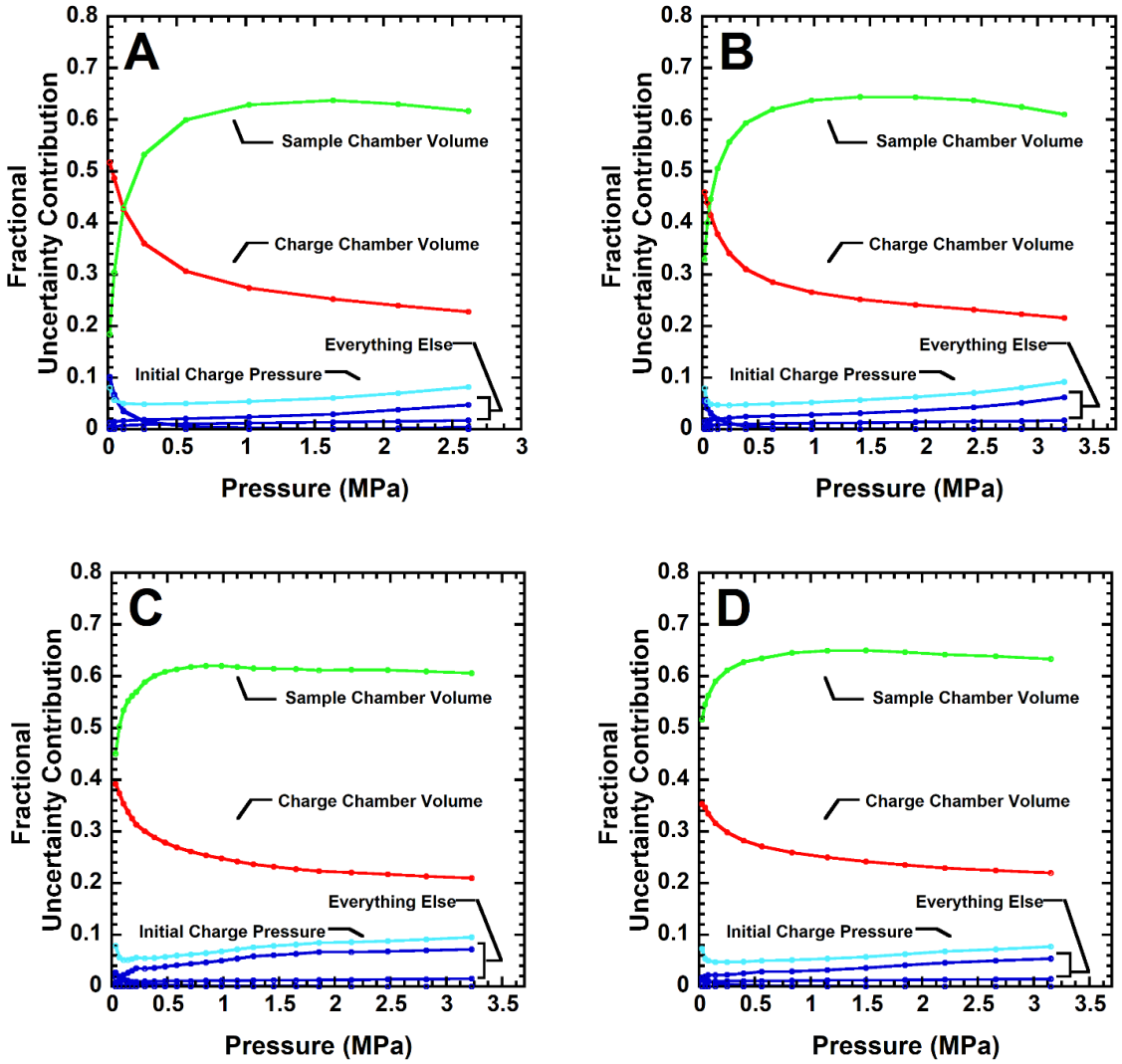


Figure 32: *Individual linear error propagation uncertainty contributions to experimental CO_2 sorption isotherms in TPBO-0.25 at A) 5°C, B) 20°C, C) 35°C, and D) 50°C. Dark blue plots denote contributions that provide a negligible contribution to the overall uncertainty, including final charge pressure, Pitzer acentric factor, penetrant critical temperature, penetrant critical pressure, polymer density, polymer mass, and final sample chamber pressure.*

Therefore, while in the vapor sorption apparatus the sampling chamber volume does not have a significant effect on the total uncertainty and thus isn't included in the contribution plot, it is the leading contributor to uncertainty in gas sorption measurements. This is due to two key design aspects that distinguish how sorption is measured in the two apparatuses. In the vapor sorption apparatus, the valve between the sampling and charge chambers is left open during the experiment, leading to the charge chamber accounting for most of the observed volume during pressure decay. Moreover, for the apparatus used in this laboratory, the sampling chamber volume is nearly one-fourth that of the charge chamber (see Table 11). In contrast, the valve between the charge and sampling chambers is closed during gas sorption measurements. Moreover, the volumes of the charge and sampling chambers are comparable in the latter case (see Table 12).

As mentioned previously, in the gas sorption apparatus, chamber volume uncertainties contribute significantly to the overall uncertainty of concentration. Unlike other contributors to concentration error, which are either inherent to the devices being used (e.g., pressure transducers, temperature controllers), the materials involved in the experiment (e.g., polymer density), or measured constants (e.g., gas critical properties, gas molecular weight), the accuracy of the chamber volumes is controllable in that it can be improved by the operator. Indeed, while the accuracy of the pressure transducer or temperature controller is given by the factory which produced it, the volumes are measured by the operator through subsequent gas expansions (i.e., the Burnett method

[104]), therefore more accurate measurements will lead to more accurate estimate of the volumes. If the chamber volumes used in the calculation of CO_2 sorption in TPBO-0.25 at 35°C were to be made twice as accurate (that is, the uncertainties were cut in half), the overall uncertainty of concentration would improve by 40.6% on average for all steps in the isotherm, and would reduce the percent uncertainty contribution of both chamber volumes by 24.8% (at step 4, lowest change) to 35.5% (at step 22, highest change), with an average reduction of 29% (see Figure 33). This sensitivity analysis shows the efficacy of improving the accuracy of volumes calibration, especially when considering that an improvement to these values can be useful even if done after sorption experiments have been completed, as the pressure data collected during the experiment remain valid if volumes are re-calibrated to gain higher accuracy. In Figure 33, the contributions of the single experimental variable to the overall uncertainty of CO_2 sorption data in TPBO-0.25 at 35°C is compared by assuming the actual uncertainty of the volumes (continuous lines) and by halving it (dashed lines), while keeping all other uncertainties unchanged.

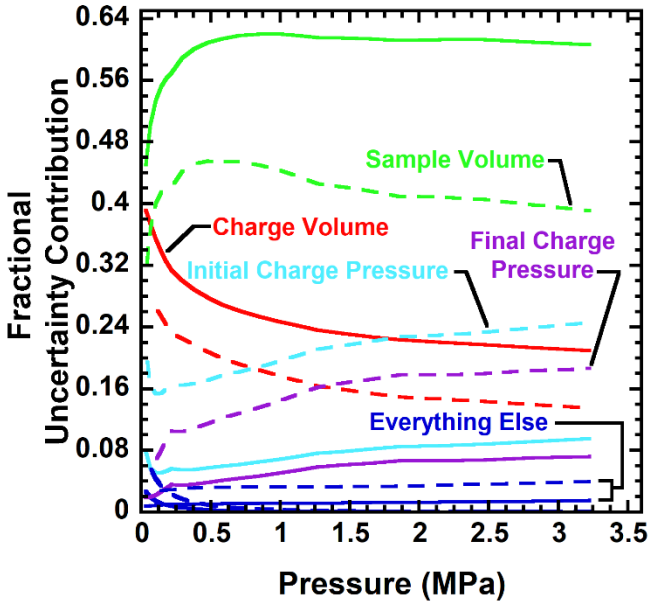


Figure 33: *Fractional uncertainty contributions of CO_2 sorption in TPBO-0.25 at 35°C using the true chamber volumes uncertainty (continuous lines, $\sigma_{V_{Charge}}$ = 0.04 cm^3, $\sigma_{V_{Sampling}}$ = 0.06 cm^3) and the halved chamber volumes uncertainties, (dashed lines, $\sigma_{V_{Charge}}$ = 0.02 cm^3, $\sigma_{V_{Sampling}}$ = 0.03 cm^3), while all other uncertainties remained constant. Lines are drawn to guide the eye. The chamber volumes are $V_C = 18.442\ cm^3$ and $V_S = 15.707\ cm^3$.*

Finally, to validate the legitimacy that MCEP and LEP can both be used to calculate the uncertainty, the convergence of uncertainty values must extend into the single variable contributions. This aspect is discussed in Section 5.4.5

5.4.5. Contribution of individual variables to gas/vapor sorption uncertainty from Monte Carlo error propagation

Uncertainty contributions from both LEP and MCEP methods matched for all variables involved in the calculation. The convergence of both methods for two significantly contributing variables are shown in Figure 34, where the uncertainty contribution of the charge chamber volume in the gas sorption experiment, and the uncertainty contribution of polymer mass in the vapor sorption experiment is compared between the two methods.

Specifically, in Figure 34 the percentage departure of MCEP from LEP is shown as a function of the number of Monte Carlo iterations. The percent difference between the variable's contribution obtained through each method reached near or below 1% after 10^5 iterations.

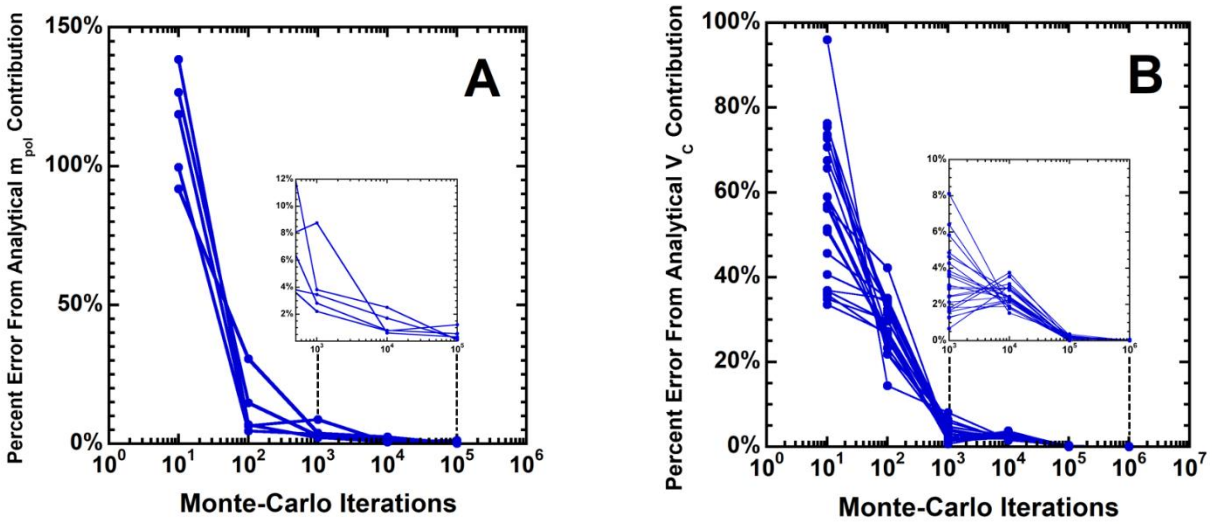


Figure 34: *Percentage deviation of MCEP method from LEP method in evaluating the contribution of a single experimental variable to the sorption experimental uncertainty as a function of the number of Monte Carlo iterations. A) Contribution of polymer mass to uncertainty of methanol vapor sorption in PBI at 35°C. B) Contribution of the charge chamber volume to uncertainty of CO_2 sorption in TPBO-0.25 at 35°C. The insert is shown to confirm that the two methods converge to the same result.*

As a result, each contribution to uncertainty as evaluated from the linear error propagation method is effectively equivalent to the Monte Carlo method and can be used in place of it without compromising contribution accuracy.

The analysis provided in this study confirms that not only the LEP and MCEP total uncertainties match for all cases discussed, but individual uncertainty contributions from

both methods also match, validating the use of results from either method in optimizing the accuracy of sorption experiments.

A summary of the uncertainties estimated with the Monte Carlo method is shown in Figure A21 (CO_2 sorption data in TPBO-0.25) and Figure A22 (methanol sorption data in PBI) of the Appendices.

5.4.6. Recommendations and best practices for accurate and reliable sorption measurements

In this section we report some final recommendations to get accurate and reliable gas and vapor sorption/adsorption data. Vapor sorption/adsorption measurements require a very accurate estimate of the dry polymer mass and its density. A large amount of polymer sample should be used when its sorption capacity is expected to be small. If this is not possible, we recommend the following best practices: *i)* large activity jumps should be considered between subsequent sorption steps; *ii)* the integral method should be used instead of the differential one, by pulling full vacuum between subsequent sorption steps; *iii)* the dead (i.e., unoccupied) volume in the sorption cell should be reduced as much as possible by inserting stainless steel beads, which are available in the commerce and whose volume is reported by the factory with high accuracy. An accurate pressure transducer and chamber volume calibration is recommended as well.

A very accurate chamber volume calibration is the key factor to getting reliable gas sorption/adsorption data. In any case, volume calibration should be run using the Burnett

(i.e., expansions) method and helium as service gas [104]. Gravimetric calibration, to be run by weighing the cell before and after filling it with a liquid whose density is known, is not recommended, as *i)* air bubbles may form inside the cell, which would introduce severe errors, *ii)* the liquid density may be sensitive to temperature, and *iii)* liquid droplets might inadvertently spill from the cell while pipetting.

It is well known that different samples of the same material may have vastly different sorption/adsorption properties. Since the scope of this study is to make sorption/adsorption data more comparable across laboratories and provide guidelines to propagate errors in lieu of repeating time-consuming experiments, it is important to show that the sample-to-sample variability is captured, at least in part, by the proposed error propagation method, and verify that uncertainty coming from sample-to-sample variability falls in the error bounds obtained from error propagation. As shown in the Appendices (Figure A23), two independent nitrogen sorption tests in TPBO-0.25 at 35°C and up to 35 atm were run on the same apparatus using two different virgin samples. The two datasets departed by about $\pm$5% of each other, which falls within the bound predicted by the error propagation method. It is worth noting as well that sample-to-sample variability can arise largely from systemic and nonrandom components (e.g., different synthesis methods). Therefore, samples prepared in different ways may potentially reside outside of the errors calculated using the error propagation methods discussed in this work, which only account for random error and do not include systemic

errors (with the exception of polymer density due to swelling, see Section A17, Appendices).

Another relevant point deserving some discussion is the correct determination of the final equilibrium pressure, which is essential to get reliable sorption/adsorption data. In the laboratory where this study was conducted, a given sorption step is considered to be at equilibrium when the pressure does not change for at least 50% of the time needed to first reach that final equilibrium value. For example, if the final equilibrium pressure is reached for the first time 24 h after the experiment started and it maintains that value for the next 12 h, after that time (i.e., 36 h) we consider the sorption step at equilibrium (see Figure A24). In both gas and vapor sorption systems, when equilibrium is reached, the pressure uncertainty (i.e., the pressure noise) at equilibrium falls within the uncertainty of the reading provided by the factory specifications (see Table 11 and Table 12).

The way the apparatus is evacuated and degassed is also considered a critical step during sorption/adsorption measurements. In the laboratory where this study was conducted, vacuum is pulled throughout the system until the transducers (which are recalibrated at the beginning of the sorption experiment when the vacuum is stable) indicate a pressure equal to zero and, starting from that moment (which is evaluated using the time-scale provided by automated data collection software), dynamic vacuum is maintained for the next 24 h before starting the sorption test. At that moment, all valves are closed and at the

system is left alone for 1h before starting the actual measurement, to identify any possible leaking.

5.5. Conclusions

A standard method to evaluate the experimental uncertainty of gas and vapor sorption/adsorption measurements in polymers is proposed and tested in a variety of operating conditions and using different experimental protocols. The individual influence of different experimental parameters, such as the mass and density of the polymer sample, the volume of the system, temperature, pressure, and equation of state parameters, on the total uncertainty associate to sorption/adsorption data is evaluated and discussed. The latter effort should help scientists design their experimental setup to generate data exhibiting the highest possible accuracy and make experimental data coming from different laboratories in the world easier to compare. Of equal importance, the validity of the linear error propagation method, generally used to evaluate the uncertainty of sorption/adsorption data, is demonstrated by a *vis-à-vis* comparison with the Monte Carlo statistical method. These results provide new knowledge of practical interest to researchers seeking to use configurational free volume to rationally design highly selective polymer membranes, as well as aid in their efforts to improve the tools needed to study them.

Chapter 6. Summary and Recommendations for Future Research

6.1. Summary

This dissertation provides a major step forward in understanding configurational free volume as a tool for advanced molecular separations. This project began with a study investigating bulky vapors, discovering that while conventional solution-diffusion polymers transport materials with the solubility and diffusivity contributions to selectivity working against each other, this was not the case for polymers which contained configurational free volume. In configurational free volume, the two components of selectivity worked together to provide an extremely high overall selectivity. A follow-up study revealed that this was not the case for light components (e.g., CO_2, CH_4, N_2), with these molecules likely residing below the configurational element size and not being subject to the same entropic restrictions as bulky vapors. It instead uncovered the mechanism by which configurational free volume improves selectivity for these light gasses. Further analysis of the limitations and best-practices of our instruments which measure polymer solubility were necessary to acquire data that was both comparable and accurate enough to make these aforementioned conclusions, which lead to an entirely separate work, as well as multiple methods to acquire solubility uncertainty and design recommendations and insights for sorption apparatuses. Using the strategies learned in improving these existing measurement techniques, we then developed an entirely new one which measures polymer dilation. This new analysis

technique applies computer vision, a sub-field in artificial intelligence, in combination with uncertainty analysis techniques to measure dilation isotherms and kinetics with superior accuracy and, unlike other dilatometry techniques, both automation and parallelism. After doing similar work to understand the capabilities and sources of both systematic and random error of the instrument, we use this tool to uncover the final aspect that covers the surface level of configurational free volume knowledge: plasticization and swelling resistance. At this point in the project, the surface level understanding of configurational free volume has almost been understood. Specifically, upper bound behavior, aging, and harsh environment resistance had been characterized before the start of this work. During this work, the individual components of permeability (solubility and diffusivity) were investigated, and a molecular level understanding was achieved for the selection mechanisms that configurational elements provide, as well as the anomalous way in which it changes as a function of molecule size. Finally, this dilation apparatus would provide the accuracy necessary to investigate the opposing component to physical aging: swelling and plasticization. After reproducing existing work to verify the apparatuses accuracy and consistency, dilation isotherms were quantified for TPBO and its precursor TPHI, revealing that configurational free volume and thermal rearrangement synergize to produce swelling resistance against plasticizing agents such as CO_2.

6.2. Future work

This research provides a surface level start into the fundamental understanding of configurational free volume, but it is indeed only the start. There are many open threads to be pursued.

First, the only element considered in this work which generates configurational free volume is triptycene, however, there are many other molecular structures known to generate permanent free volume elements inherent to the molecular configuration of the polymer. Examples of these are pentiptycene and benzotriptycene, which have larger internal element sizes. These structures could be used to generate materials which target individual "challenging" separations that are currently unsolved or stagnant. As a product of this, investigation into the sizes of molecules which experience entropically driven sorption as a function of the structure which generates the configurational elements is key to further understanding of this strategy. This contrasts with the strategy utilized in this work, which varies the *amount* of presence of one kind of structure, in this case, the triptycene content.

Secondly, the end of Chapter 2 gave us insight into the almost zeolite-like transport behavior that occurs when one component being separated is larger than the configurational element size and another component is smaller. Chapter 3 demonstrated behavior when both components are smaller than this element size. A study that seeks to complete this picture would need to seek out two main tasks:

1. Probe the dilation characteristics during the separation of a real mixture of two molecules definitively larger than the configurational free volume element size generated by triptycene. This information would complete the picture of plasticization resistance due to configurational free volume in mixed conditions.
2. Rather than pure vapor sorption data, investigate real mixed gas, mixed vapor, and possibly even mixed liquid transport, which would further bridge the gap between academic pursuits and practical applications. This achievement and subsequent insights would provide a cornerstone for affirming and understanding the extent to which the zeolite-like behavior previously seen can be utilized.

The first task could also be probed by the relaxation time found through fitting vapor sorption kinetics to the Berens Hopfenberg model as an alternative to (or ideally in addition to) polymer dilatometry. For pure components, these vapor kinetics experienced a dramatic shift once penetrant sizes met and exceeded that of linear propanol. A longer relaxation time (k_r) paired with little contribution from the relaxation equilibrium parameter (M_r) would greatly support the behavior observed in the study presented in Chapter 2. The second task would be particularly interesting if done with pentiptycene or benzotriptycene elements, as the sizes of molecules in liquid applications (particularly organic solvent reverse osmosis i.e., OSRO) could possibly reveal separations where the configurational free volume element size effectively divides the two penetrants.

These two projects mainly arise out of the need to investigate competitive (and other) effects that would show up in real applications, as well as confirm the resistance to harsh environments that have previously only been investigated (until this work initial light on it via mixed-gas dilation) for pure components.

Appendices

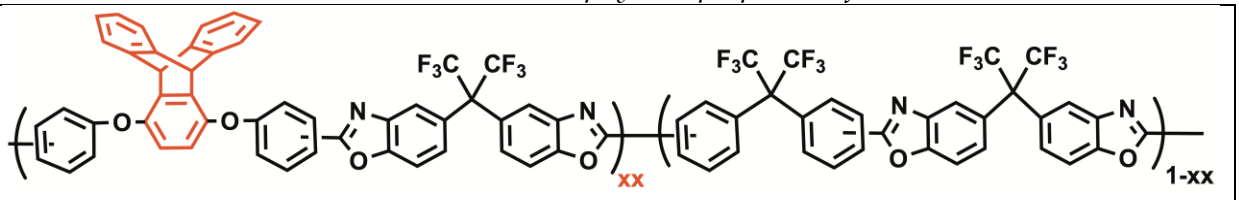
A1. Polymer Synthesis Protocols

For the polymers prepared in Chapter 2, triptycene dianhydride (TPDAn) monomer was prepared following our previously reported procedure and dried at 160 °C overnight under vacuum before use [22]. The poly(o-hydroxyimide) copolymer precursor containing 25 mol% triptycene unit (TPHI-0.25) was synthesized via polycondensation of TPDAn, 6FDA, and 6FAP in 0.25:0.75:1 molar ratio using the solution imidization method, as reported in a previous study [20]. Films of TPHI-0.25 precursor were prepared via solution casting. A 7 wt% polymer solution in DMAc was filtered with a 0.45 μm Teflon syringe filter before casting onto a leveled glass plate. Films were formed after drying under an infra-red lamp (~60 °C) overnight. Following this procedure, the nascent membranes were peeled off and dried at 160 °C in a vacuum oven overnight to remove any residual solvent. The subsequent thermal rearrangement conversion to polybenzoxazole is described in the main paper. The final films (TPBO) were ~130-260 μm thick [20]. Full conversion of the pristine co-polyimide film to the PBO form was verified via TGA and FTIR. Details are reported in ref. [20].

The array of TPBOs in used in Chapter 3 were synthesized using the same protocol [20]. Flat, free standing films of the triptycene-containing co-polyimides were thermally rearranged at 300°C for 2h and then at 450°C for 30 min, under nitrogen purge, to form fully converted triptycene-based polybenzoxazoles (TPBOs). The TPBOs structure for

each triptycene content is shown in Table A1, along with some relevant structural and physical properties.

Table A1. *Structure and physical properties of TPBOs.*



triptycene molar content (xx)	*density* (g/cm³)*	*T_g (°C)*	*FFV§ (%)*	*d-spacing† (Å)*	*%TR conversion‡*
25%	*1.393 ± 0.002*	*> 400*	*22.6*	*6.4*	*100*
50%	*1.369 ± 0.015*	*> 400*	*20.5*	*6.6*	*100*
75%	*1.346 ± 0.016*	*> 400*	*18.9*	*7.0*	*100*
100%	*1.324 ± 0.004*	*> 400*	*17.4*	*7.2*	*100*

** density was determined at room temperature using an Archimede's balance and water as the buoyant fluid. The experimental uncertainty was calculated from the standard deviation of 6-8 independent measurements.*

§ FFV was calculated using the group contribution method [213].

† d-spacing was calculated from WAXD experiments [20].

‡ full (i.e., 100%) thermal conversion to TPBOs was confirmed by FTIR spectroscopy [20].

In Chapter 4, synthesis was conducted using a slightly modified method. Triptycene dianhydride (TPDAn), 4,4′-hexafluoroisopropylidene bisphthalic dianhydride (6FDA), and 2,2′-bis (3- amino-4-hydroxyphenyl) hexafluoro propane (6FAP) was reacted via a condensation polymerization reaction to form triptycene-containing poly(o-hydroxyimide) copolymer (TPHI-x, where x = 25%, 50%, 75%, and 100%). As an example, TPHI-0.75 was prepared as follows: 6FAP (2.1262 g, 5.7 mmol) was stirred with m-cresol (10.6 mL) in a flame-dried 3-necked flask fitted with a mechanical stirrer under nitrogen flow, then, TPDAn (2.5 g, 4.3 mmol) and m-cresol (2 mL) was added while the mixture

was maintained at 120 °C until complete dissolution. Then, the heating mantle was removed, and 6FDA (0.6464 g, 1.4 mmol) was added. The reaction was left to progress at room temperature for 24 h under N_2; the viscous co-polyamic acid was then converted to the triptycene-based poly(o-hydroxyimide) copolymer via the solution thermal imidization method by adding isoquinoline (0.4 mL) as the catalyst and toluene (5 mL) for azeotropic removal of water at 180 °C for 12 h. The reaction product was precipitated into a 1:1 methanol-water mixture to obtain a solid polymer product in chunks, indicating a high molecular weight. The product was filtered, rinsed with methanol, and dried in a vacuum oven at 180 °C for 12 h. ^{1}H NMR was used to confirm the structures of the triptycene-based co-polyimides.

To prepare polymer film samples of these TPHIs, which will eventually be thermally treated to produce the triptycene containing polybenzoxazole (TPBO) polymer, a 7 % w/v solution of TPHI-x in NMP was filtered using a 0.45μm PTFE syringe filter on to a leveled glass plate. The resulting free-standing film formed after slow evaporation of NMP under an infrared lamp at 70 °C for 24h was dried in a vacuum oven at 180 °C for 12 h to remove any residual NMP solvent. This precursor TPHI-x film is then thermally rearranged by inserting it between two porous ceramic plates, placing it in a muffle furnace (Thermolyne Type 479) under N_2 flow, and allowing it to sit for 15 minutes before applying heating to flush out any oxygen from the system. The furnace was then ramped at 10 °C min^{-1} until reaching 350 °C and was maintained at this temperature for

2 h. Finally, the furnace was ramped at 50 °C min^{-1} to 450 °C, where it was held for 30 min to form triptycene containing polybenzoxazoles (TPBOs). Afterward, the muffle furnace was cooled to room temperature at a cooling rate of 10 °C min^{-1}. The complete thermal rearrangement of TPBO-x was confirmed with FTIR.

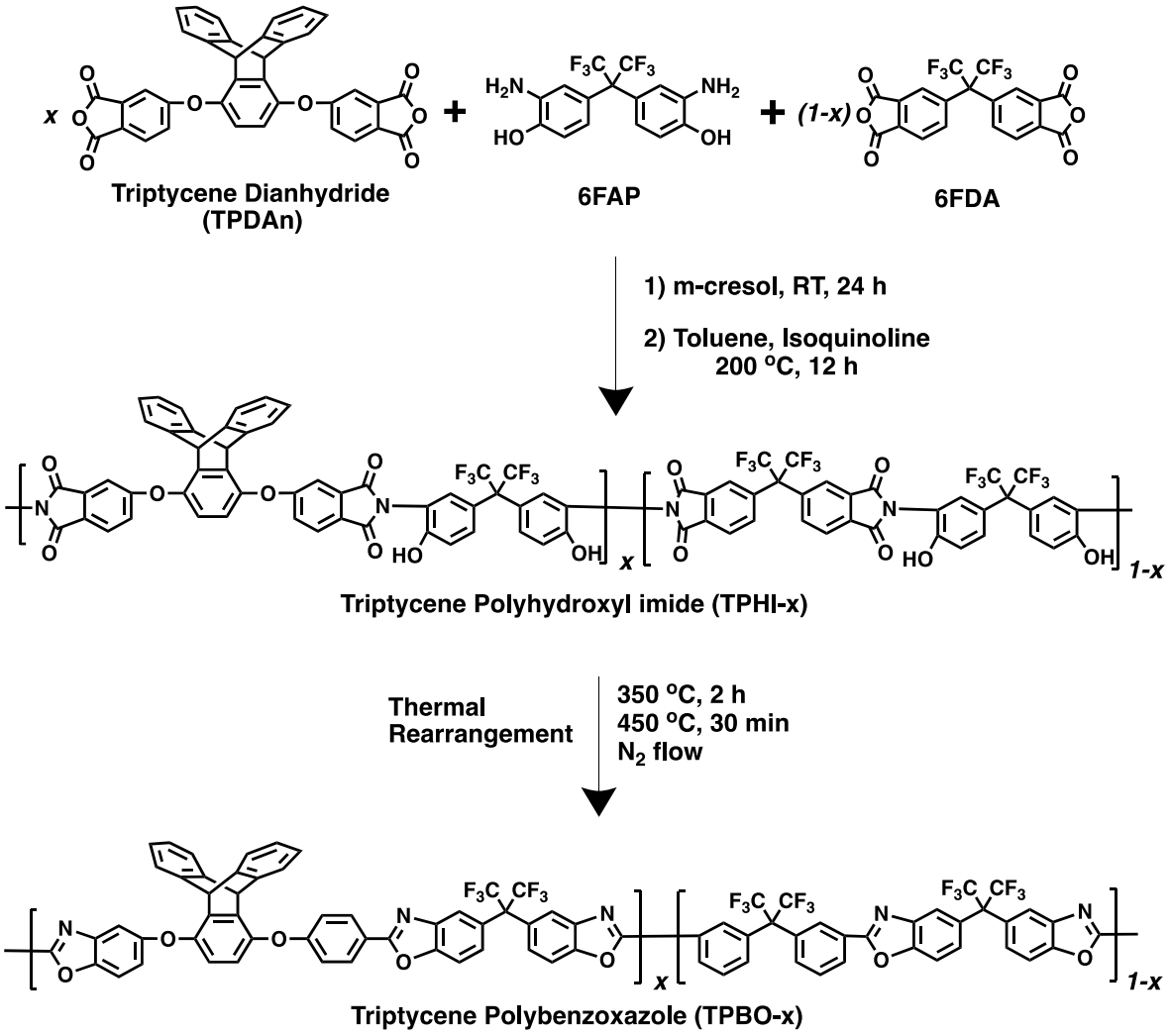


Figure A1: *Synthetic route for producing triptycene containing polyhydroxyimide (TPHI) and triptycene containing polybenzoxazole (TPBO).*

A2. Comparison between water vapor isotherms in PIM-1 and TPBO-0.25

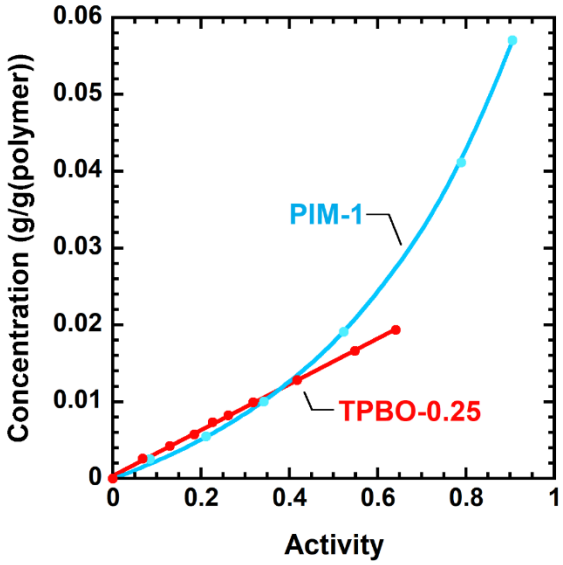


Figure A2: *Experimental water vapor sorption isotherms at 25°C in TPBO-0.25 (red circles) and PIM-1 (blue circles) as a function of water vapor activity. Continuous lines are the GAB model fittings. Data for PIM-1 are from ref. [109]*

A3. Zimm-Lundberg analysis for TPBO-0.25

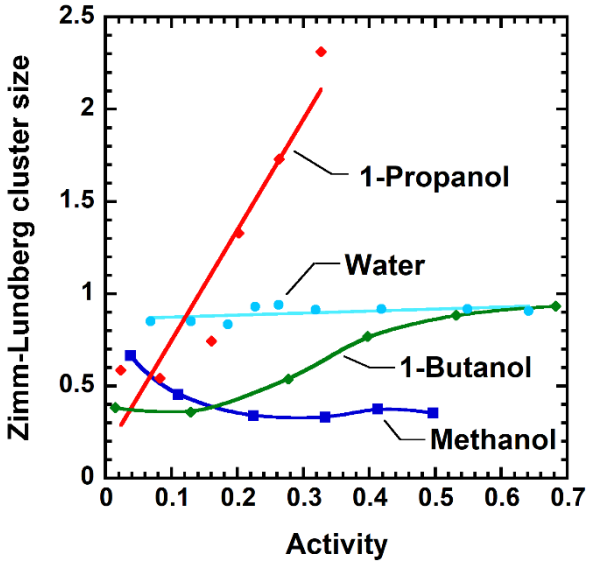


Figure A3: *Zimm-Lundberg predicted clusters size: methanol (solid blue squares), 1-propanol (solid red diamonds), 1-butanol (solid green diamonds), and water (solid sky circles) in TPBO-0.25 at 25°C. Lines are drawn to guide the eye.*

A4. Berens-Hopfenberg parameters

Table A2: *Berens-Hopfenberg fittings of 1-propanol diffusion in TPBO-0.25 at 25°C*

Step	*activity*	M_f/M_r	k_f	k_r	$\bar{D}_i$
1	0.023	0.658 ± 0.016	$1.49 \cdot 10^{-5} \pm 2.73 \cdot 10^{-7}$	$4.13 \cdot 10^{-5} \pm 2.12 \cdot 10^{-7}$	$8.29 \cdot 10^{-11} \pm 3.66 \cdot 10^{-11}$
2	0.083	0.626 ± 0.027	$5.60 \cdot 10^{-5} \pm 1.59 \cdot 10^{-6}$	$1.78 \cdot 10^{-5} \pm 3.38 \cdot 10^{-7}$	$3.12 \cdot 10^{-10} \pm 1.38 \cdot 10^{-10}$
3	0.161	1.888 ± 0.020	$2.43 \cdot 10^{-6} \pm 7.14 \cdot 10^{-8}$	$3.70 \cdot 10^{-5} \pm 1.93 \cdot 10^{-7}$	$1.36 \cdot 10^{-11} \pm 6.00 \cdot 10^{-12}$
4	0.202	0.929 ± 0.022	$1.12 \cdot 10^{-5} \pm 1.87 \cdot 10^{-7}$	$3.75 \cdot 10^{-5} \pm 2.53 \cdot 10^{-7}$	$6.22 \cdot 10^{-11} \pm 2.75 \cdot 10^{-11}$
5	0.263	0.590 ± 0.021	$4.68 \cdot 10^{-5} \pm 1.12 \cdot 10^{-6}$	$1.46 \cdot 10^{-5} \pm 2.22 \cdot 10^{-7}$	$2.61 \cdot 10^{-10} \pm 1.15 \cdot 10^{-10}$
6	0.327	0.763 ± 0.049	$4.25 \cdot 10^{-5} \pm 1.94 \cdot 10^{-6}$	$1.19 \cdot 10^{-5} \pm 7.61 \cdot 10^{-7}$	$2.37 \cdot 10^{-10} \pm 1.05 \cdot 10^{-10}$

Table A3: *Berens-Hopfenberg fittings of methanol diffusion in TPBO-0.25 at 25°C*

Step	*activity*	M_f/M_r	k_f	k_r	$\bar{D}_i$
1	0.038	53.27 ± 2.10	$0.00132 \pm 6.31 \cdot 10^{-6}$	$3.18 \cdot 10^{-5} \pm 2.66 \cdot 10^{-6}$	$6.59 \cdot 10^{-9} \pm 4.23 \cdot 10^{-10}$
2	0.110	23.57 ± 0.45	$0.00126 \pm 1.06 \cdot 10^{-5}$	$1.17 \cdot 10^{-5} \pm 7.39 \cdot 10^{-7}$	$6.32 \cdot 10^{-9} \pm 4.07 \cdot 10^{-10}$
3	0.224	9.34 ± 0.11	$0.00191 \pm 2.69 \cdot 10^{-5}$	$5.56 \cdot 10^{-6} \pm 1.55 \cdot 10^{-7}$	$9.57 \cdot 10^{-9} \pm 6.26 \cdot 10^{-10}$
4	0.333	3.83 ± 0.03	$0.00409 \pm 1.31 \cdot 10^{-4}$	$9.15 \cdot 10^{-6} \pm 2.77 \cdot 10^{-7}$	$2.05 \cdot 10^{-8} \pm 1.46 \cdot 10^{-9}$
5	0.413	2.06 ± 0.02	$0.00535 \pm 1.73 \cdot 10^{-4}$	$3.85 \cdot 10^{-6} \pm 8.35 \cdot 10^{-8}$	$2.68 \cdot 10^{-8} \pm 1.92 \cdot 10^{-9}$
6	0.497	1.95 ± 0.01	$0.01084 \pm 2.93 \cdot 10^{-4}$	$5.65 \cdot 10^{-6} \pm 8.67 \cdot 10^{-8}$	$5.43 \cdot 10^{-8} \pm 3.77 \cdot 10^{-9}$

Table A4: *Berens-Hopfenberg fittings of 1-butanol diffusion in TPBO-0.25 at 25°C*

Step	*activity*	M_f/M_r	k_f	k_r	$\bar{D}_i$
1	0.015	2.59 ± 0.11	$3.22 \cdot 10^{-5} \pm 4.28 \cdot 10^{-7}$	$6.22 \cdot 10^{-5} \pm 1.16 \cdot 10^{-6}$	$1.79 \cdot 10^{-10} \pm 7.92 \cdot 10^{-11}$
2	0.135	0.95 ± 0.06	$2.04 \cdot 10^{-5} \pm 8.95 \cdot 10^{-7}$	$4.20 \cdot 10^{-5} \pm 9.26 \cdot 10^{-7}$	$1.14 \cdot 10^{-10} \pm 5.04 \cdot 10^{-11}$
3	0.289	1.28 ± 0.06	$3.56 \cdot 10^{-5} \pm 9.79 \cdot 10^{-7}$	$1.95 \cdot 10^{-5} \pm 4.27 \cdot 10^{-7}$	$1.98 \cdot 10^{-10} \pm 8.77 \cdot 10^{-11}$
4	0.414	1.54 ± 0.08	$1.73 \cdot 10^{-5} \pm 5.31 \cdot 10^{-7}$	$3.10 \cdot 10^{-5} \pm 9.13 \cdot 10^{-7}$	$9.64 \cdot 10^{-11} \pm 4.26 \cdot 10^{-11}$
5	0.554	4.23 ± 0.40	$1.72 \cdot 10^{-5} \pm 5.18 \cdot 10^{-7}$	$3.05 \cdot 10^{-5} \pm 1.47 \cdot 10^{-6}$	$9.58 \cdot 10^{-11} \pm 4.24 \cdot 10^{-11}$
6	0.711	5.53 ± 0.55	$1.45 \cdot 10^{-5} \pm 1.95 \cdot 10^{-7}$	$5.10 \cdot 10^{-5} \pm 1.03 \cdot 10^{-6}$	$8.08 \cdot 10^{-11} \pm 3.57 \cdot 10^{-11}$

A5. Comparison among Berens-Hopfenberg (BH), modified Berens-Hopfenberg (MBH) and Fick's model fitting to methanol sorption kinetics in TPBO-0.25

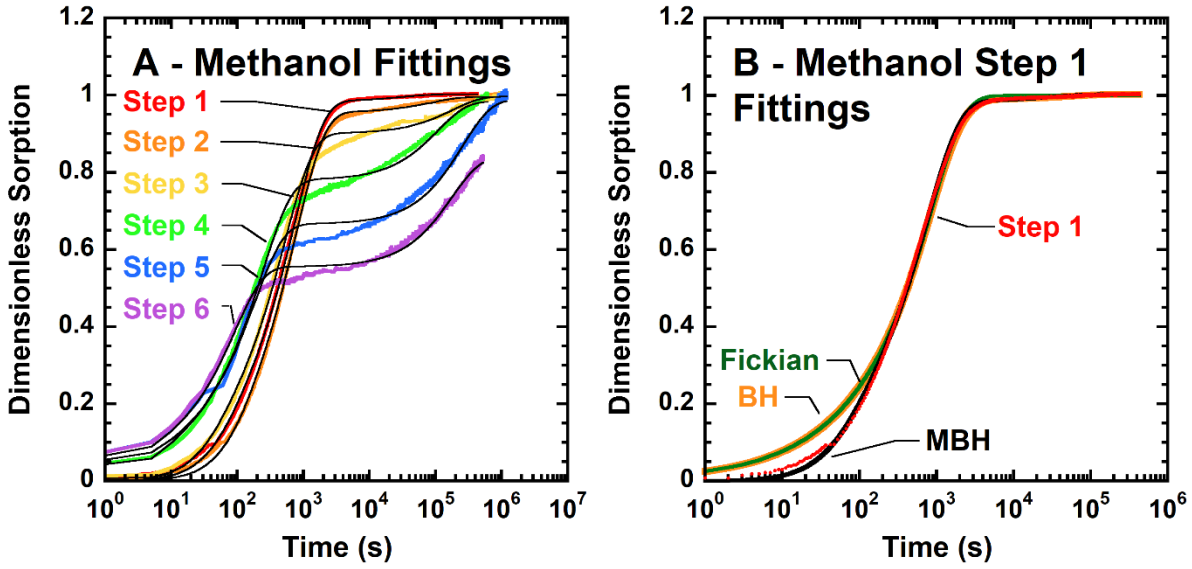


Figure A4: *A) Methanol sorption kinetics (in units of dimensionless sorption* $\left(\frac{M(t)}{M_\infty}\right)$*) plotted as a function of time on a logarithmic scale (colored lines). Experimental sorption kinetics were fitted to the modified Berens-Hopfenberg model (black lines). B) Alternative model results for step 1 (red points), namely Fickian model (green line), Berens-Hopfenberg model (yellow line) and the modified Berens-Hopfenberg model (black line).*

As shown in Figure A4B, the modified Berens-Hopfenberg model is more accurate than the unmodified Berens-Hopfenberg model and the Fickian model in describing methanol sorption kinetics in TPBO-0.25. While the modified Berens-Hopfenberg fittings predicts a diffusivity as $6.59 \cdot 10^{-9} \frac{cm^2}{s}$ (step 1), the unmodified version predicts $6.02 \cdot 10^{-9} \frac{cm^2}{s}$ (-9%), and the Fickian model predicts $5.82 \cdot 10^{-9} \frac{cm^2}{s}$ (-12%).

A6. Numerical considerations on the Berens-Hopfenberg model fitting

The Berens-Hopfenberg model and its modifications were implemented in Julia. In most languages, calculating gradients and hessians is done using finite differencing methods, i.e., by calculating functions at very close input values and approximating the gradient through the resultant slope between those two points. Unfortunately, when the difference between values becomes small enough, floating-point errors can negate the benefit of bringing the points closer together in an effort to increase gradient accuracy. For complex functions that change rapidly based on input changes, this can cause optimizers to miss local minima entirely and falsely believe they have converged, as is sometimes the case with the modified Berens-Hopfenberg model. Julia offers an inherent advantage as it can calculate gradients from arbitrary Julia-implemented functions exactly and without finite differencing.

The Berens-Hopfenberg model has a fundamental issue in that the optimization of parameters to experimental transient sorption data results in two major local minima which occur by swapping the Fickian and relaxation terms respectively, as the relaxation and Fickian contributions, when used standalone, produce similar plots. Assuming relaxation is usually the slower of the two (a reliable assumption in high T_g glassy polymers), it can help to simply initialize the optimization parameters with $k_f > k_r$ and $M_f = M_r$, however this is often not enough to reliably reach a global minimum. Optimization methods such as *particle swarm optimization*, which pick many random

starting points and allow each to converge independently, can also be used in an attempt to thwart this problem. However, it was found to be unreliable when used on the transient vapor sorption data collected in this study and when Monte Carlo resampling methods (namely bootstrapping) were applied to it. The best method we found to determine optimal and physically realistic model parameters can be described by the following example.

Let us consider methanol diffusion in TPBO. The experimental sorption kinetics require, to be modeled, the Berens-Hopfenberg model with a modification to the surface concentration and will usually contain around a few days to a few weeks of data. If the pressure transducer sampling rate during the experimental step is adjusted, then the step usually results in only a few thousand data points. These data points will not be evenly distributed. In total, it will require the optimization of 5 adjustable parameters, the only one of which we truly care about is k_f, as this is what allows us to determine the concentration averaged diffusion coefficient ($\bar{D}$) of the penetrant in the polymer. The fitting procedure included the following steps:

1. Calculate the dimensionless mass sorption data as a function of time i.e., $\frac{M(t)}{M_\infty}$.
2. Interpolate the data on a square-root scale for time such that it contains a lower number of data points. In this work we chose $n = 1000$ for interpolating the data. Most samples had 3000-4000 data points initially.

3. Fit the data for the simplest case: the Fickian model. Even if the model doesn't adequately describe the sorption, it gives us good initial guesses for M_f and k_f. Since the sorption is dimensionless, M_f should be close to unity if the step truly reached equilibrium and Fickian sorption is the only modeled contribution.
4. Assuming diffusion happens faster than relaxation, use the Fickian model fittings as the initial parameters for the Berens-Hopfenberg fitting, starting M_r and k_r as some value lower than that of their Fickian counterparts. In this study, we chose $\frac{M_f}{10}$ and $\frac{k_f}{10}$.
5. Use these four fitted parameters as the initial parameters for the modified Berens-Hopfenberg model, starting β as some low value that would certainly affect the sorption predictions initially, which gives the optimizer the opportunity to adjust it to better match the data, while already having all other parameters at least in the correct ballpark.

A7. Peng-Robinson Parameters Used in this Work

Table A5: *Peng-Robinson parameters used to calculate gas sorption from pressure data.*

	$\boldsymbol{M_W}\ \left(\frac{\boldsymbol{g}}{\boldsymbol{mol}}\right)$	$\boldsymbol{T_c}\ (\boldsymbol{K})$	$\boldsymbol{P_c}\ (\boldsymbol{atm})$	acentric factor $\boldsymbol{\omega}$
CO_2	44	304.19	72.8	0.228
CH_4	16.04	190.8	45.79	0.012
N_2	28.01	126.2	33.5	0.04

A8. Pure CO_2, CH_4, and N_2 sorption isotherms at multiple temperatures and triptycene molar content

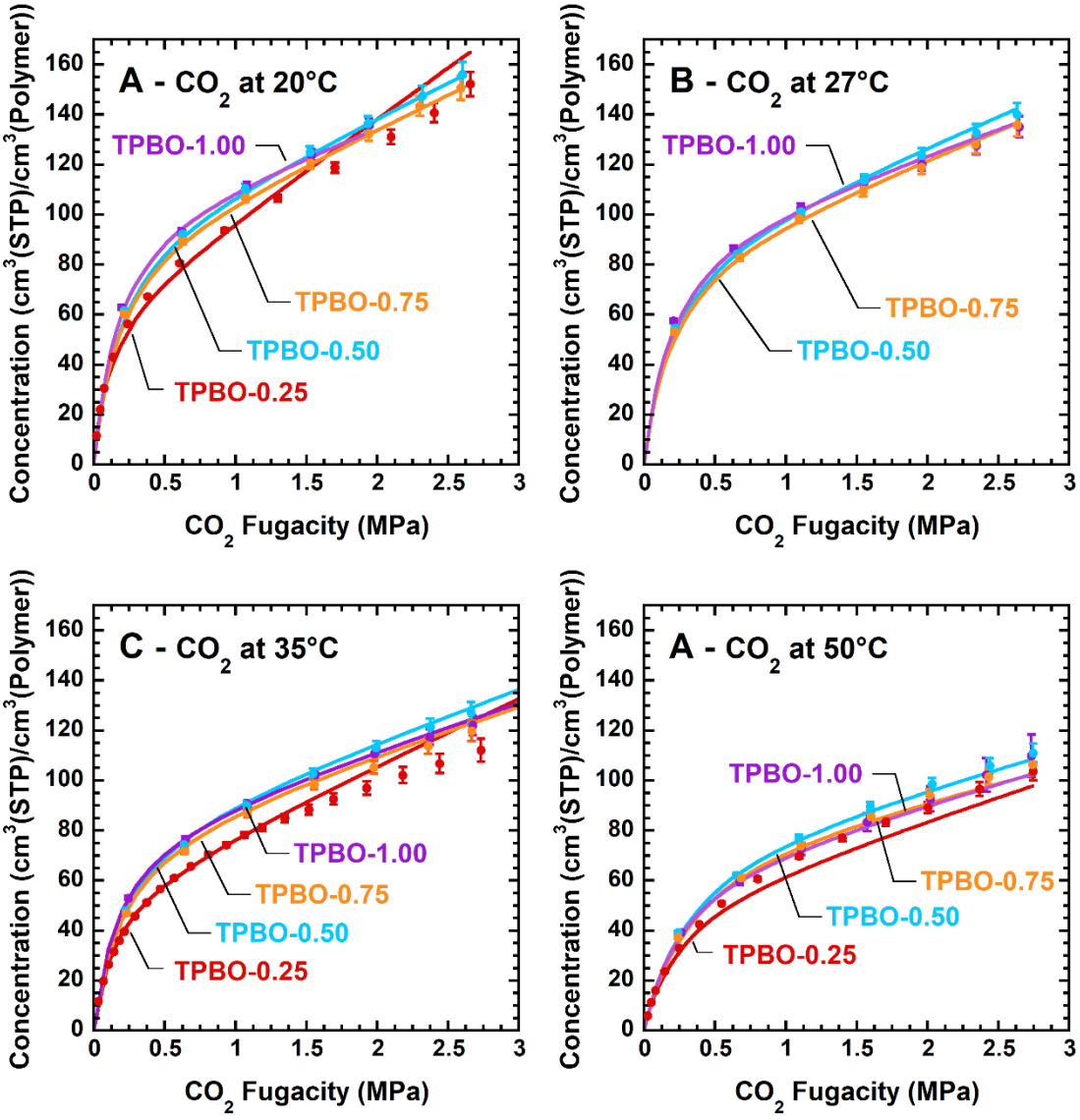


Figure A5: *CO_2 sorption in TPBOs at varying temperatures ranging from 20°C to 50°C taken at pressures up to 3 MPa. Solid points represent experimental data, continuous lines represent the dual mode fitting. Error bars were calculated using linear error propagation [96,98].*

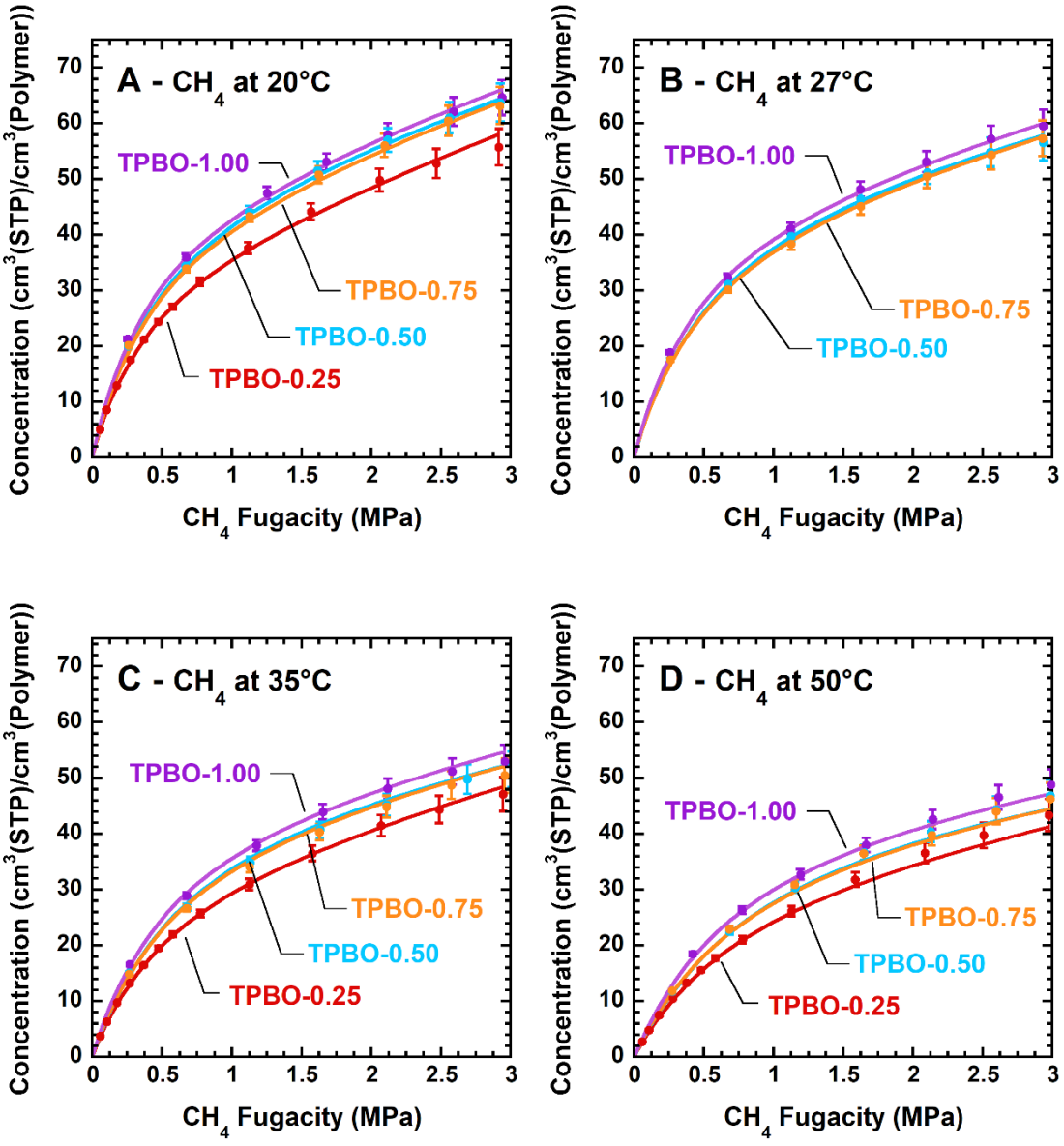


Figure A6: *CH_4 sorption in TPBOs at varying temperatures ranging from 20°C to 50°C taken at pressures up to 3 MPa. Solid points represent experimental data, continuous lines represent the dual mode fitting. Error bars were calculated using linear error propagation [96,98].*

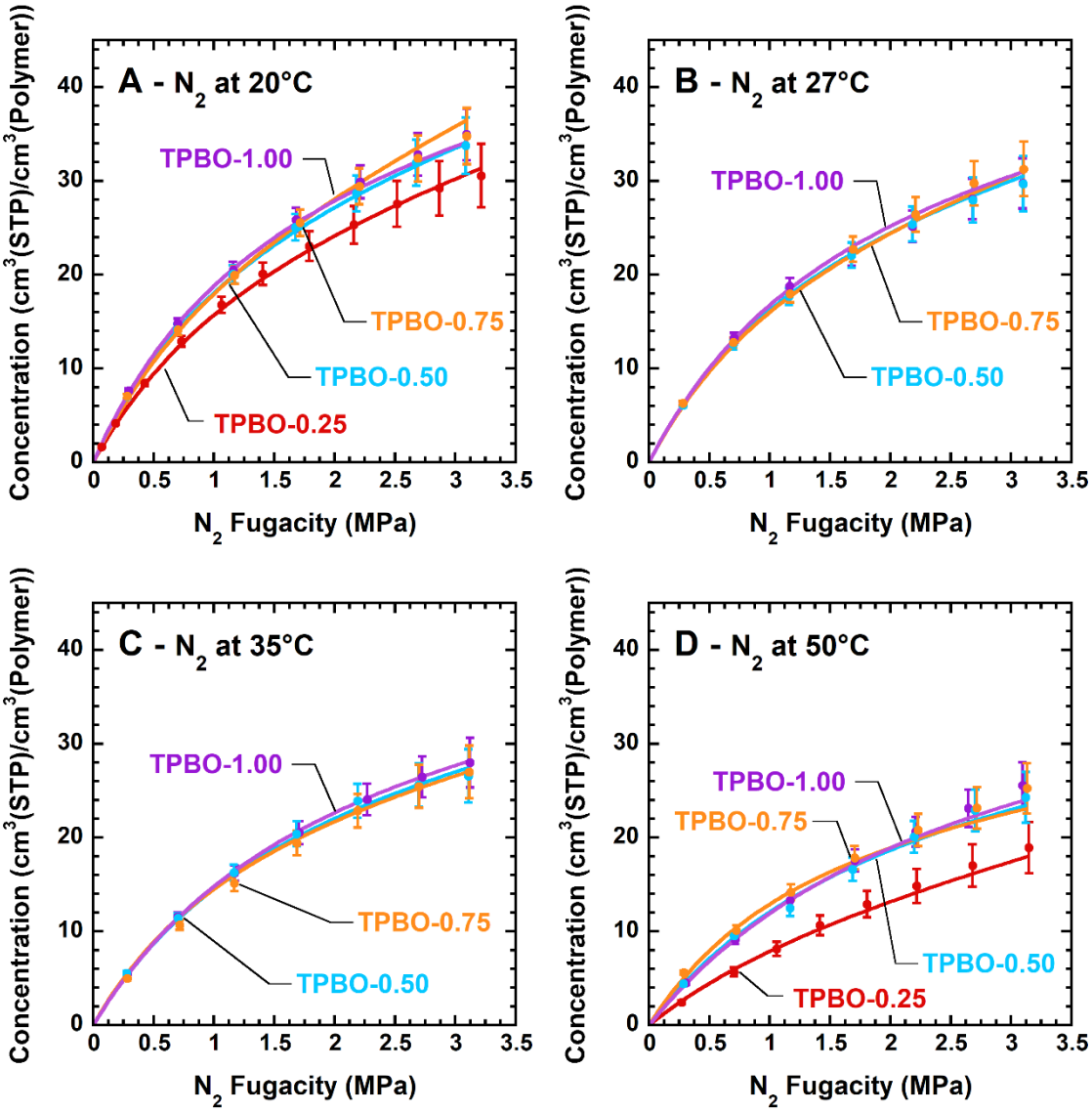


Figure A7: *N_2 sorption in TPBOs at varying temperatures ranging from 20°C to 50°C taken at pressures up to 3 MPa. Solid points represent experimental data, continuous lines represent the dual mode fitting. Error bars were calculated using linear error propagation [96,98].*

A9. Pure CH_4 and N_2 Sorption Isotherms in TPBOs

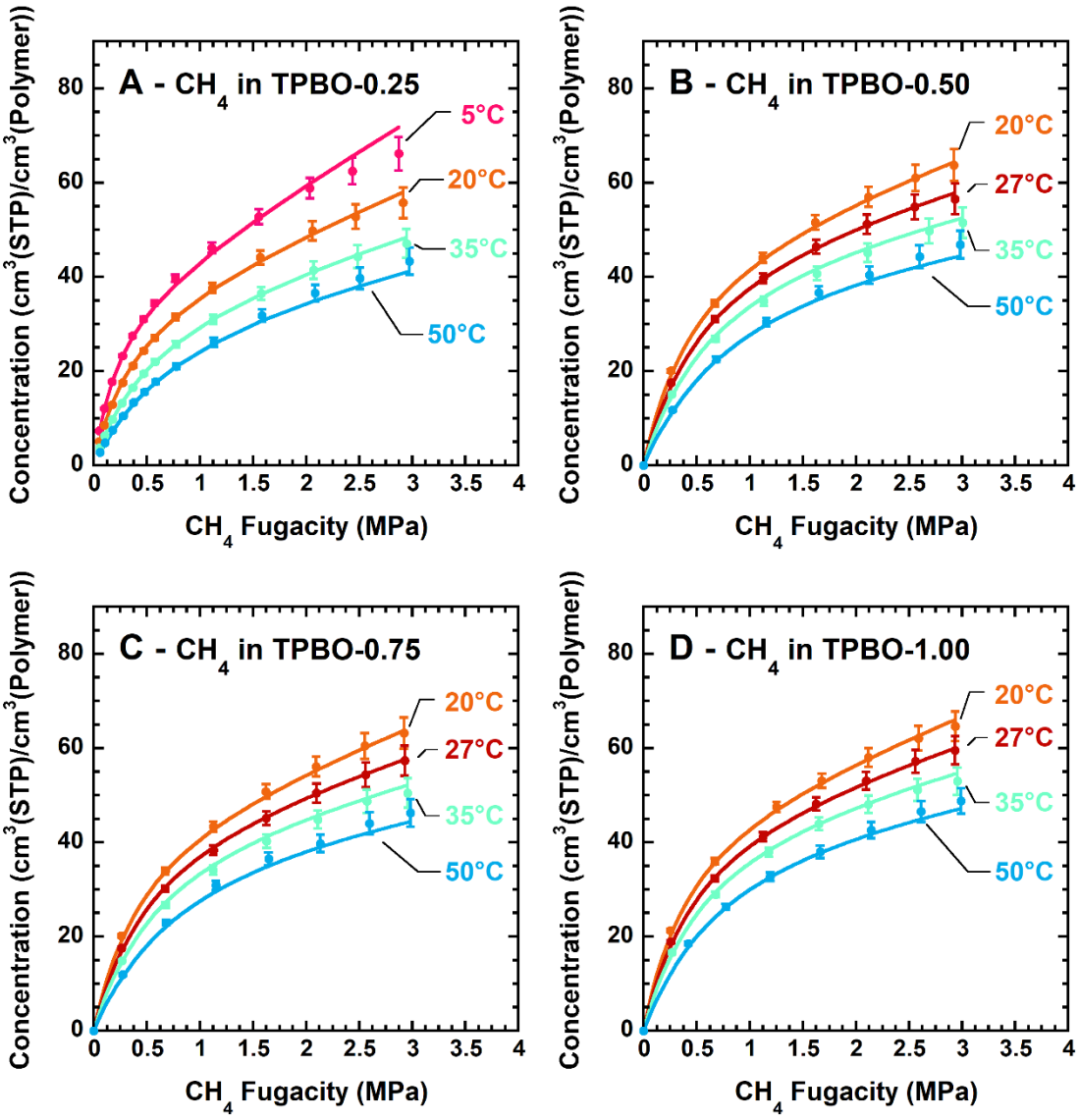


Figure A8: *CH_4 sorption in TPBOs as a function of triptycene content at temperatures ranging from 5°C to 50°C taken at pressures up to 3 MPa. Solid points represent experimental data, continuous lines represent the dual mode fitting. Error bars were calculated using linear error propagation [96,98].*

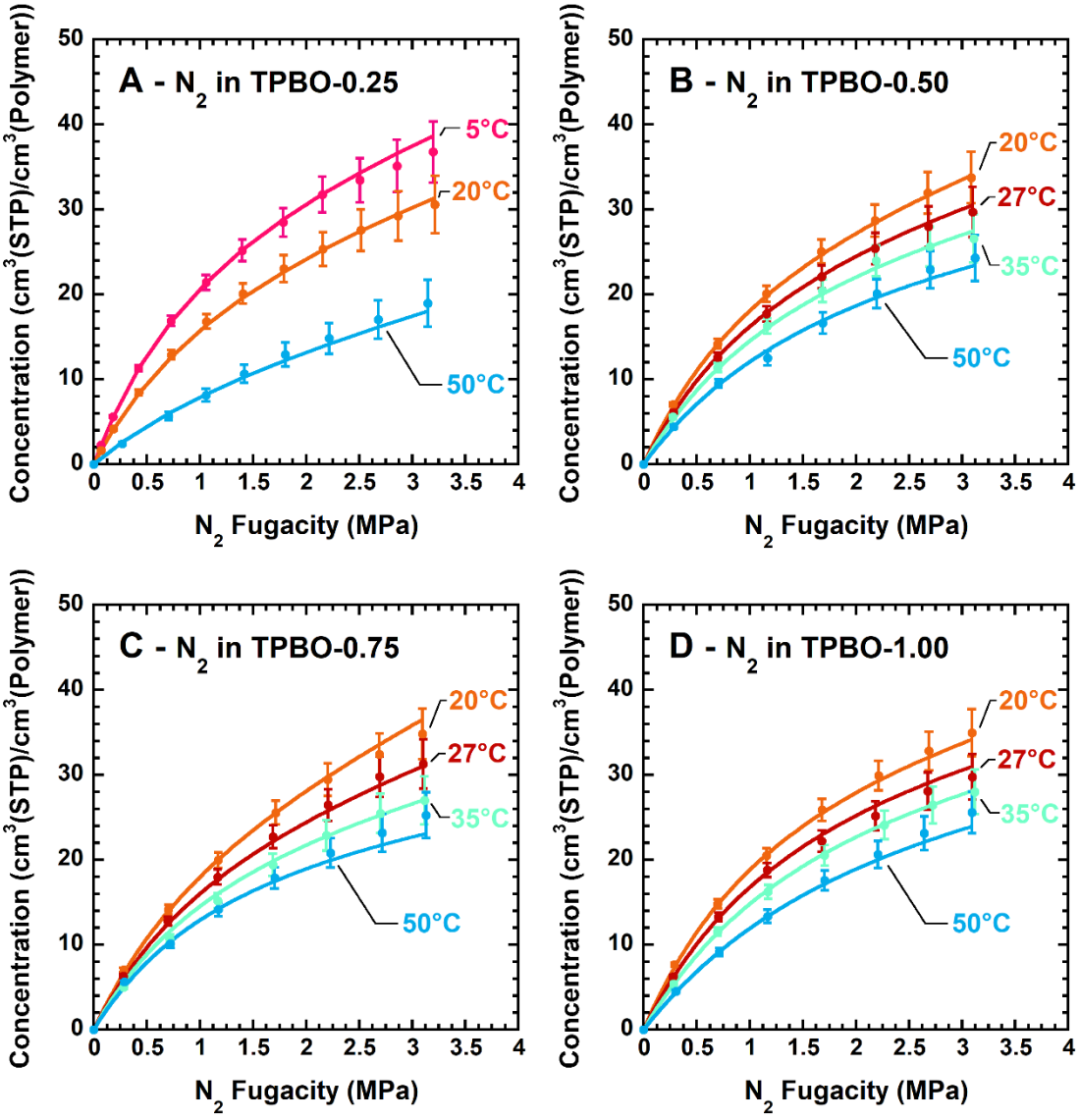


Figure A9: *N_2 sorption in TPBOs as a function of triptycene content at temperatures ranging from 5°C to 50°C taken at pressures up to 3 MPa. Solid points represent experimental data, continuous lines represent the dual mode fitting. Error bars were calculated using linear error propagation [96,98].*

A10. Analysis of fitted dual mode parameters

Remarkably, the dual mode implementation under the constraints described in the main manuscript, is able to catch, for all TPBOs, the linearity of $\ln(K_D)$ as a function of penetrant critical temperature, according to what is reported in ref. [15]. The dual mode parameters at any temperature do not change much among TPBO samples (within the uncertainty), which is consistent with the fact that the sorption isotherms are essentially independent of triptycene content.

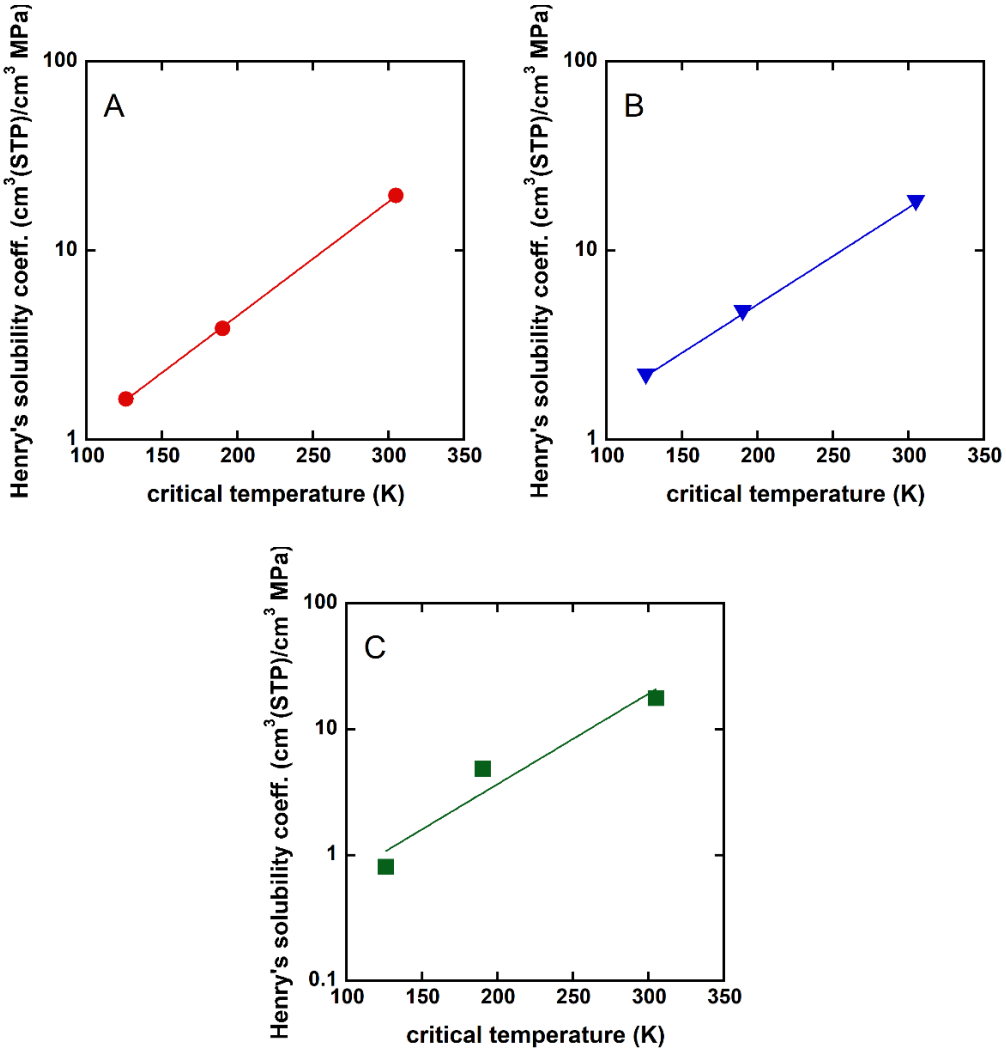


Figure A10: *Logarithm of K_D (i.e., Henry's solubility coefficient) vs. penetrant critical temperature at 35°C. A): TPBO-0.50, B): TPBO-0.75, and C): TPBO-1.00. The three data points in each figure refer to N_2 (critical T = 126K), CH_4 (critical T = 190.1K) and CO_2 (critical T = 304.9K). As expected, the slope of this correlation is 0.015 K^{-1}.*

A11. Isosteric heats as function of triptycene content for both CO_2 and CH_4

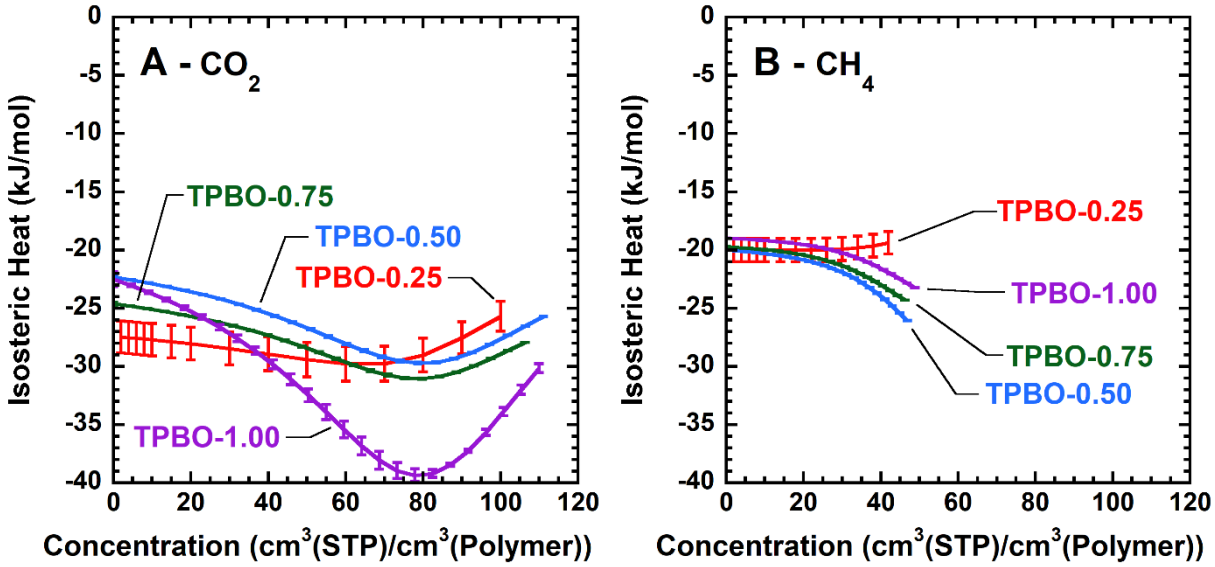


Figure A11: *Isosteric heats of CO_2 (A) and CH_4 (B) sorption in TPBOs as a function of penetrant concentration. Error bars are obtained using the standard deviation of weighted linear regression [98,101].*

A12. Dual mode prediction of CO_2/CH_4 mixed-gas solubility and solubility-selectivity, comparison with pure-gas data and uncertainty analysis

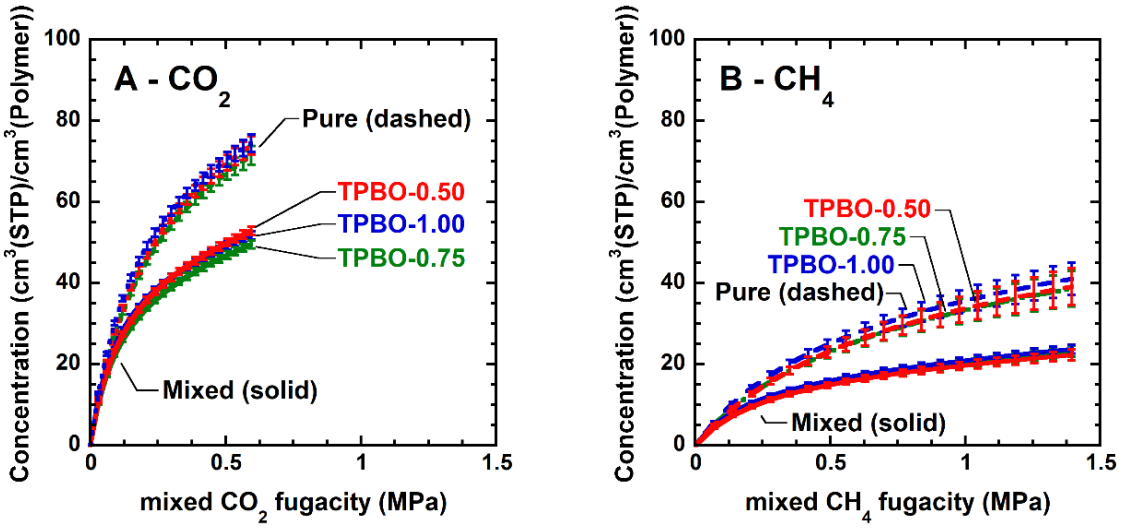


Figure A12: *CO_2 and CH_4 mixed-gas sorption isotherms (solid lines, predicted using the dual mode model) from a 30%mol CO_2/70%mol CH_4 gas mixture in TPBOs as a function of mixed gas fugacity at 35°C: A) CO_2 and B) CH_4. Uncertainty was calculated via linear error propagation [96,98]. Dual mode fittings of pure-gas data are shown for the sake of comparison (dashed lines).*

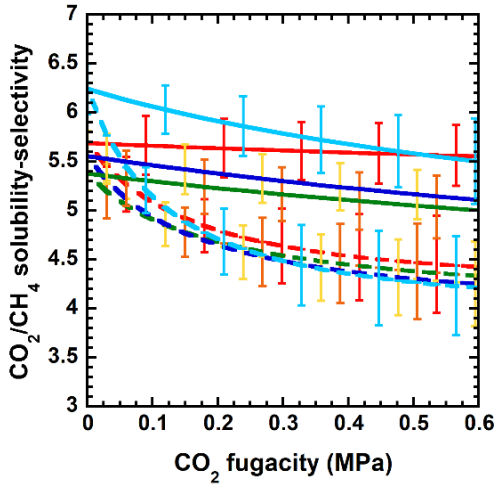


Figure A13: *Dual mode predictions of CO_2/CH_4 real (continuous lines) and ideal (dashes lines) solubility-selectivity for a 30%mol CO_2 / 70%mol CH_4 mixture in TPBOs as a function of mixed CO_2 fugacity at 35°C. Uncertainty associated to ideal solubility-selectivity was linearly propagated from the original isotherms. Uncertainty associated to real (i.e., mixed-gas) selectivity was estimated via the percent error resulting from linear error propagation of the original isotherms. TPBO-0.25 data is taken from [75] and shown for comparison. Legend: sky lines represent TPBO-0.25. Red lines represent TPBO-0.50. Green lines represent TPBO-0.75. Blue lines represent TPBO-1.00.*

A13. Ideal and real CO_2/CH_4 solubility selectivity as a function of temperature

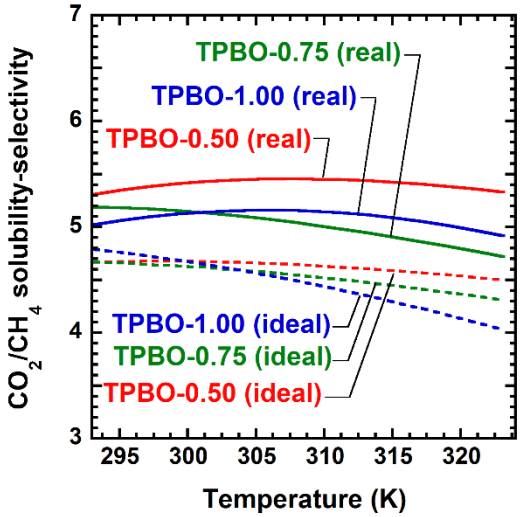


Figure A14: *Real (solid lines) and ideal (dashed lines) CO_2/CH_4 solubility selectivity in TPBOs as a function of temperature, predicted via the dual mode model. CO_2 fugacity = 0.3 MPa, CH_4 fugacity = 0.7 MPa.*

Ideal and mixed-gas CO_2/CH_4 solubility-selectivity slightly increases with decreasing temperature. This behavior is a consequence of CO_2 sorption being more exothermic than CH_4 sorption [75]:

$$\alpha_{ij} = \alpha_{ij,0} exp\left(-\frac{\Delta H_{s,i} - \Delta H_{s,j}}{RT}\right)$$

A14. Logarithm of permeability versus 1/FFV

While the logarithm of permeability is expected to be a linear function of reciprocal FFV [20], TPBO-1.00 deviates from the expected trend (see Figure A15), indicating that the configurational free volume plays an active role in regulating small molecule transport in polymers exhibiting iptycene units. If a linear trend was observed in Figure A15, the results presented in this study could simply be explained by invoking the fact that a loss of conformational free volume results in low permeability and high selectivity. The lack of linearity provides further evidence of the unique role played by configurational free volume.

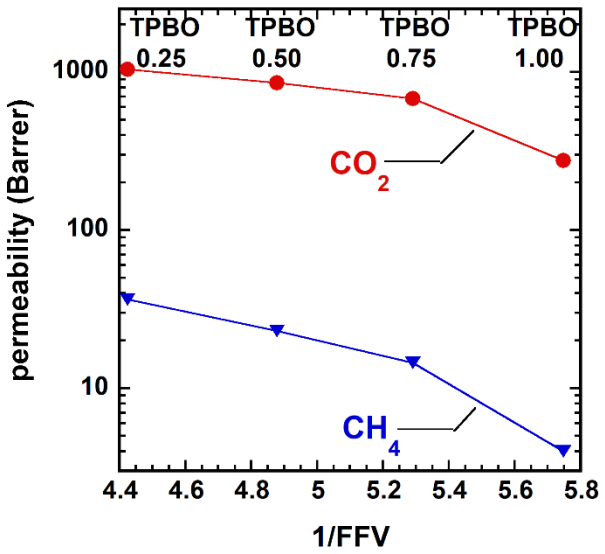


Figure A15: *Logarithm of CO_2 and CH_4 permeability as a function of polymer's FFV^{-1} at 35°C and 1 MPa (i.e., 10 atm).*

A15. Evaluation of D_D and D_H

According to the partial immobilization model (See Equation 7 in the main manuscript), small molecule permeability in glassy polymers can be parametrized as follows [74]:

$$\wp = k_D D_D \left(1 + \frac{KF}{1+bf}\right)$$

where $F = D_H/D_D$ and $K = C_H' b/k_D$. This expression can be re-cast as: $\wp = k_D D_D + \frac{C_H' b}{1+bf} D_H$ so that it may be easily fit to experimental permeability data. To do this, two sets of data are needed.

1. A pure-gas solubility isotherm which has been fit to the dual mode model (i.e., the parameters k_D, C_H', and b) as a function of pure component fugacity, and
2. Pure-gas permeability taken within the same fugacity range as solubility data.

The D_H and D_D parameters of the partial immobilization model are then fit via linear regression. where $k_D D_D$ is the intercept and D_H is the slope, respectively, of the linear diagram $\wp$ vs $\frac{C_H' b}{1+bf}$ (See Figure A16).

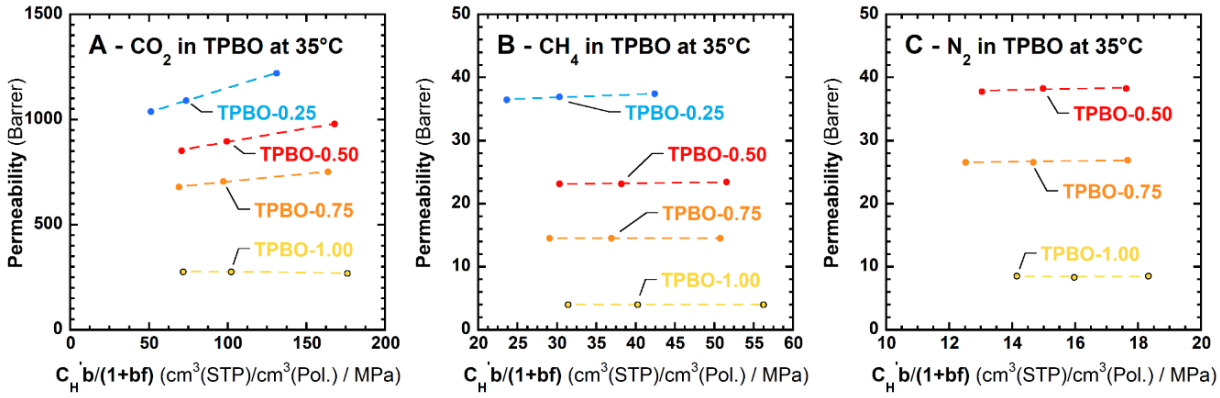


Figure A16: *Pure gas CO_2 (A), CH_4 (B) and N_2 (C) permeability at 35°C as a function of $\frac{C_H' b}{1+bf}$ in TPBO-0.25 (blue dots), TPBO-0.50 (red dots), TPBO-0.75 (orange dots), and TPBO-1.00 (yellow dots). Dashed lines are drawn to guide the eye.*

A16. Dual-mode parameters for TPBOs as function of penetrant fugacity

Table A6: *Fitted parameters of the temperature-constrained dual mode model for CO_2.*

CO_2 parameters	TPBO-0.50	TPBO-0.75	TPBO-1.00
C'_{H_0} *(cm³(STP)/cm³(pol))*	242.69 ± 54.59	204.22 ± 34.54	438.21 ± 138.54
b_0 *(MPa⁻¹)*	0.00396 ± 0.00413	0.00105 ± 0.000366	0.0617 ± 0.250
k_{D_0} *(cm³(STP)/cm³(pol)MPa)*	0.045 ± 0.099	0.0111 ± 0.0255	1.0 ± 3.7
$m_{C'_H}$ *(K⁻¹)*	-0.519 ± 0.178	-0.400 ± 0.115	-1.1559 ± 0.459
$\Delta H_b \left(J/_{mol}\right)$	-18377 ± 2698	-21762 ± 1122	-11706 ± 10100
$\Delta H_{k_D} \left(J/_{mol}\right)$	-15560 ± 5457	-18916 ± 5624	-7367 ± 9331

Table A7: *Fitted parameters of the temperature-constrained dual mode model for CH_4.*

CH_4 parameters	TPBO-0.50	TPBO-0.75	TPBO-1.00
C'_{H_0} *(cm³(STP)/cm³(pol))*	49.98 ± 64.50	46.24 ± 73.37	48.20 ± 53.29
b_0 *(MPa⁻¹)*	0.000763 ± 0.000190	0.000863 ± 0.000247	0.00128 ± 0.000463
k_{D_0} *(cm³(STP)/cm³(pol)MPa)*	$2.04E^{-5} \pm 0.000386$	0.000142 ± 0.00239	0.000214 ± 0.00208
$m_{C'_H}$ *(K⁻¹)*	$-1.72E^{-9} \pm 0.236$	$-4.68E^{-9} \pm 0.269$	$-1.44E^{-10} \pm 0.180$
$\Delta H_b \left(J/_{mol}\right)$	-19414 ± 130	-19333 ± 1395	-18554 ± 1228
$\Delta H_{k_D} \left(J/_{mol}\right)$	-31151 ± 45409	-26656 ± 40502	-25657 ± 23497

Table A8: *Fitted parameters of the temperature-constrained dual mode model for N_2.*

N_2 parameters	TPBO-0.50	TPBO-0.75	TPBO-1.00
C'_{H_0} *(cm³(STP)/cm³(pol))*	35.82 ± 155.92	29.16 ± 163.34	42.10 ± 134.74
b_0 *(MPa⁻¹)*	0.00572 ± 0.0183	0.186 ± 1.112	0.00124 ± 0.000757
k_{D_0} *(cm³(STP)/cm³(pol)MPa)*	$3.85E^{-6} \pm 0.000165$	$1.13E^{-7} \pm 1.35E^{-6}$	$1.13E^{-7} \pm 2.00E^{-6}$
$m_{C'_H}$ *(K⁻¹)*	-0.00530 ± 0.466	$-1.01E^{-12} \pm 0.507$	$-4.77E^{-11} \pm 0.374$
$\Delta H_b \left(J/_{mol}\right)$	-11955 ± 8799	-3539 ± 15473	-15384 ± 2188
$\Delta H_{k_D} \left(J/_{mol}\right)$	-33214 ± 100453	-42965 ± 28149	-40451 ± 41766

Uncertainty of the fitted parameters were estimated using the inverse Hessian array of the sum of squared residuals error (SSE) with respect to the fitted parameters. These uncertainties reflect the empirical nature of the dual-mode model and the constraints imposed on temperature across isotherms of the same component and polymer.

Table A9: *Dual-mode parameters for CO_2, CH_4, and N_2 at multiple temperatures in TPBOs.*

penetrant: CO_2 **polymer: TPBO-0.50**	C'_H (cm^3(STP)/cm^3(pol))	b (MPa^{-1})	k_D (cm^3(STP)/cm^3(pol)MPa)
20°C	90.42	7.45	26.69
27°C	86.79	6.25	23.00
35°C	82.63	5.16	19.56
50°C	74.84	3.70	14.76

penetrant: CO_2 **polymer: TPBO-0.75**	C'_H (cm^3(STP)/cm^3(pol))	b (MPa^{-1})	k_D (cm^3(STP)/cm^3(pol)MPa)
20°C	86.92	7.90	26.00
27°C	84.12	6.41	21.70
35°C	80.91	5.11	17.82
50°C	74.91	3.45	12.65

penetrant: CO_2 **polymer: TPBO-1.00**	C'_H (cm^3(STP)/cm^3(pol))	b (MPa^{-1})	k_D (cm^3(STP)/cm^3(pol)MPa)
20°C	99.37	7.52	20.55
27°C	91.28	6.72	19.15
35°C	82.03	5.95	17.73
50°C	64.69	4.81	15.52

penetrant: CH_4 **polymer: TPBO-0.50**	C'_H (cm^3(STP)/cm^3(pol))	b (MPa^{-1})	k_D (cm^3(STP)/cm^3(pol)MPa)
20°C	49.98	2.20	7.24
27°C	49.98	1.82	5.37
35°C	49.98	1.49	3.89
50°C	49.98	1.05	2.21

penetrant: CH_4 **polymer: TPBO-0.75**	C'_H (cm^3(STP)/cm^3(pol))	b (MPa^{-1})	k_D (cm^3(STP)/cm^3(pol)MPa)
20°C	46.24	2.40	7.97
27°C	46.24	1.20	6.18

35°C	46.24	1.63	4.68
50°C	46.24	1.15	2.89

penetrant: CH_4 **polymer: TPBO-1.00**	C'_H (cm^3(STP)/cm^3(pol))	b (MPa^{-1})	k_D (cm^3(STP)/cm^3(pol)MPa)
20°C	48.20	2.59	7.99
27°C	48.20	2.17	6.25
35°C	48.20	1.79	4.78
50°C	48.20	1.28	3.01

penetrant: N_2 **polymer: TPBO-0.50**	C'_H (cm^3(STP)/cm^3(pol))	b (MPa^{-1})	k_D (cm^3(STP)/cm^3(pol)MPa)
20°C	34.27	0.77	3.19
27°C	34.23	0.69	2.32
35°C	34.19	0.61	1.64
50°C	34.11	0.49	0.90

penetrant: N_2 **polymer: TPBO-0.75**	C'_H (cm^3(STP)/cm^3(pol))	b (MPa^{-1})	k_D (cm^3(STP)/cm^3(pol)MPa)
20°C	29.17	0.80	5.09
27°C	29.17	0.77	3.38
35°C	29.17	0.74	2.16
50°C	29.17	0.69	0.99

penetrant: N_2 **polymer: TPBO-1.00**	C'_H (cm^3(STP)/cm^3(pol))	b (MPa^{-1})	k_D (cm^3(STP)/cm^3(pol)MPa)
20°C	42.10	0.68	1.82
27°C	42.10	0.59	1.23
35°C	42.10	0.50	0.81
50°C	42.10	0.38	0.39

A17. Analytical assessment of the effect of polymer swelling (i.e., change in polymer density) on sorption uncertainty

For any given pressure decay, the concentration uncertainty decreases with decreasing polymer density. Even if swelling occurs, using the dry polymer density in the uncertainty calculations represents the most conservative estimate of the error. The concentration itself also decreases with decreasing density, shifting both its value and uncertainty range. In order for the uncertainties in the cases when the swollen density or the dry density is used overlap, the following constraint must be verified during the *j-th* differential sorption step:

$$\left[C_{pol,j} - \phi\sigma_{C_{pol,j}}\right]_{\rho_{pol,d}} \leq \left[C_{pol,j} + \phi\sigma_{C_{pol,j}}\right]_{\rho_{pol,s}} \quad \text{Equation A1}$$

where $\rho_{pol,d}$ represents the dry polymer density and $\rho_{pol,s}$ represents the density of the swollen polymer, respectively. ϕ is the number of standard deviations taken under consideration. For example, $\phi = 2$ represents the 95% confidence interval of two standard deviations. The constraint is shown graphically at different ϕ values in Figure A17A.

Using the definition of percent swelling:

$$\%\, S = 100 \times \left(\frac{\rho_{pol,d}}{\rho_{pol,s}} - 1\right) \quad \text{Equation A2}$$

the following constraint is made for any differential sorption step *j:*

$$\%\, S_j \leq 100 \times \left[\frac{1+\phi\left(\frac{\sigma_{C_j}}{C_j}\right)|_{\rho_{pol,s}}}{1-\phi\left(\frac{\sigma_{C_j}}{C_j}\right)|_{\rho_{pol,d}}} - 1\right] \quad \text{Equation A3}$$

The previous two equations can be solved simultaneously for the percent swelling and swollen polymer density. The solution results in the swelling threshold at which the choice of using the dry or swollen polymer density results in no overlap of the uncertainty range. In the case of CO_2 in TPBO-0.25 at 35°C, the swelling thresholds calculated using $\phi = 0.25, 0.5, 1$ and 2 (see Figure A17B) are far above the CO_2-induced TPBO swelling at 30 atm predicted using the *Non-Equilibrium Lattice Fluid model*, that is, 4% [94]. Thus, swelling is fairly negligible in the case of the light gas sorption experiments.

In the case of methanol sorption in PBI at 35°C, the swelling thresholds calculated using $\phi = 0.25, 0.5, 1$, and 2, similar to that of the gas sorption case, are shown in Figure A17C. As expected, vapor sorption measurements are much more sensitive to the effects of polymer swelling than light gas sorption experiments. For example, a 5% degree of swelling would change the measured concentration by one standard deviation of the nominal uncertainty at a pressure of 0.004 MPa.

A dilation experiment could be used to correct sorption data. Unfortunately, such swelling data are not experimentally available right now. Instead, this threshold serves mainly as an indication of how much the true answer could vary due to swelling and how much error can be tolerated.

Measurements with higher expected swelling (and where this swelling cannot be accounted for) needn't focus on extremely accurate experimental data, as the swelling threshold increases along with the uncertainty of the concentration, and by extension all

contributors to it. For example, if the error in the dry density, $\sigma_{\rho,dry}$, is doubled in the methanol and PBI vapor sorption experiments, the swelling threshold for the density would be shifted up by around 1.5%. In other words, swelling will be less likely to bring the measured concentration to a measurably different value if the measured concentration's error is comparatively large.

In the case of methanol sorption in PBI at 35°C, the swelling threshold at $\phi = 1$ with two distinct dry polymer density uncertainties (i.e., $\sigma(\rho)$) are shown in Figure A17D as a function of pressure.

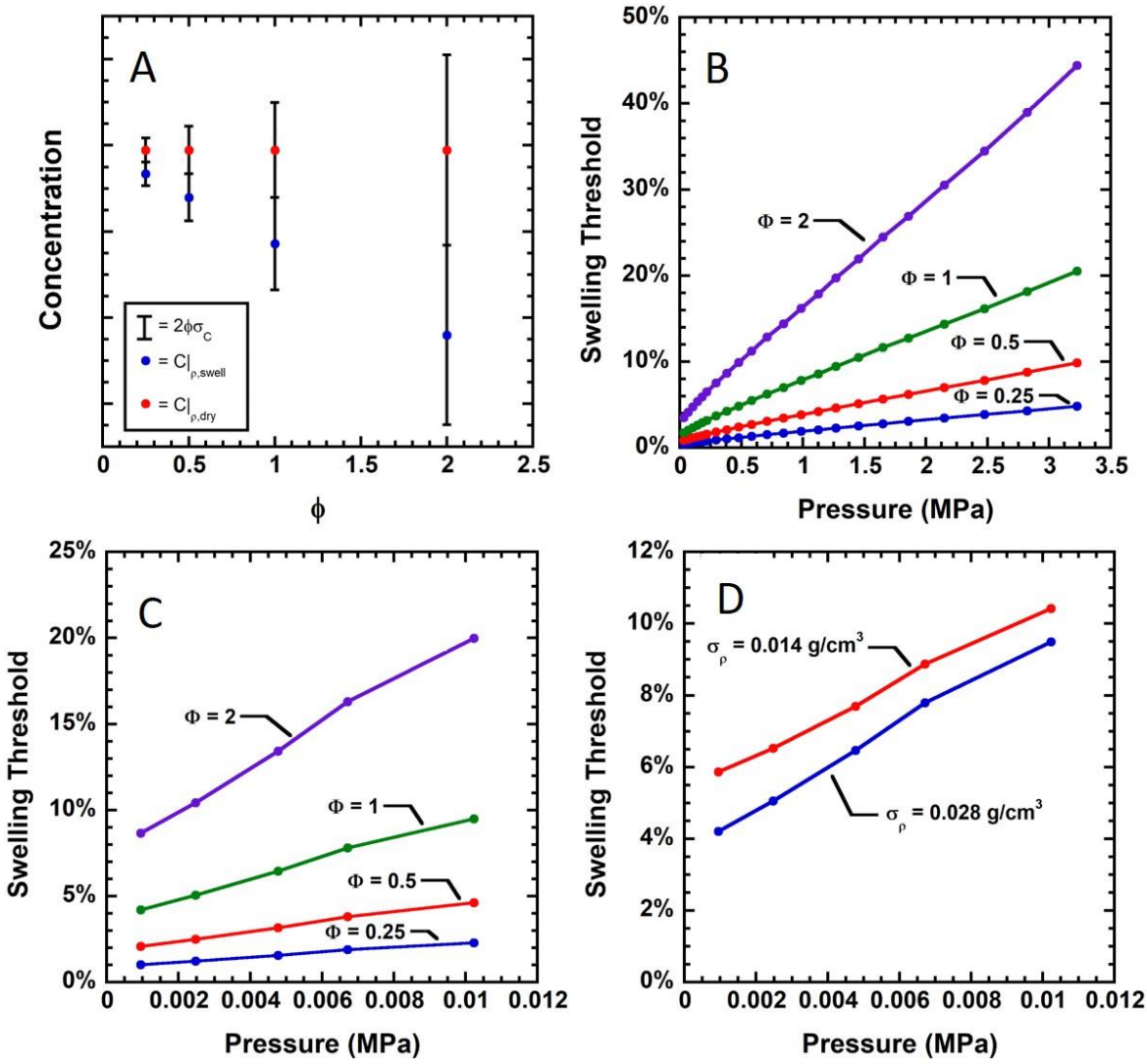


Figure A17: *Graphical representation of the constraint represented by Equation A1, that is, overlapping condition for the error bars when using the dry and swollen polymer density (A). Swelling thresholds in the case of CO_2 sorption in TPBO-0.25 at 35°C (B). Swelling thresholds in the case of methanol sorption in Celazole PBI at 35°C (C). Swelling thresholds in the case of methanol sorption in Celazole PBI at 35°C using two different dry polymer density uncertainties (D).*

A18. Comparison between linear error propagation and Monte Carlo methods: an example

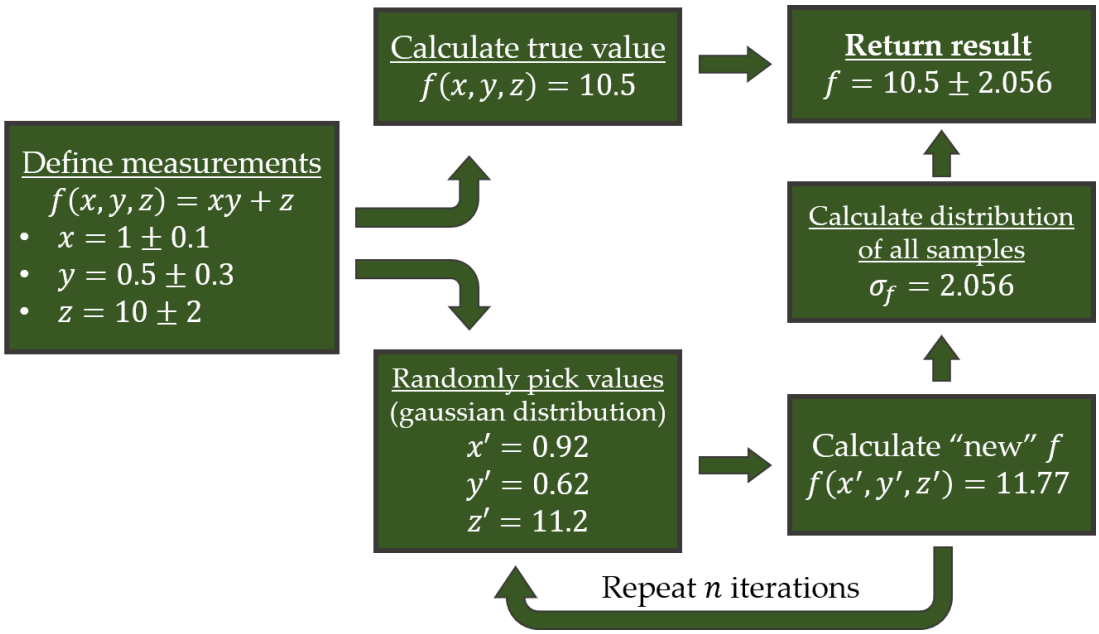


Figure A18: *Application of the Monte Carlo method to evaluate the uncertainty of the function* $f(x,y,z) = xy + z$*. 2700 iterations were used.*

Within a specific distribution (typically Gaussian) defined by each variables error, values are chosen as possible measurements to calculate *f*. This process is repeated to obtain the output distribution and thus the uncertainty of $f(x,y,z)$.

As an example, we will compare this result to linearly propagated error.

$f(x,y,z) = xy + z$

Where $x = 1 \pm 0.1$, $y = 0.5 \pm 0.3$, and $z = 10 \pm 2$

$$\sigma_f = \sqrt{\left(\frac{\partial f}{\partial x}\right)^2 \sigma_x^2 + \left(\frac{\partial f}{\partial y}\right)^2 \sigma_y^2 + \left(\frac{\partial f}{\partial z}\right)^2 \sigma_z^2} = \sqrt{y^2\sigma_x^2 + x^2\sigma_y^2 + \sigma_z^2}$$

$$\hookrightarrow \sqrt{0.5^2 \cdot 0.1^2 + 1^2 \cdot 0.3^2 + 2^2} = \sqrt{4.0925} = 2.023$$

Thus, the answer provided by the Monte Carlo method after 2700 iterations (i.e., σ_f = 2.056), differs only by 1.6% from that provided by linear error propagation (i.e., σ_f = 2.023). Additional iterations will further reduce the difference between the two results.

A19. Analytical LEP uncertainty of vapor sorption measurements

Vapor sorption uncertainty can be analytically derived for a generic step *j*, resulting in the following equation:

$$\sigma_{C_{pol,j}} = \mathrm{C_{pol,j}} \sqrt{\begin{array}{l} \left(\frac{\sigma_{\rho_{pol}}}{\rho_{pol}}\right)^2 + \left(\frac{\sigma_{\mathrm{g_{pol,dry}}}}{\mathrm{g_{pol,dry}}}\right)^2 + \left(\frac{\sigma_T}{\mathrm{T}}\right)^2 + \left(\left(\frac{1}{V_C} + \frac{P_{f,j}V_S}{\beta_j V_C^2}\right)\sigma_{V_C}\right)^2 \\ + \left(\frac{P_{f,j}}{\beta_j V_C}\sigma_{V_S}\right)^2 + \left(\frac{1}{\beta_j^2}\sum_{i=1}^{j}\left(\sigma_{P_{S,i}}^2 + \sigma_{P_{Cf,i-1}}^2\right)\right) + \left(\frac{\left(1+\frac{V_S}{V_C}\right)}{\beta_j}\sigma_{P_{f,j}}\right)^2 \end{array}} \qquad \text{Equation A4}$$

Where

$$\beta_j = \left(\sum_{i=1}^{j}\left(P_{S,i} - P_{Cf,i-1}\right) - P_{f,j}\left(\frac{V_S}{V_C} + 1\right)\right) \qquad \text{Equation A5}$$

where the nomenclature is consistent with that defined in the main manuscript. This equation shows, from a predictive standpoint, that the uncertainty of pressure measurements used to generate vapor sorption isotherms in the differential mode tend to accumulate throughout subsequent steps. This was observed directly in MCEP analyses of both vapor and gas isotherm uncertainties (see Figure 28 and Figure 29 in the main manuscript). Uncertainty associated to other variables, such as chamber volumes, temperature and polymer density is not predicted to accumulate in this manner, which is the basis for why the latter variables lose importance in the uncertainty contribution plots shown in Figure 31 and Figure 32 in the main manuscript for vapor and gas respectively as additional sorption steps are taken.

A20. Coefficient of variation and sorption uncertainty

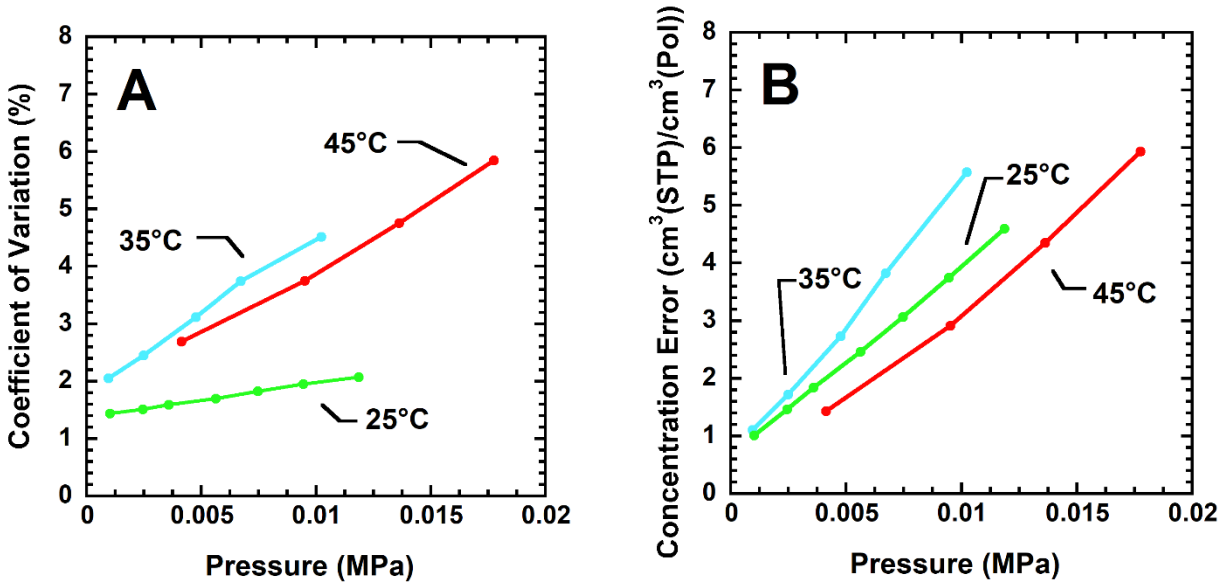


Figure A19: *Coefficient of variation, CV, (A) and error (i.e., uncertainty) (B) of methanol vapor sorption in PBI as a function of pressure. Isotherms are shown at 25°C (green), 35°C (blue), and 45°C (red). Lines are drawn to guide the eye.*

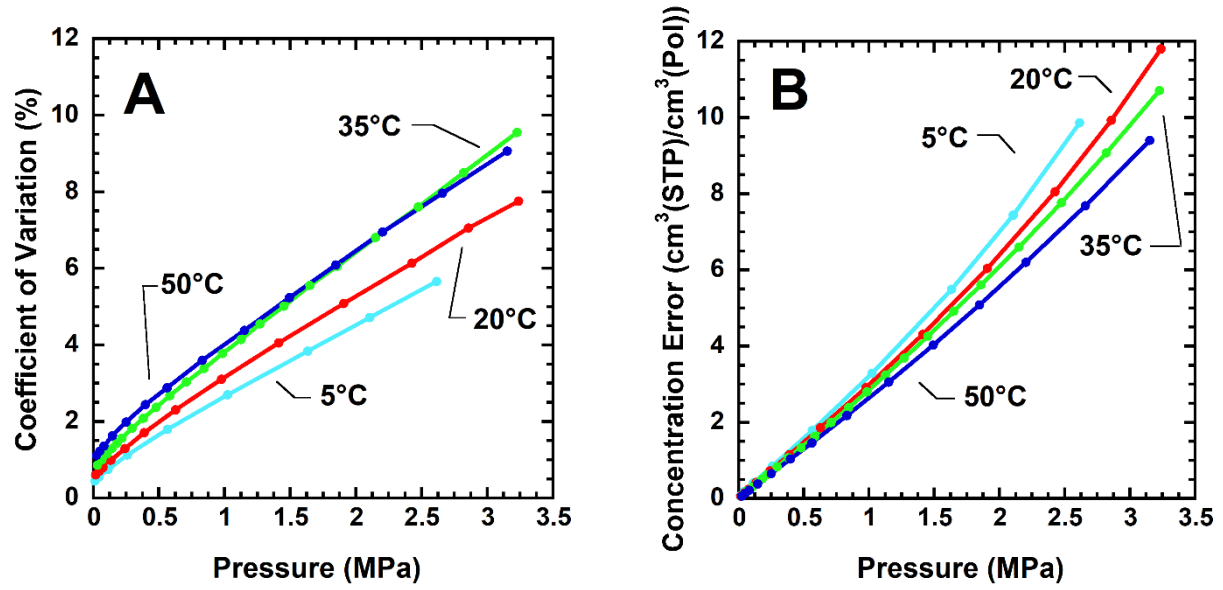
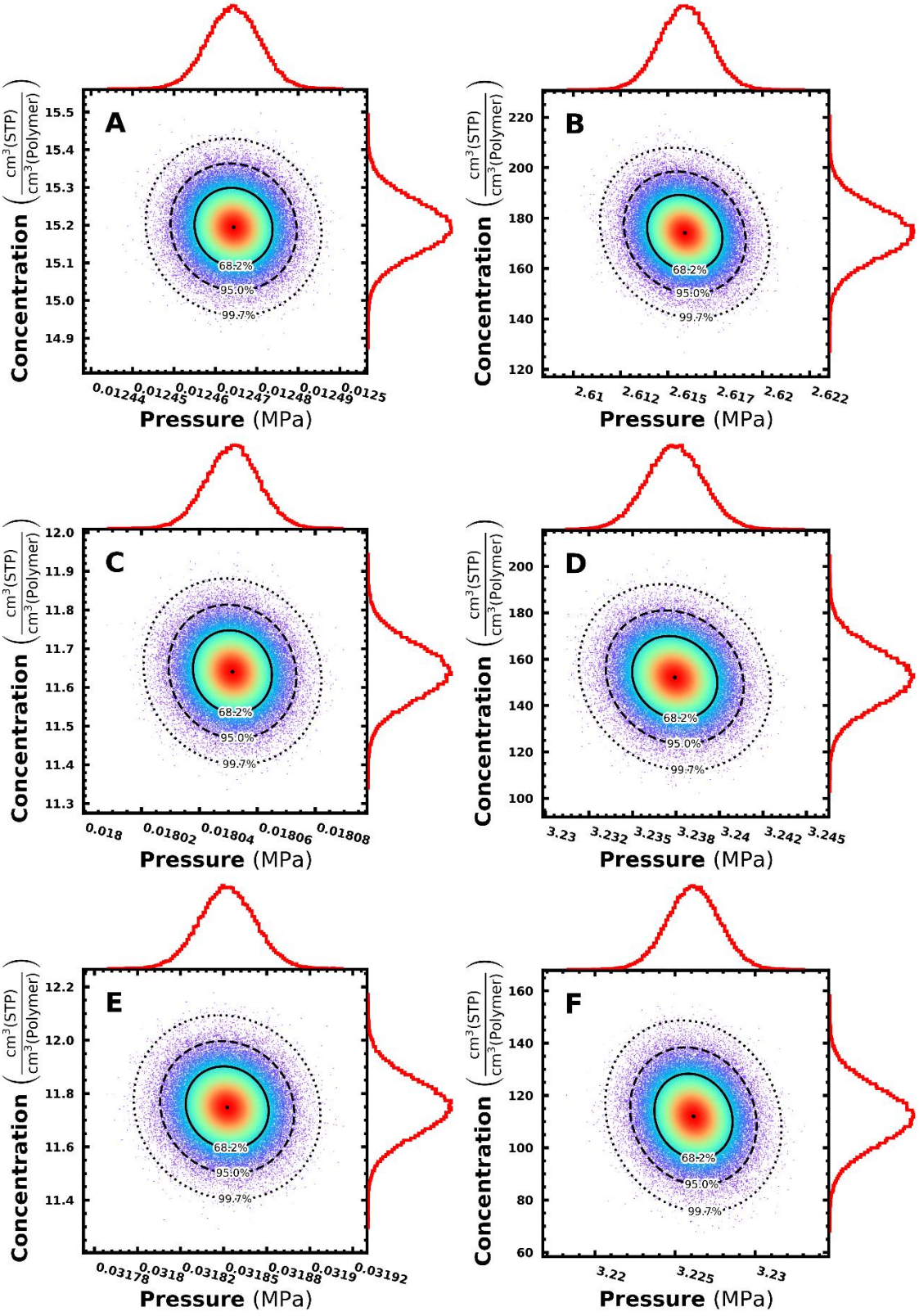


Figure A20: *Coefficient of variation, CV, (A) and error (i.e., uncertainty) (B) of CO_2 sorption in TPBO-0.25 as a function of pressure. Isotherms are shown at 5°C (light blue), 20°C (red), 35°C (green), and 50°C (dark blue). Lines are drawn to guide the eye.*

A21. Monte Carlo Scatterplots of selected CO_2 sorption steps



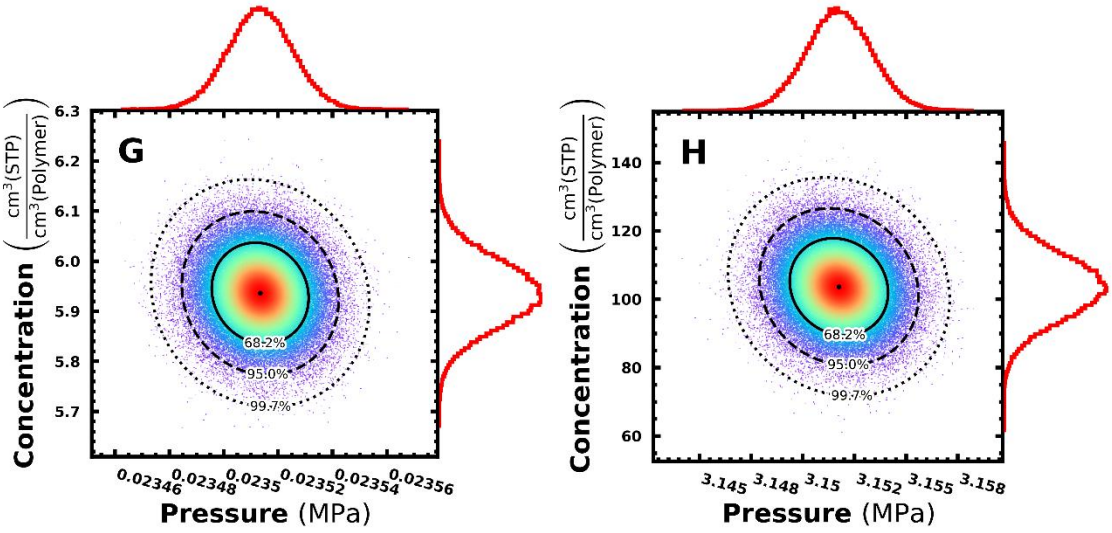
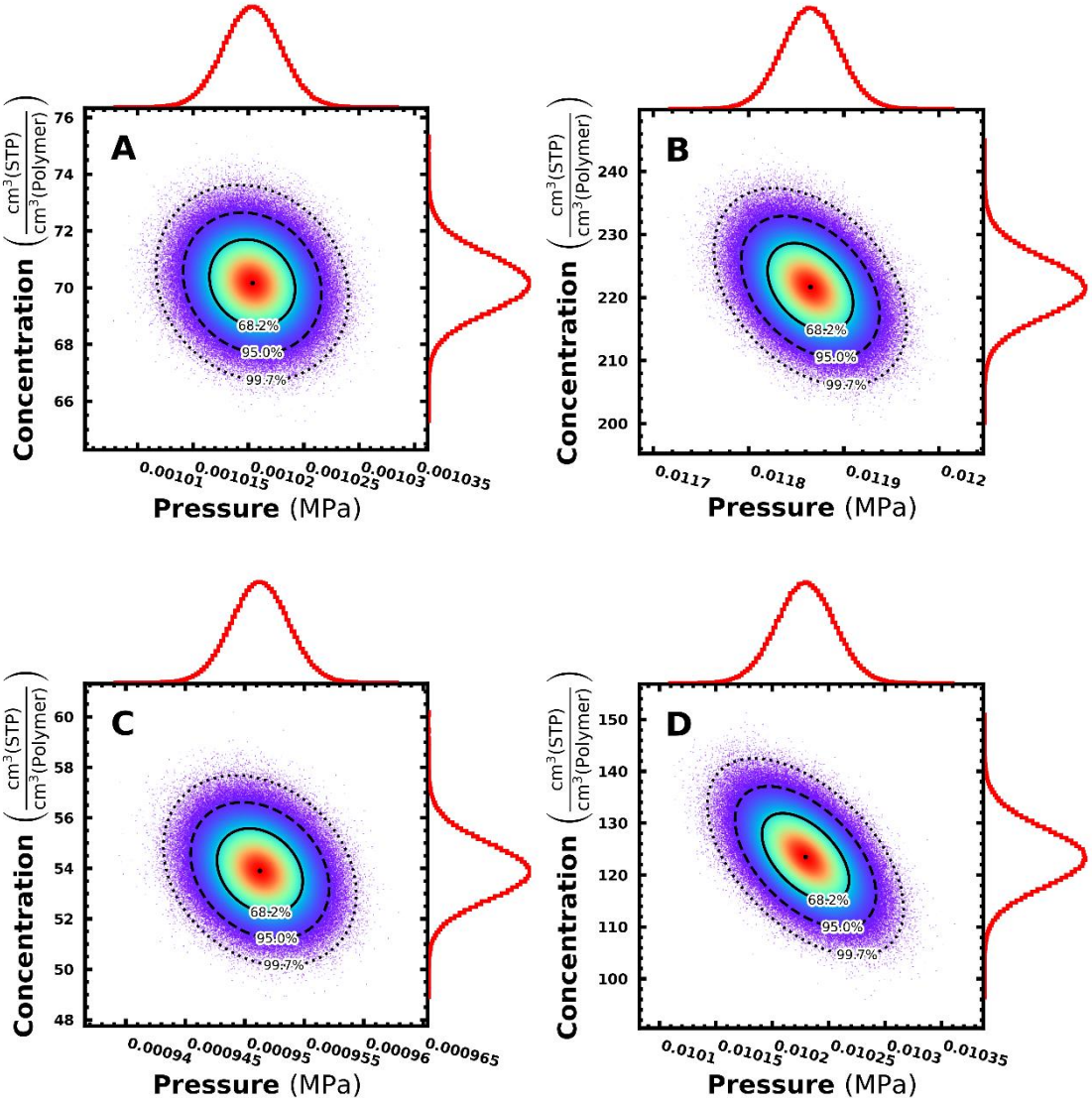


Figure A21: *100,000 Monte-Carlo simulations of selected CO_2 sorption steps in TPBO-0.25 plotted as a function of pressure (MPa). Color is assigned via a bivariate probability density function using the data's covariance matrix. Marginal histograms (red lines) denote the pressure or concentration distribution. Error ellipses (solid, dashed, and dotted black lines) show the 68.2%, 95%, and 99.7% confidence intervals, respectively. Figures are labeled for A) 5°C step 1, B) 5°C step 9, and C) 20°C step 1, D) 20°C step 13, E) 35°C step 1, F) 35°C step 22, G) 50°C step 1, H) 50°C step 14.*

A22. Monte Carlo Scatterplots of selected methanol sorption steps



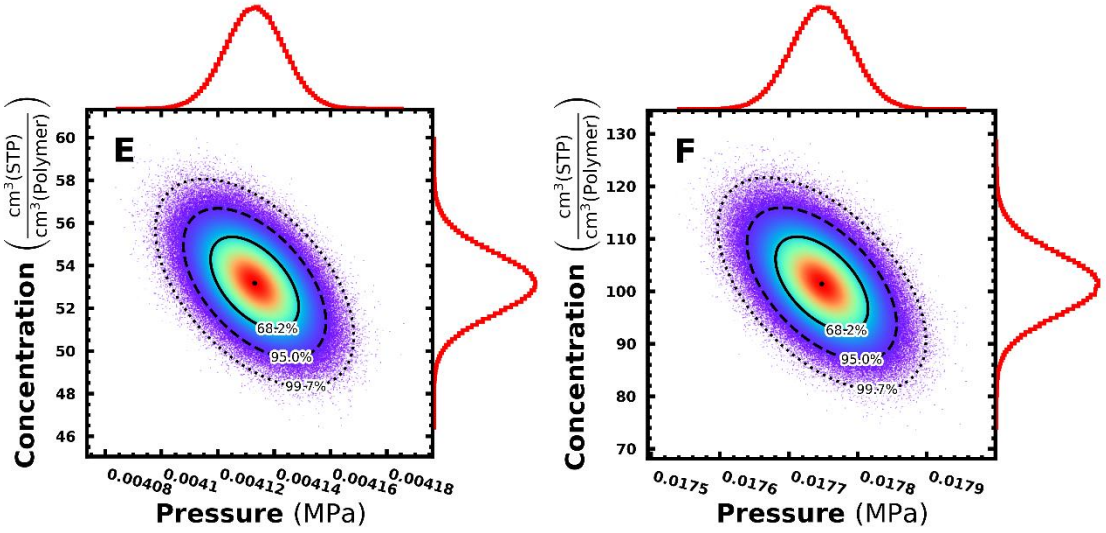


Figure A22: *1,000,000 Monte-Carlo simulations of selected methanol vapor sorption steps in PBI plotted as a function of pressure (MPa). Color is assigned via a bivariate probability density function using the data's covariance matrix. Marginal histograms (red lines) denote the pressure or concentration distribution. Error ellipses (solid, dashed, and dotted black lines) show the 68.2%, 95%, and 99.7% confidence intervals, respectively. Figures are labeled for A) 25°C step 1, B) 25°C step 7, and C) 35°C step 1, D) 35°C step 5, E) 45°C step 1, F) 45°C step 4.*

A23. Reproducibility of sorption data and variability among samples

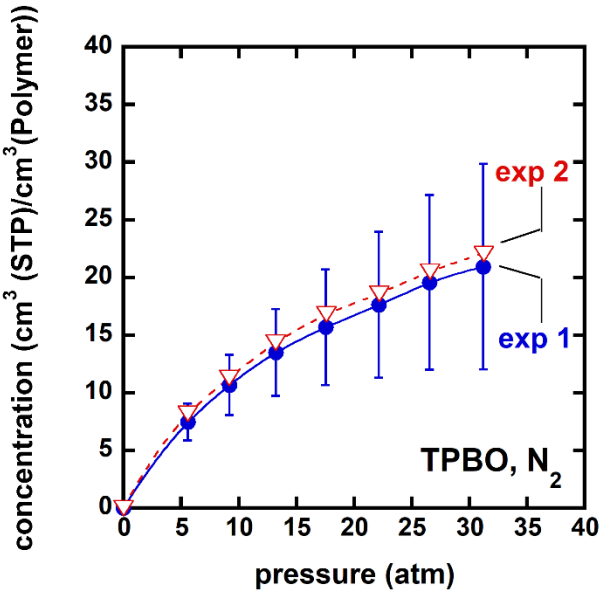


Figure A23: *Results of two independent N_2 sorption measurements in TPBO at 35°C, using two different polymer samples. The casual error, i.e., the departure between the two measurements, falls within the uncertainty window predicted by the linear error propagation method.*

A24. Evaluation of the final equilibrium pressure during barometric (pressure decay) sorption measurements

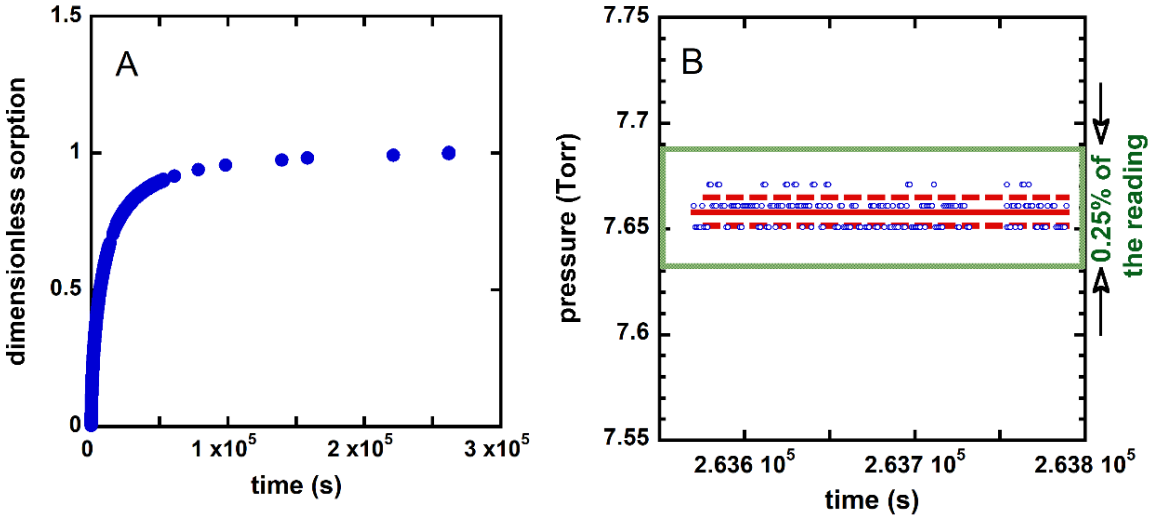


Figure A24: *A) methanol vapor sorption kinetics in Celazole at 25°C, step 1 (activity jump 0.06-0.14). B) Equilibrium pressure, at the end of the same sorption step: open circles are experimental pressure data; continuous red line is the average equilibrium pressure used to calculate the equilibrium solubility; dashed red line is the standard deviation of pressure reading.*

A25. Image Stabilization Algorithm Applied to Dilatometry Images

To determine the (x,y) shift which minimizes the differences between the initial image's reference region and the current image, an objective function to optimize is first defined. This function is the sum of squared errors between all overlapping pixels in the shifted image. i.e., $objective(shift) = \sum_{i,j=0} \left[\left(M_{i,j}^{ref} - M_{i,j}^{current}(shift) \right)^2 \right]$, hereafter referred to as "overlap error". Since finding an optimal position requires that the current image be shifted away from the reference, a padded border is used in the reference image, with the size of the border representing the largest expected disturbance the camera could possibly have. Furthermore, noise can have a significant impact on whether a true minimum is found or skipped when optimizing, and a number of numerical techniques can be applied to mitigate these problems, such as blurring the image intentionally to smooth out potential noise, normalizing the image to mitigate brightness changes, or other interpolative measures. In this work, only the former technique is applied via a 5x5 Gaussian blur kernel with $\sigma = 2$, as brightness was controlled directly and did not vary significantly over the course of an experiment. Finally, $shift$ values need not be restricted to integers. Most image handling libraries (OpenCV and ImageTransformations.jl, for instance) will allow the user to interpolate the image while shifting by non-integer distances.

After this, the following optimization process is applied:

1. An initial pixel search distance is chosen, in this work, we begin with a single pixel and refer to this value as δpx.
2. Shift the reference region of the current image by δpx in all ordinal and cardinal directions and calculate the overlap error that each shift creates when compared to the initial image, also calculate the overlap error when no shift occurs.
3. Compare all errors to find which shift minimized the overlap error.
    a. If the overlap error was minimized due to shifting in a direction, move the entire image in that direction and repeat step 2.
    b. If the error is minimized at the original position:
        i. If δpx is acceptably low, return the shifted position.
        ii. Otherwise, cut δpx by a factor (e.g., 2 or 3, etc) and repeat step 2.

A visualization of this process can be seen in Figure A25, demonstrating an example optimization where: in step one, a shift directly to the right minimized the error, so the position moved one pixel directly to the right and repeated shifting in step two, finding that no direction continued to decrease the overlap error, thus the shifting distance was cut by a factor of three and repeated, finding that a shift of $^1/_3\, px$ in the upper right direction continued to minimize the error.

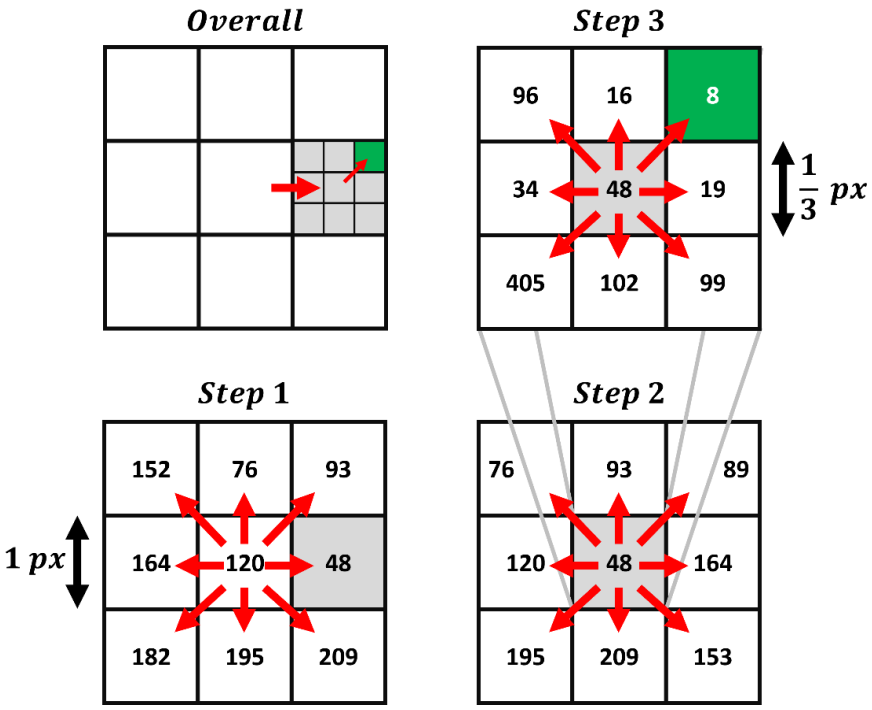


Figure A25: *Example image shifting search process going through three steps. The overall result is shown in the upper left quadrant of the figure. Red arrows denote shift attempts, values in the images' "pixels" represent the overlap error calculated by that corresponding shift. The optimal position found both in steps one and two is shown in gray, while the optimal position found in step 3 is shown in green.*

A26. Selected Polycarbonate and TPBO-0.25 Dilation Analyses (Animated)

In this section, we demonstrate two dilation steps of interest in this study. The first (Figure A26), demonstrates the acquisition of sub-pixel resolution of the apparatus.

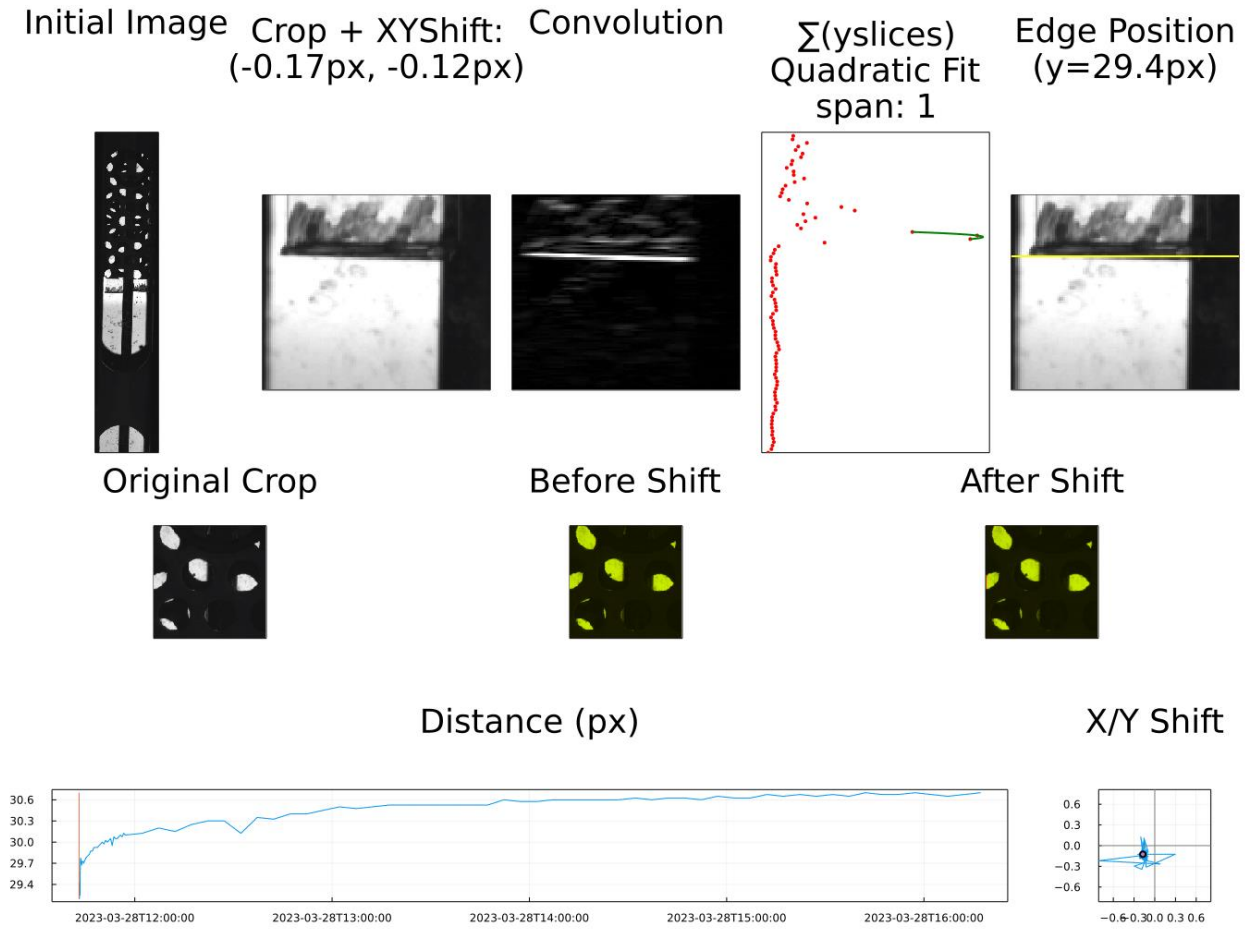


Figure A26: *Polycarbonate run 2 dilation analysis animation at 27.7 atm. The top row, from left to right, displays the original image, the cropped region (shifted), the convolved image, the edge position likelihood estimate and corresponding continuous function fit, and the final position indicator (yellow line). The middle row denotes shifting corrections, which were not significant in this step. The bottom row tracks distance over time, as well as the X/Y shift optimized, which did not exceed 0.25 pixels.*

Note that despite the entire range of the dilation during this step spans just 1.5 pixels, the analysis is able to pick up a comparatively smooth transition from the beginning of the

step to the next. The analysis animation demonstrates how this process occurs for each image taken during the step. Though stabilization may not have been required in the step shown above in Figure A26, in Figure A28 the need for stabilization can be directly seen in the shifting visualization row. Throughout the course of the experiment, the camera drifted up to three pixels down, slowly rising back to the original position in this particular step, then beginning to fall once more. This motion occurs quite slowly- around one pixel of motion per day -and would easily confound the step, which moved a total distance of 5 pixels. Finally, the pixel changes shown in the plot at the bottom of Figure A26 allow us to ascertain some information about the precision (though not necessarily the accuracy) of the experiment. Length changes of around 0.1 pixels are reliably able to be resolved with the apparatus in this case. Noting the calibrated pixel to centimeter conversion of $126\,\frac{px}{cm}$, this corresponds to resolving around $8\mu m$ distance changes reliably. This resolution can change depending on experimental conditions, as the particular resolution of the apparatus depends strongly on the ability to correct for camera motion, the distance of the camera from the same, the resolution of the camera, and the sharpness of the sample against the background. For example, in Figure A28 in the 1.14 atm step, distance changes are resolved to about 0.3 pixels, which corresponds to a resolution of roughly $20\mu m$.

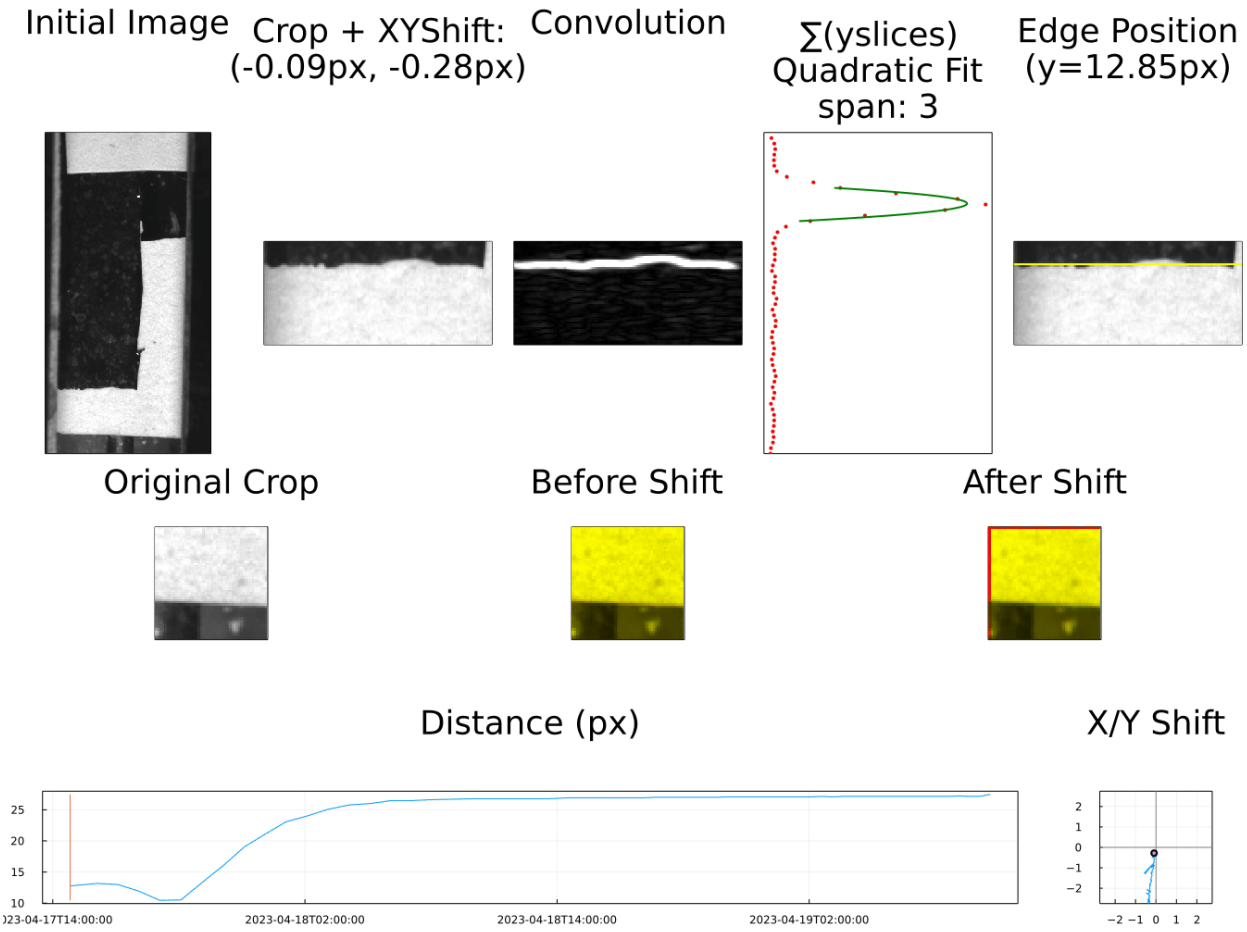


Figure A27: *Dilation analysis animation of a thermally rearranged polymer (TPBO-0.25) being dilated with butane at 0.68 atm. The top row, from left to right, displays the original image, the cropped region (shifted), the convolved image, the edge position likelihood estimate and corresponding continuous function fit, and the final position indicator (yellow line). The middle row denotes shifting corrections where red is the reference image, green is the current image, and yellow denotes pixel overlap. The bottom row tracks distance over time, as well as the X/Y shift optimized.*

Figure A27 presents an interesting case that spurred the requirement to use brass coupons to maintain sample straightness in future experiments that use thermally rearranged polymers. At the beginning of dilation, the application of around 0.68 atm butane caused no apparent dilation for the first 4 hours of the experiment, after which the sample initially appears to shrink when only looking at the analysis pixel distance output.

Looking towards the time lapse image of the sample reveals that during this initial 4 hour period, the sample is curling towards the camera, reducing its apparent length. During the next 2 days following this initial curling, the sample proceeds to relax to a straight position while it also dilates, reaching equilibrium while the sample to the right of it (TPBO-0.75, not shown in this analysis) appears to display the same qualitative behavior.

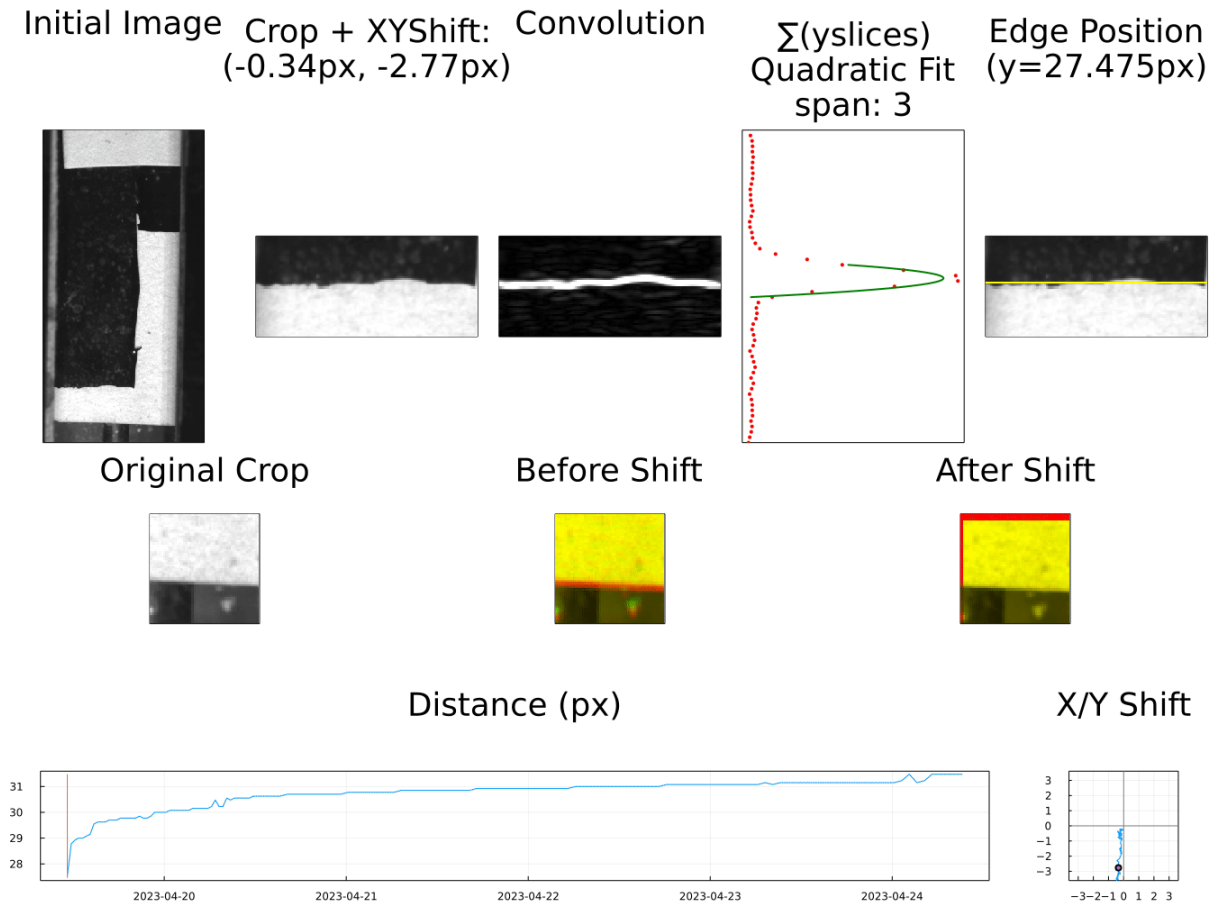


Figure A28: *Dilation analysis animation of a thermally rearranged polymer (TPBO-0.25) being dilated with butane at 1.14 atm. The top row, from left to right, displays the original image, the cropped region (shifted), the convolved image, the edge position likelihood estimate and corresponding continuous function fit, and the final position indicator (yellow line). The middle row denotes shifting corrections where red is the reference image, green is the current image, and yellow denotes pixel overlap. The bottom row tracks distance over time, as well as the X/Y shift optimized.*

Note that future steps do not result in this behavior for TPBO-0.25, as can be seen in the subsequent 1.14 atm step shown in Figure A28. This implies that, given residual stresses did indeed originally exist, that they are now unlocked. For TPBO-0.75 (the right sample), the sample continues to curl and relax for an additional step, before returning to Fickian-like dilation behavior in further steps. This behavior is present regardless of the initial step pressure. For example, a run was conducted with TPBO-0.25 and TPBO-0.00 in parallel, shown in Figure A29 with butane at 0.33 atm, demonstrating much more dramatic curling in the TPBO-0.25 sample. A summary of these step kinetics can also be found in Section A32.

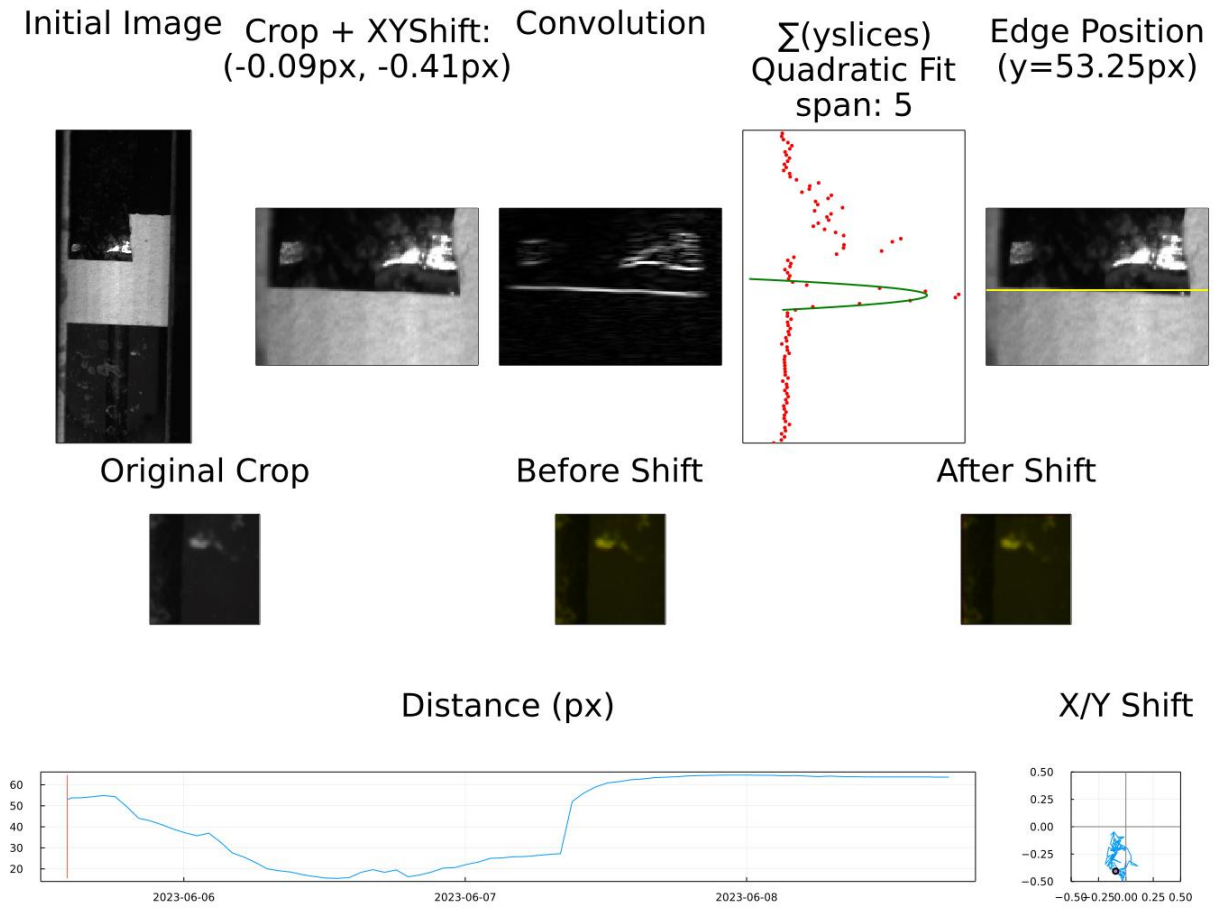


Figure A29: *Dilation analysis animation of a thermally rearranged polymer (TPBO-0.25) being dilated with butane at 0.33 atm. The top row, from left to right, displays the original image, the cropped region (shifted), the convolved image, the edge position likelihood estimate and corresponding continuous function fit, and the final position indicator (yellow line). The middle row denotes shifting corrections where red is the reference image, green is the current image, and yellow denotes pixel overlap. The bottom row tracks distance over time, as well as the X/Y shift optimized.*

A27. Camera calibration factor

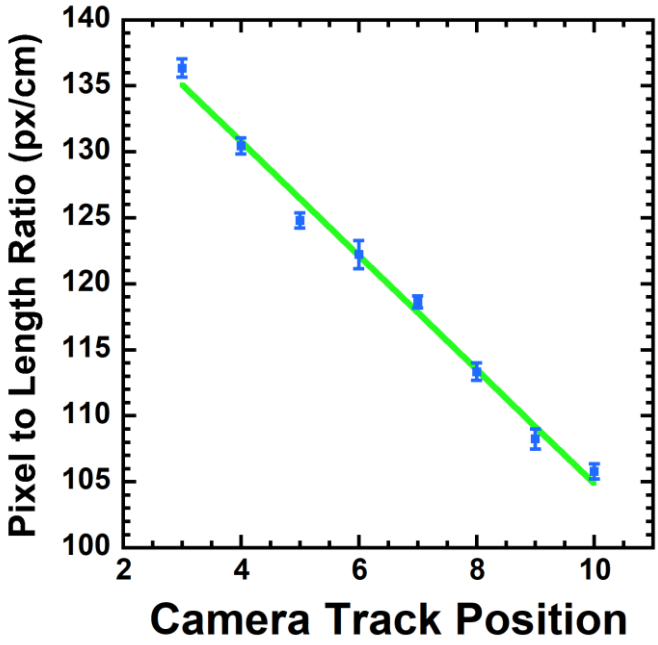


Figure A30: *Camera calibration for sample distance estimation based on dimensionless camera track position markers, which are arbitrary (but evenly spaced) points along the camera track. The calibration curve relates the number of pixels observed by the camera to the length that many pixels represent, expressed in pixels per centimeter.*

Camera calibrations were found via suspending a ruler in the Jerguson gage and determining how many pixels corresponded to a distance change in the ruler (where the polymer sample would be placed during an experiment). An example image can be seen in Figure A31 and the corresponding calibration data can be seen in Figure A30. It is worth noting that though pixel to distance calibrations are not expected to follow a linear relationship, the total distance which the camera's track spans is small enough that a linear approximation is more than sufficient to generate pixel to distance conversion factors within the error of the available measurement methods used in this work.

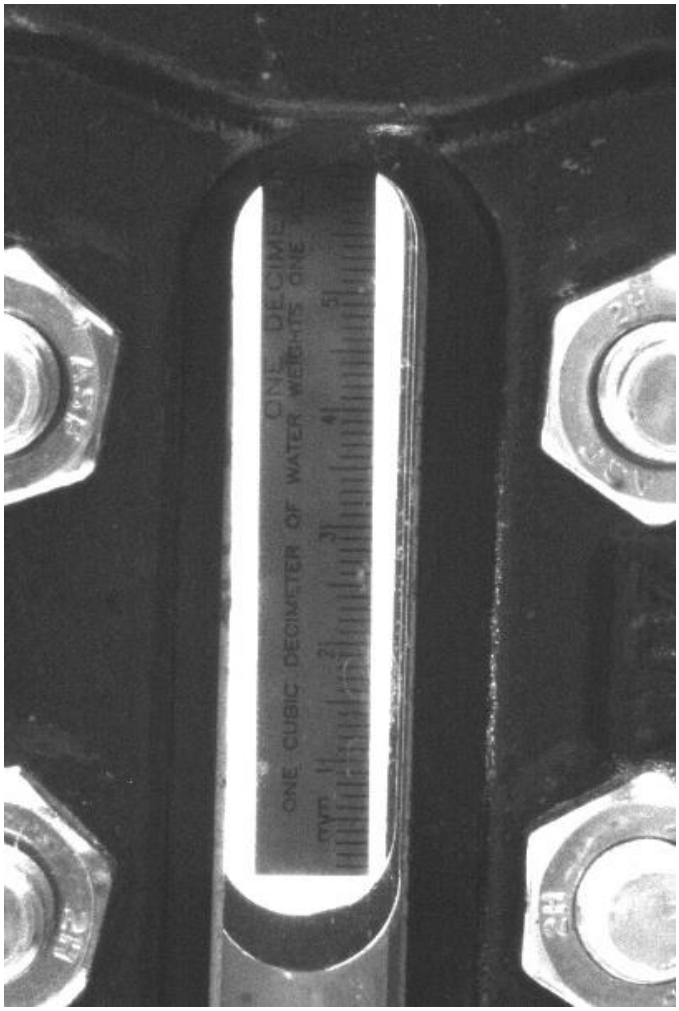


Figure A31: *Example image for determining the apparatus pixel to length calibration factor for a single camera position.*

A28. Verification of both Isotropic Dilation Behavior via Polycarbonate and Apparatus Consistency via TPBO-0.25 using CO_2 Dilation

A key systematic error that could affect polymer dilation results is the assumption of isotropic dilation being invalidated for a particular sample [191]. To test this in the case of polycarbonate, two additional samples were cut orthogonally to each other from the original sheet with which samples 1-3 were cut. These samples were similar in length, with the "vertical" sample being $5.0 \pm 0.1\ cm$ and the "horizontal" sample being $4.7 \pm 0.1\ cm$, and the run using the same pixel to centimeter ratio as the previous runs of $126.5 \pm 0.7 \frac{px}{cm}$.

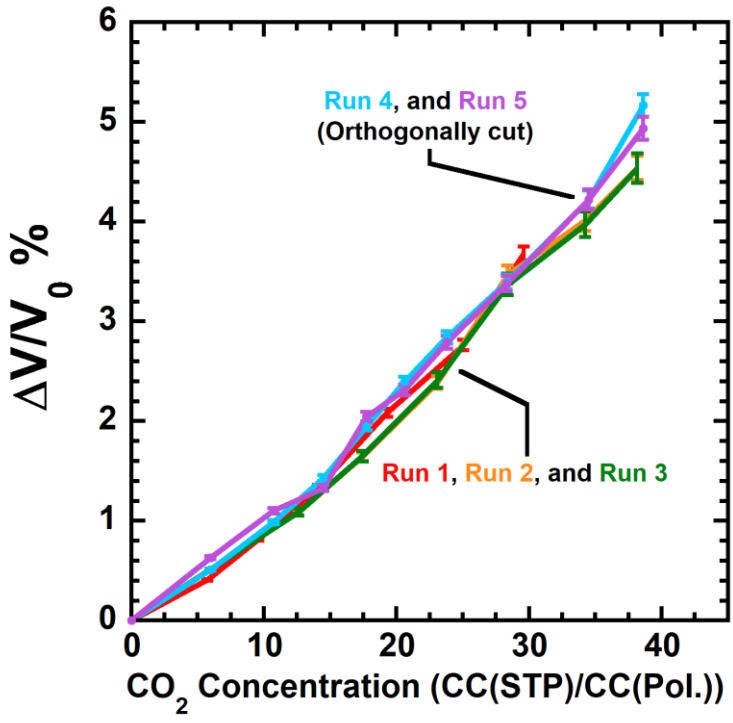


Figure A32: *Fractional dilation of orthogonally cut polycarbonate samples (4, blue and 5, purple) at 35°C, as a function of CO_2 concentration in the polymer sample and compared to previous data shown in this work (runs 1-3). Error bars were estimated via linear error propagation*[96–98] *without covariance. Run 1 was completed alone, runs 2 and 3 were completed in parallel and runs 4 and 5 were completed in parallel.*

These two runs, denoted as runs 4 (vertically cut) and 5 (horizontally cut), display identical dilation behavior (see Figure 21 in Section 4.5.1) within experimental uncertainty. Minor deviations near the end of the run can be attributed to sample straightness prior to the experiment, where even minor curling can introduce error due to plasticizing agents allowing the sample to straighten during the run, artificially inflating the degree of dilation. This key source of systematic error that can inherently be controlled for via longer samples, which will straighten the sample prior to dilation. Other techniques, such as a sample fixture designed to hold the sample straight while still allowing downward movement, may also further reduce this issue.

Though these results verify that dilation occurs isotopically for polycarbonate (a bulk, glassy polymer), more exotic materials may not exhibit the same behavior. Examples of this include thermally rearranged polymers, which have the potential to contain internal stresses that may cause directional swelling, and polymers with nanofiller agents that may preferentially align themselves (such as carbon nanotubes), which may restrict or permit swelling along the filler agents' alignment. This potential behavior can be verified and even investigated directly in the same manner as was conducted for the polycarbonate samples in this work. That is, a dilation experiment utilizing multiple samples measured in parallel and which were cut in variable directions.

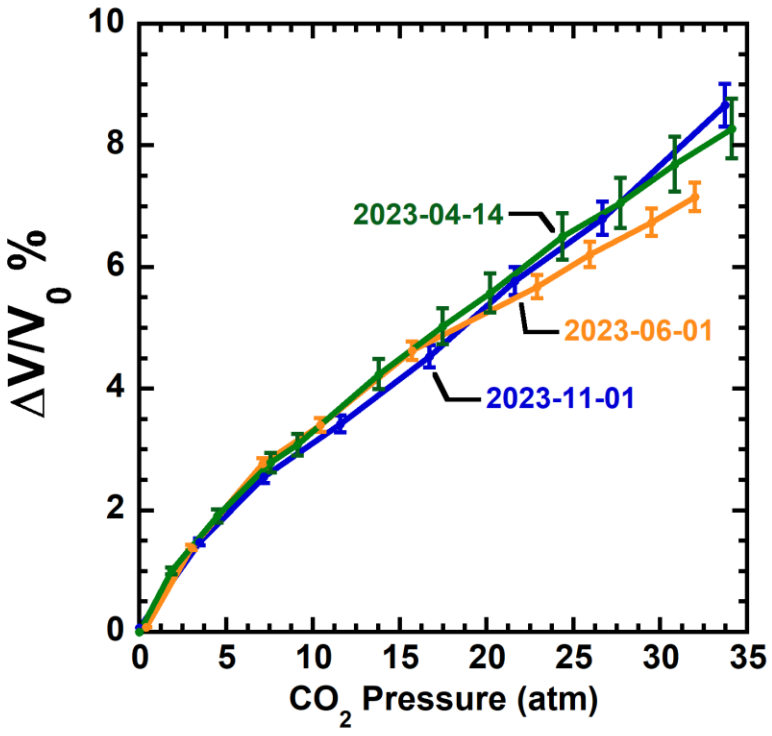


Figure A33: *Fractional dilation of TPBO-0.25 samples at 35°C, as a function of CO_2 pressure. Samples were taken from multiple batches spanning 2023, beginning with April, 2023 (green), June, 2023 (yellow), and November 2023 (blue). Error bars were estimated via linear error propagation*[96–98] *without covariance.*

To further assess both the consistency of the apparatus as well as the variability of the dilation characteristics of TPBO polymers, TPBO-0.25 was chosen as a case study and experiments were repeated three times throughout the year 2023 (see Figure A33). Results show that, within error, the same dilation isotherm was collected each time, with the highest variability appearing in the June, 2023 run. This run likely experienced a slight downturn in apparent dilation due to sample curling without a coupon in place to remove this source of systematic error. Samples from the April, 2023 run were unlikely to swell due to being backed by a metal clip and the November, 2023 samples were constrained via a brass coupon.

A29. Dual Mode and Dual Mode Dilation Parameters Used in This Work

Table A10: *Fitted dual mode dilation and dual mode values for CO_2 sorption in various polymers used in this work at 35°C. Uncertainties were determined using the jackknife uncertainty method[199].*

Polymer	V_D $\left(\frac{cm^3}{mol}\right)$	f	C'_H $\left(\frac{cm^3(STP)}{cm^3(pol)}\right)$	b (MPa^{-1})	k_D $\left(\frac{cm^3(STP)}{cm^3(pol)}MPa^{-1}\right)$	Source
TPBO-0.00	40.95 ± 0.42	0.10 ± 0.01	82.18 ± 2.31	3.56 ± 0.26	12.67 ± 0.58	*This work*
TPBO-0.25	36.21 ± 0.71	0.09 ± 0.01	68.54 ± 0.43	4.86 ± 0.06	18.64 ± 0.17	[75]*
TPBO-0.50	29.97 ± 0.61	0.15 ± 0.01	82.63 ± 3.07	5.16 ± 0.44	19.56 ± 0.77	*This work*
TPBO-0.75	29.77 ± 0.66	0.13 ± 0.01	80.91 ± 2.32	5.11 ± 0.37	17.82 ± 0.56	*This work*
TPBO-1.00	25.50 ± 1.12	0.22 ± 0.02	82.03 ± 4.05	5.95 ± 0.60	17.73 ± 1.04	*This work*
TPHI-1.00	25.81 ± 0.98	0.35 ± 0.04	15.82 ± 4.50	2.437**	7.25 ± 1.22	*This work*
PC	32.36 ± 0.10	0.20 ± 0.01	12.64	2.46	8.25	[186]
PTMSP	1.64 ± 0.72	2.6 ± 3.1	80.17	0.82	15.70	[174]
AF1600	51.21 ± 0.89	−0.48 ± 0.02	21.58	0.72	11.04	[198]
AF2400	20.77 ± 0.43	−0.38 ± 0.03	26.44	0.65	15.73	[198]
CTA	22.09 ± 0.17	0.65 ± 0.04	5.98	14.74	20.64	[76]
PIM-1	54.69 ± 0.47	0.000 ± 0.003	63.10	3.88	16.45	[76]

**All V_D and f values were fit within this work, the source field denotes that both sorption and dilation data was found within the work cited, with the exception of TPBO-0.25, with which dilation data was taken specifically for this work.*

***Due to very low solubility and a much more linear sorption behavior that TPBOs, there is near infinite variance in TPHI-1.00's affinity value, that is, many values can successfully represent this isotherm within the other parameter's uncertainties. The dual mode values are simply used as interpolative tools in an effort to acquire the (physically meaningful) V_D and f values.*

PTMSP fits exhibits such high uncertainty due to its dilation isotherm, which does not behave in a way that can be readily described by the dual mode dilation model. Similarly, to fit well, f values for the two perfluorinated polymers Teflon AF1600 and AF2400, must be negative. Normally, constraints should be applied which limit $0 \leq f \leq 1$. However, in this case the model is primarily used to act as an interpolator to calculate $\frac{d\left(\frac{\Delta V}{V_0}\right)}{dp}$, thus, limits were not applied to ensure fits which describe the original data as closely as possible.

A30. Propagating Uncertainty through the Fractional Dilation Formula

Fractional dilation can be expressed as

$$\nu = \frac{\Delta V}{V_0} = \frac{V_f - V_i}{V_i} = \left(\frac{L_f}{L_i}\right)^3 - 1$$

Where ν is fractional dilation, and V_f, L_f and V_i, L_i are the final and initial volumes and lengths of the sample during dilation.

In addition, we can break L_f into directly measured variables, via

$$L_f = L_i + \Delta L$$

$$\Delta L = {}^{\Delta px}/_{\vartheta}$$

Where ΔL is the change in sample length in centimeters and ϑ is the camera pixel-to-length conversion ratio in units of $\frac{px}{cm}$. We can then express fractional dilation as

$$\nu = \left(\frac{L_i + \frac{\Delta px}{\vartheta}}{L_i}\right)^3 - 1$$

In this work, we acquire direct uncertainties on L_i and ϑ. Δpx is a special case, that is, since Δpx is evaluated by computer vision techniques and not direct measurement (i.e., using conventional tools), a straightforward definition of the uncertainty this value contains is difficult to provide. So long as certain conditions are met which conveniently minimize the overall uncertainty, Δpx contributes little to the overall error of the experiment.

Linear error propagation simplifies to the following formula in the absence of covariance.

$$\sigma_v = \sqrt{\left(\frac{\partial v}{\partial L_i}\right)^2 \sigma_{L_i}^2 + \left(\frac{\partial v}{\partial \vartheta}\right)^2 \sigma_C^2 + \left(\frac{\partial v}{\partial \Delta px}\right)^2 \sigma_{\Delta px}^2}$$

1. $\frac{\partial v}{\partial L_i}$
   A. $\frac{\partial v}{\partial L_i}\left(\left(\frac{L_i+\frac{\Delta px}{\vartheta}}{L_i}\right)^3 - 1\right) = (u)^3 - 1$ where $u = \frac{L_i+\frac{\Delta px}{\vartheta}}{L_i} \rightarrow 3u^2 du$

      Completing the substitution yields $du = \frac{d}{dL_i}\left(\frac{L_i+\frac{\Delta px}{\vartheta}}{L_i}\right) = \frac{d}{dL_i}\left(1 + \frac{\Delta px}{\vartheta \cdot L_i}\right) = -\frac{\Delta px}{\vartheta \cdot L_i^2} dL_i$

   B. Recombing

      $3u^2 du = 3\left(\frac{L_i+\frac{\Delta px}{\vartheta}}{L_i}\right)^2 \cdot \left(-\frac{\Delta px}{\vartheta \cdot L_i^2}\right) dL_i = -3\frac{\left(L_i+\frac{\Delta px}{\vartheta}\right)^2}{L_i^2} \cdot \left(\frac{\Delta px}{\vartheta \cdot L_i^2}\right) dL_i = -3 \cdot \Delta px \frac{\left(L_i+\frac{\Delta px}{\vartheta}\right)^2}{L_i^4 \cdot \vartheta} dL_i$

   C. The term $\left(L_i + \frac{\Delta px}{\vartheta}\right)^2$ can then be rearranged as:

$\left(L_i + \frac{\Delta px}{\vartheta}\right)^2 = L_i^2 + 2 \cdot L_i \frac{\Delta px}{\vartheta} + \frac{(\Delta px)^2}{\vartheta^2} = \frac{1}{\vartheta^2}(L_i^2\vartheta^2 + 2L_i(\Delta px)\vartheta + (\Delta px)^2) = \frac{1}{\vartheta^2}(L_i\vartheta + \Delta px)^2$

$$\hookrightarrow \frac{\partial v}{\partial L_i} = -3 \cdot \Delta px \frac{(L_i\vartheta + \Delta px)^2}{L_i^4 \cdot \vartheta^3} dL_i$$

2. $\frac{\partial v}{\partial \vartheta}$
   A. $\frac{\partial}{\partial \vartheta}\left(\left(\frac{L_i+\frac{\Delta px}{\vartheta}}{L_i}\right)^3 - 1\right) = \frac{\partial}{\partial \vartheta}\left(\frac{\left(L_i+\frac{\Delta px}{\vartheta}\right)^3}{L_i{}^3} - 1\right) = \left(\frac{1}{L_i{}^3}\right)\frac{\partial}{\partial \vartheta}\left(\left(L_i + \frac{\Delta px}{\vartheta}\right)^3\right) = \left(\frac{1}{L_i{}^3}\right)\frac{\partial}{\partial \vartheta}(u^3)$
      where $u = L_i + \frac{\Delta px}{\vartheta}$
   B. $\left(\frac{1}{L_i{}^3}\right)\frac{\partial}{\partial \vartheta}(u^3) = \frac{1}{(L_i)^3} 3u^2 du$ where $du = \frac{d}{d\vartheta}\left(L_i + \frac{\Delta px}{\vartheta}\right) = -\frac{\Delta px}{\vartheta^2} d\vartheta$
   C. Recombining

      $\left(\frac{1}{L_i{}^3}\right) 3u^2 du = \frac{3\left(L_i+\frac{\Delta px}{\vartheta}\right)^2}{L_i{}^3} \cdot \left(-\frac{\Delta px}{\vartheta^2}\right) d\vartheta = -3 \cdot \Delta px \frac{\left(L_i+\frac{\Delta px}{\vartheta}\right)^2}{L_i^3 \cdot \vartheta^2} d\vartheta$

   D. Noting 1C, we see that 2C can be expressed as $-3 \cdot \Delta px \frac{\frac{1}{\vartheta^2}(L_i\vartheta+\Delta px)^2}{L_i^3 \cdot \vartheta^2} d\vartheta$

$$\hookrightarrow \frac{\partial v}{\partial \vartheta} = -3 \cdot \Delta px \frac{(L_i\vartheta + \Delta px)^2}{L_i^3 \cdot \vartheta^4} d\vartheta$$

3. $\frac{\partial v}{\partial(\Delta px)}$

A. $\frac{\partial}{\partial(\Delta px)}\left(\left(\frac{L_i+\frac{\Delta px}{\vartheta}}{L_i}\right)^3-1\right)=\frac{1}{{L_i}^3}\frac{\partial}{\partial(\Delta px)}(u^3)$ where $u=L_i+\frac{\Delta px}{\vartheta}$

B. $\frac{1}{(L_i)^3}\frac{\partial}{\partial(\Delta px)}(u^3)=\frac{1}{(L_i)^3}3u^2du$ where $du=\frac{d}{d(\Delta px)}\left(L_i+\frac{\Delta px}{\vartheta}\right)=\frac{1}{\vartheta}d(\Delta px)$

C. Recombining $\left(\frac{1}{{L_i}^3}\right)3u^2du=\frac{3\left(L_i+\frac{\Delta px}{\vartheta}\right)^2}{L_i^3}\cdot\frac{1}{\vartheta}d(\Delta px)=3\frac{\left(L_i+\frac{\Delta px}{\vartheta}\right)^2}{L_i^3\cdot\vartheta}d(\Delta px)$

D. Again, using 1C, the expression in 3C. becomes $3\frac{\frac{1}{\vartheta^2}(L_i\vartheta+\Delta px)^2}{L_i^3\cdot\vartheta}d(\Delta px)$

$$\frac{\partial v}{\partial(\Delta px)}=3\frac{(L_i\vartheta+\Delta px)^2}{L_i^3\cdot\vartheta^3}d(\Delta px)$$

Applying these expressions towards the linear error propagation formula yields

$$\sigma_v$$

$$=\sqrt{\left(-3\cdot\Delta px\frac{(L_i\vartheta+\Delta px)^2}{L_i^4\cdot\vartheta^3}\right)^2\sigma_{L_i}^2+\left(-3\cdot\Delta px\frac{(L_i\vartheta+\Delta px)^2}{L_i^3\cdot\vartheta^4}\right)^2\sigma_\vartheta^2+\left(3\frac{(L_i\vartheta+\Delta px)^2}{L_i^3\cdot\vartheta^3}\right)^2\sigma_{\Delta px}^2}$$

$$\hookrightarrow\sqrt{9\left(\Delta px\frac{(L_i\vartheta+\Delta px)^2}{L_i^4\cdot\vartheta^3}\right)^2\sigma_{L_i}^2+9\left(\Delta px\frac{(L_i\vartheta+\Delta px)^2}{L_i^3\cdot\vartheta^4}\right)^2\sigma_\vartheta^2+9\left(\frac{(L_i\vartheta+\Delta px)^2}{L_i^3\cdot\vartheta^3}\right)^2\sigma_{\Delta px}^2}$$

$$\hookrightarrow 3\cdot\sqrt{\Delta px^2\frac{(L_i\vartheta+\Delta px)^4}{L_i^8\cdot\vartheta^6}\sigma_{L_i}^2+\Delta px^2\frac{(L_i\vartheta+\Delta px)^4}{L_i^6\cdot\vartheta^8}\sigma_\vartheta^2+\frac{(L_i\vartheta+\Delta px)^4}{L_i^6\cdot\vartheta^6}\sigma_{\Delta px}^2}$$

$$\hookrightarrow 3\cdot\sqrt{\frac{(L_i\vartheta+\Delta px)^4}{L_i^6\cdot\vartheta^6}\left(\Delta px^2\frac{\sigma_{L_i}^2}{L_i^2}+\Delta px^2\frac{\sigma_\vartheta^2}{\vartheta^2}+\sigma_{\Delta px}^2\right)}$$

$$\boldsymbol{\sigma_v=3\cdot\frac{(L_i\vartheta+\Delta px)^2}{(L_i\vartheta)^3}\sqrt{\Delta px^2\left(\frac{\sigma_{L_i}^2}{L_i^2}+\frac{\sigma_\vartheta^2}{\vartheta^2}\right)+\sigma_{\Delta px}^2}}$$

As an example calculation using this relationship, a system with

- A sample length (L_i) of $4\pm0.1cm$
- A pixel to cm calibration (ϑ) of $125\pm0.5\frac{px}{cm}$
- And a change in sample length (Δpx) of $5\pm0.025px$

The fractional dilation would be 0.0301 ± 0.00079. If this analysis was to be done without fractional differences in the pixel change, that is, if the uncertainty of the pixel change spanned one pixel ($\sigma_{\Delta px} = 0.5px$) as would likely be the case if this analysis was done manually rather than through computational means, then the uncertainty in fractional dilation would be much (nearly 10 times) higher at 0.0303 ± 0.00824.

Given the simplification $\sigma_\nu \approx 3 \cdot \frac{(L_i\vartheta+\Delta px)^2}{L_i^4\vartheta^3}\Delta px \cdot \sigma_{L_i}$, used in the main manuscript for demonstrating the importance of L_i and lack of importance of σ_{L_i}, the same conditions shown above would result in an uncertainty of 0.00077 rather than 0.00079, or a 3.1% error in the actual uncertainty value.

A31. Evidence of Thermally Induced Camera Position Error

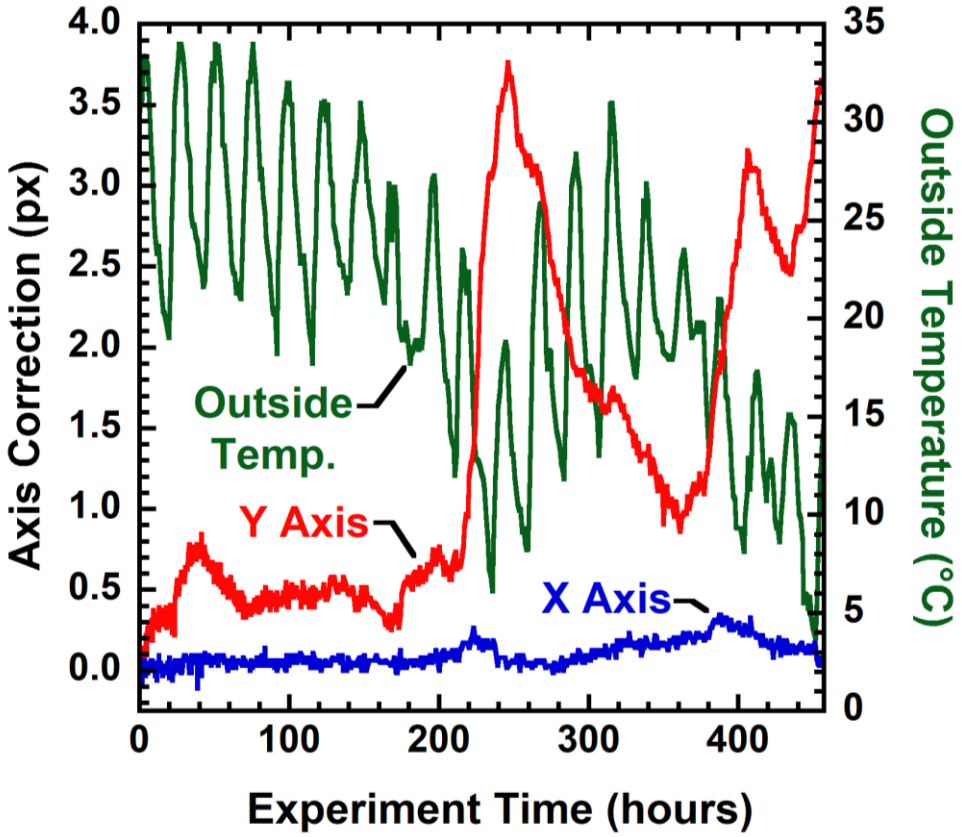


Figure A34: *Image stabilization shifts in pixels (left Y axis) required to stabilize a dilation experiment's sample images over several hundred hours. Shift distances are shown in pixels for the X axis (blue curve) and Y axis (red curve) of the sample image at a given experiment time (hours). The right Y axis denotes the outdoor air temperature in °C on the University of Oklahoma Norman Campus (green curve) at the same time the data was being taken.*

From September 27th, 2023 to October 16th, 2023, images were taken at rates spanning from once a minute at the fastest (at the start of the experiment) to once an hour at the slowest (starting September 29th, until the end of the experiment). During this time, the outdoor temperature was observed to drop over three days on (Oct. 4th – 7th), then again over Oct. 10th – 16th. Both of these temperature changes corresponded to an extremely large upward shift in the camera image correction, with little horizontal shift necessary to stabilize the

image. This matches the concern that the camera stand, which is not inside of a temperature-controlled hood, is contracting due to a small change in the building temperature and requiring an opposing upward correction of the image.

Unfortunately, indoor temperature data in the building was not recorded. However, it is likely that linear movement alone is not the only factor influencing the shift required. This experiment used a camera pixel to cm calibration factor of 135 $\frac{px}{cm}$, at this distance, a vertical correction of roughly 3 pixels due to temperature changes would correspond to 0.022cm of camera movement. With the camera being placed 10 inches above the base of the stand and the stand being made of steel, which has a linear thermal expansion coefficient in the range of 10-17 $°C^{-1}$ (this large uncertainty is due to the uncertainty in the type of steel used in the stand) [214], the expected motion due to a 10°C change is 0.001cm, an order of magnitude lower. Though air conditioning may lag behind fluctuating or unexpected weather to some degree, a 10°C change is unlikely, and the additional motion could possibly be due to the stand bending slightly while expanding. This is unlikely to invalidate experimental results or even image stabilization corrections due to the small angle approximation allowing extremely slight changes in camera angle to be modeled as linear motion [215].

A32. n-Butane swelling kinetics in TPBOs

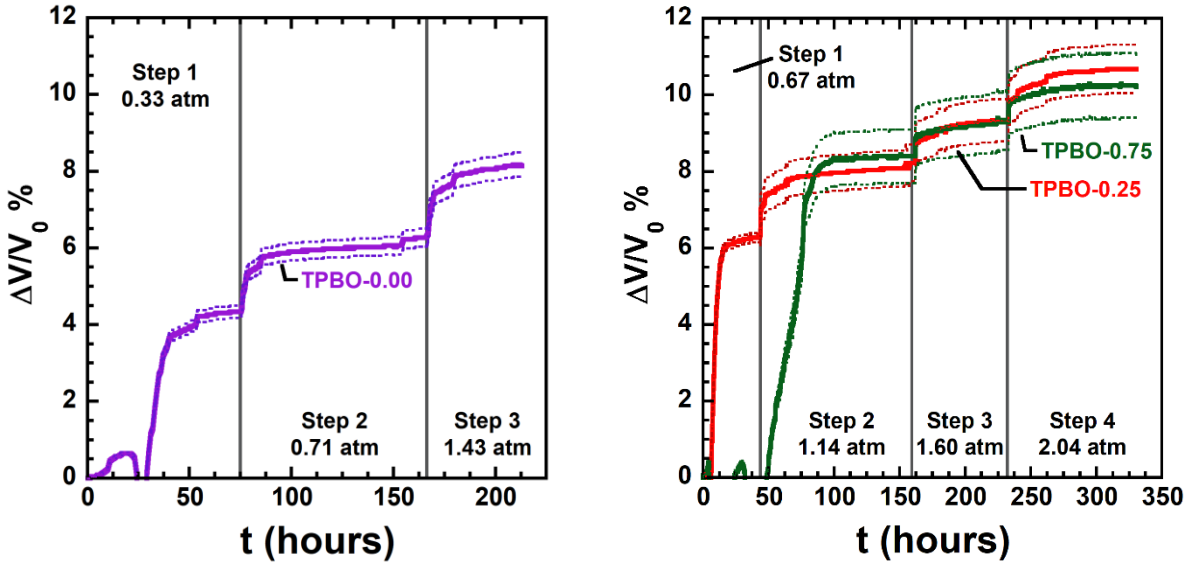


Figure A35: *Butane in TPBO-0.25 (red line), TPBO-0.75 (green line), and TPBO-0.00 (purple line) dilation kinetics in percent volume dilation at 35°C as a function of time since the first dilation step. Dashed lines denote experimental uncertainty found via linear error propagation*[96–98]*, one standard deviation from the measured value.*

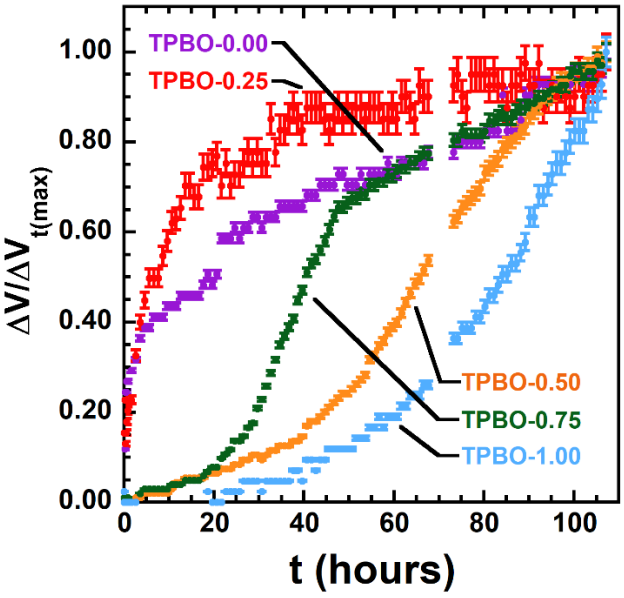


Figure A36: *Butane dilation kinetics expressed as for various TPBO polymers, including 00 (purple), 25 (red), 50 (orange), 75 (green), and 100 (blue) at 35°C as a function of time and at 0.88 atm. Dashed lines denote experimental uncertainty found via linear error propagation*[96–98]*, one standard deviation from the measured value.*

References

[1] M. Galizia, W.S. Chi, Z.P. Smith, T.C. Merkel, R.W. Baker, B.D. Freeman, *50th Anniversary Perspective*: Polymers and Mixed Matrix Membranes for Gas and Vapor Separation: A Review and Prospective Opportunities, Macromolecules 50 (2017) 7809–7843. https://doi.org/10.1021/acs.macromol.7b01718.

[2] Membrane Filtration Market to hit USD 23.7 billion by 2028, (n.d.). https://www.globenewswire.com/en/news-release/2021/05/28/2237983/0/en/Membrane-Filtration-Market-to-hit-USD-23-7-billion-by-2028-Insights-on-Recent-Trends-Size-Share-Growth-Opportunities-Key-Developments-and-Future-Outlook-Adroit-Market-Research.html (accessed November 12, 2021).

[3] M. Das, J.D. Perry, W.J. Koros, Gas-Transport-Property Performance of Hybrid Carbon Molecular Sieve−Polymer Materials, Ind. Eng. Chem. Res. 49 (2010) 9310–9321. https://doi.org/10.1021/ie100843r.

[4] A. Thran, G. Kroll, F. Faupel, Correlation between fractional free volume and diffusivity of gas molecules in glassy polymers, J. Polym. Sci. Part B Polym. Phys. 37 (1999) 3344–3358. https://doi.org/10.1002/(SICI)1099-0488(19991201)37:23<3344::AID-POLB10>3.0.CO;2-A.

[5] P.H. Pfromm, W.J. Koros, Accelerated physical ageing of thin glassy polymer films: evidence from gas transport measurements, Polymer 36 (1995) 2379–2387. https://doi.org/10.1016/0032-3861(95)97336-E.

[6] C. Zhou, The accelerated CO2 plasticization of ultra-thin polyimide films and the effect of surface chemical cross-linking on plasticization and physical aging, J. Membr. Sci. 225 (2003) 125–134. https://doi.org/10.1016/j.memsci.2003.07.006.

[7] B.W. Rowe, B.D. Freeman, D.R. Paul, Influence of previous history on physical aging in thin glassy polymer films as gas separation membranes, Polymer 51 (2010) 3784–3792. https://doi.org/10.1016/j.polymer.2010.06.004.

[8] J.D. Wind, C. Staudt-Bickel, D.R. Paul, W.J. Koros, The Effects of Crosslinking Chemistry on CO 2 Plasticization of Polyimide Gas Separation Membranes, Ind. Eng. Chem. Res. 41 (2002) 6139–6148. https://doi.org/10.1021/ie0204639.

[9] A.M.W. Hillock, W.J. Koros, Cross-Linkable Polyimide Membrane for Natural Gas Purification and Carbon Dioxide Plasticization Reduction, Macromolecules 40 (2007) 583–587. https://doi.org/10.1021/ma062180o.

[10] H. An, A.S. Lee, I. Kammakakam, S. Sang Hwang, J.-H. Kim, J.-H. Lee, J. Suk Lee, Bromination/debromination-induced thermal crosslinking of 6FDA-Durene for aggressive gas separations, J. Membr. Sci. 545 (2018) 358–366. https://doi.org/10.1016/j.memsci.2017.09.083.

[11] T.-S. Chung, L.Y. Jiang, Y. Li, S. Kulprathipanja, Mixed matrix membranes (MMMs) comprising organic polymers with dispersed inorganic fillers for gas separation, Prog. Polym. Sci. 32 (2007) 483–507. https://doi.org/10.1016/j.progpolymsci.2007.01.008.

[12] M. Minelli, S. Campagnoli, M.G. De Angelis, F. Doghieri, G.C. Sarti, Predictive Model for the Solubility of Fluid Mixtures in Glassy Polymers, Macromolecules 44 (2011) 4852–4862. https://doi.org/10.1021/ma200602d.

[13] M.C. Ferrari, M. Galizia, M.G. De Angelis, G.C. Sarti, Gas and Vapor Transport in Mixed Matrix Membranes Based on Amorphous Teflon AF1600 and AF2400 and Fumed Silica, Ind. Eng. Chem. Res. 49 (2010) 11920–11935. https://doi.org/10.1021/ie100242q.

[14] M. Alberto, R. Bhavsar, J.M. Luque-Alled, A. Vijayaraghavan, P.M. Budd, P. Gorgojo, Impeded physical aging in PIM-1 membranes containing graphene-like fillers, J. Membr. Sci. 563 (2018) 513–520. https://doi.org/10.1016/j.memsci.2018.06.026.

[15] K.A. Stevens, Z.P. Smith, K.L. Gleason, M. Galizia, D.R. Paul, B.D. Freeman, Influence of temperature on gas solubility in thermally rearranged (TR) polymers, J. Membr. Sci. 533 (2017) 75–83. https://doi.org/10.1016/j.memsci.2017.03.005.

[16] S.H. Han, J.E. Lee, K.-J. Lee, H.B. Park, Y.M. Lee, Highly gas permeable and microporous polybenzimidazole membrane by thermal rearrangement, J. Membr. Sci. 357 (2010) 143–151. https://doi.org/10.1016/j.memsci.2010.04.013.

[17] Z.P. Smith, K. Czenkusch, S. Wi, K.L. Gleason, G. Hernández, C.M. Doherty, K. Konstas, T.J. Bastow, C. Álvarez, A.J. Hill, A.E. Lozano, D.R. Paul, B.D. Freeman, Investigation of the chemical and morphological structure of thermally rearranged polymers, Polymer 55 (2014) 6649–6657. https://doi.org/10.1016/j.polymer.2014.10.055.

[18] A.M.W. Hillock, S.J. Miller, W.J. Koros, Crosslinked mixed matrix membranes for the purification of natural gas: Effects of sieve surface modification, J. Membr. Sci. 314 (2008) 193–199. https://doi.org/10.1016/j.memsci.2008.01.046.

[19] M. Askari, T.-S. Chung, Natural gas purification and olefin/paraffin separation using thermal cross-linkable co-polyimide/ZIF-8 mixed matrix membranes, J. Membr. Sci. 444 (2013) 173–183. https://doi.org/10.1016/j.memsci.2013.05.016.

[20] S. Luo, Q. Zhang, L. Zhu, H. Lin, B.A. Kazanowska, C.M. Doherty, A.J. Hill, P. Gao, R. Guo, Highly Selective and Permeable Microporous Polymer Membranes for Hydrogen Purification and CO 2 Removal from Natural Gas, Chem. Mater. 30 (2018) 5322–5332. https://doi.org/10.1021/acs.chemmater.8b02102.

[21] S. Luo, J. Liu, H. Lin, B.A. Kazanowska, M.D. Hunckler, R.K. Roeder, R. Guo, Preparation and gas transport properties of triptycene-containing polybenzoxazole (PBO)-based polymers derived from thermal rearrangement (TR) and thermal cyclodehydration (TC) processes, J. Mater. Chem. A 4 (2016) 17050–17062. https://doi.org/10.1039/C6TA03951K.

[22] S. Luo, J.R. Wiegand, B. Kazanowska, C.M. Doherty, K. Konstas, A.J. Hill, R. Guo, Finely Tuning the Free Volume Architecture in Iptycene-Containing Polyimides for Highly Selective and Fast Hydrogen Transport, Macromolecules 49 (2016) 3395–3405. https://doi.org/10.1021/acs.macromol.6b00485.

[23] T.J. Corrado, Z. Huang, D. Huang, N. Wamble, T. Luo, R. Guo, Pentiptycene-based ladder polymers with configurational free volume for enhanced gas separation performance and physical aging resistance, Proc. Natl. Acad. Sci. 118 (2021) e2022204118. https://doi.org/10.1073/pnas.2022204118.

[24] R.D. Crist, Z. Huang, R. Guo, M. Galizia, Effect of thermal treatment on the structure and gas transport properties of a triptycene-based polybenzoxazole exhibiting configurational free volume, J. Membr. Sci. 597 (2020) 117759. https://doi.org/10.1016/j.memsci.2019.117759.

[25] J.G. Wijmans, R.W. Baker, The solution-diffusion model: a review, J. Membr. Sci. 107 (1995) 1–21. https://doi.org/10.1016/0376-7388(95)00102-I.

[26] K.P. Bye, V. Loianno, T.N. Pham, R. Liu, J.S. Riffle, M. Galizia, Pure and mixed fluid sorption and transport in Celazole® polybenzimidazole: Effect of plasticization, J. Membr. Sci. 580 (2019) 235–247. https://doi.org/10.1016/j.memsci.2019.03.031.

[27] L.M. Robeson, W.F. Burgoyne, M. Langsam, A.C. Savoca, C.F. Tien, High performance polymers for membrane separation, Polymer 35 (1994) 4970–4978. https://doi.org/10.1016/0032-3861(94)90651-3.

[28] K. Ghosal, B.D. Freeman, Gas separation using polymer membranes: an overview, Polym. Adv. Technol. 5 (1994) 673–697. https://doi.org/10.1002/pat.1994.220051102.

[29] C.L. Aitken, W.J. Koros, D.R. Paul, Gas transport properties of biphenol polysulfones, Macromolecules 25 (1992) 3651–3658. https://doi.org/10.1021/ma00040a008.

[30] L.M. Robeson, Correlation of separation factor versus permeability for polymeric membranes, J. Membr. Sci. 62 (1991) 165–185. https://doi.org/10.1016/0376-7388(91)80060-J.

[31] I. Blume, E. Smit, M. Wessling, C.A. Smolders, Diffusion through rubbery and glassy polymer membranes, Makromol. Chem. Macromol. Symp. 45 (1991) 237–257. https://doi.org/10.1002/masy.19910450125.

[32] D.S. Pope, I.C. Sanchez, W.J. Koros, G.K. Fleming, Statistical thermodynamic interpretation of sorption/dilation behavior of gases in silicone rubber, Macromolecules 24 (1991) 1779–1783. https://doi.org/10.1021/ma00008a014.

[33] F. Doghieri, G.C. Sarti, Nonequilibrium Lattice Fluids: A Predictive Model for the Solubility in Glassy Polymers, Macromolecules 29 (1996) 7885–7896. https://doi.org/10.1021/ma951366c.

[34] J.Y. Park, D.R. Paul, Correlation and prediction of gas permeability in glassy polymer membrane materials via a modified free volume based group contribution method, J. Membr. Sci. 125 (1997) 23–39. https://doi.org/10.1016/S0376-7388(96)00061-0.

[35] V.P. Shantarovich, I.B. Kevdina, Yu.P. Yampolskii, A.Yu. Alentiev, Positron Annihilation Lifetime Study of High and Low Free Volume Glassy Polymers: Effects of Free Volume Sizes on the Permeability and Permselectivity, Macromolecules 33 (2000) 7453–7466. https://doi.org/10.1021/ma000551+.

[36] W.J. Koros, Model for sorption of mixed gases in glassy polymers, J. Polym. Sci. Polym. Phys. Ed. 18 (1980) 981–992. https://doi.org/10.1002/pol.1980.180180506.

[37] P. Kubica, A. Wolinska-Grabczyk, Correlation between Cohesive Energy Density, Fractional Free Volume, and Gas Transport Properties of Poly(ethylene- *co* -vinyl acetate) Materials, Int. J. Polym. Sci. 2015 (2015) 1–8. https://doi.org/10.1155/2015/861979.

[38] W.J. Koros, D.R. Paul, G.S. Huvard, Energetics of gas sorption in glassy polymers, Polymer 20 (1979) 956–960. https://doi.org/10.1016/0032-3861(79)90192-7.

[39] L.M. Robeson, Q. Liu, B.D. Freeman, D.R. Paul, Comparison of transport properties of rubbery and glassy polymers and the relevance to the upper bound relationship, J. Membr. Sci. 476 (2015) 421–431. https://doi.org/10.1016/j.memsci.2014.11.058.

[40] B.D. Freeman, Basis of Permeability/Selectivity Tradeoff Relations in Polymeric Gas Separation Membranes, Macromolecules 32 (1999) 375–380. https://doi.org/10.1021/ma9814548.

[41] A.X. Wu, J.A. Drayton, K. Mizrahi Rodriguez, F.M. Benedetti, Q. Qian, S. Lin, Z.P. Smith, Elucidating the Role of Fluorine Content on Gas Sorption Properties of Fluorinated Polyimides, Macromolecules 54 (2021) 22–34. https://doi.org/10.1021/acs.macromol.0c01746.

[42] J. Deng, W.J. Box, L.C. Condes, Y. Okamoto, M. Galizia, Effect of halogen substituents on polymer membrane hydrophobicity, swelling and transport mechanism: chlorine versus fluorine, J. Membr. Sci. 662 (2022) 120964. https://doi.org/10.1016/j.memsci.2022.120964.

[43] W.J. Box, Z. Huang, R. Guo, M. Galizia, The mechanism of light gas transport through configurational free volume in glassy polymers, J. Membr. Sci. (2022) 120608. https://doi.org/10.1016/j.memsci.2022.120608.

[44] M. Rungta, C. Zhang, W.J. Koros, L. Xu, Membrane-based ethylene/ethane separation: The upper bound and beyond, AIChE J. 59 (2013) 3475–3489. https://doi.org/10.1002/aic.14105.

[45] M. Galizia, K.P. Bye, Advances in Organic Solvent Nanofiltration Rely on Physical Chemistry and Polymer Chemistry, Front. Chem. 6 (2018) 511. https://doi.org/10.3389/fchem.2018.00511.

[46] P. Bernardo, E. Drioli, G. Golemme, Membrane Gas Separation: A Review/State of the Art, Ind. Eng. Chem. Res. 48 (2009) 4638–4663. https://doi.org/10.1021/ie8019032.

[47] R.W. Baker, B.T. Low, Gas Separation Membrane Materials: A Perspective, Macromolecules 47 (2014) 6999–7013. https://doi.org/10.1021/ma501488s.

[48] A. Bottino, G. Capannelli, S. Munari, A. Turturro, Solubility parameters of poly(vinylidene fluoride), J. Polym. Sci. Part B Polym. Phys. 26 (1988) 785–794. https://doi.org/10.1002/polb.1988.090260405.

[49] M.W. Hellums, W.J. Koros, G.R. Husk, D.R. Paul, Fluorinated polycarbonates for gas separation applications, J. Membr. Sci. 46 (1989) 93–112. https://doi.org/10.1016/S0376-7388(00)81173-4.

[50] T.C. Merkel, V. Bondar, K. Nagai, B.D. Freeman, Sorption and transport of hydrocarbon and perfluorocarbon gases in poly(1-trimethylsilyl-1-propyne), J. Polym.

Sci. Part B Polym. Phys. 38 (2000) 273–296. https://doi.org/10.1002/(SICI)1099-0488(20000115)38:2<273::AID-POLB1>3.0.CO;2-X.

[51] W.J. Box, Z. Huang, R. Guo, M. Galizia, Evidence for Size-Sieving Driven Vapor Sorption and Diffusion in a Glassy Polybenzoxazole Exhibiting Configurational Free Volume, Ind. Eng. Chem. Res. 60 (2021) 13326–13337. https://doi.org/10.1021/acs.iecr.1c02660.

[52] M.M. Merrick, R. Sujanani, B.D. Freeman, Glassy polymers: Historical findings, membrane applications, and unresolved questions regarding physical aging, Polymer 211 (2020) 123176. https://doi.org/10.1016/j.polymer.2020.123176.

[53] C.L. Staiger, S.J. Pas, A.J. Hill, C.J. Cornelius, Gas Separation, Free Volume Distribution, and Physical Aging of a Highly Microporous Spirobisindane Polymer, Chem. Mater. 20 (2008) 2606–2608. https://doi.org/10.1021/cm071722t.

[54] Z.-X. Low, P.M. Budd, N.B. McKeown, D.A. Patterson, Gas Permeation Properties, Physical Aging, and Its Mitigation in High Free Volume Glassy Polymers, Chem. Rev. 118 (2018) 5871–5911. https://doi.org/10.1021/acs.chemrev.7b00629.

[55] C.H. Lau, P.T. Nguyen, M.R. Hill, A.W. Thornton, K. Konstas, C.M. Doherty, R.J. Mulder, L. Bourgeois, A.C.Y. Liu, D.J. Sprouster, J.P. Sullivan, T.J. Bastow, A.J. Hill, D.L. Gin, R.D. Noble, Ending Aging in Super Glassy Polymer Membranes, Angew. Chem. Int. Ed. 53 (2014) 5322–5326. https://doi.org/10.1002/anie.201402234.

[56] A.F. Ismail, W. Lorna, Penetrant-induced plasticization phenomenon in glassy polymers for gas separation membrane, Sep. Purif. Technol. 27 (2002) 173–194. https://doi.org/10.1016/S1383-5866(01)00211-8.

[57] A. Bos, I.G.M. PuÈnt, M. Wessling, H. Strathmann, CO2-induced plasticization phenomena in glassy polymers, J. Membr. Sci. (1999).

[58] V. Loianno, K.P. Bye, M. Galizia, P. Musto, Plasticization mechanism in polybenzimidazole membranes for organic solvent nanofiltration: Molecular insights from in situ FTIR spectroscopy, J. Polym. Sci. 58 (2020) 2547–2560. https://doi.org/10.1002/pol.20200151.

[59] S.W. Kim, Y.H. Bae, T. Okano, Hydrogels: Swelling, Drug Loading, and Release, Pharm. Res. 09 (1992) 283–290. https://doi.org/10.1023/A:1015887213431.

[60] B. Comesaña-Gándara, J. Chen, C.G. Bezzu, M. Carta, I. Rose, M.-C. Ferrari, E. Esposito, A. Fuoco, J.C. Jansen, N.B. McKeown, Redefining the Robeson upper bounds

for CO_2/CH_4 and CO_2/N_2 separations using a series of ultrapermeable benzotriptycene-based polymers of intrinsic microporosity, Energy Environ. Sci. 12 (2019) 2733–2740. https://doi.org/10.1039/C9EE01384A.

[61] L.M. Robeson, The upper bound revisited, J. Membr. Sci. 320 (2008) 390–400. https://doi.org/10.1016/j.memsci.2008.04.030.

[62] Z. Dai, J. Deng, X. He, C.A. Scholes, X. Jiang, B. Wang, H. Guo, Y. Ma, L. Deng, Helium separation using membrane technology: Recent advances and perspectives, Sep. Purif. Technol. 274 (2021) 119044. https://doi.org/10.1016/j.seppur.2021.119044.

[63] M.A. Bashir, M. Al-haj Ali, V. Kanellopoulos, J. Seppälä, Modelling of multicomponent olefins solubility in polyolefins using Sanchez–Lacombe equation of state, Fluid Phase Equilibria 358 (2013) 83–90. https://doi.org/10.1016/j.fluid.2013.08.009.

[64] A.X. Wu, J.A. Drayton, Z.P. Smith, The perfluoropolymer upper bound, AIChE J. 65 (2019) e16700. https://doi.org/10.1002/aic.16700.

[65] B. Lopez-Iglesias, F. Suárez-García, C. Aguilar-Lugo, A. González Ortega, C. Bartolomé, J.M. Martínez-Ilarduya, J.G. de la Campa, Á.E. Lozano, C. Álvarez, Microporous Polymer Networks for Carbon Capture Applications, ACS Appl. Mater. Interfaces 10 (2018) 26195–26205. https://doi.org/10.1021/acsami.8b05854.

[66] C. Aguilar-Lugo, F. Suárez-García, A. Hernández, J.A. Miguel, Á.E. Lozano, J.G. de la Campa, C. Álvarez, New Materials for Gas Separation Applications: Mixed Matrix Membranes Made from Linear Polyimides and Porous Polymer Networks Having Lactam Groups, Ind. Eng. Chem. Res. 58 (2019) 9585–9595. https://doi.org/10.1021/acs.iecr.9b01402.

[67] Y. He, F.M. Benedetti, S. Lin, C. Liu, Y. Zhao, H. Ye, T. Van Voorhis, M.G. De Angelis, T.M. Swager, Z.P. Smith, Polymers with Side Chain Porosity for Ultrapermeable and Plasticization Resistant Materials for Gas Separations, Adv. Mater. 31 (2019) 1807871. https://doi.org/10.1002/adma.201807871.

[68] J. Deng, Z. Huang, B.J. Sundell, D.J. Harrigan, S.A. Sharber, K. Zhang, R. Guo, M. Galizia, State of the art and prospects of chemically and thermally aggressive membrane gas separations: Insights from polymer science, Polymer 229 (2021) 123988. https://doi.org/10.1016/j.polymer.2021.123988.

[69] Y. Huang, D.R. Paul, Physical aging of thin glassy polymer films monitored by gas permeability, Polymer 45 (2004) 8377–8393. https://doi.org/10.1016/j.polymer.2004.10.019.

[70] S.J.D. Smith, R. Hou, K. Konstas, A. Akram, C.H. Lau, M.R. Hill, Control of Physical Aging in Super-Glassy Polymer Mixed Matrix Membranes, Acc. Chem. Res. 53 (2020) 1381–1388. https://doi.org/10.1021/acs.accounts.0c00256.

[71] R.M. Felder, C.J. Patton, W.J. Koros, Dual-mode sorption and transport of sulfur dioxide in kapton polyimide, J. Polym. Sci. Polym. Phys. Ed. 19 (1981) 1895–1909. https://doi.org/10.1002/pol.1981.180191208.

[72] R.M. Barrer, Diffusivities in glassy polymers for the dual mode sorption model, J. Membr. Sci. 18 (1984) 25–35. https://doi.org/10.1016/S0376-7388(00)85023-1.

[73] J.H. Petropoulos, On the dual mode gas transport model for glassy polymers, J. Polym. Sci. Part B Polym. Phys. 26 (1988) 1009–1020. https://doi.org/10.1002/polb.1988.090260506.

[74] D.R. Paul, W.J. Koros, Effect of partially immobilizing sorption on permeability and the diffusion time lag, J. Polym. Sci. Polym. Phys. Ed. 14 (1976) 675–685. https://doi.org/10.1002/pol.1976.180140409.

[75] V. Loianno, S. Luo, Q. Zhang, R. Guo, M. Galizia, Gas and water vapor sorption and diffusion in a triptycene-based polybenzoxazole: effect of temperature and pressure and predicting of mixed gas sorption, J. Membr. Sci. 574 (2019) 100–111. https://doi.org/10.1016/j.memsci.2018.12.054.

[76] W. Ogieglo, G. Genduso, J. Rubner, J. Hofmann-Préveraud De Vaumas, M. Wessling, I. Pinnau, CO_2/CH_4 Pure- and Mixed-Gas Dilation and Sorption in Thin (~500 nm) and Ultrathin (~50 nm) Polymers of Intrinsic Microporosity, Macromolecules 53 (2020) 8765–8774. https://doi.org/10.1021/acs.macromol.0c01163.

[77] D. Punsalan, W.J. Koros, Drifts in penetrant partial molar volumes in glassy polymers due to physical aging, Polymer 46 (2005) 10214–10220. https://doi.org/10.1016/j.polymer.2005.06.061.

[78] J.D. Moon, M. Galizia, H. Borjigin, R. Liu, J.S. Riffle, B.D. Freeman, D.R. Paul, Water Vapor Sorption, Diffusion, and Dilation in Polybenzimidazoles, Macromolecules 51 (2018) 7197–7208. https://doi.org/10.1021/acs.macromol.8b01659.

[79] Y. Kamiya, T. Hirose, Y. Naito, K. Mizoguchi, Sorptive dilation of polysulfone and poly(ethylene terephthalate) films by high-pressure carbon dioxide, J. Polym. Sci. Part B Polym. Phys. 26 (1988) 159–177. https://doi.org/10.1002/polb.1988.090260109.

[80] W.J. Koros, D.R. Paul, CO2 sorption in poly(ethylene terephthalate) above and below the glass transition, J. Polym. Sci. Polym. Phys. Ed. 16 (1978) 1947–1963. https://doi.org/10.1002/pol.1978.180161105.

[81] E.U. Franck, Applications of Statistical Mechanics. Von W. A. Guggenheim. Clarendon Press/Clarendon University Press, London 1966. 1. Aufl., 211 S., zahlr. Abb., Gl 55s, Angew. Chem. 79 (1967) 732–732. https://doi.org/10.1002/ange.19670791621.

[82] R.B. Anderson, Modifications of the Brunauer, Emmett and Teller Equation [1], J. Am. Chem. Soc. 68 (1946) 686–691. https://doi.org/10.1021/ja01208a049.

[83] E.O. Timmermann, A B. E. T.-like three sorption stage isotherm, J. Chem. Soc. Faraday Trans. 1 Phys. Chem. Condens. Phases 85 (1989) 1631. https://doi.org/10.1039/f19898501631.

[84] A.R. Berens, H.B. Hopfenberg, Diffusion and relaxation in glassy polymer powders: 2. Separation of diffusion and relaxation parameters, Polymer 19 (1978) 489–496. https://doi.org/10.1016/0032-3861(78)90269-0.

[85] J. Crank, The mathematics of diffusion, 2. ed., reprint, Clarendon Press, Oxford, 1976.

[86] F.A. Long, D. Richman, Concentration Gradients for Diffusion of Vapors in Glassy Polymers and their Relation to Time Dependent Diffusion Phenomena [1,2], J. Am. Chem. Soc. 82 (1960) 513–519. https://doi.org/10.1021/ja01488a002.

[87] T.C. Merkel, V. Bondar, K. Nagai, B.D. Freeman, Yu.P. Yampolskii, Gas Sorption, Diffusion, and Permeation in Poly(2,2-bis(trifluoromethyl)-4,5-difluoro-1,3-dioxole- *c o* -tetrafluoroethylene), Macromolecules 32 (1999) 8427–8440. https://doi.org/10.1021/ma990685r.

[88] M.L. Jue, C.S. McKay, B.A. McCool, M.G. Finn, R.P. Lively, Effect of Nonsolvent Treatments on the Microstructure of PIM-1, Macromolecules 48 (2015) 5780–5790. https://doi.org/10.1021/acs.macromol.5b01507.

[89] M. Galizia, M.G. De Angelis, E. Finkelshtein, Y.P. Yampolskii, G.C. Sarti, Sorption and transport of hydrocarbons and alcohols in addition-type poly(trimethyl silyl norbornene). I: Experimental data, J. Membr. Sci. 385–386 (2011) 141–153. https://doi.org/10.1016/j.memsci.2011.09.032.

[90] E.M. Davis, Y.A. Elabd, Water Clustering in Glassy Polymers, J. Phys. Chem. B 117 (2013) 10629–10640. https://doi.org/10.1021/jp405388d.

[91] B.H. Zimm, Simplified Relation Between Thermodynamics and Molecular Distribution Functions for a Mixture, J. Chem. Phys. 21 (1953) 934–935. https://doi.org/10.1063/1.1699065.

[92] B.H. Zimm, J.L. Lundberg, Sorption of Vapors by High Polymers, J. Phys. Chem. 60 (1956) 425–428. https://doi.org/10.1021/j150538a010.

[93] Y. Kamiya, Y. Naito, K. Terada, K. Mizoguchi, A. Tsuboi, Volumetric Properties and Interaction Parameters of Dissolved Gases in Poly(dimethylsiloxane) and Polyethylene, Macromolecules 33 (2000) 3111–3119. https://doi.org/10.1021/ma991536b.

[94] V. Loianno, Q. Zhang, S. Luo, R. Guo, M. Galizia, Modeling Gas and Vapor Sorption and Swelling in Triptycene-Based Polybenzoxazole: Evidence for Entropy-Driven Sorption Behavior, Macromolecules 52 (2019) 4385–4395. https://doi.org/10.1021/acs.macromol.9b00577.

[95] R. Guo, Design, Synthesis and Characterization of Triptycene-Containing Macromolecules with Hierarchically Controlled Architectures as Functional Membrane Materials for Energy Applications, 2019. https://doi.org/10.2172/1499993.

[96] W.J. Box, M.T. Webb, M. Galizia, Evaluating the Experimental Uncertainty in Gas and Vapor Sorption/Adsorption Measurements: Fundamental Considerations and Experimental Design Implications, Ind. Eng. Chem. Res. 61 (2022) 9856–9868. https://doi.org/10.1021/acs.iecr.2c01414.

[97] M. Giordano, Uncertainty propagation with functionally correlated quantities, ArXiv161008716 Phys. (2016). http://arxiv.org/abs/1610.08716 (accessed June 29, 2021).

[98] P.R. Bevington, Data reduction and error analysis for the physical sciences, McGraw-Hill, London, 1969.

[99] G.M. Anderson, Error propagation by the Monte Carlo method in geochemical calculations, Geochim. Cosmochim. Acta 40 (1976) 1533–1538. https://doi.org/10.1016/0016-7037(76)90092-2.

[100] L. Vandenbroeke, S. Nuhuis, R. Krishna, Monte Carlo simulations of diffusion in zeolites and comparison with the generalized Maxwell-Stefan theory, J. Catal. 136 (1992) 463–477. https://doi.org/10.1016/0021-9517(92)90076-T.

[101] M.S. Caceci, Estimating error limits in parametric curve fitting, Anal. Chem. 61 (1989) 2324–2327. https://doi.org/10.1021/ac00195a023.

[102] J. Nocedal, S.J. Wright, Numerical optimization, 2nd ed, Springer, New York, 2006.

[103] J. Tellinghuisen, Statistical Error Propagation, J. Phys. Chem. A 105 (2001) 3917–3921. https://doi.org/10.1021/jp003484u.

[104] E.S. Burnett, Compressibility Determinations Without Volume Measurements, J. Appl. Mech. 3 (1936) A136–A140. https://doi.org/10.1115/1.4008721.

[105] J.A. Turner, A Realizable Renewable Energy Future, Science 285 (1999) 687–689. https://doi.org/10.1126/science.285.5428.687.

[106] R. Kumar, A.K. Ghosh, P. Pal, Sustainable Production of Biofuels through Membrane-Integrated Systems, Sep. Purif. Rev. 49 (2020) 207–228. https://doi.org/10.1080/15422119.2018.1562942.

[107] M. Galizia, M.G. De Angelis, G.C. Sarti, Sorption of hydrocarbons and alcohols in addition-type poly(trimethyl silyl norbornene) and other high free volume glassy polymers. II: NELF model predictions, J. Membr. Sci. 405–406 (2012) 201–211. https://doi.org/10.1016/j.memsci.2012.03.009.

[108] N. Hajilary, M. Rezakazemi, S. Shirazian, Biofuel types and membrane separation, Environ. Chem. Lett. 17 (2019) 1–18. https://doi.org/10.1007/s10311-018-0777-9.

[109] O. Vopička, K. Friess, V. Hynek, P. Sysel, M. Zgažar, M. Šípek, K. Pilnáček, M. Lanč, J.C. Jansen, C.R. Mason, P.M. Budd, Equilibrium and transient sorption of vapours and gases in the polymer of intrinsic microporosity PIM-1, J. Membr. Sci. 434 (2013) 148–160. https://doi.org/10.1016/j.memsci.2013.01.040.

[110] K. Friess, J.C. Jansen, J. Poživil, V. Hanta, V. Hynek, O. Vopička, M. Zgažar, P. Bernardo, P. Izák, E. Drioli, Anomalous Phenomena Occurring during Permeation and Sorption of C_1–C_6 Alcohol Vapors in Teflon AF 2400, Ind. Eng. Chem. Res. 52 (2013) 10406–10417. https://doi.org/10.1021/ie303013y.

[111] W.J. Koros, A.H. Chan, D.R. Paul, Sorption and transport of various gases in polycarbonate, J. Membr. Sci. 2 (1977) 165–190. https://doi.org/10.1016/S0376-7388(00)83242-1.

[112] M. Galizia, K.A. Stevens, Z.P. Smith, D.R. Paul, B.D. Freeman, Nonequilibrium Lattice Fluid Modeling of Gas Solubility in HAB-6FDA Polyimide and Its Thermally Rearranged Analogues, Macromolecules 49 (2016) 8768–8779. https://doi.org/10.1021/acs.macromol.6b01479.

[113] M.G. De Angelis, G.C. Sarti, F. Doghieri, NELF model prediction of the infinite dilution gas solubility in glassy polymers, J. Membr. Sci. 289 (2007) 106–122. https://doi.org/10.1016/j.memsci.2006.11.044.

[114] Z.P. Smith, R.R. Tiwari, M.E. Dose, K.L. Gleason, T.M. Murphy, D.F. Sanders, G. Gunawan, L.M. Robeson, D.R. Paul, B.D. Freeman, Influence of Diffusivity and Sorption on Helium and Hydrogen Separations in Hydrocarbon, Silicon, and Fluorocarbon-Based Polymers, Macromolecules 47 (2014) 3170–3184. https://doi.org/10.1021/ma402521h.

[115] J.R. Weidman, S. Luo, C.M. Doherty, A.J. Hill, P. Gao, R. Guo, Analysis of governing factors controlling gas transport through fresh and aged triptycene-based polyimide films, J. Membr. Sci. 522 (2017) 12–22. https://doi.org/10.1016/j.memsci.2016.09.013.

[116] T. Bowen, Driving force for pervaporation through zeolite membranes, J. Membr. Sci. 225 (2003) 165–176. https://doi.org/10.1016/j.memsci.2003.07.016.

[117] K. Zhang, R.P. Lively, M.E. Dose, A.J. Brown, C. Zhang, J. Chung, S. Nair, W.J. Koros, R.R. Chance, Alcohol and water adsorption in zeolitic imidazolate frameworks, Chem. Commun. 49 (2013) 3245. https://doi.org/10.1039/c3cc39116g.

[118] R. Krishna, B. Smit, S. Calero, Entropy effects during sorption of alkanes in zeolites, Chem. Soc. Rev. 31 (2002) 185–194. https://doi.org/10.1039/b101267n.

[119] T.C. Merkel, I. Pinnau, R. Prabhakar, B.D. Freeman, Gas and Vapor Transport Properties of Perfluoropolymers, in: Y. Yampolskii, I. Pinnau, B. Freeman (Eds.), Mater. Sci. Membr. Gas Vap. Sep., 1st ed., Wiley, 2006: pp. 251–270. https://doi.org/10.1002/047002903X.ch9.

[120] R. Prabhakar, B. Freeman, Application of hydrocarbon—fluorocarbon interactions in membrane-based gas separations, Desalination 144 (2002) 79–83. https://doi.org/10.1016/S0011-9164(02)00292-8.

[121] Y. Li, M. Yavari, A. Baldanza, E. Di Maio, Y. Okamoto, H. Lin, M. Galizia, Volumetric Properties and Sorption Behavior of Perfluoropolymers with Dioxolane Pendant Rings, Ind. Eng. Chem. Res. 59 (2020) 5276–5286. https://doi.org/10.1021/acs.iecr.9b03411.

[122] M. Omidvar, H. Nguyen, J. Liu, H. Lin, Sorption-enhanced membrane materials for gas separation: a road less traveled, Curr. Opin. Chem. Eng. 20 (2018) 50–59. https://doi.org/10.1016/j.coche.2018.02.003.

[123] A. Singh, B.D. Freeman, I. Pinnau, Pure and mixed gas acetone/nitrogen permeation properties of polydimethylsiloxane [PDMS], (n.d.) 13.

[124] F. Körösy, Two rules concerning solubility of gases and crude data on solubility of krypton, Trans Faraday Soc 33 (1937) 416–425. https://doi.org/10.1039/TF9373300416.

[125] S. Matteucci, Y. Yampolskii, B.D. Freeman, I. Pinnau, Transport of Gases and Vapors in Glassy and Rubbery Polymers, in: Y. Yampolskii, I. Pinnau, B. Freeman (Eds.), Mater. Sci. Membr. Gas Vap. Sep., John Wiley & Sons, Ltd, Chichester, UK, 2006: pp. 1–47. https://doi.org/10.1002/047002903X.ch1.

[126] Y. Dong, C. Dai, Z. Lei, Separation of the Methanol–Ethanol–Water Mixture Using Ionic Liquid, Ind. Eng. Chem. Res. 57 (2018) 11167–11177. https://doi.org/10.1021/acs.iecr.8b01617.

[127] J.R. Weidman, R. Guo, The Use of Iptycenes in Rational Macromolecular Design for Gas Separation Membrane Applications, Ind. Eng. Chem. Res. 56 (2017) 4220–4236. https://doi.org/10.1021/acs.iecr.7b00540.

[128] P.M. Budd, B.S. Ghanem, S. Makhseed, N.B. McKeown, K.J. Msayib, C.E. Tattershall, Polymers of intrinsic microporosity (PIMs): robust, solution-processable, organic nanoporous materials, Chem. Commun. (2004) 230. https://doi.org/10.1039/b311764b.

[129] P.M. Budd, N.B. McKeown, D. Fritsch, Polymers of Intrinsic Microporosity (PIMs): High Free Volume Polymers for Membrane Applications, Macromol. Symp. 245–246 (2006) 403–405. https://doi.org/10.1002/masy.200651356.

[130] H.B. Park, C.H. Jung, Y.M. Lee, A.J. Hill, S.J. Pas, S.T. Mudie, E. Van Wagner, B.D. Freeman, D.J. Cookson, Polymers with Cavities Tuned for Fast Selective Transport of Small Molecules and Ions, Science 318 (2007) 254–258. https://doi.org/10.1126/science.1146744.

[131] H. Lin, E. Van Wagner, B.D. Freeman, L.G. Toy, R.P. Gupta, Plasticization-Enhanced Hydrogen Purification Using Polymeric Membranes, Science 311 (2006) 639–642. https://doi.org/10.1126/science.1118079.

[132] M. Yavari, M. Fang, H. Nguyen, T.C. Merkel, H. Lin, Y. Okamoto, Dioxolane-Based Perfluoropolymers with Superior Membrane Gas Separation Properties, Macromolecules 51 (2018) 2489–2497. https://doi.org/10.1021/acs.macromol.8b00273.

[133] Y. Okamoto, H.-C. Chiang, M. Fang, M. Galizia, T. Merkel, M. Yavari, H. Nguyen, H. Lin, Perfluorodioxolane Polymers for Gas Separation Membrane Applications, Membranes 10 (2020) 394. https://doi.org/10.3390/membranes10120394.

[134] Z. Ali, B.S. Ghanem, Y. Wang, F. Pacheco, W. Ogieglo, H. Vovusha, G. Genduso, U. Schwingenschlögl, Y. Han, I. Pinnau, Finely Tuned Submicroporous Thin-Film Molecular Sieve Membranes for Highly Efficient Fluid Separations, Adv. Mater. 32 (2020) 2001132. https://doi.org/10.1002/adma.202001132.

[135] A.M. Tandel, W. Guo, K. Bye, L. Huang, M. Galizia, H. Lin, Designing organic solvent separation membranes: polymers, porous structures, 2D materials, and their combinations, Mater. Adv. 2 (2021) 4574–4603. https://doi.org/10.1039/D1MA00373A.

[136] G.M. Geise, H.B. Park, A.C. Sagle, B.D. Freeman, J.E. McGrath, Water permeability and water/salt selectivity tradeoff in polymers for desalination, J. Membr. Sci. 369 (2011) 130–138. https://doi.org/10.1016/j.memsci.2010.11.054.

[137] P. Marchetti, M.F. Jimenez Solomon, G. Szekely, A.G. Livingston, Molecular Separation with Organic Solvent Nanofiltration: A Critical Review, Chem. Rev. 114 (2014) 10735–10806. https://doi.org/10.1021/cr500006j.

[138] Y.J. Cho, H.B. Park, Gas Separation Properties of Triptycene-Based Polyimide Membranes, in: I. Escobar, B. Van Der Bruggen (Eds.), ACS Symp. Ser., American Chemical Society, Washington, DC, 2011: pp. 107–128. https://doi.org/10.1021/bk-2011-1078.ch008.

[139] T. Corrado, Z. Huang, J. Aboki, R. Guo, Microporous Polysulfones with Enhanced Separation Performance via Integration of the Triptycene Moiety, Ind. Eng. Chem. Res. 59 (2020) 5351–5361. https://doi.org/10.1021/acs.iecr.9b04861.

[140] S. Luo, J.R. Wiegand, P. Gao, C.M. Doherty, A.J. Hill, R. Guo, Molecular origins of fast and selective gas transport in pentiptycene-containing polyimide membranes and their physical aging behavior, J. Membr. Sci. 518 (2016) 100–109. https://doi.org/10.1016/j.memsci.2016.06.034.

[141] M. Woźny, A. Mames, T. Ratajczyk, Triptycene Derivatives: From Their Synthesis to Their Unique Properties, Molecules 27 (2021) 250. https://doi.org/10.3390/molecules27010250.

[142] Y. Jiang, C. Chen, Recent Developments in Synthesis and Applications of Triptycene and Pentiptycene Derivatives, Eur. J. Org. Chem. 2011 (2011) 6377–6403. https://doi.org/10.1002/ejoc.201100684.

[143] D.-Y. Peng, D.B. Robinson, A New Two-Constant Equation of State, Ind. Eng. Chem. Fundam. 15 (1976) 59–64. https://doi.org/10.1021/i160057a011.

[144] R.S. Prabhakar, M.G. De Angelis, G.C. Sarti, B.D. Freeman, M.C. Coughlin, Gas and Vapor Sorption, Permeation, and Diffusion in Poly(tetrafluoroethylene- *co* -perfluoromethyl vinyl ether), Macromolecules 38 (2005) 7043–7055. https://doi.org/10.1021/ma050546b.

[145] J.R. Elliott, B.E. Poling, The properties of gases and liquids, Sixth edition, McGraw Hill, New York, 2023.

[146] E.S. Sanders, W.J. Koros, H.B. Hopfenberg, V.T. Stannett, Mixed gas sorption in glassy polymers: Equipment design considerations and preliminary results, J. Membr. Sci. 13 (1983) 161–174. https://doi.org/10.1016/S0376-7388(00)80159-3.

[147] E.S. Sanders, W.J. Koros, H.B. Hopfenberg, V.T. Stannett, Pure and mixed gas sorption of carbon dioxide and ethylene in poly(methyl methacrylate), J. Membr. Sci. 18 (1984) 53–74. https://doi.org/10.1016/S0376-7388(00)85025-5.

[148] S.I. Sandler, Chemical, biochemical, and engineering thermodynamics, Fifth edition, Wiley, Hoboken, NJ, 2017.

[149] T.C. Merkel, V.I. Bondar, K. Nagai, B.D. Freeman, I. Pinnau, Gas sorption, diffusion, and permeation in poly(dimethylsiloxane), J. Polym. Sci. Part B Polym. Phys. 38 (2000) 415–434. https://doi.org/10.1002/(SICI)1099-0488(20000201)38:3<415::AID-POLB8>3.0.CO;2-Z.

[150] P. Li, T.S. Chung, D.R. Paul, Gas sorption and permeation in PIM-1, J. Membr. Sci. 432 (2013) 50–57. https://doi.org/10.1016/j.memsci.2013.01.009.

[151] A.Y. Houde, B. Krishnakumar, S.G. Charati, S.A. Stern, Permeability of dense (homogeneous) cellulose acetate membranes to methane, carbon dioxide, and their mixtures at elevated pressures, J. Appl. Polym. Sci. 62 (1996) 2181–2192. https://doi.org/10.1002/(SICI)1097-4628(19961226)62:13<2181::AID-APP1>3.0.CO;2-F.

[152] H. Lin, B.D. Freeman, Gas solubility, diffusivity and permeability in poly(ethylene oxide), J. Membr. Sci. 239 (2004) 105–117. https://doi.org/10.1016/j.memsci.2003.08.031.

[153] T.A. Barbari, W.J. Koros, D.R. Paul, Gas transport in polymers based on bisphenol-A, J. Polym. Sci. Part B Polym. Phys. 26 (1988) 709–727. https://doi.org/10.1002/polb.1988.090260401.

[154] R. Wang, C. Cao, T.-S. Chung, A critical review on diffusivity and the characterization of diffusivity of 6FDA–6FpDA polyimide membranes for gas separation, J. Membr. Sci. 198 (2002) 259–271. https://doi.org/10.1016/S0376-7388(01)00665-2.

[155] L.M. Robeson, M.E. Dose, B.D. Freeman, D.R. Paul, Analysis of the transport properties of thermally rearranged (TR) polymers and polymers of intrinsic microporosity (PIM) relative to upper bound performance, J. Membr. Sci. 525 (2017) 18–24. https://doi.org/10.1016/j.memsci.2016.11.085.

[156] D.S. Sholl, R.P. Lively, Seven chemical separations to change the world, Nature 532 (2016) 435–437. https://doi.org/10.1038/532435a.

[157] K.S. Walton, D.S. Sholl, Research Challenges in Avoiding "Showstoppers" in Developing Materials for Large-Scale Energy Applications, Joule 1 (2017) 208–211. https://doi.org/10.1016/j.joule.2017.06.005.

[158] H. Fang, J. Findley, G. Muraro, P.I. Ravikovitch, D.S. Sholl, A Strong Test of Atomically Detailed Models of Molecular Adsorption in Zeolites Using Multilaboratory Experimental Data for CO 2 Adsorption in Ammonium ZSM-5, J. Phys. Chem. Lett. 11 (2020) 471–477. https://doi.org/10.1021/acs.jpclett.9b02986.

[159] J. Park, J.D. Howe, D.S. Sholl, How Reproducible Are Isotherm Measurements in Metal–Organic Frameworks?, Chem. Mater. 29 (2017) 10487–10495. https://doi.org/10.1021/acs.chemmater.7b04287.

[160] F. Gharagheizi, D. Tang, D.S. Sholl, Selecting Adsorbents to Separate Diverse Near-Azeotropic Chemicals, J. Phys. Chem. C 124 (2020) 3664–3670. https://doi.org/10.1021/acs.jpcc.9b10955.

[161] D. Wahlsten, P. Metten, T.J. Phillips, S.L. Boehm, S. Burkhart-Kasch, J. Dorow, S. Doerksen, C. Downing, J. Fogarty, K. Rodd-Henricks, R. Hen, C.S. McKinnon, C.M. Merrill, C. Nolte, M. Schalomon, J.P. Schlumbohm, J.R. Sibert, C.D. Wenger, B.C. Dudek, J.C. Crabbe, Different data from different labs: Lessons from studies of gene–environment interaction, J. Neurobiol. 54 (2003) 283–311. https://doi.org/10.1002/neu.10173.

[162] G. Zhu, C. Kim, A. Chandrasekarn, J.D. Everett, R. Ramprasad, R.P. Lively, Polymer genome–based prediction of gas permeabilities in polymers, J. Polym. Eng. 40 (2020) 451–457. https://doi.org/10.1515/polyeng-2019-0329.

[163] F. Prinz, T. Schlange, K. Asadullah, Believe it or not: how much can we rely on published data on potential drug targets?, Nat. Rev. Drug Discov. 10 (2011) 712–712. https://doi.org/10.1038/nrd3439-c1.

[164] M. Agrawal, R. Han, D. Herath, D.S. Sholl, Does repeat synthesis in materials chemistry obey a power law?, Proc. Natl. Acad. Sci. 117 (2020) 877–882. https://doi.org/10.1073/pnas.1918484117.

[165] C.G. Begley, L.M. Ellis, Raise standards for preclinical cancer research, Nature 483 (2012) 531–533. https://doi.org/10.1038/483531a.

[166] D.S. Sholl, Five Easy Ways To Make Your Research More Reproducible, Langmuir 35 (2019) 13257–13258. https://doi.org/10.1021/acs.langmuir.9b02963.

[167] H.G.T. Nguyen, L. Espinal, R.D. Van Zee, M. Thommes, B. Toman, M.S.L. Hudson, E. Mangano, S. Brandani, D.P. Broom, M.J. Benham, K. Cychosz, P. Bertier, F. Yang, B.M. Krooss, R.L. Siegelman, M. Hakuman, K. Nakai, A.D. Ebner, L. Erden, J.A. Ritter, A. Moran, O. Talu, Y. Huang, K.S. Walton, P. Billemont, G. De Weireld, A reference high-pressure CO2 adsorption isotherm for ammonium ZSM-5 zeolite: results of an interlaboratory study, Adsorption 24 (2018) 531–539. https://doi.org/10.1007/s10450-018-9958-x.

[168] W.J. Koros, D.R. Paul, Design considerations for measurement of gas sorption in polymers by pressure decay, J. Polym. Sci. Polym. Phys. Ed. 14 (1976) 1903–1907. https://doi.org/10.1002/pol.1976.180141014.

[169] D. Shade, B.W.S. Bout, D.S. Sholl, K.S. Walton, Opening the Toolbox: 18 Experimental Techniques for Measurement of Mixed Gas Adsorption, Ind. Eng. Chem. Res. 61 (2022) 2367–2391. https://doi.org/10.1021/acs.iecr.1c03756.

[170] D.W. Jennlngs, R. Lee, A.S. Teja', + Vapor-Liquid Equilibria in the Carbon Dioxide Ethanol and + Carbon Dioxide l-Butanol Systems, (n.d.).

[171] R.M. Felder, R.W. Rousseau, L.G. Bullard, Elementary principles of chemical processes, 4th edition, Wiley, Hoboken, NJ, 2015.

[172] J.D. Wind, S.M. Sirard, D.R. Paul, P.F. Green, K.P. Johnston, W.J. Koros, Carbon Dioxide-Induced Plasticization of Polyimide Membranes: Pseudo-Equilibrium Relationships of Diffusion, Sorption, and Swelling, Macromolecules 36 (2003) 6433–6441. https://doi.org/10.1021/ma0343582.

[173] Th. Schalkhammer, Ch. Lobmaier, F. Pittner, A. Leitner, H. Brunner, F.R. Aussenegg, The use of metal-island-coated pH-sensitive swelling polymers for biosensor applications, Sens. Actuators B Chem. 24 (1995) 166–172. https://doi.org/10.1016/0925-4005(95)85036-8.

[174] D.S. Pope, W.J. Koros, H.B. Hopfenberg, Sorption and Dilation of Poly(1-(trimethylsilyl)-1-propyne) by Carbon Dioxide and Methane, Macromolecules 27 (1994) 5839–5844. https://doi.org/10.1021/ma00098a043.

[175] D.S. Pope, G.K. Fleming, W.J. Koros, Effect of various exposure histories on sorption and dilation in a family of polycarbonates, Macromolecules 23 (1990) 2988–2994. https://doi.org/10.1021/ma00213a029.

[176] G.K. Fleming, W.J. Koros, Dilation of polymers by sorption of carbon dioxide at elevated pressures. 1. Silicone rubber and unconditioned polycarbonate, Macromolecules 19 (1986) 2285–2291. https://doi.org/10.1021/ma00162a030.

[177] B.S. Ghanem, R. Swaidan, E. Litwiller, I. Pinnau, Ultra-Microporous Triptycene-based Polyimide Membranes for High-Performance Gas Separation, Adv. Mater. 26 (2014) 3688–3692. https://doi.org/10.1002/adma.201306229.

[178] J.R. Wiegand, Z.P. Smith, Q. Liu, C.T. Patterson, B.D. Freeman, R. Guo, Synthesis and characterization of triptycene-based polyimides with tunable high fractional free volume for gas separation membranes, J Mater Chem A 2 (2014) 13309–13320. https://doi.org/10.1039/C4TA02303J.

[179] T. Corrado, T. Wang, Z. Huang, J. Aboki, H.O. Ford, J.L. Schaefer, R. Guo, Polymer Morphological Effect on Gas Transport within Triptycene-Based Polysulfones, ACS Appl. Polym. Mater. (2021) acsapm.1c01412. https://doi.org/10.1021/acsapm.1c01412.

[180] S. Luo, Q. Zhang, T.K. Bear, T.E. Curtis, R.K. Roeder, C.M. Doherty, A.J. Hill, R. Guo, Triptycene-containing poly(benzoxazole-co-imide) membranes with enhanced mechanical strength for high-performance gas separation, J. Membr. Sci. 551 (2018) 305–314. https://doi.org/10.1016/j.memsci.2018.01.052.

[181] E. Piccinini, M. Giacinti Baschetti, G.C. Sarti, Use of an automated spring balance for the simultaneous measurement of sorption and swelling in polymeric films, J. Membr. Sci. 234 (2004) 95–100. https://doi.org/10.1016/j.memsci.2003.12.024.

[182] M. Giacinti Baschetti, E. Piccinini, T.A. Barbari, G.C. Sarti, Quantitative Analysis of Polymer Dilation during Sorption Using FTIR-ATR Spectroscopy, Macromolecules 36 (2003) 9574–9584. https://doi.org/10.1021/ma0302457.

[183] Y.P. Handa, Z. Zhang, Sorption, Diffusion, and Dilation in Linear and Branched Polycarbonate–CO_2 Systems in Relation to Solid State Processing of Microcellular Foams, Cell. Polym. 21 (2002) 221–235. https://doi.org/10.1177/026248930202100401.

[184] J. Guo, T.A. Barbari, A dual mode interpretation of the kinetics of penetrant-induced swelling and deswelling in a glassy polymer, Polymer 51 (2010) 5145–5150. https://doi.org/10.1016/j.polymer.2010.08.065.

[185] J.S. Ham, M.C. Bolen, J.K. Hughes, The use of high pressure to study polymer—solvent interaction, J. Polym. Sci. 57 (1962) 25–40. https://doi.org/10.1002/pol.1962.1205716503.

[186] G.K. Fleming, W.J. Koros, Carbon dioxide conditioning effects on sorption and volume dilation behavior for bisphenol A-polycarbonate, Macromolecules 23 (1990) 1353–1360. https://doi.org/10.1021/ma00207a020.

[187] R.W. Baker, K.A. Lokhandwala, I. Pinnau, S. Segelke, Methane/nitrogen separation process, US5669958A, 1997. https://patents.google.com/patent/US5669958A/en (accessed January 22, 2024).

[188] R. Raharjo, B. Freeman, E. Sanders, Pure and mixed gas CH4 and n-C4H10 sorption and dilation in poly(dimethylsiloxane), J. Membr. Sci. 292 (2007) 45–61. https://doi.org/10.1016/j.memsci.2007.01.012.

[189] R.D. Raharjo, B.D. Freeman, E.S. Sanders, Pure and mixed gas CH4 and n-C4H10 sorption and dilation in poly(1-trimethylsilyl-1-propyne), Polymer 48 (2007) 6097–6114. https://doi.org/10.1016/j.polymer.2007.07.057.

[190] M. Wessling, I. Huisman, Th.V.D. Boomgaard, C.A. Smolders, Dilation kinetics of glassy, aromatic polyimides induced by carbon dioxide sorption, J. Polym. Sci. Part B Polym. Phys. 33 (1995) 1371–1384. https://doi.org/10.1002/polb.1995.090330907.

[191] T. Shinkai, K. Ito, H. Yokoyama, Swelling measurement of polymers in high pressure carbon dioxide using a spectroscopic reflectometer, J. Supercrit. Fluids 95 (2014) 553–559. https://doi.org/10.1016/j.supflu.2014.09.003.

[192] J. Guo, T.A. Barbari, Unified Dual Mode Description of Small Molecule Sorption and Desorption Kinetics in a Glassy Polymer, Macromolecules 42 (2009) 5700–5708. https://doi.org/10.1021/ma9007576.

[193] D. Ziou, S. Tabbone, "Edge detection techniques: An overview," Int. J. Patttern Recognit. Image Anal. 4 (1998) 537–559.

[194] T.R. Reed, J.M.H. Dubuf, A Review of Recent Texture Segmentation and Feature Extraction Techniques, CVGIP Image Underst. 57 (1993) 359–372. https://doi.org/10.1006/ciun.1993.1024.

[195] P.-E. Danielsson, O. Seger, Generalized and Separable Sobel Operators, in: Mach. Vis. Three-Dimens. Scenes, Elsevier, 1990: pp. 347–379. https://doi.org/10.1016/B978-0-12-266722-0.50016-6.

[196] M. Rungta, L. Xu, W.J. Koros, Carbon molecular sieve dense film membranes derived from Matrimid® for ethylene/ethane separation, Carbon 50 (2012) 1488–1502. https://doi.org/10.1016/j.carbon.2011.11.019.

[197] S.Y. Tam, L.E. Scriven, H.K. Stolarski, Stress Effects in Drying Polymer Films, MRS Proc. 356 (1994) 547. https://doi.org/10.1557/PROC-356-547.

[198] M.G. De Angelis, T.C. Merkel, V.I. Bondar, B.D. Freeman, F. Doghieri, G.C. Sarti, Gas Sorption and Dilation in Poly(2,2-bistrifluoromethyl-4,5-difluoro-1,3-dioxole- *co* -tetrafluoroethylene): Comparison of Experimental Data with Predictions of the Nonequilibrium Lattice Fluid Model, Macromolecules 35 (2002) 1276–1288. https://doi.org/10.1021/ma0106090.

[199] P.R. Bevington, D.K. Robinson, Data reduction and error analysis for the physical sciences, 3. ed., [Nachdr.], McGraw-Hill, Boston, Mass., 2003.

[200] A. Tokarev, K. Friess, J. Machkova, M. Šipek, Yu. Yampolskii, Sorption and diffusion of organic vapors in amorphous Teflon AF2400, J. Polym. Sci. Part B Polym. Phys. 44 (2006) 832–844. https://doi.org/10.1002/polb.20725.

[201] R.R. Tiwari, Z.P. Smith, H. Lin, B.D. Freeman, D.R. Paul, Gas permeation in thin films of "high free-volume" glassy perfluoropolymers: Part I. Physical aging, Polymer 55 (2014) 5788–5800. https://doi.org/10.1016/j.polymer.2014.09.022.

[202] A.Yu. Alentiev, V.P. Shantarovich, T.C. Merkel, V.I. Bondar, B.D. Freeman, Yu.P. Yampolskii, Gas and Vapor Sorption, Permeation, and Diffusion in Glassy Amorphous Teflon AF1600, Macromolecules 35 (2002) 9513–9522. https://doi.org/10.1021/ma020494f.

[203] S. Thomas, I. Pinnau, N. Du, M.D. Guiver, Pure- and mixed-gas permeation properties of a microporous spirobisindane-based ladder polymer (PIM-1), J. Membr. Sci. 333 (2009) 125–131. https://doi.org/10.1016/j.memsci.2009.02.003.

[204] J.D. Moon, M. Galizia, H. Borjigin, R. Liu, J.S. Riffle, B.D. Freeman, D.R. Paul, Modeling water diffusion in polybenzimidazole membranes using partial immobilization and free volume theory, Polymer 189 (2020) 122170. https://doi.org/10.1016/j.polymer.2020.122170.

[205] Q. Liu, M. Galizia, K.L. Gleason, C.A. Scholes, D.R. Paul, B.D. Freeman, Influence of toluene on CO2 and CH4 gas transport properties in thermally rearranged (TR) polymers based on 3,3′-dihydroxy-4,4′-diamino-biphenyl (HAB) and 2,2′-bis-(3,4-dicarboxyphenyl) hexafluoropropane dianhydride (6FDA), J. Membr. Sci. 514 (2016) 282–293. https://doi.org/10.1016/j.memsci.2016.04.043.

[206] S.-E.K. Fateen, M.M. Khalil, A.O. Elnabawy, Semi-empirical correlation for binary interaction parameters of the Peng–Robinson equation of state with the van der Waals mixing rules for the prediction of high-pressure vapor–liquid equilibrium, J. Adv. Res. 4 (2013) 137–145. https://doi.org/10.1016/j.jare.2012.03.004.

[207] C.P. Ribeiro, B.D. Freeman, Carbon dioxide/ethane mixed-gas sorption and dilation in a cross-linked poly(ethylene oxide) copolymer, Polymer 51 (2010) 1156–1168. https://doi.org/10.1016/j.polymer.2010.01.012.

[208] M.G. De Angelis, T.C. Merkel, V.I. Bondar, B.D. Freeman, F. Doghieri, G.C. Sarti, Hydrocarbon and fluorocarbon solubility and dilation in poly(dimethylsiloxane): Comparison of experimental data with predictions of the Sanchez-Lacombe equation of state, J. Polym. Sci. Part B Polym. Phys. 37 (1999) 3011–3026. https://doi.org/10.1002/(SICI)1099-0488(19991101)37:21<3011::AID-POLB11>3.0.CO;2-V.

[209] T. Visser, G.H. Koops, M. Wessling, On the subtle balance between competitive sorption and plasticization effects in asymmetric hollow fiber gas separation membranes, J. Membr. Sci. 252 (2005) 265–277. https://doi.org/10.1016/j.memsci.2004.12.015.

[210] E. Ricci, A.E. Gemeda, N. Du, N. Li, M.G. De Angelis, M.D. Guiver, G.C. Sarti, Sorption of CO2/CH4 mixtures in TZ-PIM, PIM-1 and PTMSP: Experimental data and NELF-model analysis of competitive sorption and selectivity in mixed gases, J. Membr. Sci. 585 (2019) 136–149. https://doi.org/10.1016/j.memsci.2019.05.026.

[211] C.A. Scholes, S. Kanehashi, G.W. Stevens, S.E. Kentish, Water permeability and competitive permeation with CO 2 and CH 4 in perfluorinated polymeric membranes, Sep. Purif. Technol. 147 (2015) 203–209. https://doi.org/10.1016/j.seppur.2015.04.023.

[212] H. Liu, J. Li, Y. Hu, A transport model for sorption and desorption of penetrants in glassy polymer membrane, Fluid Phase Equilibria 158–160 (1999) 1035–1044. https://doi.org/10.1016/S0378-3812(99)00073-4.

[213] D.W. Krevelen, K. te Nijenhuis, Properties of polymers: their correlation with chemical structure their numerical estimation and prediction from additive group contributions, 4th, completely rev. ed ed., Elsevier, Amsterdam, 2009.

[214] A.F. Clark, Low temperature thermal expansion of some metallic alloys, Cryogenics 8 (1968) 282–289. https://doi.org/10.1016/S0011-2275(68)80003-7.

[215] J.J. Bissell, Proof of the small angle approximation sin $\theta \approx \theta$ using the geometry and motion of a simple pendulum, Int. J. Math. Educ. Sci. Technol. (2023) 1–7. https://doi.org/10.1080/0020739X.2023.2258885.